Alma Mater Studiorum - Università di Bologna

DOTTORATO DI RICERCA IN
ASTROFISICA
Ciclo XXXII

The AGN fuelling/feedback cycle in LERGs: the molecular gas component and its interplay with radio jets

Tesi di Dottorato

Presentata da:
Ilaria Ruffa

Supervisore:
Dott.ssa
Isabella Prandoni

Coordinatore Dottorato:
Chiar.mo Prof.
Francesco Rosario Ferraro

Co-supervisore:
Dott.
Robert A. Laing

Esame finale anno 2020

Settore concorsuale: 02/C1−Astronomia, Astrofisica, Fisica della Terra e dei Pianeti
Settore scientifico−disciplinare: FIS/05−Astronomia e Astrofisica

This Thesis has been carried out as part of an international research project involving the Istituto di Radioastronomia - Istituto Nazionale di Astrofisica (INAF) in Bologna, the Square Kilometre Array Organization (SKAO), and Oxford and Cardiff Universities

"E cosí questo immenso occhio
comincia a guardare
nella profonditá dello spazio,
forse proprio a centomila
milioni di miliardi di chilometri,
e noi comprendiamo che in fondo,
come tutte le cose fatte dall'uomo,
esso serve soltanto
a guardare dentro di noi"
Marcello Ceccarelli - Fisico e Astronomo

Contents

List of Tables

List of Figures

Introduction

Understanding the processes of galaxy formation and evolution is a key topic in modern astronomy. One of the most demanding requirements on galaxy formation theories is to reproduce the large-scale properties and scaling relations of early-type galaxies (ETGs) in the local Universe. How to prevent over-cooling of gas, why star formation (SF) quenches at late times, which processes are responsible for the observed scaling relations between super-massive black holes (SMBH) and stellar bulges, are all subjects of long-standing debates.

It is now widely believed that feedback processes associated with Active Galactic Nuclei (AGN) can play a role in shaping galaxies over cosmic time, by changing the physical conditions of the surrounding inter-stellar medium (ISM) or expelling it from the nuclear regions, thus impacting the star formation processes and the subsequent evolution of the host galaxy (e.g. Combes 2017; Harrison 2017). The many details of these processes, however, still remain poorly understood.

Feedback from AGN is commonly invoked in two (non exclusive) flavors: radiative and kinetic (see e.g. Fabian 2012, for a review). The former is postulated to occur through powerful winds that are typically associated to radiatively efficient (Quasar- or Seyfert-like) AGN; the latter is associated to strong radio-emitting outflows of relativistic particles (i.e. the radio jets).

In the local Universe ($z < 0.1$), radio galaxies (RGs), which by definition show strong kinetic (jet-induced) feedback, are typically hosted by massive ETGs: feedback from their jets is believed to play an important role in preventing cooling of hot gas in these objects, thereby suppressing star formation and maintaining them as passive, "red and dead" spheroids. Local RGs can be divided into two classes, mainly defined in terms of their optical spectra (e.g. Heckman & Best 2014): high-excitation radio galaxies (HERGs) and Low-excitation radio galaxies (LERGs). HERGs have spectra showing strong, quasar/Seyfert-like emission lines, accrete material at $\geq 0.01\ \dot{M}_{\rm Edd}$ (where $\dot{M}_{\rm Edd}$ is the Eddington accretion rate) and are radiatively efficient, thereby producing radiative as well as kinetic feedback. LERGs have spectra with weak, LINER-like emission lines, accrete at low rates ($\ll 0.01\dot{M}_{\rm Edd}$) and their feedback is almost entirely kinetic. LERGs are the dominant radio galaxy population in the local Universe (e.g. Hardcastle et al. 2007), and they are typically hosted by the most massive early-type galaxies (ETGs), with absolute K-band magnitude $M_{\rm K} \leq -25$ mag (corresponding to $M_* \geq 10^{11}\ M_\odot$; e.g.

Best & Heckman 2012).

Historically, it has been proposed that the dichotomy between HERGs and LERGs is a consequence of different fuelling sources (e.g. Hardcastle et al. 2007). In this scenario, HERGs are fuelled by cold gas transported to their nuclei through merging or collisions with gas-rich galaxies, whereas LERGs are powered by accretion from the hot phase of the inter-galactic medium (IGM), either directly (e.g. Allen et al. 2006) or more realistically after chaotic cooling (e.g. Gaspari et al. 2013; King & Nixon 2015; Gaspari et al. 2015, 2017). In this latter mechanism (now refereed to as *chaotic cold accretion*) thermal instabilities lead the hot gas from the galaxy halo to cool down to temperatures $\ll 10^3$ K, forming dense clouds of cold gas that can literally "rain" towards the central SMBH.

The most compelling evidence that cold gas can play a role in fuelling LERGs is that it is frequently detected in these sources, with masses that are potentially capable of powering the jets by accretion ($M_{\rm H_2} \sim 10^7 - 10^{10}$ M$_\odot$, e.g. Okuda et al. 2005; Prandoni et al. 2007, 2010; Ocaña Flaquer et al. 2010). The origin of the observed gas still remains unclear: it may cool from the hot gas phase or come from stellar mass loss, interactions or minor mergers. Despite the prevalence of LERGs, spatially-resolved studies of their molecular gas content are currently very few, thus the trigger mechanisms of these objects and associated AGN feeding/feedback processes are still poorly understood (e.g. Hardcastle 2018): investigating the nature of LERGs is crucial to shed light on the mechanisms which determine the observed properties of massive ETGs in the local Universe.

This Thesis is carried out as part of an international collaboration involving INAF-IRA, SKA Organisation, Oxford and Cardiff Universities. The overall project aims at a multi-phase study (stars, warm/cold gas, dust and radio jets) in the cores of a volume- and flux-limited ($z < 0.03$, $S_{2.7\ \rm GHz} \geq 0.25$ Jy) sample of eleven LERGs in the southern sky, with the primary aim of developing a better understanding of the fuelling mechanism in these sources. A comprehensive study of the various gas phases, as well as the stellar and dust components in this representative sample of massive, radio-loud ETGs would also enable us to isolate the role played by jet-induced feedback in the overall formation and evolution of ETGs. To this aim we have acquired Atacama Pathfinder EXperiment (APEX) ^{12}CO(2-1) integrated spectra (Prandoni et al. 2010, Laing et al. in preparation) and Very Large Telescope (VLT) Visible Multi Object Spectrograph (VIMOS) integral-field-unit spectroscopy for the entire sample (Warren et al., in preparation), Karl G. Jansky Very Large Array (JVLA) high-resolution continuum observations at 10 GHz for a sub-set of five sources and Atacama Large Millimeter/submillimeter Array (ALMA) Cycle 3 ^{12}CO(2-1) and 230 GHz continuum observations of nine objects. Archival Hubble Space Telescope (HST; or from ground-based optical telescopes), Multi Unit Spectroscopic Explorer (MUSE), and VLA images are also used, when available.

Within this general context, this Thesis aims at:

- shedding light on the physics, kinematics and origin (internal or external) of the molecular gas component;
- investigating the radio jets/molecular gas interplay on (sub-)kpc scales.

The study presented here is then focused on the analysis of the ALMA and the newly-acquired 10 GHz JVLA data of a sub-set of the overall sample.

The thesis is organised in seven Chapters:

- In the first Chapter, we summarise the general properties of the local AGN population, describing the observed dichotomy between HERGs and LERGs. Fuelling and feedback mechanisms are then illustrated for LERGs, the targets of this study.
- The second Chapter introduces the overall sample, first describing its general properties and then focusing on the characteristics of the sample members analysed in this Thesis.
- In the third Chapter we present ALMA observations, reporting the data reduction and analysis, and discussing the main results obtained for each source.
- Chapter four is focused on the modelling of the kinematics of the six sample members detected in CO(2-1) with ALMA. A discussion of the results is also provided.
- In Chapter five we discuss in detail the issue of the origin of the observed cold gas distributions, connecting the results of our kinematical modelling and other multi-wavelength constraints with theoretical expectations.
- Chapter six addresses the problem of the relative jet/CO disc orientation, which is analysed first in projection using ALMA observations only and then in 3D using also the newly-acquired JVLA data.
- In the conclusive Chapter we summarise the main results and discuss the future perspectives of this work.

Throughout this work we assume a standard ΛCDM cosmology with $H_0 = 70\,\mathrm{km\,s^{-1}\,Mpc^{-1}}$, $\Omega_\Lambda = 0.7$ and $\Omega_\mathrm{M} = 0.3$.

Chapter 1

Scientific background

1.1 Introduction

Recent studies of the contemporary (low-redshift) Universe have benefitted greatly from the information made available by high-quality wide-area imaging and spectroscopic surveys. Among these, the Sloan Digital Sky Survey (SDSS; York et al. 2000) has given a major contribution to our understanding of local galaxy populations. In particular, results from the SDSS have revealed the existence of a statistically significant bimodality in the colour and mass distribution of local galaxies (e.g. Baldry et al. 2004). Late Hubble type (disc) galaxies with significant ongoing star formation (i.e. blue optical colours) have typically small stellar masses (M_*) and are characterised by a tight, nearly linear correlation between their star formation rate (SFR) and M_* (e.g. Schiminovich et al. 2007). Such correlation is referred to as "star-forming main sequence". Early Hubble type galaxies (i.e. elliptical or lenticular galaxies; ETGs) with little ongoing star formation (and therefore red optical colours) have typically large M_* and give rise to the so-called "red - or passive - sequence"). The characteristic stellar mass that marks the transition between these two main populations is $M_* \sim 10^{10.5}$ $M_\odot$. A minor fraction of galaxies populates the region between the two sequences, the so-called "green valley". This bimodality is illustrated in Figure 1.1, which shows the volume-weighted distribution of galaxies in the plane identified by specific star-formation rate (sSFR = SFR/M_*) and stellar mass. Since the latter can be seen as a tracer of the averaged past star formation, sSFR is a measure of the current (ongoing) star formation compared to the averaged past one. The blue and red contours in Figure 1.1 indicate the volume-weighted distribution of the two main classes of active galactic nuclei (AGN) in the local Universe (radiative- and jet-mode AGN; see Section 1.2 for details). Interestingly, AGN tend to populate the green valley.

The bimodality has been interpreted as the result of galaxy evolution (e.g. Baldry et al. 2006; Salim et al. 2007; Faber et al. 2007; Drory et al. 2009; Lilly et al. 2013). Blue star-forming galaxies grow with time through the accretion of

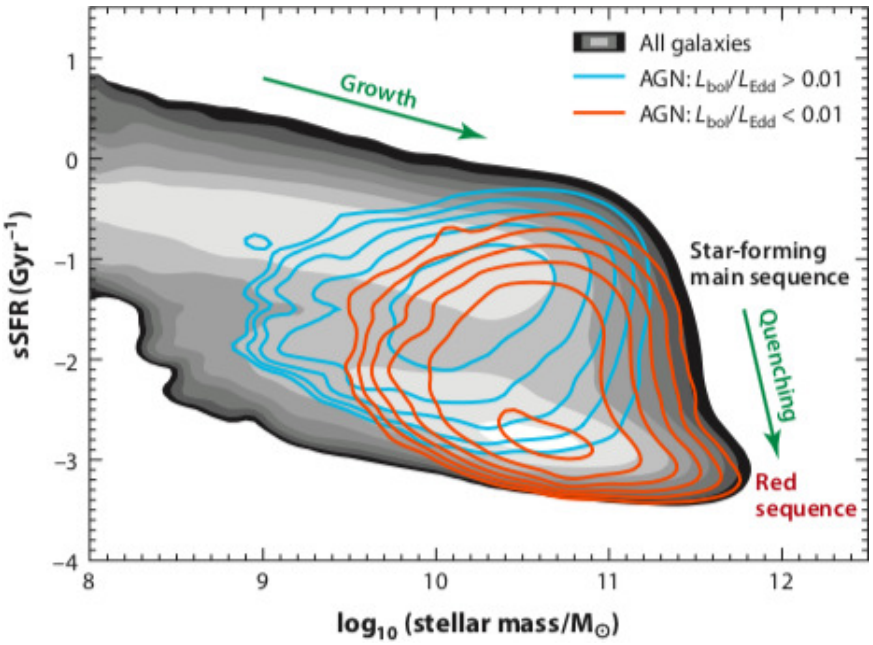

Figure 1.1: The distribution of galaxies in the local Universe in the plane specific star-formation rate (sSFR) vs stellar mass, adapted from Heckman & Best (2014). Data are taken from the SDSS main galaxy sample (Strauss et al. 2002). The grayscale indicates the volume-weighted distribution of all galaxies, with each lighter band indicating an increase by a factor of two. The blue and red contours show the volume-weighted distributions of high ($> 1\%$; mostly radiative-mode) and low ($< 1\%$; mostly jet-mode) Eddington-scaled accretion rate AGNs, with contours spaced by a factor of two.

cold gas from the cosmic web and (secondarily) through mergers with other galaxies, moving at nearly constant SFR along or towards the main sequence, where they are believed to spend most of their lifetime (e.g. Mancuso et al. 2016, and references therein). Various observational constraints (e.g. analysis of specific star formation rates, dust-corrected UV-optical colours, etc.) seem to suggest that main sequence galaxies can then follow two possible pathways to evolve towards the red sequence, depending on their optical classification as early- (i.e. bulge dominated) or late-type disc galaxies; see e.g. Schawinski et al. 2014). When late-type main sequence galaxies approach a certain critical mass (it is not yet clear whether this critical mass pertains to the stellar or the dark matter halo mass), the supply of gas gets interrupted, initiating the quenching of the star formation and causing them to travel across the transitional green valley, on timescales of up to several Gyrs. In early-type, bulge-dominated, main sequence galaxies it is likely to be a dissipative wet merger between gas-rich star-forming galaxies that first channels large amounts of gas reservoirs into the newly formed bulge, triggering a burst of star formation, then followed by the nearly instantaneous destruction of the newly acquired gas reservoirs, quenching the star formation process and causing the galaxy to rapidly

($\approx$ 1 Gyr) move towards the red sequence. Dissipationless dry mergers of red sequence galaxies are then believed to be responsible for the formation of the most massive (and passive) early-type galaxies (e.g. Oser et al. 2010).

The physical mechanism(s) that efficiently suppress episodes of star formation (either violently - as in early-type main sequence galaxies - or more slowly - as in late-type main sequence galaxies), expels gas from the system and maintains it gas-free over long times reproducing the observed properties is still unclear. Quenching may be due to various processes. Mechanisms like a change in the nature of gas accretion (i.e. rapid accretion of cold externally accreted gas at low mass versus slow accretion of hot gas at high mass, e.g. Dekel et al. 2009) or stellar feedback (i.e. supernova winds) are both included in numerical and semi-analytic simulations of galaxy evolution, but additional mechanisms are required to reproduce the observed properties of massive ($M_* > 10^{10.5}$ $M_\odot$) galaxies. One of the most popular scenarios invokes AGN feedback as a mechanism capable of suppressing the star forming activity by heating and/or expelling the available cold gas reservoirs (e.g. Combes 2017; Harrison 2017). In addition, heating due to AGN feedback is required in models to suppress star formation episodes in massive spheroids and maintain them on the red sequence (i.e. "red and dead"; e.g. Choi et al. 2015). Thus, in the current scenario, AGN play a crucial role in the evolution of galaxies. The many details of these processes, however, as well as their effective impact on the subsequent evolution of host galaxies are still poorly understood.

1.2 The AGN population in the local Universe

It is widely accepted that almost every galaxy hosts a super-massive black hole (SMBH; M$\simeq 10^6 - 10^{10}$ $M_\odot$) in its nuclear regions (e.g. Kormendy & Ho 2013), but only a fraction of them ($\sim 10\%$) have an active one (e.g. Padovani et al. 2011). Indeed, a SMBH primarily grows by accretion of the surrounding material and it is called "active" when, during this activity, the central engine reveals itself through some type of emission that is not related to the stellar activity within the galaxy. Mass accretion can be quantified through the mass accretion rate

$$\dot{M}_{\rm SMBH} = \frac{L_{\rm bol}}{\varepsilon c^2} \tag{1.1}$$

where ε is the mass-energy conversion factor (typically assumed to be 0.1), c is the speed of light, and $L_{\rm bol}$ is the bolometric luminosity. Since SMBH mass accretion produces huge amounts of energy ($10^{40} < L_{\rm bol} < 10^{48}$ erg s^{-1}, from the lowest to the highest luminosities) in small volumes (1$-$2 pc^3), it is considered one of the most powerful engines in the Universe, providing a significant contribution to the energy radiated over cosmic times. Galaxies which host an active SMBH are called active galactic nuclei (AGN).

Although the AGN population presents a large variety of observational properties (see e.g. Padovani et al. 2017, for a recent review on this subject), different AGN classes have historically been brought into a single framework by the standard Unified Model (e.g. Antonucci 1993; Urry & Padovani 1995), according to which all AGN belong to a small number of physical classes and many of the observed differences between them result from different viewing angles with respect to the observer's line of sight (the so-called "unification by inclination"). This unification scheme seems to explain well the differences observed within many of the AGN classes and has been tested and refined over the years (e.g. Elvis 2012; Bianchi et al. 2012; Netzer 2015; Mateos et al. 2016; Ramos Almeida & Ricci 2017; Padovani et al. 2017, and reference therein). These studies have emphasised that, in addition to the inclination, other physical parameters affect the observed differences between the various AGN classes. Such parameters include: the morphological type of the host galaxy, the accretion rate, the presence (or absence) of strong radio-emitting outflows of relativistic particles (i.e. the radio jets), and possibly the host galaxy environment. In particular, Heckman & Best (2014) present strong empirical evidence that the low-redshift ($z < 0.1$) AGN population can be divided into two main (intrinsically different) categories, mainly differentiated by the nature of their dominant (but not exclusive) energetic output (see also Antonucci 2012): radiative-mode and jet- (or kinetic-) mode AGN. These two AGN populations are disjoint not only in terms of the basic properties of the accretion process, but also on that of their host galaxies. A schematic representation of the two classes is shown in Figure 1.2.

Radiative-mode AGN possess all the characteristics typical of the "conventional" AGN described in the framework of the Unified Model (panel a of Figure 1.2). In this scheme, the central SMBH is surrounded by an optically thick and geometrically thin disc (Shakura & Sunyaev 1973) of infalling material, extending from spatial scales of the order of $\sim 10^{-3}$ pc down to a few gravitational radii[1]. The accretion disc has a radial temperature gradient, and the resulting total thermal (black body) continuum emission emerges from the extreme UV through to the visible portion of the electromagnetic spectrum. The accretion disc is surrounded by a hot ($T \approx 10^5$ K) corona that Compton-up-scatters the soft photons from the disc into the X-ray regime. As the X-rays impact the accretion disc their spectral energy distribution is modified through fluorescence and reflection off the accretion disc, producing characteristic features such as the K-shells iron lines visible in the soft ($2-10$ keV) X-ray band. The ionizing radiation from the disc and corona heats and photoionizes dense clouds of gas extending above and below the nuclear region, in

[1]The gravitational radius ($R_{\rm g}$) is usually defined as half of the Schwarzschild radius, $R_{\rm s} = \frac{2G\ M_{\rm SMBH}}{c^2}$, where G is the gravitational constant, $\rm M_{SMBH}$ is the black hole mass and c is the speed of light. $R_{\rm s}$ is defined as the radius of a sphere such that, if all the mass of an object is compressed within that sphere, the escape speed from its surface would equal the speed of light. A black hole is an example of an object smaller than its Schwarzschild radius.

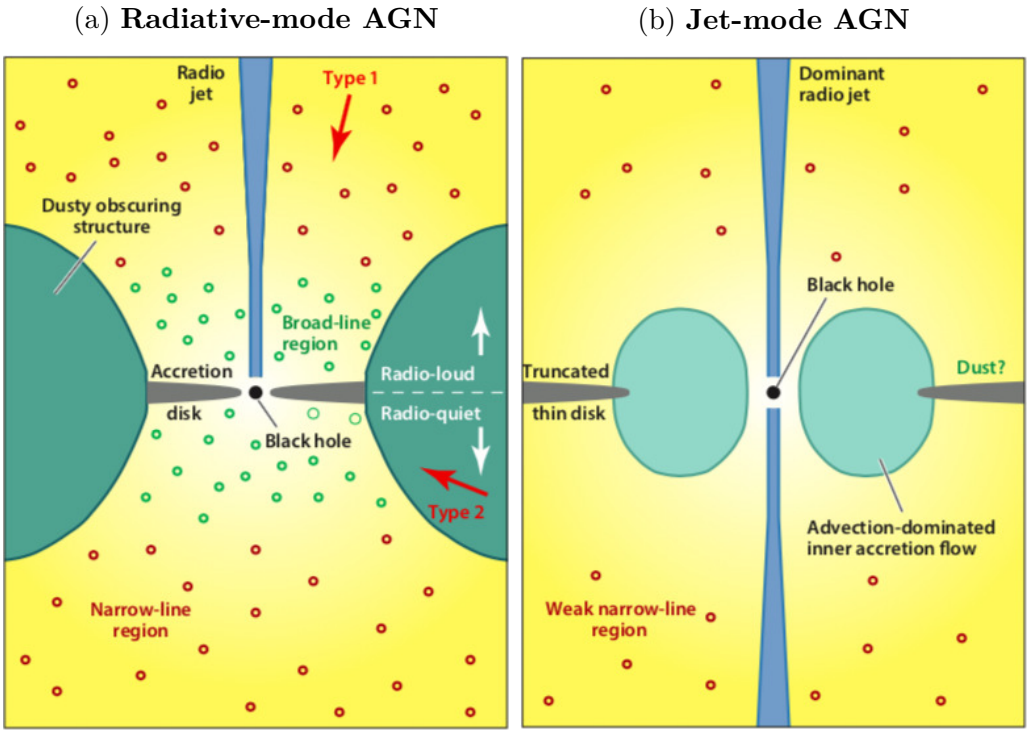

Figure 1.2: Scheme of the central engines of radiative-mode (panel a) and jet-mode (panel b) AGN adapted from Heckman & Best (2014). See the text for details.

close proximity to the central black hole ($r \sim 0.01 - 0.1$ pc), leading to the production of UV, optical, and near-infrared (NIR) permitted emission lines. The velocity dispersion of this population of clouds is typically several thousand kilometers per second, resulting in spectra characterised by broad ($\approx$5000 km s^{-1}) emission lines and leading to its designation as the broad-line region (BLR). On larger scales ($r \sim 1 - 100$ pc), the SMBH and accretion disc are surrounded by an axisymmetric region of dusty molecular gas (called the torus). In this region some of the incident UV/visible radiation from the accretion disc and the soft X-rays from the corona is absorbed by the dust, and then re-emitted as thermal infrared (IR) emission. The total column density of the torus ranges from $\approx 10^{23}$ to 10^{25} cm^{-2}. The highest column densities are sufficient to absorb even hard X-rays (up to 10 keV), and such heavily absorbed objects are called Compton-thick AGN. As ionizing radiation escapes along the polar axis of the torus, it photoionizes gas on circumnuclear scales ($r \sim 100 - 1000$ pc). This low density and velocity dispersion population of clouds produces narrow ($\approx 200 - 1000$ km s^{-1}) UV, optical, and IR forbidden and permitted emission lines and is therefore called the narrow-line region (NLR). According to the Unified Model, observing radiative-mode AGN from a sight line near the polar axis of the torus yields a direct view of the SMBH, the disc/corona, and the BLR. These are called Type 1 (or unobscured) objects. When radiative-mode AGN

are observed from a sight line near the equatorial plane of the torus, the central region is hidden and these are called Type 2 (or obscured) objects. The presence of an AGN can still be inferred in Type 2 objects from the thermal IR emission from the torus, from the hard X-rays transmitted through it, and from the NLR emission lines.

Historically, radiative-mode AGN have been called Seyfert galaxies or quasars (QSOs) depending upon their luminosity. In these objects the accretion occurs at high rates ($\gg 0.01\ \dot{M}_{\rm Edd}$, where $\dot{M}_{\rm Edd}$ is the Eddington accretion rate[2]), and is radiatively efficient, thus the dominant energetic output is in the form of electromagnetic radiation produced by the efficient conversion of the potential energy of the material accreted by the SMBH. A small fraction of radiative-mode AGN also launch an outflow of magnetically-confined relativistic particles, i.e. the jets, which are the source of the radio synchrotron emission. These objects are then called *radio-loud* AGN[3].

The second AGN category (jet-mode or kinetic-mode AGN; panel b of Figure 1.2) differs in many aspects from that of radiative-mode AGN. Jet-mode AGN lack many of the observational features typical of radiative-mode AGN (e.g. there is no clear evidence for the presence of the infrared-emitting dusty torus, accretion-driven emission lines are absent in their optical spectra, etc.), indicating they may represent a distinct class of sources, with a distinct formation history. The geometrically thin accretion disc is either absent or truncated at some inner radius (the transition may happen at radii of the order of a few tens of Schwarzschild radii), and replaced by a geometrically thick and optically thin structure in which the inflow time is much shorter than the radiative cooling time (e.g. Narayan & Yi 1995; Ho 2008). Such structures are called advection-dominated or radiatively inefficient accretion flows (ADAFs/RIAFs), whereby the material is accreted onto the SMBH at low rates ($\ll 0.01\dot{M}_{\rm Edd}$). A fundamental property of these radiatively-inefficient flows is that they are capable of launching two-sided radio-emitting jets (e.g. Merloni & Heinz 2007). The associated kinetic energy represents the dominant energetic

[2]It is useful, when comparing different kind of objects, to indicate the rate of accretion in terms of the Eddington limit. This is defined as the maximum luminosity beyond which radiation pressure will overcome gravity, and then material surrounding the SMBH will be forced away from it rather than falling inwards. The Eddington accretion rate is then a limiting quantity, that can be easily derived by setting the Eddington luminosity equal to the accretion luminosity: $L_{\rm Edd} = \dfrac{4\pi\, G\, M_{\rm SMBH}\, m_{\rm p} c}{\sigma_{\rm T}} = \varepsilon \dot{M}_{\rm Edd} c^2$. It then follows: $\dot{M}_{\rm Edd} = \dfrac{4\pi\, G\, M_{\rm SMBH}\, m_{\rm p}}{\varepsilon\, c\, \sigma_{\rm T}}$, where G is the gravitational constant, $M_{\rm SMBH}$ is the mass of the central SMBH, $m_{\rm p}$ is the mass of the proton, ε is the accretion efficiency, c is the speed of light and $\sigma_{\rm T}$ is the cross-section for Thomson scattering.

[3]There are many operational definitions of radio-loud AGN. The first (and still most widespread) one classifies AGN as *radio-loud* when the ratio between the radio (5 GHz) and optical (4400 Å) flux densities is > 10, they are considered *radio-quiet*, otherwise (Kellermann et al. 1989). In a recent review (Padovani 2017), however, it has been argued that AGN can be broadly classified as radio-loud whenever a significant fraction of their energy is released in the radio domain through the radio jets, and a new classification was proposed: jetted and non-jetted AGN (see also Padovani 2016).

output of this AGN class. Radiative emission in kinetic-mode AGN is weak, but can generate low-excitation emission lines, especially where the truncation radius of the thin disc is relatively small.

Missing from the above description are those AGN classified as low-ionization nuclear emission-line regions, or LINERs, characterized by very weak optical emission lines. Evidence has grown that at least some of them are not bona fide AGN (e.g. Yan & Blanton 2012). However, the more powerful LINERs are very likely to be members of the jet-mode AGN population (e.g. Ho 2008), albeit with rather modest radio luminosities ($10^{19} - 10^{21}$ W Hz^{-1} at 5 GHz).

1.3 The HERG/LERG dichotomy

According to the Unified Model, galaxies hosting a jetted AGN whose jets point at large angles ($\gg 0°$) with respect to the observer line-of-sight are called radio galaxies (RGs). These are an important class of objects for many reasons. First, they represent excellent laboratories to study the formation and ejection of relativistic radio jets and their connection to the central SMBH. Indeed, the powering mechanism of the jets is not yet fully understood: they may be powered by the accretion process or by extraction of mechanical energy from a spinning SMBH (e.g. McKinney et al. 2012). Studies of RGs are also the key to understand the different modes of accretion onto the SMBH, the origin and lifetime of the AGN, and the interplay between the central SMBH and the surrounding interstellar medium (ISM). Moreover, it has long been known that RGs are preferentially hosted by massive ETGs ($M_* > 10^{10}$ M$_\odot$) in the local Universe (e.g. Kauffmann et al. 2003; Best et al. 2005a), likely harbouring the most massive BHs ($M_{\rm SMBH} > 10^6$ M$_\odot$; e.g. Chiaberge & Marconi 2011). Therefore, these objects can be used to probe of the formation and evolution of giant nearby ETGs in relation to their BH activity.

Optical spectroscopy, and its cross-match with data from large radio surveys (e.g. NVSS[4], FIRST[5], etc.), provides a unique tool in the analysis of RGs, because it allows us to investigate the links between the radio structures, the properties of the AGN accretion mechanisms and their host galaxies. Indeed, narrow (permitted and forbidden) optical emission lines and their relative intensities (i.e. flux ratios) are powerful diagnostics to distinguish gas clouds ionized by young O stars associated with star-forming regions from those ionized by AGN radiation fields (see e.g. the well-known BPT diagnostic diagrams; Heckman 1980 and Baldwin et al. 1981). In addition they can be used to differentiate the intensity of the excitation radiation, and then obtain useful clues on the type of the nuclear activity in different AGN classes (e.g. Kauffmann et al. 2003; Kewley et al. 2006; Buttiglione et al. 2008). More specifically, the [OIII]λ5007Å line intensity and its ratio with the narrow

[4]NRAO (National Radio Astronomy Observatory) VLA (Very Large Array) Sky Survey (Condon et al. 1998).

[5]Faint Images of the Radio Sky at Twenty centimeters (Becker et al. 1995).

lines of the Balmer series (i.e. [OIII]λ5007Å/Hα and [OIII]λ5007Å/Hβ ratios) are the most widespread proxies used in such kind of studies (e.g. Kewley et al. 2006; Kauffmann & Heckman 2009; Heckman & Best 2014, and references therein); the [NII]λ6538Å/Hα, [SII]λ6717,6731Å/Hα and [OI]λ6300Å/Hα flux ratios are also typically used to distinguish low from high excitation conditions.

On the basis of such optical spectral properties, it is currently well established that the RG population in the local Universe can be divided into two main categories: High Excitation Radio Galaxies (HERGs) and Low Excitation Radio Galaxies (LERGs). This classification was first suggested by Laing et al. (1994), based on a spectrophotometric study of a well-defined sub-samples of 88 radio galaxies radio-selected from the 3CR catalog[6]. Indeed, they found a pronounced division in the narrow emission line optical properties of their sample of RGs, and classified as HERGs those sources with [OIII]λ5007Å/H$\alpha > 0.2$ flux ratios and the equivalent width of [OIII]> 3 Å (upper panel of Figure 1.3). On the other hand, galaxies with weak or undetectable [OIII] emission in comparison to Hydrogen lines were classified as LERGs (lower panel of Figure 1.3). Buttiglione et al. (2008, 2010) subsequently strengthened the results of Laing et al. by carrying out a more accurate optical spectroscopy analysis for a complete sub-sample of 113 radio sources from the 3CR catalog. They defined an "excitation index" parameter, EI$= \log_{10}$ ([OIII]/Hβ) $-1/3$ [$\log_{10}$([NII]/Hα) + $\log_{10}$ ([SII]/Hα) + $\log_{10}$ ([OI]/Hα)] and demonstrated this parameter to be bimodal. They then used it to classify galaxies, dividing the LERG and HERG populations at a value of EI$= 0.95$. As shown in the diagnostic diagrams presented in Figure 1.4, the separation between HERGs and LERGs is approximately located at [OIII]/Hβ line ratios ~ 5.

Best & Heckman (2012) later investigated about the HERG/LERG dichotomy by analysing the radio and optical properties of a sample of about 10000 sources within the redshift range $0.01 < z < 0.3$. To date, this constitutes the most complete and statistically significant work on this subject. Therefore, although a different selection method was adopted for the targets of this Thesis (see Chapter 2), in the following we use Best & Heckman (and correlated works) as main reference for describing the properties of HERGs/LERGs and their host galaxies. Best & Heckman (2012) constructed their sample by combining the spectroscopical data of the seventh data release of the SDSS (to first discriminate between HERGs and LERGs among the sample sources) with the NVSS and the FIRST surveys (to then analyse their relative radio properties). For many of the radio galaxies in this sample the set of emission lines needed to classify the host galaxies via the excitation index are either not detected, or the signal-to-noise ratio of the detections is too low. They therefore combined multiple approaches to carry out the classifications, depending

[6]The Revised version of the 3C catalogue (3CR) is based on new observations at a frequency of 178 MHz, and represents a survey of all sources North of $-5°$ with a flux density brighter than 9 Jy, except in the areas near the ridge of galactic emission. The 3CR catalog contains 298 extragalactic source identified as 195 radio galaxies and 53 radio quasars (Spinrad et al. 1985).

on the type and the strength of the line detection in each source (i.e. excitation index when all six emission lines were detected; diagnostic diagrams in Figure 1.4 when only four lines were reliably detected; strength of the [OIII] emission line, etc.). The obtained distribution was then plotted on the plane of EI versus [OIII] equivalent width (Fig. 1.5), for galaxies with both parameters measured (about a third of the overall sample). It is clear for this Figure that these two approaches provide a suitable classification of the radio sources, showing a clear bimodality in their distribution (albeit with a small contamination of LERGs on the left-hand side of the plot). Thanks to the high statistics, these results provide a valuable support to the scenario of a bimodal distribution of the local radio galaxy population.

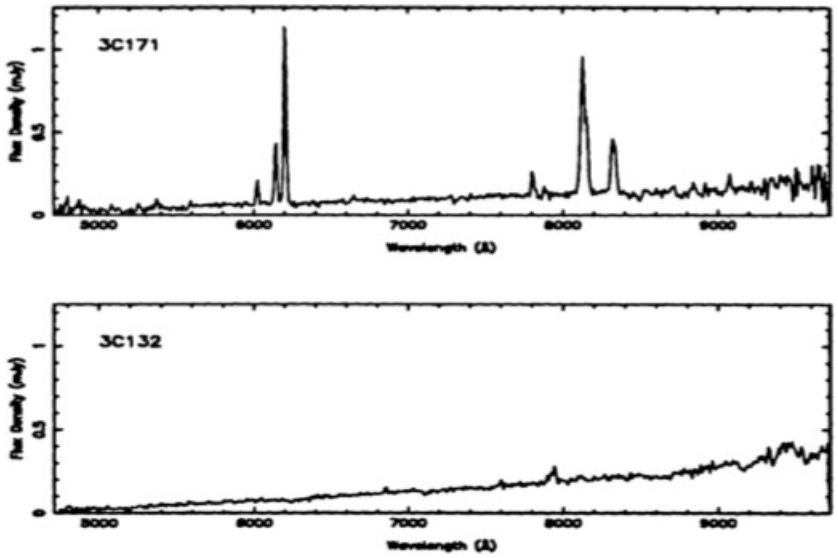

Figure 1.3: Examples of high excitation (upper panel) and low-excitation (lower panel) radio galaxies optical spectra adapted from Laing et al. (1994). See text for details.

The existence of such bimodality is also supported by the comparison between the radio and the [OIII]λ5007Å line luminosity (Fig. 1.6), showing that HERGs and LERGs tend to follow different correlations: HERGs have systematically higher [OIII] luminosities than LERGs at a given radio luminosity. Furthermore, there is a large overlap in the radio power distributions for HERGs and LERGs. This suggests that the two classes of objects should be associated with different accretion mechanisms, able to produce similar AGN manifestations in terms of radio emission and jet properties. Following these studies, it is now well established that the HERG/LERG bimodality can be associated with the two populations of AGN described in Section 1.2, whereby HERGs form a small sub-population of radiative-mode AGN (i.e. the sub-population that produces powerful radio jets), while LERGs are typically associated with kinetic-mode AGN (e.g. Heckman & Best 2014). Several studies (e.g. Best et al. 2005a,b, 2006; Kewley et al. 2006; Hardcastle et al. 2007; Kauffmann & Heckman 2009; Lin et al. 2010; Best & Heckman 2012; Sabater

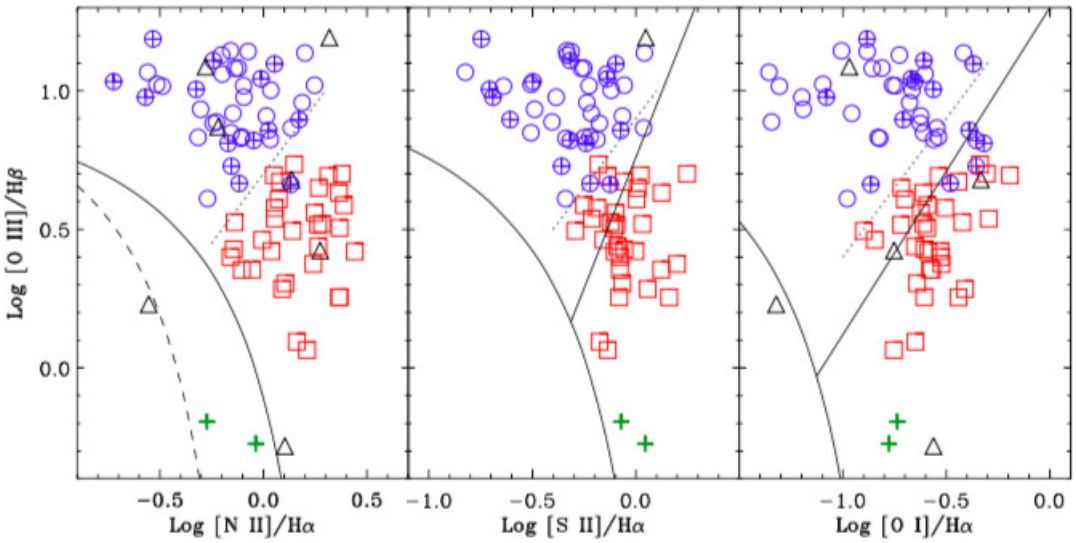

Figure 1.4: Optical line flux ratio diagnostic diagrams adapted from Buttiglione et al. (2010). Blue circles and red squares indicate HERGs and LERGs, respectively. Green crosses are for objects classified as "relic" AGN (i.e. objects with extremely low [OIII]λ5007Å/Hβ ratios). The black solid curves in each panel represent the separation between AGN (above the line) and starburst galaxies (below the line). The oblique dotted lines mark the approximate boundaries between HERGs and LERGs, while the oblique solid lines divide Seyfert-like from LINER-like objects.

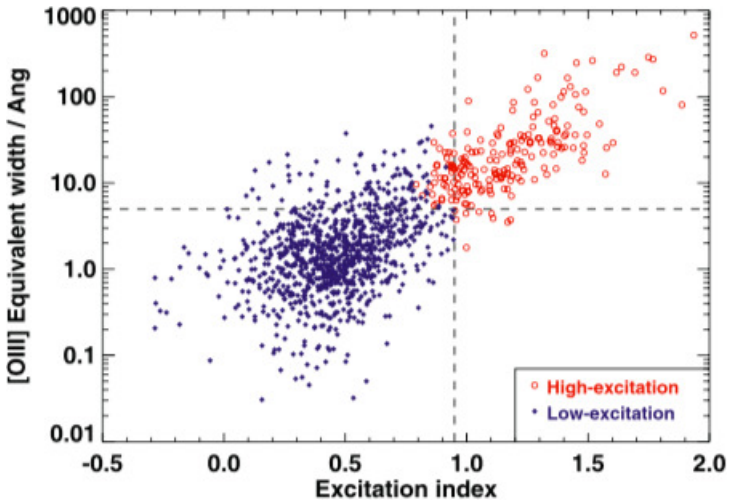

Figure 1.5: The distribution of the radio source sample of Best & Heckman (2012) on the [OIII] equivalent width versus excitation index (Buttiglione et al. 2010) plane.

et al. 2013, 2015, and reference therein) have also demonstrated that this dichotomy show up in a number of other fundamental properties, such as the radio morphology and luminosity, and the properties of the host galaxies, as discussed below.

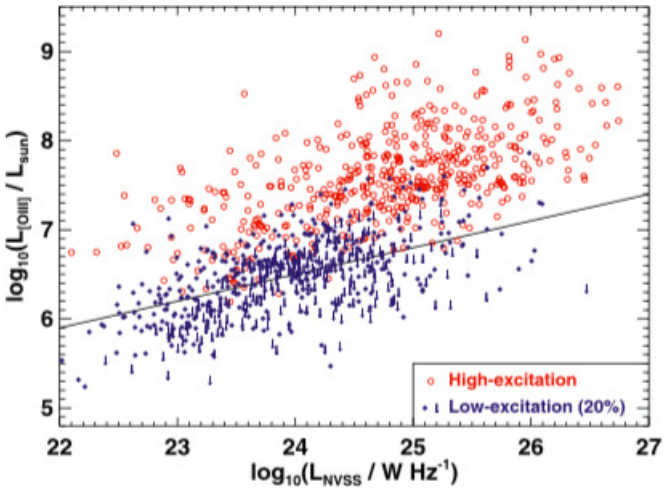

Figure 1.6: [OIII]λ5007Å emission line luminosity versus radio luminosity plane, adapted from Best & Heckman (2012). The solid line indicates an approximate lower limit to the distribution of the HERGs, below which all the sources can be classified as LERGs.

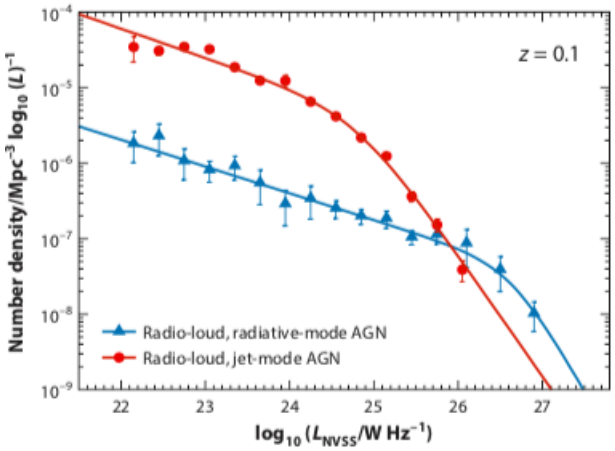

Figure 1.7: The local radio luminosity function at 1.4 GHz,derived separately for the HERG and LERG populations (adapted from Best & Heckman 2012).

The local radio luminosity functions of HERGs and LERGs were derived individually by Best & Heckman (2012), and are shown in Figure 1.7: LERGs dominate the radio source population at relatively low radio luminosities, while HERGs begin to dominate at the highest luminosities, beyond $P_{1.4\mathrm{GHz}} \sim 10^{26}$ W Hz^{-1} . However, both populations are found across the full range of the studied radio luminosities: at radio luminosities around $P_{1.4\mathrm{GHz}} \sim 10^{23}$ W Hz^{-1}, HERGs still constitute a few per cent of the overall radio-loud AGN population.

Strong observational evidence suggests that HERGs and LERGs are mostly disjoint in the properties of their host galaxies (e.g. Kauffmann et al. 2003; Best et al. 2005b; Kewley et al. 2006; Best & Heckman 2012). Figure 1.8 shows the distribu-

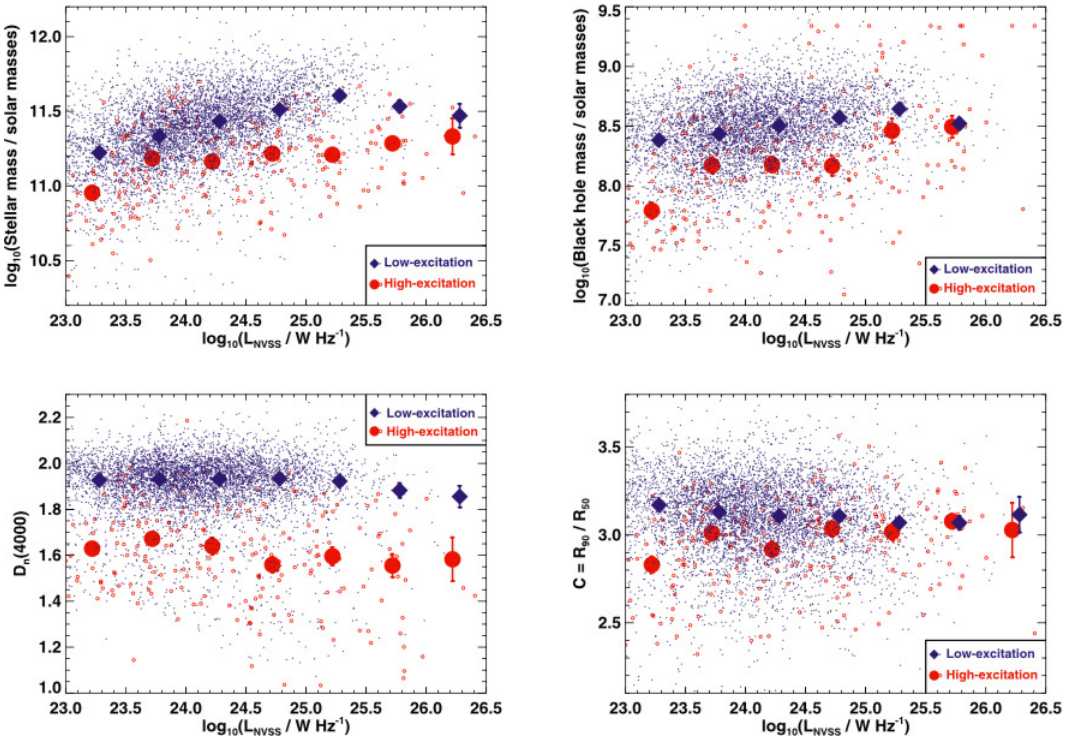

Figure 1.8: The distributions of stellar mass (upper left),black hole mass (upper right), 4000Å break strength (lower left) and concentration index ($C = R_{90}/R_{50}$, where R_{90} and R_{50} are the radii containing 90 and 50 per cent of the light, respectively; lower right), as a function of radio luminosity, for the LERG and HERG populations separately. The larger symbols indicate the mean values for each population in radio luminosity bins (adapted from Best & Heckman 2012).

tions of stellar mass, black hole mass, 4000 Å break strength[7] and concentration index[8] for the host galaxies of the LERG and HERG populations, as a function of radio luminosity. It is immediately clear from these plots that HERG host galaxies are less massive and have lower black hole masses than LERGs of the same radio luminosity. The 4000 Å break strengths of the HERGs are also lower than those of the LERGs of the same mass and radio luminosity, indicating the presence of a younger stellar population and more ongoing star formation. At low radio lu-

[7]The 4000 Å break (D) is a primary feature of the optical spectrum of a galaxy, caused by the blanket absorption of high energy radiation from metals in stellar atmospheres and by a deficiency of hot, blue stars. It is used to measure the mean stellar age of the galaxy. The 4000 Å break is expected to be stronger (i.e. larger D values) in ETGs (mainly populated by an old stellar population), and weaker in disc (late-type) galaxies (mainly formed of young stars).

[8]$C = R_{90}/R_{50}$, where R_{90} and R_{50} are the radii containing 90% and 50% of the light in the r optical band. C is a parameter providing information on the light concentration of a galaxy and, in turn, on its structure. It then allows to discriminate between early and late Hubble type objects. The characteristic value that marks the transition between the two types is $C \sim 2.8$.

minosities the concentration indices of the HERGs are also lower, whereas LERGs have larger concentration values and more extended light profiles. The average sizes and concentration indices may be related to the large-scale environment of these sources and, in turn, to their triggering mechanism (see Section 1.4). In this scenario, HERGs are preferentially located in poor environments, whereas LERGs are more likely hosted by central galaxies of groups and clusters (e.g. Gendre et al. 2013).

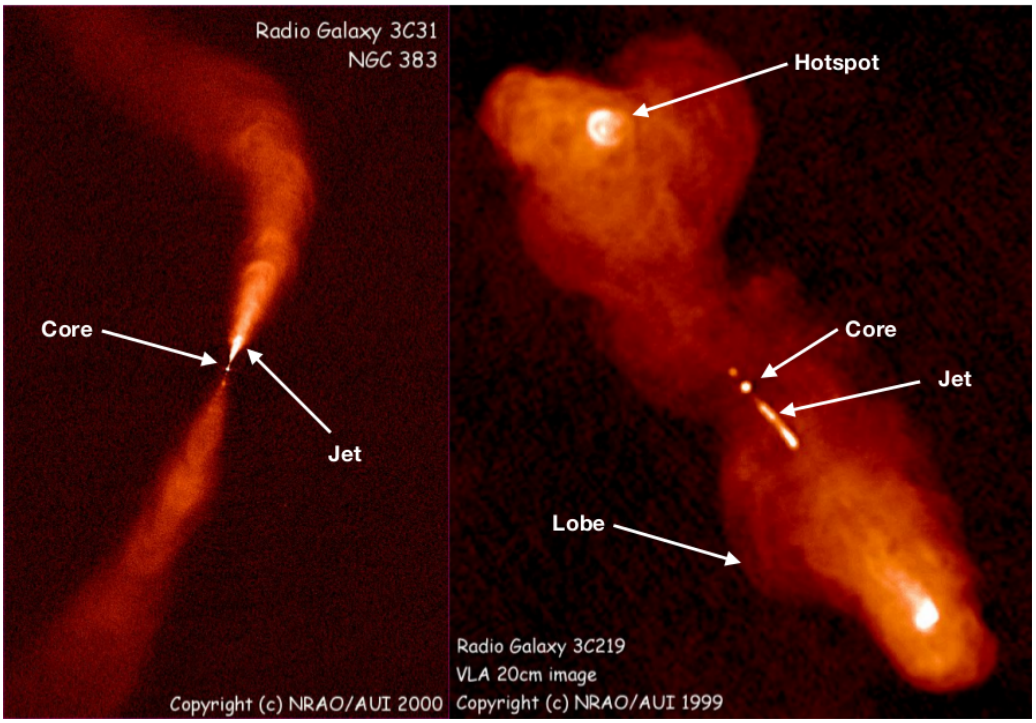

Figure 1.9: **Left panel:** VLA image at 8 GHz (3.6 cm) of the FRI radio galaxy 3C31 ($z = 0.017$) with $0.3''$ (FWHM) resolution. **Right panel:** Combined 1.4+1.6 GHz VLA image of the FRII radio galaxy 3C219 ($z = 0.1745$) with $1.4''$ (FWHM) resolution.

On the basis of their radio morphology, RGs have been historically classified by Fanaroff & Riley (1974) into two classes, known as FRI and FRII (Fig. 1.9). In this scheme, radio galaxies are classified as FRI when they are "edge-darkened": i.e. their emission is dominated by the core (i.e. the central compact component) and the inner jets. The outer regions of FRI sources typically consist of diffuse emission which progressively fades at increasing distances from the nucleus (left panel of Figure 1.9). Radio galaxies are instead classified as FRII when they are "edge-brightened": i.e. the dominant emission is far from the centre (right panel of Figure 1.9). In FRII sources the jets remain collimated (i.e. they do not show large radiative losses) and end in bright hot-spots (i.e. compact regions with high luminosity, presumably associated with jet termination shock). Hot-spots are embedded in large-scale extended structures known as lobes (probably tracing the emission of

swept-back material or back-flow from the regions shocked by the transit of the jet). In addition to morphology, the FRI and FRII populations are also differentiated in their typical radio luminosities and in the optical luminosity of their host galaxies. Sources with radio luminosity $L_{1.4\mathrm{GHz}} \lesssim 2 \times 10^{25}$ W Hz^{-1} sr^{-1} are often (but not always) FRI, while brighter sources are typically FRII (e.g. Gendre et al. 2010). There are indications that the separation between FRI/II in radio luminosity is strongly dependent on the optical luminosity of the host galaxy ($\propto L_{\mathrm{opt}}^2$; e.g. Owen & White 1991; Owen 1993; Owen & Ledlow 1994; Ledlow & Owen 1996), although recent work suggest instead that there is an upper bound to the FRI distribution in the $L_{\mathrm{opt}} - L_{\mathrm{radio}}$ plane (Mingo et al. 2019). The FRI/II morphological classification shows a broad overlap with the classification based on optical emission lines: indeed FRI and FRII sources are mostly associated with LERGs and HERGs, respectively (e.g. Lin et al. 2010). However, the relation is not one-to-one: there exists a large cross-population of FRII LERGs (Laing et al. 1994) and a smaller population of FRI HERGs (e.g. Heywood et al. 2007).

Recently, a third morphological class of radio galaxies has been proposed: the so-called FR0. FR0 sources are core-dominated (i.e. dominated by the core emission), with little (i.e. on scales of $1 - 3$ kpc) or no extended emission associated with the radio jets (e.g. Baldi et al. 2015, 2018, 2019). These objects are substantially weaker than the other two FR classes ($L_{1.4\mathrm{GHz}} \lesssim 2 \times 10^{20}$ W Hz^{-1} sr^{-1}), but show various characteristics typical of local LERGs (e.g. host galaxy properties, optical emission line spectra). For this reason they are believed to be a scaled-down version of FRI LERGs.

1.4 Origin of the dichotomy: the fuelling/feedback cycle

As outlined in Section 1.2, AGN are powered by accretion of the ISM onto the SMBH. There are three main elements that it is necessary to take into account when examining the fuelling of AGN: the source of the accreting gas, the mechanism by which it is transported to the vicinity of the BH (e.g. Hopkins & Quataert 2011), and the nature of the accretion flow onto the SMBH. A long-established scenario suggests a picture in which the HERG/LERG dichotomy is a consequence of different sources for the accreting gas (e.g. Hardcastle et al. 2007; Best & Heckman 2012). In this framework, high-excitation (radiative-mode) objects are fuelled at high rates in radiatively efficient standard accretion discs by cold gas, perhaps transported to their nuclei through mergers, collisions or interactions with gas-rich galaxies. In contrast, low-excitation (kinetic-mode) AGN are fuelled at relative low rates through radiatively inefficient accretion flows by gas associated with the hot X-ray emitting haloes surrounding the galaxy or its group or cluster. The different accretion modes trigger two types of feedback (described in detail in Section 1.4.2),

allowing the setting up of a fuelling/feedback cycle that it is thought to be responsible for the observed properties of AGN hosts in the local Universe (e.g. Best et al. 2006; Gendre et al. 2013, and reference therein).

The main aim of this work is to get a better understanding of the fuelling/feedback loop in LERGs which are, in term of their number, the dominant radio galaxy population in the contemporary Universe (e.g. Best & Heckman 2012; Janssen et al. 2012). Despite their importance, however, the many details of the AGN feeding/feedback processes in these objects are as yet poorly understood.

1.4.1 Fuelling

As outlined in Section 1.3, LERGs are typically hosted by the most massive nearby ETGs, with typical absolute K-band magnitudes of $M_{\rm K} \leq -25$ mag (corresponding to $M_* \geq 10^{11}$ $M_\odot$; e.g. Heckman & Best 2014). These objects are also generally dominated by an old stellar population, already formed at $z = 2$ (e.g. Thomas et al. 2005; Greene et al. 2015). Their red optical colours, along with their typical masses, place these objects in the high-mass tip of the "red sequence" of the diagram in Figure 1.1. Given these properties, LERGs have traditionally been believed to be mostly devoid of cool ISM reservoirs. This has been one of the strongest argument favouring the hypothesis that they are powered by accretion directly from the X-ray emitting hot phase of the inter-galactic medium (IGM; e.g. Hardcastle et al. 2007). In addition, massive ETGs, the typical hosts of LERGs, are predominantly found at the centres of groups and clusters, with associated hot gaseous X-ray-emitting haloes that provide not only a potential source of accreting gas, but also a repository for the bulk kinetic energy transported through the radio jet (e.g. Fabian 2012, see Section 1.4.2).

The rate of accretion of the hot gas at the accretion radius (the radius within which the gravitational potential of the central black hole dominates over the thermal energy of the surrounding gas) can be written using the Bondi formalism (Bondi 1952):

$$\dot{M}_{\rm Bondi} = 4\pi\lambda(GM_{\rm SMBH})^2 c_{\rm s}\rho \tag{1.2}$$

where ρ is the density of the gas at the accretion radius, $M_{\rm SMBH}$ is the central super massive black hole mass, G is the gravitational constant, $c_{\rm s}$[9] is the adiabatic sound speed of the gas at the accretion radius, and λ is a order-unity scaling numerical coefficient determining the accretion rate (and typically assumed to be equal to 0.25). For an efficiency η, the maximum power released from the black hole system

[9] $c_{\rm s} = \sqrt{\frac{\gamma kT}{\mu m_{\rm p}}}$, where T is the gas temperature at the accretion radius, k is the Boltzmann constant, γ is the adiabatic index of the hot gas, $\mu = 0.62$ is the mean atomic weight, and $m_{\rm p}$ is the proton mass.

accreting at the Bondi rate is:

$$P_{\rm Bondi} = \eta \dot{M}_{\rm Bondi} c^2 \tag{1.3}$$

Although very simplistic in its description of the circumnuclear environment of kinetic-mode AGN (i.e. it assumes spherically symmetrical geometry of the accreting gas with negligible angular momentum or magnetic fields), the hot accretion scenario was initially supported by Allen et al. (2006) by analysing a sample of nine nearby X-ray luminous LERGs. Indeed, they found that a strong correlation exists between the Bondi power ($P_{\rm Bondi}$) and the jet kinetic power ($P_{\rm jet}$), the latter computed from the estimated energy E required for the jets to inflate cavities in the surrounding X-ray emitting gas, normalized for the life time of these cavities $t_{\rm age}$:

$$P_{\rm jet} = \frac{E}{t_{\rm age}} \tag{1.4}$$

The correlation can be described by a power law of the form:

$$\log \frac{P_{\rm Bondi}}{10^{43} \text{erg s}^{-1}} = (0.65 \pm 0.16) + (0.77 \pm 0.20) \log \frac{P_{\rm jet}}{10^{43} \text{erg s}^{-1}} \tag{1.5}$$

and is shown in Figure 1.10. Both the slope and normalization of the relation (close to unity) indicate that simple Bondi accretion of hot gas could be powering these objects.

Based on the X-ray spectral analysis of 40 nearby ($z < 0.5$) radio galaxies observed with *Chandra* and XMM-*Newton*, Hardcastle et al. (2007) subsequently extended the work performed by Allen et al. (2006) by including in the analysis the HERG systems. They estimated the Bondi accretion rate through the X-ray observations of the hot gas using Equation 1.3. The (kinetic plus radiative) jet power, $P_{\rm jet}$, was estimated using the relation given by Willott et al. (1999):

$$P_{\rm jet}[W] = 3 \times 10^{38} f^{3/2} L_{151}^{6/7} \tag{1.6}$$

where L_{151} is the radio luminosity at 151 MHz in units of 10^{28} W Hz^{-1} sr^{-1}. The factor f parametrizes our ignorance of true jet powers, and is likely to depend on the type of source and its environment (as discussed by Willott et al. 1999). In the analysis of Hardcastle et al. (2007) it is assumed to be ~ 10 for both HERGs and LERGs (see also Blundell & Rawlings 2000). Figure 1.11 shows the Bondi Power versus the Willott jet Power, or (equivalently) the bulge K-band luminosity ($L_{\rm k}$) versus the 151 MHz luminosity. Here $L_{\rm k}$ is used as a proxy of the BH mass through the equation (Marconi & Hunt 2003):

$$\log_{10} M_{\rm SMBH} = 8.21 + 1.13 \times (\log_{10} L_{\rm k} - 10.9) \tag{1.7}$$

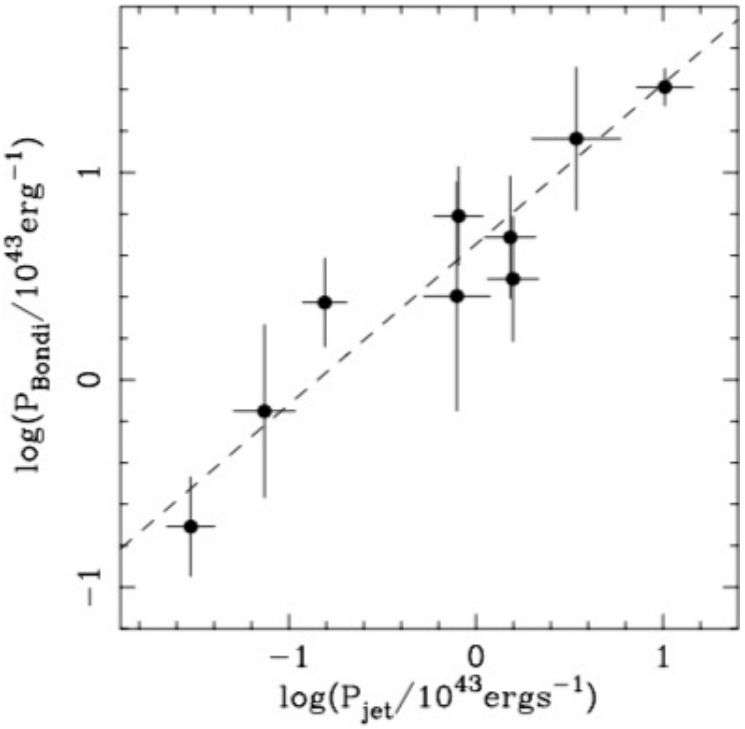

Figure 1.10: The logarithm of the Bondi accretion power (for an assumed efficiency $a = 0.1$ for the conversion of accreted rest mass into energy) versus the logarithm of the jet power, from Allen et al. (2006). Both quantities are in units of 10^{43} erg s^{-1}. The dashed line shows the best-fitting linear-plus-constant model.

As Figure 1.11 shows, FRI and FRII LERGs almost all lie within a factor of a few from the line of $P_{\rm jet} = P_{\rm Bondi}$. On the other hand, the population of FRII HERGs have jet powers exceeding the available Bondi powers by more than two orders of magnitude. In conclusion, Hardcastle et al. (2007)'s analysis confirms that jets can be fuelled by accretion of the hot X-ray emitting phase of the IGM for LERGs, while an extra supply of (cold) gas is needed for HERGs.

The validity of these results was then further extended and strengthened by Balmaverde et al. (2008), who carried out an analysis similar to that of Allen et al. (2006) for a sample of 44 nearby LERGs, finding a similar tight correlation.

Over the past decade, however, this "hot-mode" picture has been partly questioned (see Hardcastle 2018, for a review). Although the results mentioned above show that enough energy can be provided by accretion of hot gas at the Bondi rate, this does not prove that LERGs are powered in this way. The main reason is that the mass of material actually reaching the black hole may be significantly lower than the Bondi estimate, as spherical symmetry must break down at some radius. Russell et al. (2013) first reported a lower significance level for the Bondi/jet power correlation, suggesting that cold gas could also be a source of accretion in LERGs.

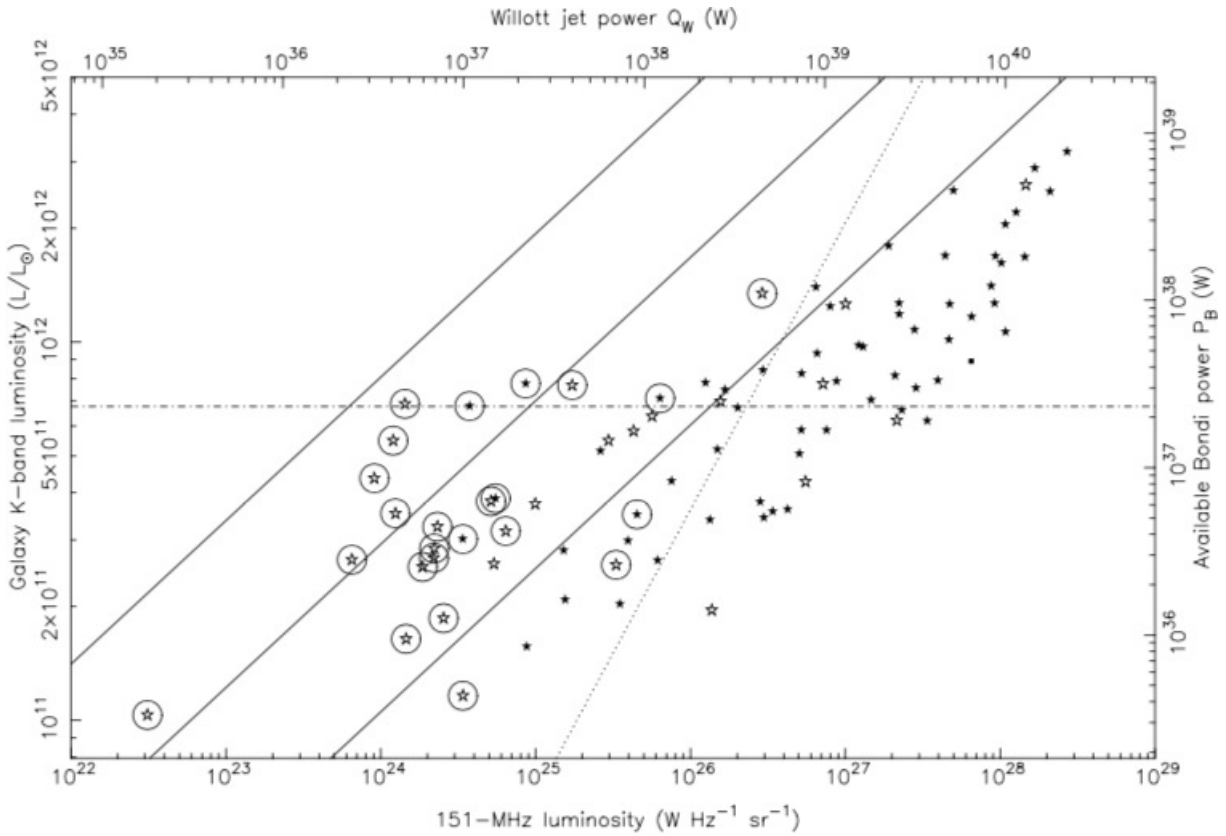

Figure 1.11: K-band host galaxy luminosity against 151 MHz radio luminosity for the HERG and LERG sample of Hardcastle et al. (2007) with available K-band magnitudes. The top and right-hand axes show the conversion of these observational quantities into jet power (derived from the Willott et al. (1999) relation) and Bondi power, respectively. Open stars are LERGs and filled stars are HERGs. A circle round a data point indicates a FRI. The central solid line shows equality between the predicted Bondi power and the Willott et al. jet power. The lines on either side are separated from the solid line by one order of magnitude, and so give an idea of the scatter expected on the Bondi luminosity from the observed dispersion in the $M_{BH} - K$ relation. The horizontal dot-dashed line shows the galaxy luminosity (corresponding to a black hole mass) at which the Bondi accretion rate is equal to 0.01 times the Eddington rate (so that $P_{\rm Bondi} = 10^{-3}$ $L_{\rm Edd}$), while the dotted line shows the line at which the Willott jet power equals 0.015 times the Eddington luminosity.

Bondi accretion cannot be ruled out, however, especially for low-power jets. For the most luminous LERGs (mainly brightest cluster galaxies, BCGs), the Bondi accretion rate estimates were found to fall more than two orders of magnitude short of the required jet powers (e.g. McNamara et al. 2011).

More realistic models for LERGs, requiring chaotic accretion, were first proposed

by Sanders (1981) and then elaborated by several authors, based on results from numerical simulations (see e.g. King & Pringle 2007; Wada et al. 2009; Nayakshin et al. 2012; Gaspari et al. 2013; King & Nixon 2015; Gaspari et al. 2015, 2017). These models (now referred to as *chaotic cold accretion*, CCA) were initially developed starting from the idea that the most powerful kinetic-mode radio sources are typically located in dense galaxy groups or clusters, frequently with strong cooling flows. Indeed, the hot plasma in galaxies, groups and clusters emits radiation mainly in the X-ray band due to bremsstrahlung from plasma at T$\geq 10^7$ K and line emission for lower temperatures. Gaspari et al. (2013, 2015), in particular, suggested that the non-linear growth of thermal instabilities in the hot haloes leads to the formation of decoupled dense cold gas clouds and filaments (that cool down to temperatures lower than 10^3 K) when the ratio between the time taken by the hot gas to cool due to radiative losses (i.e. the cooling time, $t_{\rm cool}$) and the time that would take the gas to collapse under its own gravitational attraction (i.e. the free-fall time, $t_{\rm ff}$)[10] is $\lesssim 10$. 3D simulations show that stochastic dissipative collisions between the cold gas structures significantly reduce their angular momentum, causing the cold gas to chaotically "rain" towards the central SMBH (Fig. 1.12). Within a few Bondi radii[11] chaotic inelastic collisions between the clouds are frequent enough to cancel their angular momentum, allowing them to accrete onto the SMBH at rates that can be two orders of magnitude higher than the Bondi rate. The small size of the cold gas clouds ($30 \leqslant r \leqslant 150$ pc) could explain the low accretion rates typical of kinetic-mode AGN (see Section 1.2).

The most compelling evidence that the cold ISM phase can play a role in fuelling LERGs is that cold gas and dust are often observed in LERGs, with masses in the range $\rm M_{H_2} \sim 10^7 - 10^{10} M_\odot$ (e.g. De Ruiter et al. 2002; Okuda et al. 2005; Prandoni et al. 2007, 2010; Ocaña Flaquer et al. 2010). These masses have been demonstrated to be potentially capable of powering the jets, at least in some cases. For example, the well-studied radio galaxy 3C31 (the prototypical LERG) has an estimated jet power $P_{\rm jet} \approx 10^{44}$ erg s^{-1} (Laing & Bridle 2002a), while the source lifetime is estimated to be $\sim 10^8$ years (Heesen et al. 2018). For an assumed conversion efficiency η from the rate of gravitational energy release to jet power, the required mass accretion rate for 3C31 is $\dot{M} = P_{\rm jet}/\eta c^2 \approx 0.02$ M$_\odot$ yr^{-1} if $\eta = 0.1$, and the molecular gas mass needed to fuel the AGN for 10^8 years would be $\sim 2 \times 10^6$ M$_\odot$ (assuming a constant accretion rate). The mass of molecular gas estimated in 3C31 is 2.1×10^9 M$_\odot$ (Okuda et al. 2005). This implies that, even if the efficiency is significantly smaller, there is fuel for any reasonable source lifetime. 3C31 is a luminous FR I radio galaxy ($\rm P_{.4GHz} \approx 7.1 \times 10^{23}$ W Hz^{-1}), and

[10] $t_{\rm cool} = 1.5nkT/n_{\rm e}n_{\rm i}\Lambda$, where T is the temperature of the emitting gas, k is the Boltzmann constant, $n_{\rm e}$ and $n_{\rm i}$ are the electron and ion density, respectively, and Λ is the cooling rate. $t_{\rm ff} = (2r/g)^{1/2}$.

[11] The Bondi radius is given by $r_{\rm B} = \dfrac{2G\,M_{\rm SMBH}}{c_{\rm s}^2}$, where G is the gravitational constant, $M_{\rm SMBH}$ is the mass of the SMBH, and $c_{\rm s}$ is the speed of sound.

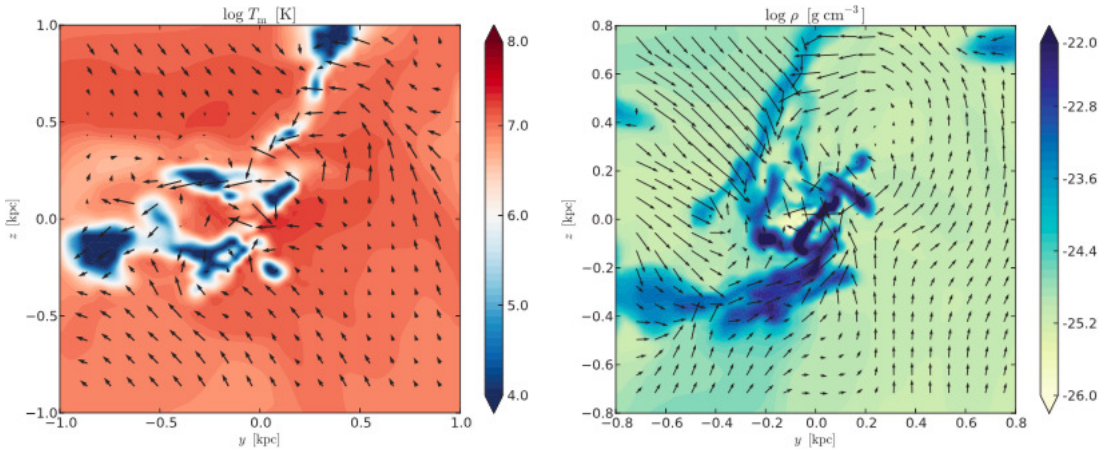

Figure 1.12: Snapshots of the logarithmic-scale temperature (left) and density (right) distributions (in units of K and g cm^{-3}, respectively) of the cooling gas in simulations of chaotic cold accretion (Gaspari et al. 2013), with the velocity field overlaid.

correspondingly smaller amounts of cold gas would be required to fuel less powerful sources, assuming efficient accretion. It is currently not clear whether the cold gas in LERGs originates from hot gas cooling (as predicted in the framework of CCA models) or it has a different origin (e.g. stellar mass loss, external accretion or interaction). The issue of the origin of the cold gas in LERGs is addressed in more detail in Chapter 5, where we present new evidence based on the multi-wavelength analysis carried out as part of this work.

The presence of large masses of cold gas alone is not a direct evidence of fuelling, however. Ocaña Flaquer et al. (2010) studied a sample of 52 nearby radio galaxies observed in CO(1-0) and CO(2-1) with, the Institute de Radioastronomie Millimetrique (IRAM) 30 m telescope. Eight of their detected galaxies (including 3C31; Figure 1.13) show CO integrated spectra exhibiting double-horned profiles, characteristic of gas in ordered rotation and stable orbits. The presence of a rotating cold gas disc in 3C31 has been clearly established first by Okuda et al. (2005) using RAINBOW (Nobeyama Millimetre Array plus the Nobeyama 45 m radio telescope) interferometric CO(1-0), and more recently by North et al. (2019) using ALMA CO(2-1) observations. The latter high-resolution ($0.18'' \times 0.1''$, corresponding to a physical scale of 58×32 pc^2) data, in particular, clearly show that the kinematics of the CO disc in 3C31 is dominated by regular circular rotation (Fig. 1.14), without evident departures from symmetry and/or clear signs of the presence of significant non-circular motions. Okuda et al. (2005) suggested that the cold gas in 3C31 is stable against gravitational collapse, preventing the fragmentation into dense gas clumps that can rapidly infalling and possibly fuelling the SMBH (e.g. Wada & Habe 1992): in cases like this there may be no or relatively little cold gas accretion.

Valuable support for the idea that cold gas can have a role in fuelling LERGs

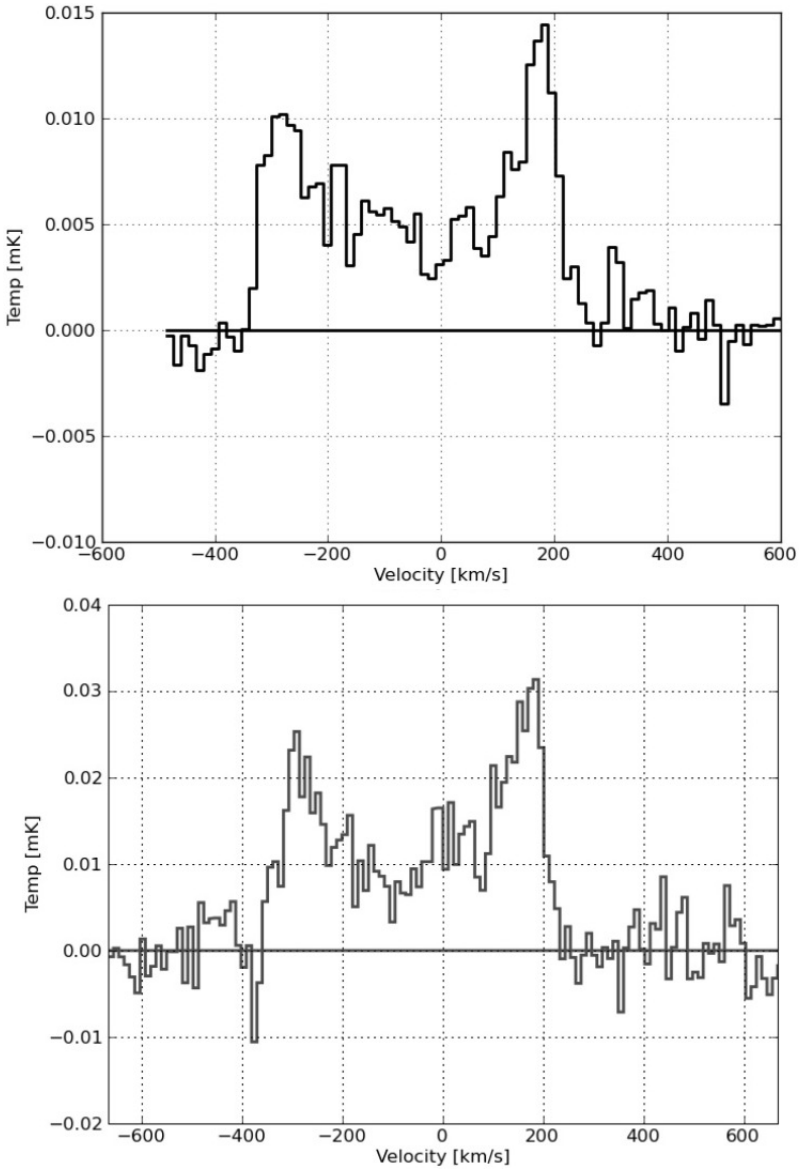

Figure 1.13: Integrated CO(1-0) and CO(2-1) spectra (upper and lower panel, respectively) of 3C31 adapted from Ocaña Flaquer et al. (2010). See text for details.

as been recently provided by Tremblay et al. (2016), who presented ALMA CO(2-1) observations of the BCG at the centre of the cluster Abell 2597 (z= 0.082). They find three deep, narrow absorption features in the integrated spectrum of this source (Fig. 1.15a), and concluded that they are inflowing cold molecular clouds moving toward the central black hole at ≈300 km s^{-1}. They suggest the clouds to be compact (≤40 pc in size) and in close proximity to the nucleus (within ≈100 pc), therefore probably playing a direct role in fuelling the black hole. Similar results have been obtained by Maccagni et al. (2018), who presented ALMA CO(2-1) ob-

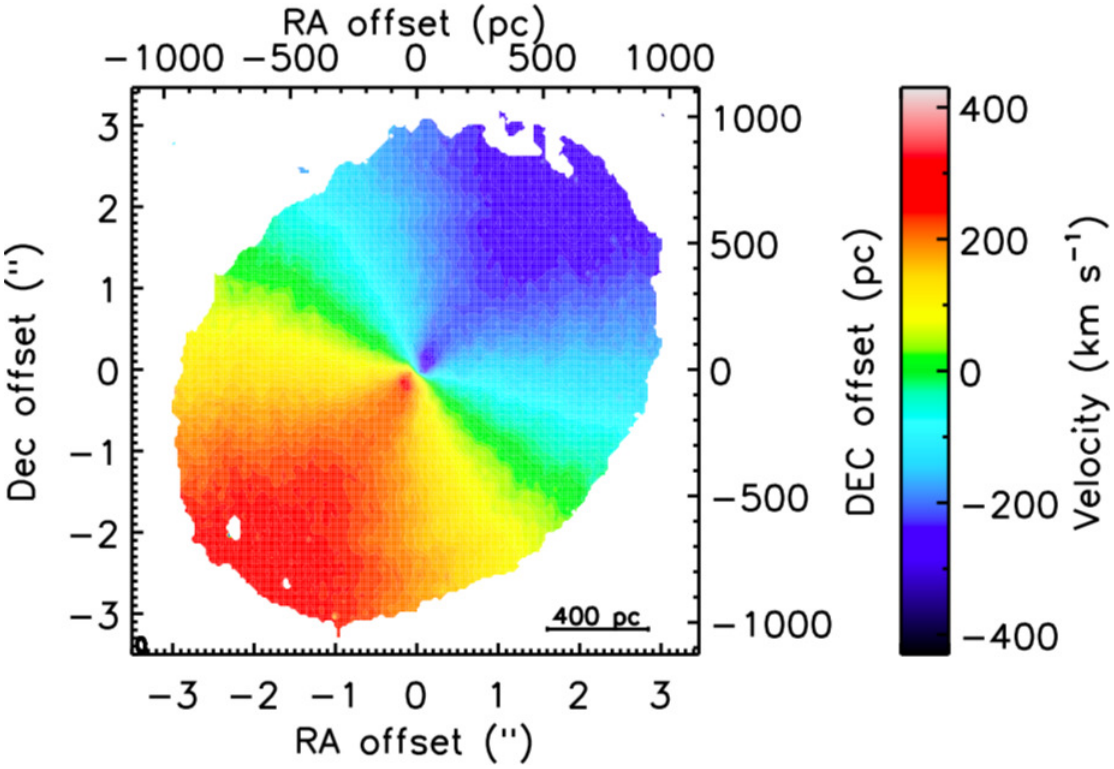

Figure 1.14: Moment one (i.e. mean velocity) map of the CO(2-1) emission in 3C31 presented by North et al. (2019). The ellipse at the bottom-left of the panel shows the synthesised beam size ($0.18'' \times 0.1''$).

servations of the LINER-like radio source PKS B1718−649. They suggest that the absorption feature observed in the integrated spectrum of the source (Fig. 1.15b) is likely tracing an ensemble of transient clouds, that are moving towards the central SMBH at a velocity of ≈365 km s^{-1}. Other spatially-resolved studies of molecular gas in radio-loud objects show a more complicated picture, with molecular gas that is outflowing or interacting with the radio jets, rather than infalling (e.g. Alatalo et al. 2011; Combes et al. 2013; Morganti et al. 2015; Oosterloo et al. 2017, See Section below).

Systematic high-resolution studies of cold gas in LERGs, like the one carried out as part of this work, are fundamental to determine the gas dynamical state and eventually assess the role of the cold ISM phase in powering these sources.

1.4.2 Feedback

As illustrated in Section 1.1, feedback from AGN is currently invoked in both semi-analytic models and numerical simulations to reproduce the observed properties of galaxies in the local Universe (e.g. Hopkins et al. 2006; Cattaneo & Best 2009; Ciotti et al. 2010). Feedback is generally proposed in two forms, which relate to the two

(a)

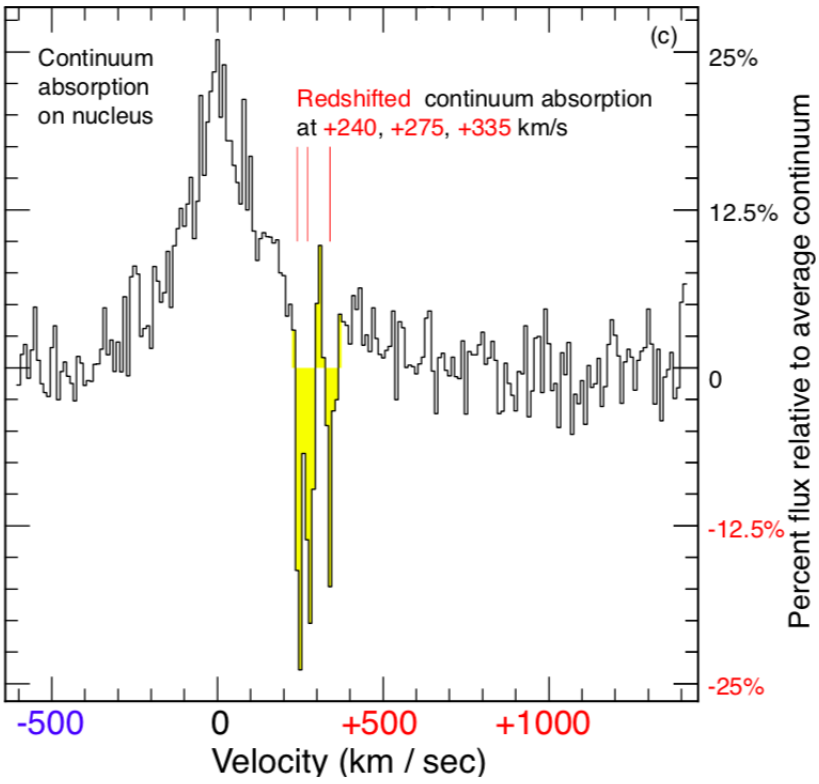

(b)

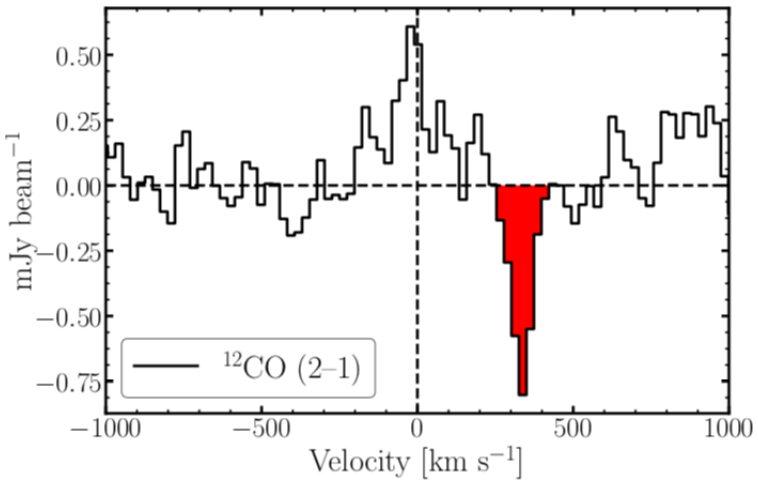

Figure 1.15: **(a)** CO(2-1) integrated spectrum of the BCG at the centre of the cluster Abell 2597 adapted from Tremblay et al. (2016). **(b)** CO(2-1) integrated spectrum of the LINER-like radio source PKS B1718â649 adapted from Maccagni et al. (2018). See the text for details.

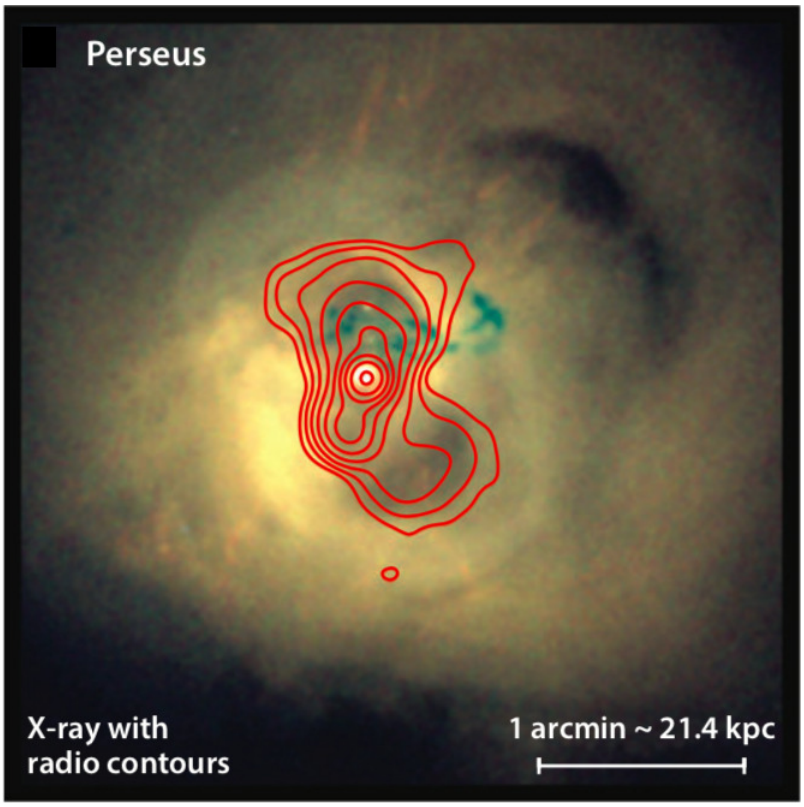

Figure 1.16: Composite X-ray map of the Perseus cluster (adapted from Heckman & Best 2014) with radio emission contours of the central BCG overlaid in red. The X-ray emission is colored such that hard X-rays (> 10 keV) are in blue and soft X-rays ($0.2 - 10$ keV) in red. The cavities in the X-ray gas inflated by the jet expansion can be identified as the dark regions co-spatial with the radio lobes.

fundamental modes of AGN activity described in Section 1.2: powerful AGN-driven winds and radio jets. Winds are thought to occur in galaxies with actively accreting BHs and are postulated to be responsible for the termination of star formation and the migration of galaxies from the blue star-forming main sequence to the red sequence. They may also be responsible for setting up the scaling relation between BH and bulge masses in early-type galaxies (e.g. $M_{\rm SMBH} \propto \sigma_*^4$; see Kormendy & Ho 2013, for a review). This feedback mode occurs in radiatively efficient objects, and will not be further discussed here.

In addition to a quenching mechanism, evolutionary models also require a mechanism that keeps red sequence galaxies "red and dead", by preventing them from growing further. Radio jets are often posited to be responsible for this mechanism. This so-called kinetic (or radio-mode) feedback is dominant in radiatively inefficient objects such as LERGs.

As discussed in Section 1.2, the bulk of the energy generated from the accretion

process in LERGs is channelled into powerful radio jets. One of the most spectacular and directly observable phenomena produced by the jets is the inflation of cavities in X-ray emitting gas. In fact, while driving their way outward, the jets, confined by the hot halo gas, produce expanding radio lobes filled with relativistic plasma, that inflate bubbles or cavities in the surrounding hot gas. The most extreme examples of this process occur in massive galaxies at the centre of groups and clusters (e.g. the Perseus cluster shown in Figure 1.16). These systems provide the most striking evidence that expanding radio jets heat the surroundings, balancing radiative cooling losses (described in Section 1.4.1) and preventing the gas from cooling further. This process is particularly emphasised in massive BCGs because the radiative cooling time of the X-ray haloes surrounding these systems can be substantially shorter than the Hubble time. In absence of a heating source, a rapid cooling flow would be expected to develop, whereby the temperature in the central regions of the cluster drops and the gas flows inward at rates of hundreds or even thousands of solar masses per year (e.g. Fabian 1994). Observations, however, show that the amount of cooling gas is only about 10% of the predicted cooling flow (e.g. David et al. 2001; Tamura et al. 2001). A heating source is then needed to balance radiative cooling losses, and this is almost certainly the energy deposited by the jets, through the mechanical work required to inflate the cavities. Analysis of cooling clusters indicates that the energy input from the radio jets is in rough balance with the energy losses from radiative cooling (see e.g. McNamara & Nulsen 2007, for a review on this subject). Because the repository of the AGN energy is the same gas which fuels the AGN, this mechanism offers the necessary conditions for a self-regulating AGN fuelling/feedback cycle. Hence this is also referred to as maintenance-mode feedback.

While massive cooling-flow clusters represent the most impressive examples of radio-mode AGN feedback, they are relatively rare. Best et al. (2006) extended the study of the role of radio-AGN feedback to a wider range of elliptical galaxies, by combining radio and X-ray luminosities. They demonstrated that the heating rate provided by radio-mode feedback provides a good match to the gas cooling rate for elliptical galaxies of all masses, and concluded that this process can efficiently counter-balance cooling and explain the old, red, and dead nature of nearby ETGs.

The impact of radio jets on the host galaxy environment can also be observed on galactic or sub-galactic scales. Indeed, numerical simulations have shown that jets expanding through the dense clouds of the ISM are forced to find the path of least resistance, while interacting and gradually dispersing the medium away from the jet axis (e.g. Wagner et al. 2012). This process produces turbulent cocoons of shocked gas along the path of the jets, that can be accelerated up to high velocities (> 1000 km s^{-1}) over a wide range of directions from the jet axis. Molecular gas outflows have been observed in a number of galaxies hosting (sub-)kpc scale radio jets through spatially-resolved studies (e.g. Alatalo et al. 2011; Combes et al. 2013; García-Burillo et al. 2014), supporting a scenario in which the distribution,

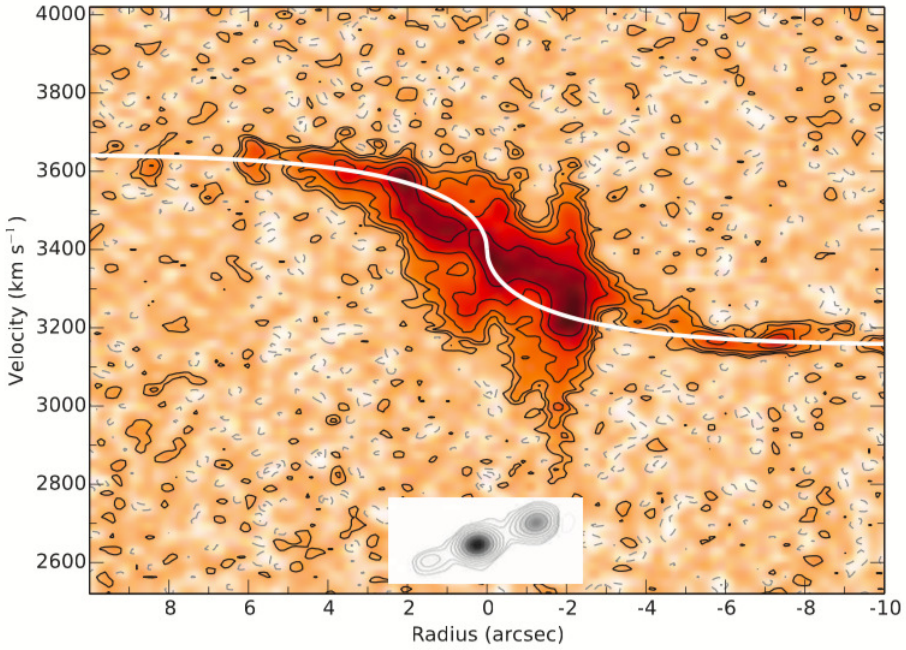

Figure 1.17: Major-axis position velocity diagram of the CO(2-1) disc of the Seyfert galaxy IC 5063 taken from Morganti et al. (2015). The white line gives the rotation curve derived from HST photometry and illustrates the expected kinematics of gas following regular rotation. The inset in the central-bottom region shows the position and morphology of the radio jet structure as seen by ALMA in a 230 GHz continuum image.

kinematics and physical condition of the gaseous ISM can be strongly affected by the interaction with the radio jets.

One extreme example of jet-ISM interaction on sub-galactic scales was reported by Morganti et al. (2015), who presented ALMA CO(2-1) observations of the southern radio-loud Seyfert galaxy IC 5063. These observations reveal the highly complex kinematics of the molecular gas in the region co-spatial with the radio jet, which appears to make its way through a circum-nuclear disc. Figure 1.17 shows the major-axis position-velocity diagram of this CO emission: while on large scales (i.e. regions far from the radio jets) the gas follows the regular rotation expected from the overall rotation curve of the galaxy (overlaid in white), the kinematics of the inner region (i.e. the region co-spatial with the radio jets) clearly deviates from it. In particular, the anomalously high gas velocities (up to 650 km s^{-1}) unequivocally indicate the presence of outflowing gas and, according to the models described above, can be explained as lateral gas dispersion driven by the expanding radio jets. Fast massive outflows co-spatial with the jet structure have been also previously observed in IC 5063 in HI (Morganti et al. 1998), warm H_2 (Tadhunter et al. 2014), and ionized (Dasyra et al. 2015) gas components, providing one of the best

examples to date of the multi-phase nature of jet-driven outflows. In a follow-up work, Oosterloo et al. (2017) used ratios of multiple molecular transitions to study the physical properties of this outflowing gas. Indeed, line ratios are modified in the vicinity of the radio source with respect to regions far from the jets, indicating significant differences in the physical conditions of the quiescent and interacting gas. Specifically, the gas conditions were found to vary from optically thick and sub-thermally excited in the unperturbed gas to optically thin with a high excitation temperature (> 50 K) in the region affected by the jet-driven outflow. Signs of gas fragmentation are also found, suggesting that the outflowing molecular gas is clumpy.

Another possible form of jet-ISM interaction is represented by entrainment of the surrounding gaseous medium into the jet flow, causing fragmentation of the gas clouds (similarly to what observed in the jet-driven cold gas outflow described above) and jets deceleration from relativistic speeds (e.g. Laing & Bridle 2002b). This is also one of the most plausible mechanisms of jet deceleration in FRI radio galaxies, which are observed to decelerate from relativistic speeds ($\sim 0.9c$) on parsec-scales to sub-relativistic speeds ($1000-10000$ km s^{-1}) on kpc-scales (e.g. Bicknell 1994; Rosen & Hardee 2000; Laing & Bridle 2002a, see also Chapter 6 for more details). Based on accurate modelling, the envisaged scenario is the following: an initially free relativistic jet comes into static pressure equilibrium with the surrounding ISM at a distance of the order of ≈ 100 pc from the nucleus. The jet starts to interact with the surrounding medium at this point, entraining matter that causes it to rapidly decelerate to sub-relativistic speeds, leading to the consequent widening of the jet flow. This picture is qualitatively supported by parsec-scale resolution VLBI observations of nearby FRI radio galaxies, such as NGC 315 (Venturi et al. 1993) and B2 1144+35 (Giovannini et al. 1999). In this latter case, in particular, a high resolution (1.46×0.66 mas, corresponding to spatial scales of the order of 2 pc) VLBI image at 8.4 GHz (Fig. 1.18) shows a core component (labelled as C) with extended symmetric structures on both sides (components D and E), identified as a two-sided jet. Emission from the South-East jet is also visible on scales between ≈ 50 and 60 pc from the core (components A, B, A1 and B1), showing a complex asymmetric structure. This morphology is interpreted as consistent with that predicted by the central spine-shear layer jet model (Laing 1996), presenting evidence of an interaction between the parsec-scale jet and the surrounding medium. Specifically, the interaction causes the deceleration of the shear layer (A, B and B1 components) from $0.95c$ (the estimated velocity of the jet flow close to the core) to $0.02c$ which thus brighten and widen, while the central (fainter) spine (A1 component) proceeds at relativistic velocities.

Resolved studies of LERGs are currently very few in number. As part of this Thesis we carry out a statistical investigation of the physical and kinematic properties of the molecular gas in a sample of LERGs, as well as a study of the interplay of the gas with the inner radio jets. This represents a significant step forward in

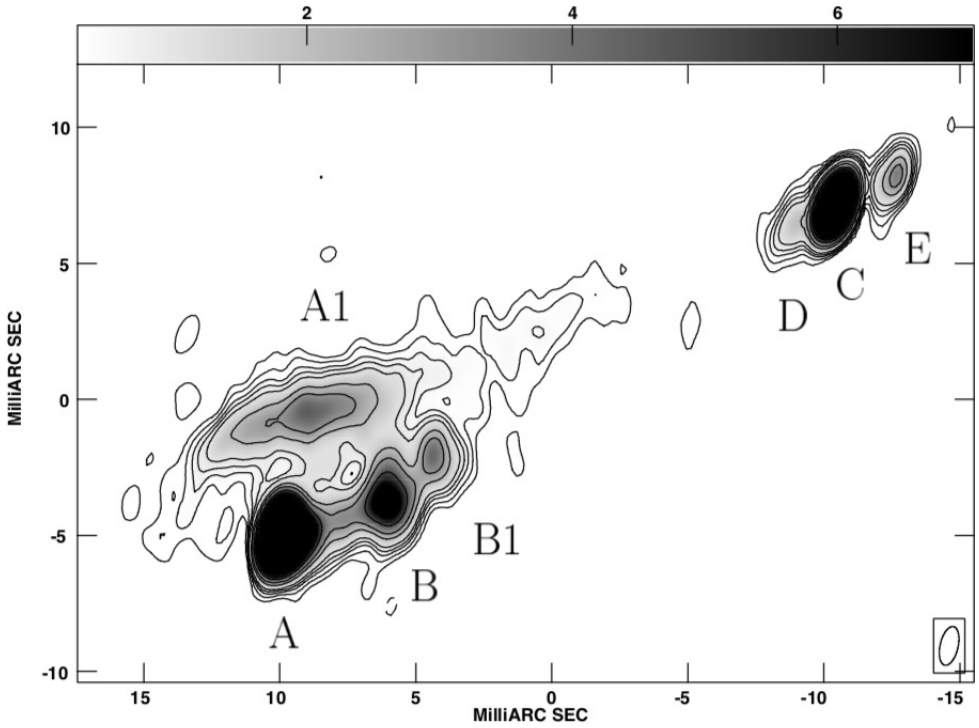

Figure 1.18: VLBI image at 8.4 GHz of the radio galaxy B2 1144+35 taken from Giovannini et al. (1999). The synthesized beam FWHM is 1.45×0.66 mas. The 1σ rms noise level is 0.05 mJy beam^{-1}. Contour levels are drawn at -0.2, 0.15, 0.3, 0.5, 0.7, 1, 2, 3, 5, 7, 10, 20, 30, 50, and 100 mJy beam^{-1}. See text for details.

our understanding on the fuelling/feedback cycle in LERGs.

Chapter 2

The sample

In this Chapter we present our radio galaxy sample. We first describe its general properties, and then we illustrate the main characteristics of the objects analysed in this Thesis, individually. This is based on the information available in the literature.

2.1 A southern radio galaxy sample

We have selected our sample from Ekers et al. (1989), who presented a complete sub-sample of 91 radio galaxies from the Southern Parkes 2.7-GHz survey. One of the main reasons behind this choice is that the Ekers et al. sources are all located in the declination range $-17^\circ < \delta < -40^\circ$, making them best-suited for ALMA observations, as well as for sub-arcsec radio imaging with the VLA ($\delta > -40^\circ$). Furthermore, this sample is well-defined in terms of radio flux density and optical magnitude, with a radio flux density limit of 0.25 Jy at 2.7 GHz and an optical magnitude limit of $m_v = 17.0$. From this sample and its cross-match with optical catalogues (such as the Carnegie−Irvine Galaxy Survey, CGS; Ho et al. 2011), we selected those sources satisfying the following criteria:

1. elliptical/S0 galaxy optical counterpart, in order to maximise the probability of selecting LERGs (see Chapter 1);

2. host galaxy redshift $z < 0.03$, i.e. objects close enough to be observed at high resolution with ALMA (within short integration times) and that can be easily detected even if hosting small amounts of CO.

This resulted in a complete volume-limited sample of eleven RGs matching the part of the (optically-selected) sample of Best & Heckman (2012) with radio and optical properties typical of LERGs (see Section 1.3). The general properties of the selected targets are listed in Table 2.1. All our sample RGs are characterised by low or intermediate 1.4 GHz radio powers ($P_{1.4GHz} \leq 10^{25.1}$ W Hz^{-1}), thus falling in the lower luminosity section of the curve in Figure 1.7, where the LERG population

Table 2.1: General properties of the southern radio galaxy sample.

Radio source	Host galaxy	z	$S_{1.4}$	log $P_{1.4}$	FR class	D_L	v_{opt}	T-type	Environment
			(Jy)	(W Hz^{-1})		(Mpc)	(km s^{-1})		
(1)	(2)	(3)	(4)	(5)	(6)	(7)	(8)	(9)	(10)
PKS 0007−325	IC 1531	0.0256	0.5	23.9	I	112.0	7681±25	-2.7 ± 1.7	isolated
PKS 0131−31	NGC 612	0.0298	5.6	25.1	I/II	130.4	8913±29	-1.2 ± 0.6	pair
PKS 0320−37	NGC 1316	0.0058	150	25.1	I	25.3	1734±10	1.7 ± 0.9	Fornax A
PKS 0336−35	NGC 1399	0.0047	2.2	23.0	I	20.4	1408±4	-4.6 ± 0.5	Fornax BCG
PKS 0718−34	–	0.0284	2.1	24.6	II	124.1	8900±128	-2.6 ± 2.7	isolated
PKS 0958−314	NGC 3100	0.0088	0.5	23.0	I	38.0	2629±20	-2.0 ± 0.5	pair
PKS 1107−372	NGC 3557	0.0103	0.8	23.3	I	44.5	3079±18	-4.8 ± 0.4	poor group
PKS 1258−321	ESO 443-G 024	0.0170	1.2	23.9	I	73.9	1689±18	-3.2 ± 0.5	A3537
PKS 1333−33	IC 4296	0.0125	4.5	24.2	I	53.9	3737±10	-4.8 ± 0.4	A3565 BCG
PKS 2128−388	NGC 7075	0.0185	0.9	23.8	I	80.3	5466±20	-3.8 ± 0.6	pair
PKS 2254−367	IC 1459	0.0060	1.2	23.9	I*	25.9	1689±18	-4.8 ± 0.6	group

Notes. Columns: (1) Name of the radio source. (2) Host galaxy name. (3) Galaxy redshift taken from the NASA/IPAC extragalactic database (NED). (4) Radio flux density at 1.4 GHz; this is the most accurate value given in NED and includes all the radio emission associated with the source. (5) Logarithmic-scale radio power at 1.4 GHz derived from $S_{1.4}$ and D_L. (6) Fanaroff-Riley class (Fanaroff & Riley 1974). (7) Luminosity distance derived from the redshift given in column (3) and assuming the cosmology stated in the Introduction. (8) Best estimate of the optical stellar velocity from NED, given in the LSRK system, for comparison with CO velocities (see Chapter 3). (9) T-type parameter indicating the morphological classification of the the host galaxy as done in the HyperLeda database, which defines as early type galaxies (Ellipticals and S0) those having $T < -0.5$. Specifically, according to this morphological classification, a galaxies is Elliptical if $T \leq -3.5$ and S0 if $-3.5 \leq T \leq -0.5$. (10) Large-scale environment.
*FR I structure on sub-arcsecond scale (see Tingay & Edwards 2015).

dominate. The majority of the sources have FR I radio morphologies (typically associated with LERGs; see Section 1.3), one is classified as intermediate between FR I and FR II, and one as FR II. Based on the optical spectroscopy available in literature (Tadhunter et al. 1993; Smith et al. 2000; Colless et al. 2003; Collobert et al. 2006; Jones et al. 2009), all of the radio galaxies in our southern sample have [O III] line luminosities such that they can be securely classified as LERGs (i.e. they fall below the solid line of Figure 1.6). Furthermore, our targets inhabit a wide range of environments (Table 2.1), allowing us to investigate the fuelling mode and feedback mechanisms also in LERGs located in low-density areas of the sky. These objects constitute a minor fraction of the local LERG population (typically found at the centre of groups and clusters; see Chapter 1) and are thus yet sparsely studied.

We note that, although part of the overall sample, NGC 1316 and NGC 1399 have not been included in the analysis carried out as part of this Thesis (see Chapter 3 for details); for this reason, they will not be discussed further.

2.2 Individual sources

2.2.1 IC 1531 (PKS 0007-325)

IC 1531 is a barred lenticular galaxy (SB0) in a low-density environment (O'Sullivan et al. 2007). It is the host galaxy of the bright extended radio source PKS 0007-325, associated with the active nucleus of the galaxy (Ekers et al. 1989). A 1.4 GHz contour map of the radio source produced from the NVSS (Condon et al. 1998) is shown in Figure 2.1.

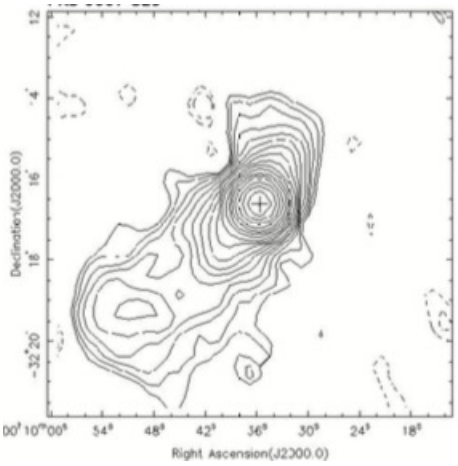

Figure 2.1: Radio contour map of IC 1531 at 1.4 GHz, produced from the NVSS data (Condon et al. 1998).

2.2.2 NGC 612 (PKS 0131-36)

NGC 612 is a peculiar lenticular galaxy viewed close to edge-on, characterised by an extensive and strongly warped dust distribution (Fig. 2.2a) in the equatorial plane and by a massive stellar disc (Westerlund & Stokes 1966; Fasano et al. 1996; Duah Asabere et al. 2016). The stellar disc was found to be regularly rotating, showing weak forbidden emission lines out to a radius of 28 kpc (corrected for our adopted cosmology) and a young stellar population (Goss et al. 1980; Holt et al. 2007). The disc is currently forming stars at a rate of ≈ 7 $M_\odot$ yr^{-1} (Duah Asabere et al. 2016). The presence of a stellar disc is exceptional for extended radio galaxies, at least in the luminosity range $10^{22} - 10^{25}$ W Hz^{-1} (e.g. Ekers et al. 1978; Véron-Cetty & Véron 2001; Emonts et al. 2008; Morganti et al. 2011; Mao et al. 2015, and references therein). NGC 612 is one of the few examples known to date.

A 140 kpc-wide disc of atomic hydrogen (HI) with $M_{HI} = 1.8 \times 10^9$ $M_\odot$ was detected by Emonts et al. (2008). A faint outer bridge of HI connects NGC 612 with the barred galaxy NGC 619, roughly 400 kpc away (Fig. 2.2b). This suggests that a past interaction between the two galaxies (or a minor merger event) may have

channelled large amounts of gas and dust into NGC 612, also triggering the associated radio source, PKS 0131-36. The large-scale radio map at 4.9 GHz published by Morganti et al. (1993) shows a weak core, a bright hot-spot at the outer edge of the more prominent eastern lobe, and a more diffuse western lobe with a total radio power $P_{1.4\,\mathrm{GHz}} = 1.5 \times 10^{25}$ W Hz^{-1}. A re-imaged version of the 4.9 GHz map of NGC 612 is presented in Figure 2.2c (see Chapter 3 for details on the archival VLA data re-analysis). The western lobe of NGC 612 show characteristics that place it at an intermediate stage between the FR I and FR II classes. NGC 612 has been proposed as the prototype of FR I/II hybrid sources (Gopal-Krishna & Wiita 2000), although this description is arguable on the basis of Figure 2.2c.

2.2.3 PKS 0718 -34

PKS 0718-34 is a radio source hosted by an elliptical galaxy located in a poor environment (Govoni et al. 2000a), and characterised by the presence of patchy dust structures in its central regions (Colbert et al. 2001). The 4.9 GHz VLA map published by Ekers et al. (1989) shows a poorly resolved, double-sided source (Fig. 2.3).

2.2.4 NGC 3100 (PKS 0958-314)

NGC 3100 is optically classified as a late-type S0 galaxy: it is characterised by a patchy dust distribution, a bright nuclear component, a nuclear bulge, and weak asymmetric arm-like structures in the outer disc (Fig. 2.4; Sandage & Brucato 1979; Laurikainen et al. 2006). It might represent a manifestation of galaxy evolution in the Hubble scheme, probably formed by gas-stripping mechanisms from late-type spiral galaxies. NGC 3100 is located in a poor group and forms a pair with the barred spiral galaxy NGC 3095 (De Vaucouleurs 1976).

Dopita et al. (2015) used the [NII]λ6584/Hα versus [OIII]λ5007/Hβ BPT diagnostic diagram (Baldwin et al. 1981) to classify the spectral properties of NGC 3100 as LINER-like.

NGC 3100 is the host galaxy of the radio source PKS 0958-314, which was classified by Ekers et al. (1989) as a symmetric double-sided object, extending down to the inner sub-kpc scales of the host galaxy.

2.2.5 NGC 3557 (PKS 1107-372)

NGC 3557 is a regular elliptical galaxy in a group (Govoni et al. 2000a). Its optical properties have been studied extensively (Colbert et al. 2001; Lauer et al. 2005; Capetti & Balmaverde 2005; Balmaverde & Capetti 2006). In particular, the optical spectrum of NGC 3557 was classified as LINER-like, with weak, low-ionization emission lines. Furthermore, a possible external origin of the ionized gas was argued, based on comparisons between the oxygen abundance and the stellar metallicity

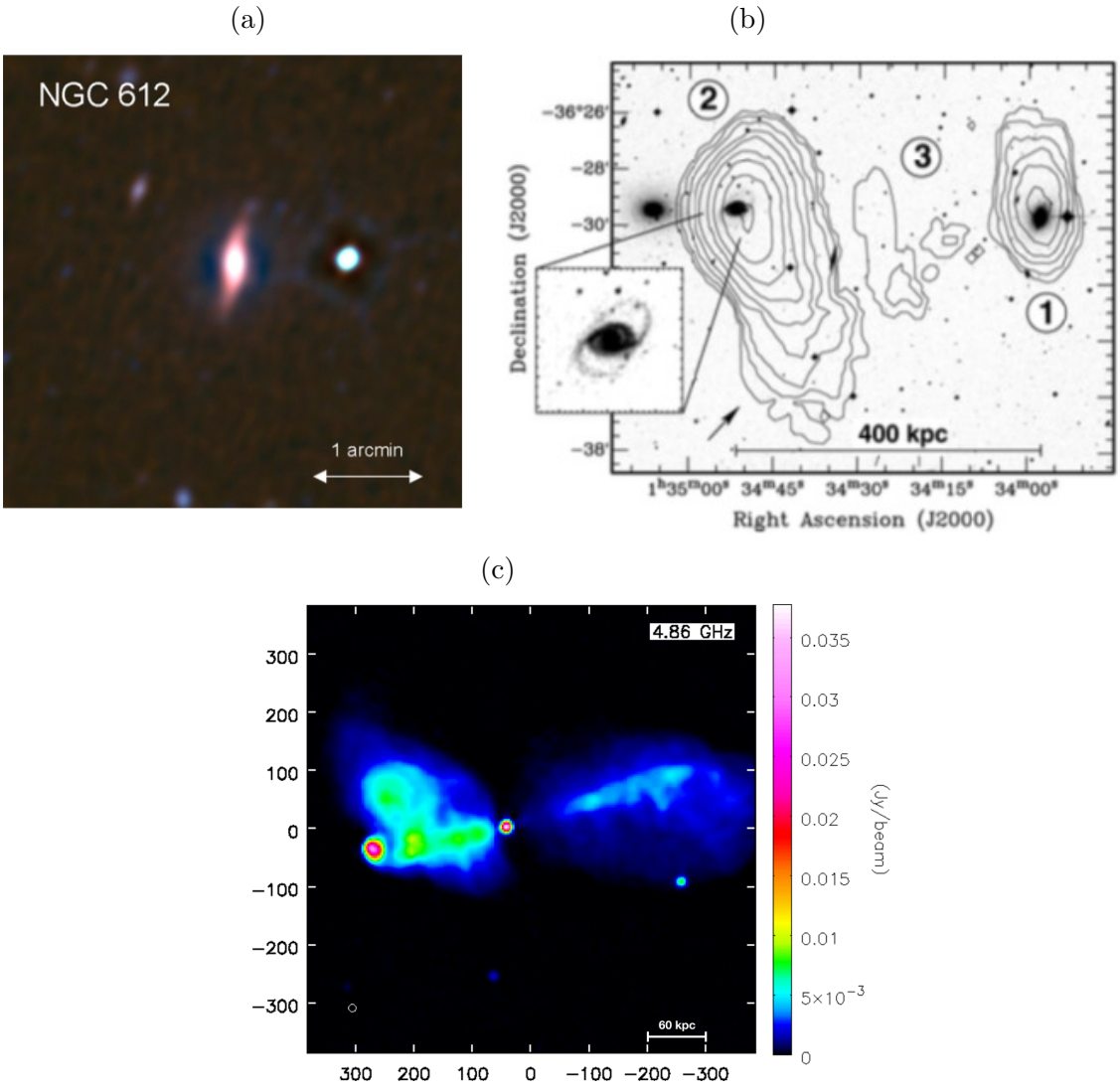

Figure 2.2: **(a):** Wide-field Infrared Survey Explorer (WISE; Wright et al. 2010) high-resolution dust image of NGC 612 adapted from Duah Asabere et al. (2016). Blue, green and red colours are for the W1 (3.4 μm), W2 (4.6 μm) and W3 (12 μm) WISE bands, respectively. **(b):** Total intensity contour map of the HI emission in NGC 612 and its companion galaxy NGC 619 taken from Emonts et al. (2008). The map is overlaid on an optical SDSS image (grey-scale). The regions marked as 1, 2 and 3 indicate the HI emission associated with NGC 612, NGC 619, and the bridge connecting the two, respectively. The spatial resolution is $218.1'' \times 178.4''$. The HI contour levels are drawn at 0.2, 0.4, 0.7, 1.1, 1.7, 2.3, 3.4, 4.5, 5.7 $\times 10^{19}$ cm^{-2}. **(c):** Total intensity radio map of NGC 612 at 4.8 GHz. The image is the result of a re-analysis of the data presented in Morganti et al. (1993), and reach a rms noise of 29 μJy beam^{-1}. The beam size ($13'' \times 13''$) and physical scale bar are drawn in the bottom-left and bottom-right corner, respectively. The wedge on the right shows the colour scale. The compact and circular pattern visible on the right-hand side of the plot is an artefact caused by the correction for primary-beam attenuation.

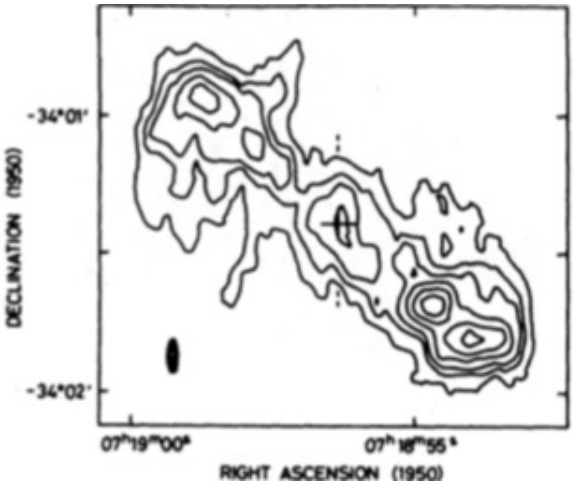

Figure 2.3: 4.89 GHz VLA map of PKS 0718-34 from Ekers et al. (1989). Contours are drawn at 40, 80, 120, 200, 300, 400 mJy beam^{-1}. The beam size (drawn in the bottom-left corner) is $2.4'' \times 8''$.

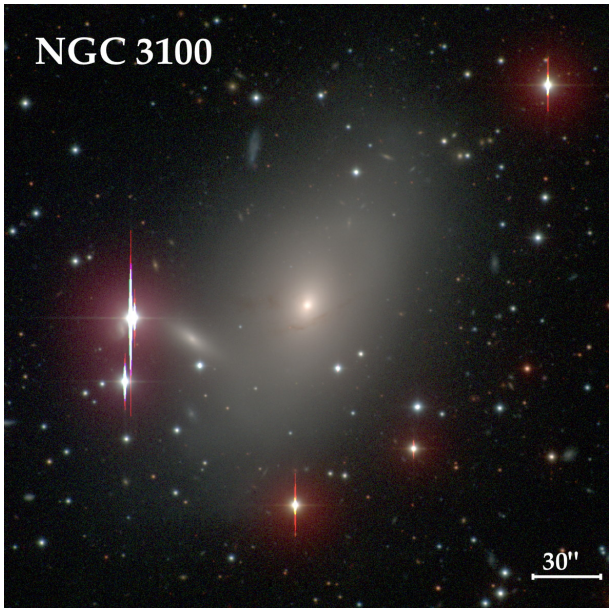

Figure 2.4: Colour-composite (Harris B, V, R and I filters; λ from 300 to 1100 nm) optical image of NGC 3100 retrieved from the Carnegie-Irvine Galaxy Survey (CGS) database. The galaxy was observed with the Tek5 CCD camera of the du Pont 2.5-meter telescope at Las Campanas Observatory. The exposure times were 120 - 360 s in each filter, with resolutions ranging from $0.77''$ (B) to $0.62''$ (I).

(Annibali et al. 2010). High-resolution HST observations of NGC 3557 clearly show the presence of a prominent dust ring in the central regions (Fig. 2.5a; Lauer et al. 2005), with a radius of $r = 0.95''$ (Capetti & Balmaverde 2005).

NGC 3557 is the host galaxy of the radio source PKS 1107-372, which was first imaged by Birkinshaw & Davies (1985) (Fig. 2.5b). Using low-resolution VLA observations at 4.9 GHz they found a double-sided source with two bright knots located to the south-west of the nucleus, and a 31 kpc long radio jet to the north-east. The structures on the two sides of the source appear well aligned.

(a) (b)

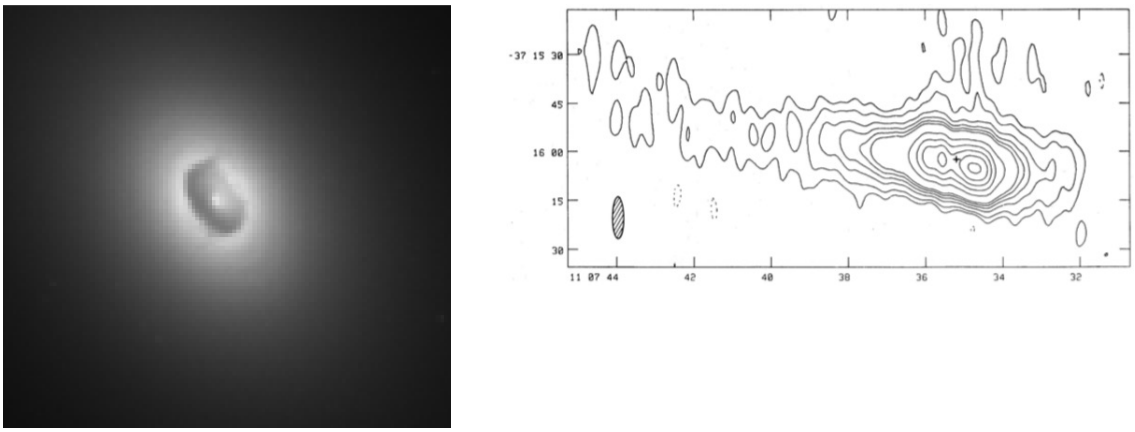

Figure 2.5: **a:** Archival HST image of NGC 3557 retrieved from the Hubble Legacy Archive at the Canadian Astronomy Data Centre (CADC). The galaxy is observed with the HST Wide-Field and Planetary Camera 2 (WFPC2) through the F555W optical filter ($\lambda \approx 472 - 595$ nm). The pixel scale, image FWHM and size are 0.1 arcsec pixel^{-1}, 0.08 arcsec, and 11×7 arcsec^2, respectively. **b:** Low-resolution radio image of NGC 3557 at 4.8 GHz taken from Birkinshaw & Davies (1985). Contours are drawn at -0.5, 0.5, 1, 2, 3, 4, 5, 10, 15, 20, 25, and 30 mJy.

2.2.6 ESO 443-G 024 (PKS 1258-321)

ESO 443-G 024 is an elliptical galaxy in the cluster Abell 3537 (Govoni et al. 2000a). It is the host galaxy of the FR I radio source PKS 1258-321. A low-resolution 4.9 GHz VLA map of this source, re-imaged from the available archival VLA data, is shown in Figure 2.6. The map shows the overall structures of the source, which has a lobed twin-jet FRI morphology. The jet structure is symmetrical on large scales; side-to-side asymmetry on scales of a few arc-seconds is also evident from Figure 2.6, likely indicating that the NW jet is approaching.

2.2.7 IC 4296 (PKS 1333-33)

IC 4296 is a giant elliptical galaxy, companion of the galaxy IC 4299 and located at the centre of the small cluster Abell 3565 (Grossova et al. 2019). Based on HST observations, it is optically classified as an obscured galaxy with a prominent

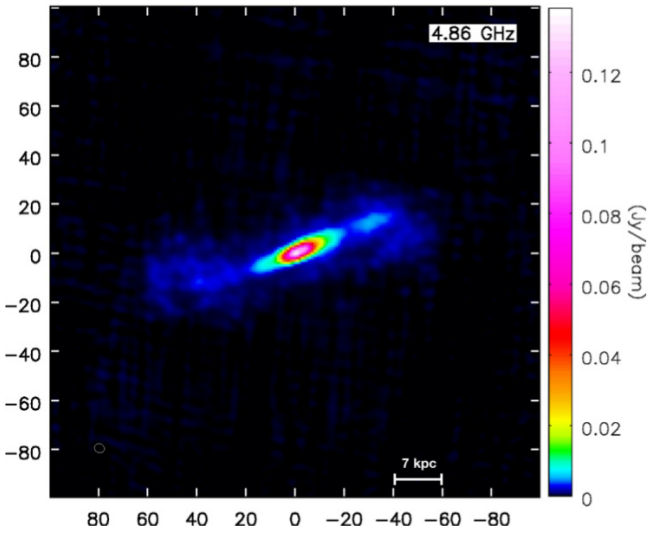

Figure 2.6: Total intensity radio map of ESO443-G024 at 4.8 GHz, made from re-reduced archival VLA data. The 1σ rms noise level is 200 μJy beam^{-1}. The beam size ($4.1'' \times 3.6''$) and physical scale bar are drawn in the bottom-left and bottom-right corner, respectively. The wedge on the right shows the colour scale.

nuclear dust disc (Fig. 2.7a; e.g. Lauer et al. 2005). The optical spectrum of IC 4296 is classified as LINER-like, but with strong emission lines (Annibali et al. 2010).

IC 4296 hosts the FR I radio source PKS 1333-33. Due to its overall radio structure, PKS 1333-33 is defined as a "triple" radio source: a large-scale, double-sided jet extends up to 5 arcmin (77 kpc, with the adopted cosmology) from the nucleus, connecting with the outer lobes at 30 arcmin (Fig. 2.7b; Killeen et al. 1986; Burke-Spolaor et al. 2009). The inner jets are remarkably symmetrical in intensity (Fig. 2.7c), consistent with their axes being close to the plane of the sky (e.g. Laing & Bridle 2014). The core is marginally resolved on scales of few parsecs (Venturi et al. 2000).

2.2.8 NGC 7075

NGC 7075 is an elliptical galaxy with an optically unresolved component in the core (Govoni et al. 2000b), companion of the lenticular galaxy ESO 343−G 03 located about 75 kpc away (Soares et al. 1995). It is the host galaxy of the radio source PKS 2128-388, classified as a FRI radio galaxy containing a double structure in the core that appears aligned with outer structures (Ekers et al. 1989). A low-resolution 4.9 GHz VLA map of NGC 7075 illustrating its large-scale radio structure is shown in Figure 2.8.

2.2.9 IC 1459

IC 1459 is a giant elliptical galaxy in a poor group of spiral galaxies (Tingay et al. 2003). A faint dust lane is detected in the HST image of IC 1459, mostly visible towards the galaxy outskirts (Fig. 2.9a); its morphology is interpreted as a transitional stage between a patchy chaotic structure and a nuclear ring (Sparks et al. 1985; Lauer et al. 2005). IC 1459 also contains one of the most prominent counter-rotating cores observed in an elliptical galaxy (Verdoes Kleijn et al. 2000; Cappellari et al. 2002; Ricci et al. 2015), probably the result of a major merger between gas-rich spiral galaxies (e.g. Hernquist & Barnes 1991). The optical spectrum of IC 1459 was classified as LINER-like with strong emission lines (Annibali et al. 2010).

IC 1459 is the host galaxy of the radio source PKS 2254−367, which was classified by Tingay et al. (2003) as a compact, GHz-peaked radio source (GPS) in a high-density environment. Figure 2.9b shows the pc-scale double-sided radio structure of IC 1459 detected at 2.3 GHz with Very-Long Baseline Interferometry (VLBI) by Tingay & Edwards (2015).

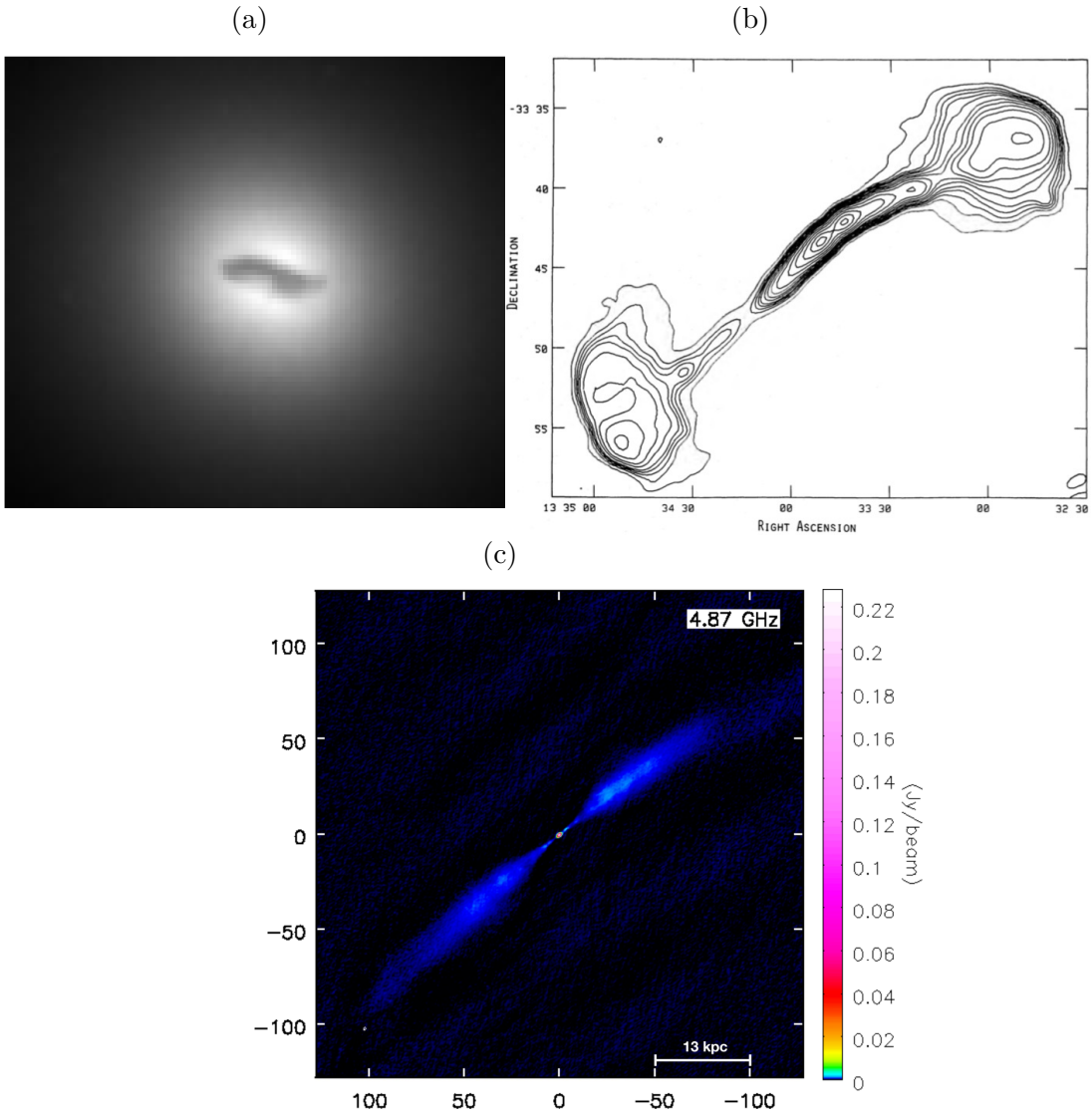

Figure 2.7: **a:** Archival HST image of IC 4296 retrieved from the Hubble Legacy Archive at the Canadian Astronomy Data Centre (CADC). The galaxy is observed with the HST Wide-Field and Planetary Camera 2 (WFPC2) through the F555W optical filter ($\lambda \approx 472 - 595$ nm). The pixel scale, image FWHM and size are 0.1 arcsec pixel^{-1}, 0.08 arcsec, and 7×7 arcsec^2, respectively. **b:** Low-resolution image showing the large-scale radio structure of IC 4296 at 4.8 GHz taken from Killeen et al. (1986). The peak flux is 778.1 mJy beam^{-1}, and the contour levels are -3%, -1.5%, 1.5%, 3%, 4%, 5%, 6%, 8%, 10%, 13%, 17%, 25%, 35%, 50%, 70%, and 90% of the peak. The 1σ rms noise level in the map is approximately 1.2 mJy beam^{-1}. **c:** High-resolution total intensity map of IC 4296 at 4.8 GHz. The image is made from the re-reduced highest-resolution dataset of Killeen et al. (1986) for which they did not present images. The 1σ rms noise level is 55 μJy beam^{-1}. The beam size ($1.58'' \times 0.93''$) and physical scale bar are drawn in the bottom-left and bottom-right corner, respectively. The wedge on the right shows the colour scale.

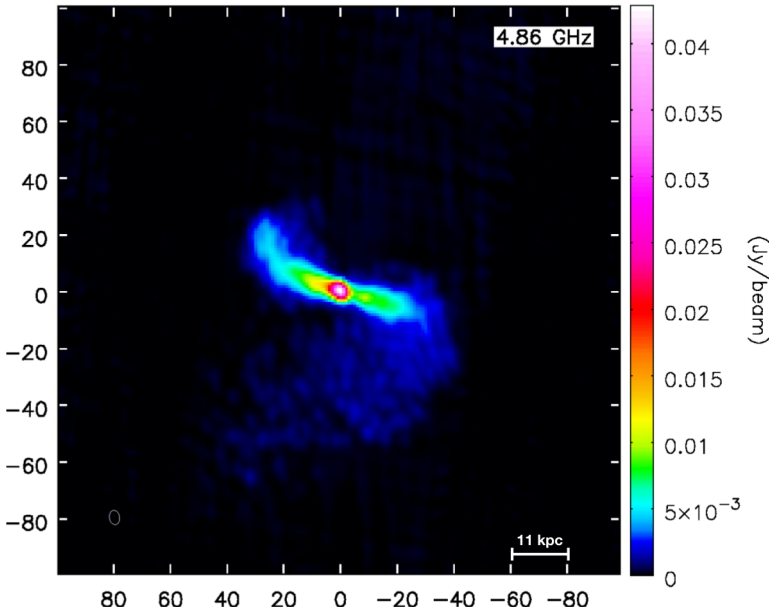

Figure 2.8: Total intensity radio map of NGC 7075 at 4.8 GHz, made from re-reduced archival VLA data. The 1σ rms noise level is 110 μJy beam^{-1}. The beam size ($5.1'' \times 3.6''$) and physical scale bar are drawn in the bottom-left and bottom-right corner, respectively. The wedge on the right shows the colour scale.

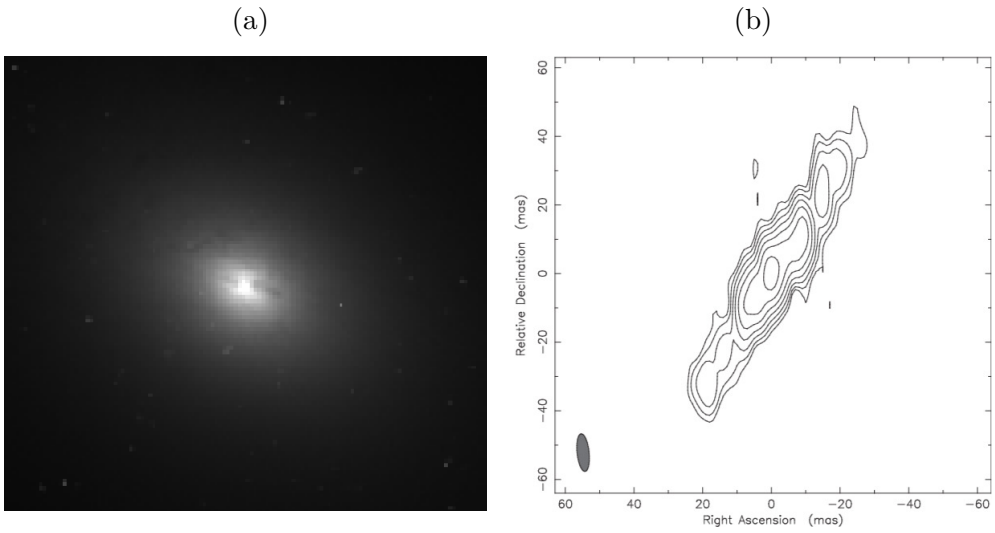

Figure 2.9: **a:** Archival HST image of IC 1459 retrieved from the Hubble Legacy Archive at the Canadian Astronomy Data Centre (CADC). The galaxy was observed with the HST Wide-Field and Planetary Camera 2 (WFPC2) through the F555W optical filter ($\lambda \approx 472 - 595$ nm). The pixel scale, image FWHM and size are 0.1 arcsec pixel^{-1}, 0.08 arcsec, and 8×8 arcsec^2, respectively. **b:** VLBI image of IC 1459 at 2.6 GHz, taken from Tingay & Edwards (2015). The synthesized beam size is 11 mas×3.5 mas and it is shown as a filled ellipse in the bottom-left corner of the panel. The image peak is 262 mJy beam^{-1} and contour levels are plotted at -1 (dashed), 1, 2, 4, 8, 16, 32, and 64 per cent of the peak.

Chapter 3

ALMA observations and data analysis

As detailed in the Introduction, in the framework of this project we have acquired APEX ^{12}CO(2-1) integrated spectra and VLT-VIMOS integral field unit spectroscopy for the entire sample, JVLA high-resolution observations at 10 GHz for five sources, ALMA Cycle 3 ^{12}CO(2-1) and 230 GHz continuum observations of nine objects. Archival optical (HST or from other ground-based telescopes) and VLA images, as well as MUSE spectroscopy are also used, when available.

The study of the molecular gas component is an important part of our project and the major focus of this Thesis. In the following we present the ALMA observations, on which our study of the cold gas is based, and describe the data reduction and analysis.

3.1 ALMA

The Atacama Large Millimeter/sub-millimeter Array (ALMA) is an aperture synthesis telescope located on the Chajnantor plain of the Chilean Andes at an elevation of about 5000 m and a latitude of $-23°$ (Fig. 3.1), and its Early Science Operations started with Cycle 0 in September 2011. The ALMA Observatory is composed of sixty-six high-precision antennas arranged into two arrays: the 12-m Array composed of fifty 12-meter dishes and the Atacama Compact Array (ACA), made of twelve 7-m antennas and four 12-m antennas used as single-dish (TP Array). The 12-m array is used for sensitive, high resolution imaging, with baseline lengths ranging from 15 m up to $\sim$ 16 km. ACA (or Morita Array) has been designed to solve the well-known *zero-spacing problem* and achieve good imaging of sources with emission on angular scales larger than those corresponding to the minimum spacing of the 12-m Array. Its four single-dish antennas provide spatial information samples equivalent spacing of their diameter (12 m), while the 7-m Array baselines range from 9 m to 30 m, bridging the baseline sampling gap between the 12-m

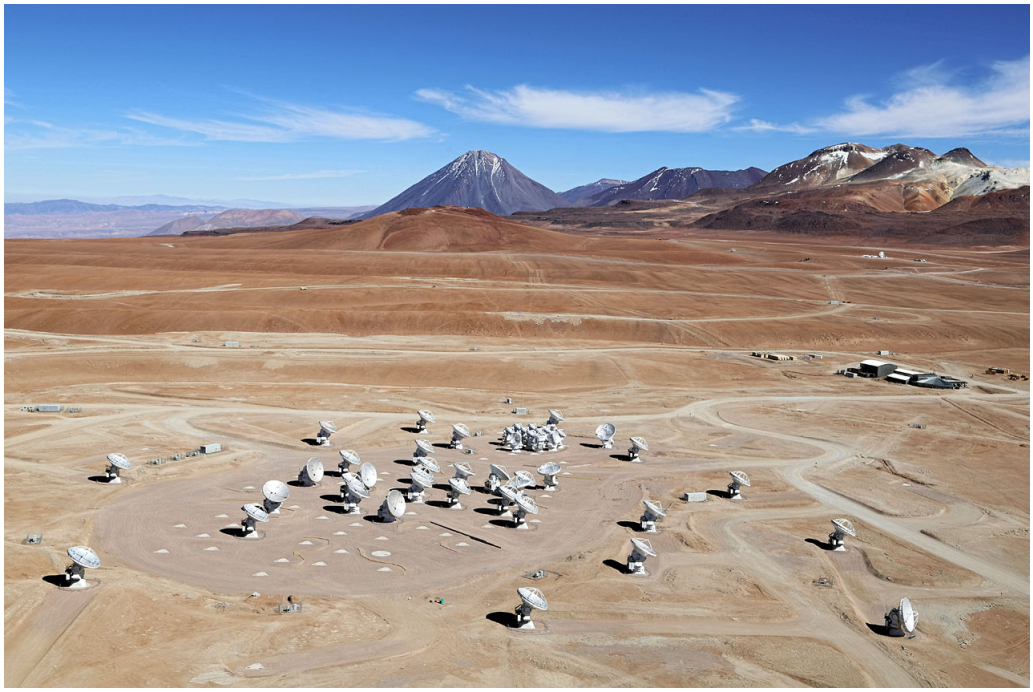

Figure 3.1: Aerial view of the Chajnantor Plateau, the ALMA site, situated in the Chilean Andes at an elevation of about 5000 meters and at a latitude of $-23°$.

Array and the TP Array. With its full set of receivers, ALMA will cover a broad range of observing frequencies in the millimeter and sub-millimeter regime, divided into ten bands from $\approx$ 30 to $\approx$950 GHz (7$-$0.4 mm). Currently, the available frequencies range from Band 3 (84$-$116 GHz) to Band 10 (787$-$950 GHz). Band 1 (31$-$45 GHz) is under construction, Band 2 (67$-$90 GHz) is under development (and will be likely extended into the Band 3 frequency range). Thanks to the wide range of possible antenna configurations and observing frequencies, ALMA allows us to obtain various combinations of spatial resolution and brightness sensitivity (Table 3.1). For instance, in the most compact 12-m array configuration (maximum baseline length$\sim$160 m), resolutions range from 0.5$''$ at 950 GHz to 4.8$''$ at 110 GHz. In the most extended 12-m array configuration (maximum baseline length$\sim$16 km), the resolutions range from 20 mas at 230 GHz to 43 mas at 110 GHz.

At mm/sub-mm wavelengths the influence of the "wet" component of the troposphere becomes important; this causes significant amplitude absorption and delay (phase) fluctuations. The ALMA site is one of the driest locations on Earth and allows to have the transparency and the stability needed to limit the negative effects of the troposphere on the observations. The large ALMA collecting area (6500 square meters) implies a reduction of the noise by two order of magnitude with respect to any other existing mm interferometer and, along with the substantial number of antennas, allows also to sample almost instantaneously many spatial scales on the sky (i.e. provide a good uv-coverage), significantly improving the quality of the

Table 3.1: ALMA capabilities updated at the last cycle of observations (Cycle 7).

					Most Compact		Most Extended	
Band	ν (GHz)	λ (mm)	FOV (")	Continuum Sensitivity (mJy beam^{-1})	Angular resolution (")	ΔT_{line} (K)	Angular resolution (mas)	ΔT_{line} (K)
(1)	(2)	(3)	(4)	(5)	(6)	(7)	(8)	(9)
1†	45-31	6.7-9.5	145-135	†	13-9	†	0.14-0.1	†
2†	90-67	3.3-4.5	91-68	†	6-4.5	†	0.07-0.05	†
3	84-116	3.6-2.6	73-53	0.09	4.0-2.9	0.16	50-36	1075
4	125-163	2.4-1.8	49-38	0.12	2.7-2.1	0.18	34-26	1104
5	158-211	1.9-1.4	37-29	0.12	2.1-1.6	0.15	26-20	962
6	211-275	1.4-1.1	29-22	0.12	1.6-1.2	0.14	20-15	947
7	275-373	1.1-0.8	22-16	0.22	1.23-0.91	0.2	15-11	1307
8	385-500	0.8-0.6	16-12	0.42	0.88-0.68	0.35	55-42	91
9	602-720	0.5-0.4	10-8.5	2.0	0.56-0.47	1.2	35-29	312
10	787-950	0.4-0.3	7.8-6.5	4.6	0.43-0.36	2.5	27-22	662

Notes. – Columns: (1) Band ID number. (2) Available frequency range in the observing Band, and (3) corresponding wavelength range. (4) Nominal field of view range of 12-m antennas at the corresponding frequency range. (5) Expected 5σ continuum flux sensitivity for an integration time of 60 seconds and a continuum bandwidth of 7.5 GHz. (7)/(9) Range of major axis FWHM of the synthesised dirty beam, and (8)/(10) brightness temperature sensitivity of spectral line observations for an integration time of 60 seconds and a spectral resolution of 0.976 MHz, both estimated considering 50 12-m antennas arranged in the most compact (i.e. maximum baseline length = 150 m) or most extended (i.e. maximum baseline length = 16 km) configuration.
†To be developed in future.

reconstructed images. This aspect also permits us to reach the best ever sensitivity at these wavelengths (Table 3.1).

Since its dedication in 2011, ALMA has opened a new window on the so-called '*Cold Universe*', i.e. molecular gas clouds and star-forming regions, which are optically dark (because of dust obscuration), but shine brightly at mm wavelengths. Thanks to its high performances in sensitivity and resolution (both spectral and spatial), ALMA enables transformational science, allowing (among others) studies of nearby radio galaxies with unprecedented detail.

ALMA is an international facility, a partnership between Europe, East Asia and North America, in cooperation with the Republic of Chile.

3.2 Observations and data reduction

We used ALMA Band 6 (≈230 GHz) to observe nine of the eleven radio galaxies in our sample. As already mentioned in Section 2.1, two objects (NGC 1316 and NGC 1399) were excluded because the observing strategies needed to obtain reliable detections (e.g. integration time, array configuration, pointing type) were estimated to be considerably more elaborate than those needed for the other sample sources. In NGC 1316 (PKS 0320−37, Fornax A) the CO is known to be distributed over an area much larger than the single-pointing field-of-view (FOV) of the ALMA main array at 230 GHz (Horellou et al. 2001); a large mosaic and short-spacing information are required to image it adequately. Based on CO single-dish measurements with APEX

Table 3.2: ALMA Cycle 3 observations.

Target	Date	$\nu_{\rm sky}$ ($v_{\rm cen}$)	Time	MRS	$\theta_{\rm maj}$	$\theta_{\rm min}$	PA	Scale
		(GHz) (km s^{-1})	(min)	(kpc, arcsec)	(arcsec)		(deg)	(pc)
(1)	(2)	(3)	(4)	(5)	(6)	(7)	(8)	(9)
IC 1531	2016-06-02	224.7774 (7702)	12.0	5.6, 10.9	0.7	0.6	87	360
NGC 612	2016-07-30	223.8426 (8974)	3.0	6.6, 11.0	0.3	0.3	-75	180
PKS 0718-34	2016-05-02 2016-05-03	223.8622 (8904)	32.2	6.3, 11.0	0.7	0.6	-80	400
NGC 3100	2016-03-22	228.6299 (2484)	28.5	1.9, 10.6	0.9	0.7	-87	160
NGC 3557	2016-06-03/04	228.2319 (2999)	22.5	2.0, 9.7	0.6	0.5	-70	130
ESO 443-G 024	2016-05-01	226.6839 (5089)	24.2	3.7, 10.8	0.7	0.6	-63	240
IC 4296	2016-06-04 2016-06-11	227.7110 (3705)	25.5	2.8, 10.8	0.6	0.6	-84	150
NGC 7075	2016-05-03	226.4196 (5483)	24.5	4.1, 10.8	0.6	0.6	-76	230
IC 1459	2016-04-11	229.1614 (1819)	11.4	1.3, 10.7	1.0	0.8	-71	120

Notes. – Columns: (1) Target name. (2) Observation dates. (3) ^{12}CO(2-1) redshifted (sky) centre frequency estimated using the redshift listed in column (3) of Table 2.1; the corresponding velocity ($v_{\rm cen}$; LSRK system, optical convention) is reported in parentheses. (4) Total integration time on-source. (5) Maximum recoverable scale in kiloparsec for the array configuration, and corresponding scale in arcseconds. (6) Major axis FWHM of the synthesized beam. (7) Minor axis FWHM of the synthesized beam. (8) Position angle of the synthesized beam. (9) Spatial scale corresponding to the major axis FWHM of the synthesized beam.

(Prandoni et al. 2010, Laing et al. in prep.), NGC 1399 (PKS 0336-35) appeared to be too faint (tentative detection at a signal-to-noise ratio of $S/N \sim 3.5$) to be detected within reasonably short integration times with ALMA. We know, however, that both sources are now the subject of dedicated observations (e.g. Morokuma-Matsui et al. 2019), which we plan to analyse in the future.

ALMA observations were taken during Cycle 3, between March and July 2016 (PI: I. Prandoni). Table 3.2 summarises the details of the observations. The total time on-source ranged from 3 to 30 minutes. The spectral configuration consisted of four spectral windows (SPWs): one centred on the redshifted frequency ($\nu_{\rm sky}$) of the ^{12}CO(J=2-1) line (rest frequency 230.5380 GHz) and divided into 1920 1.129 MHz-wide channels; the other three, used to map the continuum emission, had 128 31.25-MHz-wide channels. Between 36 and 43 12-m antennas were used, with maximum baseline lengths ranging from 460 m to 1.1 km. The maximum recoverable spatial scale (MRS), together with the major and minor axis full width half maxima (FWHM) and position angle of the synthesized beam for each observation are reported in Table 3.2. Titan and Pallas were used for primary flux calibration; the ALMA calibrators J1037−2934, J1107−4449, J2537−5311, J0538−4405 and J1427−4206 were observed as secondary standards if no solar-system object was available.

We processed the data using the Common Astronomy Software Application (CASA; McMullin et al. 2007) package, version 4.7.2, calibrating each dataset separately using customized PYTHON data reduction scripts. We used a standard calibration procedure, whose main steps can be summarised as follows:

- Data import from the archival raw data format (ALMA Science Data Model; ASDM) into the CASA data format, the so-called MEASUREMENT SET

(MS),[1] in the process obtaining information about the observing set-up from the MS.

- Initial flagging (also known as "a priori" flagging): it applies on-line and other deterministic flags (e.g. shadowed data, edge channels of each individual SPWs, etc.)[2];
- Water Vapour Radiometer (WVR) and System Temperature ($T_{\rm sys}$) corrections[3];
- Model information setting (i.e. setting of the model amplitude and phase visibilities of the primary flux calibrator);
- Frequency-dependent (bandpass) calibration (i.e. correction of the variation of phase and amplitude as a function of the spectral response of each antenna);
- Time-dependent (gain) calibration (i.e. correction of the time-dependent corruptions related to the atmospheric turbulence);
- Flux density calibration (i.e. bootstrapping the flux density scale of the secondary calibrators from the primary flux calibrator);
- Application of the calibration tables, data examination and further flagging (if necessary);
- Imaging.

[1]The MS has a table-based structure: there is a principal table, called MAIN, which is structured into several sub-tables that contain auxiliary information about the observation (e.g. sources, pointing, atmospherical conditions, antennas). Each table or sub-table appears in form of directory on disc. The MAIN table is divided into several columns. Among these, the most important are: the DATA column, which contains the information about the raw visibilities and will never be over-written; the "Scratch Columns" that are filled with the modification to the raw data, such as CORRECTED DATA (containing the calibrated data) and MODEL, which holds the information about model visibilities.

[2]Data editing, also known as flagging, consists of removing from data the spurious fluctuations due to instrumental problems that cannot be solved by the calibration. There is a group of initial flags, which can be done without any visual data inspection, such as shadowing (i.e. the blockage of the aperture of an antenna caused by the shadow of a nearby antenna), auto-correlations (i.e. the combination of the signal of each antenna with itself, usually flagged because of their high noise), edge channels (i.e. the edge channels of each SPWs, always noisier than the central ones), etc.

[3]At ALMA's working wavelengths, the Earth's troposphere introduces significant degrading effect on the observed visibilities, such as phase fluctuations and amplitude absorption. In order to improve data for the atmospheric corruptions, the WVR and T_{sys} calibration steps are executed. Specifically, the WVR calibration corrects the observed visibilities for the phase variations on short timescales related to the amount of precipitable water vapour (PWV) above each antenna; the T_{sys} calibration corrects for the effects of the atmospheric opacity which produces signal attenuation and fake absorption lines on spectra.

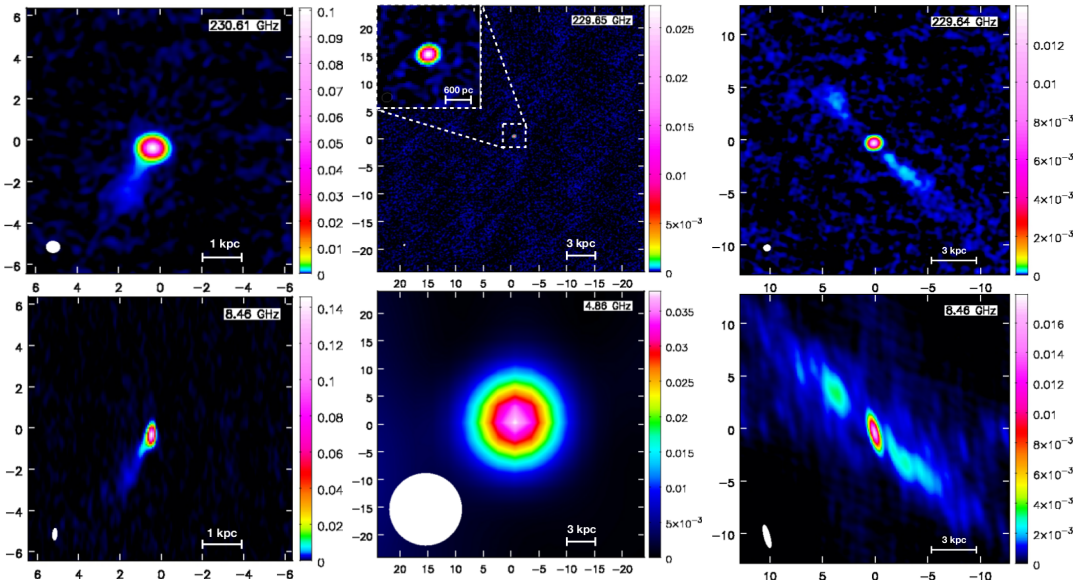

Figure 3.2: Naturally weighted ALMA Band 6 (upper panels) and archival VLA (lower panels) continuum maps of each target. The reference frequency of each observation is indicated in the top-right corner of the panel. The wedge on the right of each map shows the colour scale in Jy beam^{-1}. Coordinates are given as relative positions with respect to the image phase centre in arcseconds; East is to the left and North to the top. The synthesised beam and the scale bar are shown in the bottom-left and bottom-right corner, respectively, of each panel. The properties of the ALMA continuum images are summarised in Table 3.3. See the text for details on the archival radio images.

3.2.1 Continuum imaging

The three continuum spectral windows and the line-free channels in the line spectral window were used to produce the continuum maps, using the CLEAN task in multi-frequency synthesis (MFS) mode with one Taylor series term (Rau & Cornwell 2011). All the continuum maps were made using natural weighting in order to maximise the sensitivity, with the goal of imaging emission from the jets. Since the cores are detected at high signal-to-noise in all of the targets, multiple cycles of phase-only self calibration were performed in all cases. Additional amplitude and phase self-calibration was performed for the brightest cores only. This allowed us to obtain root-mean square (rms) noise levels ranging from 0.02 to 0.06 mJy beam^{-1} for synthesized beams of 0.3 – 1 arcsec FWHM.

All the objects observed with ALMA are detected in the 230 GHz continuum. Six out of nine sources also show extended emission on kpc/sub-kpc scales. Two-dimensional Gaussian fits were performed within the regions covered by the contin-

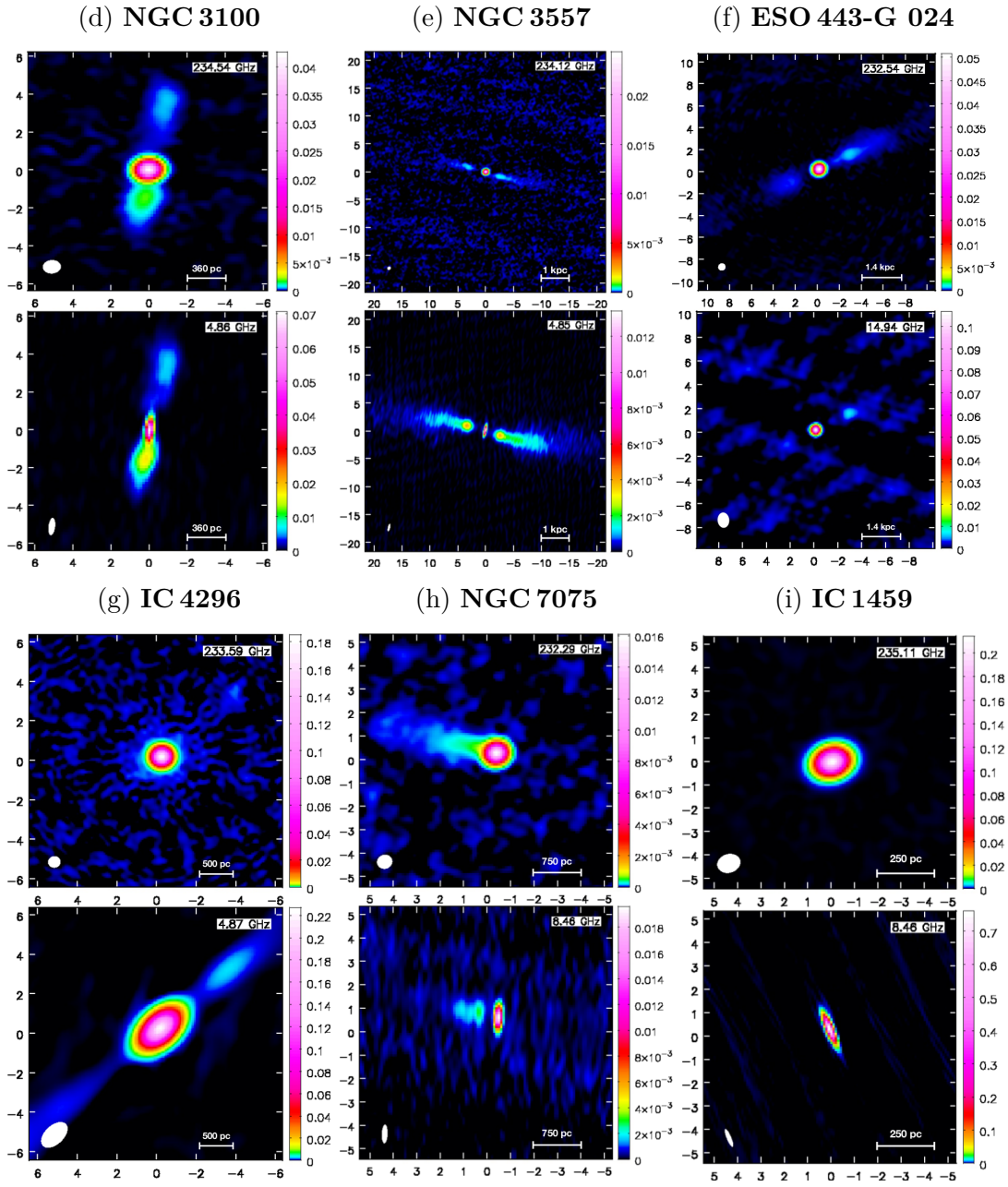

Figure 3.2: *Continued*

uum emission in order to estimate the spatial extent of each observed component. Table 3.3 summarises the main properties of the millimetre continuum maps, which are shown in Figure 3.2. For each object, the upper panel shows the ALMA millimetre continuum image, while the lower panel shows an archival VLA continuum map (at 4.9, 8.5 or 14.9 GHz), chosen to match as closely as possible the angular resolution of the corresponding ALMA image. We note that all of the archival VLA

data used in this work (included the low-resolution ones presented in Chapter 2) have been re-reduced using using standard calibration methods (i.e. those described in Section 6.3.2; see also Section 3.2). All of the datasets were then self-calibrated in phase and amplitude and the final images were made using single or multi-scale CLEAN, depending on the complexity of the brightness distributions.

It is clear from Figure 3.2 that the continuum emission at 230 GHz is morphologically very similar to the emission observed at frequencies between 4.9 and 15 GHz in the archival VLA images. It is then likely to be dominated by radio synchrotron emission from the core and jet structures, exhibiting in all the cases the typical morphologies of FRI radio galaxies (see Section 1.3). There is no evidence of thermal emission associated with extended dust or CO, although we cannot rule out the possibility of some contribution to the unresolved core emission from this mechanism. A detailed comparison between the mm and cm properties of each object is provided in Section 3.4.

3.2.2 Line imaging

After applying the continuum self-calibration, line emission was isolated in the visibility plane using the CASA task UVCONTSUB to form a continuum model from linear fits in frequency to line-free channels and to subtract it from the visibilities. We then produced a data cube of CO channel maps using the CLEAN task with natural weighting. The channel velocities were initially computed in the source frame with zero-points corresponding to the redshifted frequency of the CO(2-1) line ($\nu_{\rm sky}$, Table 3.2). The continuum-subtracted dirty cubes were cleaned in regions of line emission (identified interactively) to a threshold equal to 1.5 times the rms noise level, determined in line-free channels. Several channel widths (i.e. spectral bins) were tested to find a good compromise between signal-to-noise ratio (S/N) and resolution of the line profiles; the final channel widths range from 10 to 40 km s^{-1}.

We clearly detect ^{12}CO(2-1) emission in six out of nine sources, with S/N ranging from 8 to 45. The cleaned CO data cubes are characterised by rms noise levels (determined in line-free channels) between 0.2 and 1.3 mJy beam^{-1}.

Three targets (PKS 0718−34, ESO 443−G 024 and IC 1459) are undetected in CO. In these cases, line emission (and consequently line-free channels) could not be identified in the spectral window centred on the redshifted CO emission; the continuum was thus modelled using the three continuum spectral windows only. The continuum-subtracted dirty cubes for these targets were cleaned down to 1.5 times the expected rms noise level, with conservative spectral channel widths between 75 and 80 km s^{-1}. The 1σ noise levels measured in the cleaned channel maps ranged from 0.2 to 0.6 mJy beam^{-1}; in these cases 3σ upper limits are tabulated.

Table 3.4 summarises the properties of the CO data cubes.

Table 3.3: Properties of the ALMA continuum images.

Target	rms	S_{230}	Size FWHM		PA
	(mJy beam^{-1})	(mJy)	(arcsec^2)	(pc^2)	(deg)
(1)	(2)	(3)	(4)	(5)	(6)
IC 1531	0.05	108±10.5			
core		105±10.5	(0.3 × 0.1)	(65 × 50)	141±19
SE jet[1]		3.0±0.3	–	–	–
NGC 612	0.06	29±2.9			
core		29±2.9	(0.03 × 0.01)	(20 × 10)	137±44
PKS 0718-34	0.02	17±1.4			
core		14±1.4	(0.1×0.08)	(60×50)	107±38
NE jet		1.0±0.1	(3.1×1.5)	(1800×860)	33±5
SW jet		1.5±0.1	(5.6×1.0)	(3200×570)	49±2
NGC 3100	0.02	50±4.3			
core		43±4.3	(0.11×0.05)	(20×10)	170±89
N jet		2.2±0.2	(2.4×1.0)	(440×180)	167±2
S jet		4.3±0.4	(1.6×0.7)	(290×130)	164±4
NGC 3557	0.03	30±2.5			
core		25±2.5	(0.11×0.1)	(23×20)	62±22
E jet		2.0±0.2	(4.1×0.7)	(870×150)	77±2
W jet		2.5±0.2	(5.4×0.6)	(1145×130)	77±3
ESO 443-G 024	0.02	61±5.3			
core		53±5.3	(0.1×0.08)	(35×30)	111±19
SE jet		2.3±0.2	(2.5×1.3)	(870×450)	115±4
NW jet		5.3±0.5	(4.5×1.0)	(1570×350)	115±2
IC 4296	0.02	190±19.0			
core		190±19.0	(0.1×0.1)	(30×30)	61±35
NGC 7075	0.02	19±1.7			
core		17±1.7	(0.1×0.07)	(40×30)	70±40
E jet[1]		1.8±0.1	–	–	–
IC 1459[2]	0.03	217±21	(0.08×0.06)	(10×7)	124±12

Notes. – Columns: (1) Target name. (2) 1σ rms noise level measured in emission-free regions of the cleaned continuum map. (3) 230 GHz continuum flux density; the total, core and jet flux densities are quoted separately. The uncertainties are estimated as $\sqrt{\mathrm{rms}^2 + (0.1 \times S_{230})^2}$, and the second term dominates in all cases. Errors on total flux densities are obtained through error propagation. (4) Size (FWHM) deconvolved from the synthesized beam. The sizes were estimated by performing 2−D Gaussian fits to identifiable continuum components. (5) Spatial extent of each component corresponding to the angular sizes in column (4). (6) Position angle of the corresponding component, defined North through East.

[1]Unresolved component.

[2]The FR I structure of this source is on milli-arcsecond (mas) scales ($\leq$ 40 mas; Tingay & Edwards 2015) and is unresolved in our images.

3.3 Image Cube analysis

3.3.1 CO moment maps

For spectral line maps, the output of the imaging process is an image cube, with a frequency or velocity channel axis in addition to the two sky coordinate axes. This can be most easily thought as a series of image planes stacked along the spectral dimension. A useful product can be computed by collapsing the cube into a "moment" image, taking a linear combination of the individual planes:

$$M_{\rm m}(x_{\rm i}, y_{\rm i}) = \sum_{\rm k=1}^{\rm N} w_{\rm m}(x_{\rm i}, y_{\rm i}, v_{\rm k}) I(x_{\rm i}, y_{\rm i}, v_{\rm k}) \tag{3.1}$$

for pixel i and channel k in the cube I. There are a number of choices to form the m moment, usually approximating some polynomial expansion of the intensity distribution over velocity mean. The most commonly used moments are:

- **Moment 0.** $M_0 = \Delta\nu \sum I_{\rm i}$, where $\Delta\nu$ is the width (in world coordinate units) of a pixel along the moment axis, and $I_{\rm i}$ means "the intensity I of the ith pixel ". The moment 0 image is a map of the intensity at each pixel summed along the velocity axis (i.e. an integrated intensity map).
- **Moment 1.** Moment 1 is defined as the sum of the intensity-weighted coordinates: $M_1 = \dfrac{\sum I_{\rm i} v_{\rm i}}{M_0}$. As such it provides a map of the velocity field of the observed line emission (i.e. a mean velocity map).
- **Moment 2.** Moment 2 is defined as the intensity-weighted dispersion of the coordinates: $M_2 = \sqrt{\dfrac{\sum I_{\rm i}(v_{\rm i} - M_1)^2}{M_0}}$. It is then used to get the velocity dispersion map of the line emission (i.e. the line-of-sight velocity width).

We created the moment 0, 1 and 2 maps of the detected lines from the cleaned, continuum-subtracted CO data cubes using the masked moment technique as described by Dame (2011, see also Bosma 1981a,b; van der Kruit & Shostak 1982; Rupen 1999). In this technique, a copy of the cleaned data cube is first Gaussian-smoothed spatially (with a FWHM equal to that of the synthesised beam) and then Hanning-smoothed in velocity. A three-dimensional mask is then defined by selecting all the pixels above a fixed flux-density threshold; this threshold is chosen so as to recover as much flux as possible while minimising the noise. We used thresholds varying from 1.2 to 2σ, depending on the significance of the CO detection (higher threshold for noisier maps). The moment maps were then produced from the un-smoothed cubes using the masked regions only (e.g. Davis et al. 2017). The resulting maps are shown in Figs 3.3 − 3.8, where the velocity zero-points are defined to be the intensity-weighted centroids of the observed CO emission.

Table 3.4: Properties of the ^{12}CO(2-1) line images.

Target	rms (mJy beam^{-1})	Peak flux (mJy beam^{-1})	S/N	Δv_{chan} (km s^{-1})
(1)	(2)	(3)	(4)	(5)
IC 1531	0.7	12.4	18	20
NGC 612	1.3	18.3	14	20
PKS 0718-34	0.2	< 0.6	–	80
NGC 3100	0.6	28.3	45	10
NGC 3557	0.4	16.3	38	22
ESO 443-G 024	0.2	< 0.6	–	75
IC 4296	0.2	2.0	8	40
NGC 7075	0.4	4.0	10	40
IC 1459	0.6	< 1.8	–	80

Notes. – Columns: (1) Target name. (2) 1σ rms noise level measured in line-free channels at the channel width listed in column (5). (3) Peak flux density (or 3σ upper limit) of the line emission. (4) Peak signal-to-noise ratio of the detection. (5) Final channel width of the data cube (km s^{-1} in the source frame).

Based on their moment 0 and moment 1 maps, all detections show clear evidence of gas rotation, associated with discs or ring-like structures. There is evidence for asymmetries in the molecular gas distribution in a number of cases, particularly NGC 3100 and IC 4296 (see Sect. 3.4 for more details).

For completeness, we show the moment 2 maps of all the targets detected in CO. It is worth noting however that they represent intrinsic velocity broadening only for those sources detected with a high S/N and/or whose CO emission is well resolved by our ALMA observations (e.g. Davies et al. 2011): this is certainly the case for NGC 612 and NGC 3100. Otherwise, the velocity dispersion is likely to be dominated by the so-called beam smearing effect: due to the limited spatial resolution, velocity gradients within the host galaxy can be partially resolved and included in the observed velocity dispersions, which therefore tend to be unrealistically high for cold gas distributions (e.g. Davis et al. 2017).

The extent of the molecular gas was estimated by performing 2D Gaussian fits to the moment 0 maps within the regions covered by the CO emission. Table 3.5 summarises the estimated sizes, which are given as deconvolved major and minor axis FWHM. The detected discs are typically confined to kpc or sub-kpc scales except for NGC 612, whose CO disc extends for at least 9.6 kpc along its major axis.

3.3.2 Line widths and profiles

The integrated spectral profiles of the six galaxies detected in CO(2-1) were extracted from the observed data cubes within boxes including all of the CO emission. The spectral profiles are shown in Figures 3.3−3.8 (panel d). The dimensions of the boxes used to extract the spectra are indicated in the figure captions.

All of the integrated spectral profiles exhibit the classic double-horned shape expected from a rotating disc. In one case (IC 4296) a strong absorption feature was also detected (Fig. 3.7d). For completeness, we searched for absorption features in all the detected objects by extracting integrated spectra in small boxes around the bright nuclear continuum sources. No significant absorption features were found in any of the other sources. In particular, we do not detect CO absorption against the nucleus of NGC 612, where Morganti et al. (2001) found absorption in HI.

Line widths were measured as full-width at zero intensity (FWZI) as well as FWHM. The former was defined as the full velocity range covered by spectral channels (identified interactively in the channel map) with CO intensities $\geq 3\sigma$. These channels are highlighted in grey in Figures 3.3d−3.8d and we also tabulate the flux integrated over this range. FWHM was defined directly from the integrated spectra as the velocity difference between the two most distant channels from the line centre with intensities exceeding half of the line peak. We note that the absorption feature in IC 4296 was not included in these measurements.

For non-detections, 3σ upper limits on the integrated flux densities were calculated from the relation (e.g. Koay et al. 2016):

$$\Sigma S_{\rm CO}\Delta{\rm v}\ ({\rm Jy\ beam^{-1}\ km\ s^{-1}}) < 3\sigma\Delta{\rm v}_{\rm FWHM}\sqrt{\frac{\Delta{\rm v}}{\Delta{\rm v}_{\rm FWHM}}} \tag{3.2}$$

where Δv is the channel width of the data cube in which the rms noise level (σ) is measured (see Table 3.4) and $\Delta{\rm v}_{\rm FWHM}$ is the expected line FWHM. We assumed the line FWHM measured from APEX CO(2-1) observations (Prandoni et al. 2010, Laing et al. in prep. ; see also Table 3.5). The factor $\sqrt{\Delta{\rm v}/\Delta{\rm v}_{\rm FWHM}}$ accounts for the expected decrease in noise level with increasing bandwidth (Wrobel & Walker 1999). Equation 3.2 is only valid if all of the molecular gas is concentrated within the synthesized beam (a few hundred parsec). If, more realistically, the molecular gas is distributed on larger scales, this assumption leads to a significant underestimation of the total flux limit. In this case, an estimate of the gas surface density upper limit is more meaningful (see Section 3.3.3).

The CO(2-1) line parameters are listed in Table 3.5. $\rm v_{CO}$, the intensity-weighted velocity centroids, are our best estimates of the systemic velocity of the line emission. The errors given for $\rm v_{CO}$ are assumed to be equal to the channel widths of the corresponding integrated spectrum. The values of $\rm v_{CO}$ are all consistent (within the combined errors) with the stellar velocities $\rm v_{opt}$ listed in Table 2.1.

3.3.3 Molecular gas masses

The molecular gas mass in galaxies is dominated by molecular hydrogen, H_2, but its strongly forbidden rotational transitions make it very difficult to detect, unless shocked or heated to very high temperatures; for this reason the emission from tracer molecules is usually used to detect H_2 in galaxies (Carilli & Walter 2013). CO is the most abundant molecule in the ISM after H_2, emits strong rotational transition lines (occurring primarily through collisions with H_2): it can be considered as a "good" tracer of the molecular hydrogen. We adopted the following relation to estimate the total molecular gas masses from the integrated CO emission, including contributions from heavy elements (M_{mol}; Bolatto et al. 2013):

$$M_{\rm mol} = \frac{1.05\times10^4}{R_{21}} \left(\frac{X_{\rm CO}}{2\times10^{20}\ \frac{\rm cm^{-2}}{\rm K\ km\ s^{-1}}} \right) \times \left(\frac{1}{1+z}\right) \left(\frac{\Sigma S_{\rm CO}\Delta\nu}{\rm Jy\ km\ s^{-1}}\right) \left(\frac{D_{\rm L}}{\rm Mpc}\right)^2, \quad (3.3)$$

where $\Sigma S_{\rm CO}\Delta$v is the CO(2-1) flux integrated over the line FWZI (see Table 3.5), R_{21} is the CO(2-1) to CO(1-0) flux ratio, z is the galaxy redshift, $D_{\rm L}$ is the luminosity distance, and $X_{\rm CO}$ is the CO-to-H_2 conversion factor. $X_{\rm CO}$ depends on the molecular gas conditions (e.g. excitation, dynamics, geometry) and the properties of the environment (e.g. metallicity; see Bolatto et al. 2013) and is therefore likely to vary systematically between different galaxy types. Little is known about $X_{\rm CO}$ in nearby ETGs, because most studies are focused on gas-rich (and high gas metallicity) populations, typically late-type galaxies. Following Bolatto et al. (2013) and Tremblay et al. (2016), we assume the average Milky Way value of $X_{\rm CO}= 2\times10^{20}\,{\rm cm^{-2}K\,km\,s^{-1}}$.

Another important uncertainty concerns the CO(2-1) to CO(1-0) flux ratio, R_{21}, which depends on optical depth and excitation conditions of the molecular gas (e.g. Braine & Combes 1992). R_{21} can vary significantly between objects. Measurements of R_{21} have been made for gas-rich disc galaxies (e.g. Sandstrom et al. 2013) and for radio-quiet ETGs (e.g. Young et al. 2011), but little is known about local radio-loud ETGs. Indeed, the presence of radio jets can significantly affect the conditions of the molecular gas in the surrounding regions (e.g. Oosterloo et al. 2017), but it is not clear whether such phenomena are common.

To date, the best estimate of R_{21} for radio galaxies comes from the CO(2-1) to CO(1-0) brightness temperature ratios measured by Ocaña Flaquer et al. (2010). The mean ratio for 15 radio-loud ETGs observed in both CO transitions with the IRAM 30m telescope is 2.32. Caution is needed, however, in using line flux ratios from literature. Indeed, although naturally thought to be dimensionless, ratios of flux densities (expressed in Jy km s^{-1}) are different from ratios of brightness temperatures (expressed in K km s^{-1}). This is because, based on the Rayleigh-Jeans formula, the conversion between K and Jy is not linear:

$$T = 1.22\times10^3 \left(\frac{S}{\rm Jy}\right) \left(\frac{\nu}{\rm GHz}\right)^{-2} \left(\frac{\theta_{\rm maj}\times\theta_{\rm min}}{\rm arcsec\times arcsec}\right)^{-1} \quad (3.4)$$

where T is the brightness temperature in Kelvin, S is the flux density, ν is the observing frequency, and $\theta_{\rm maj}$ and $\theta_{\rm min}$ are the major and minor axis FWHM of the synthesized beam, respectively. Therefore, the conversion between brightness temperature and flux density ratios turns out to be:

$$\frac{S_1}{S_2} = \frac{T_1}{T_2}\left(\frac{\nu_1}{\nu_2}\right)^2 \frac{(\theta_{\rm maj} \times \theta_{\rm min})_1}{(\theta_{\rm maj} \times \theta_{\rm min})_2} \tag{3.5}$$

where the numbers 1 and 2 identify the two transitions. It is clear from Equation 3.5, however, that the brightness temperature ratio is the same as the flux density ratio provided that the CO emission is unresolved, since in this case the ratios of the square of wavelength and the beam size cancel precisely (e.g. David et al. 2014; Temi et al. 2018). Since the ratios of Ocaña Flaquer et al. (2010) are based on single-dish observations that do not resolve the observed sources, we can take R_{21}= 2.32 (although we plan to test this value directly through observations of different CO transitions for our sample).

The estimated molecular masses range from 2.0×10^7 to 2.0×10^{10} $M_\odot$; upper limits for the non-detections are in the range $1.0 - 6.7 \times 10^6$ $M_\odot$. As discussed in the previous section, these upper limits will be underestimated if the CO emission is resolved. We have therefore also measured values or limits for the CO surface density ($\Sigma_{\rm CO}$). For the detected sources, values averaged over the area covered by the CO emission range from 900 to few thousands of $M_\odot$ pc^{-2}. Limits for the undetected sources are typically a few hundred $M_\odot$ pc^{-2}. Values and limits for $M_{\rm mol}$ and $\Sigma_{\rm CO}$ are listed in Table 3.5.

Table 3.5: Main ^{12}CO(2-1) line integrated parameters.

Target	Line FWHM (km s^{-1})	Line FWZI (km s^{-1})	$\Sigma S_{\rm CO}\Delta$v (Jy km s^{-1})	$M_{\rm mol}$ ($M_\odot$)	$v_{\rm CO}$ (km s^{-1})	Size FWHM (kpc^2)	$\Sigma_{\rm CO}$ ($M_\odot$ pc^{-2})
(1)	(2)	(3)	(4)	(5)	(6)	(7)	(8)
IC 1531	260	260	2.0±0.2	$(1.1 \pm 0.1) \times 10^8$	7686±20	(0.25±0.05)×(0.22±0.06)	3.8×10^3
NGC 612	760	840	273±27	$(2.0 \pm 0.2) \times 10^{10}$	8924±20	(9.6±0.3)×(1.2±0.05)	1.0×10^4
PKS 0718-34	334[1]	480[1]	< 0.1	$< 6.7 \times 10^6$	–	–	$< 2.7 \times 10^2$
NGC 3100	340	440	18±1.8	$(1.2 \pm 0.1) \times 10^8$	2600±10	(1.6±0.3)×(0.5±0.08)	9.1×10^2
NGC 3557	440	484	7.0±0.7	$(6.2 \pm 0.6) \times 10^7$	3089±22	(0.3±0.02)×(0.2±0.01)	3.7×10^3
ESO 443-G 024	786[1]	1000[1]	< 0.1	$< 3.5 \times 10^6$	–	–	$< 3.9 \times 10^2$
IC 4296[2]	760	760	1.6±0.1	$(2.0 \pm 0.2) \times 10^7$	3760±40	(0.2±0.02)×(0.04±0.02)	3.0×10^3
NGC 7075	560	600	1.0±0.1	$(2.9 \pm 0.2) \times 10^7$	5510±40	< 0.2	3.3×10^3
IC 1459	492[1]	640[1]	< 0.4	$< 1.0 \times 10^6$	–	–	$< 7.6 \times 10^2$

Notes. – Columns: (1) Target name. (2) Line FWHM defined directly from the integrated spectra as the velocity difference between the two most distant channels from the line centre with intensities ≥50% of the line peak. (3) Line FWZI, i.e. full velocity range covered by spectral channels (identified interactively in the channel map) with CO intensities ≥3σ (grey shaded region in Figs. 3.3–3.8). (4) Integrated CO flux density measured integrating numerically over all the channels in the range defined by the line FWZI. Upper limits of the undetected sources are in units of Jy beam^{-1} km s^{-1}. The velocity ranges in columns (2) – (4) are measured in the source frame. (5) Molecular gas mass derived using Equation 3.3. (6) CO systemic velocity in the LSRK frame (optical convention), determined numerically as the intensity-weighted centroid of the mean velocity map. (7) Size (FWHM, deconvolved from the beam) of the CO emission. (8) CO surface density over the area covered by the CO emission. The surface densities of the undetected sources were estimated over the beam area.

[1]The line FWHM and FWZI of undetected sources are those estimated from APEX spectra (Prandoni et al. 2010, Laing et al. in prep.).

[2]The molecular gas mass of IC 4296 is measured considering CO emission only. If the channels of the absorption feature are included (and integrated as CO emission), we obtain $\Sigma S_{\rm CO}\Delta{\rm v} = (1.9\pm0.1)$ Jy km s^{-1}, $M_{\rm mol}=(2.3 \pm 0.8) \times 10^7$ $M_\odot$.

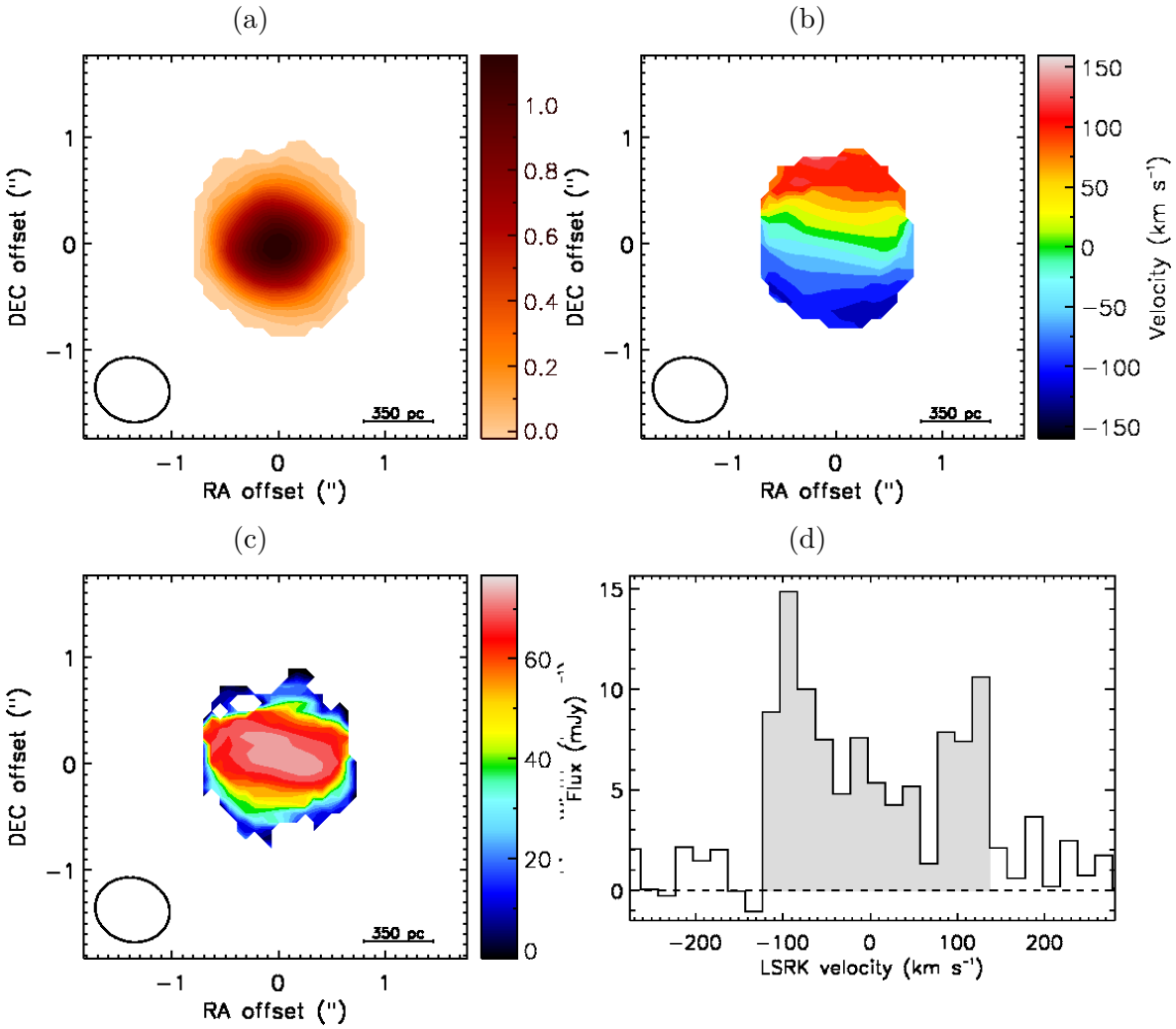

Figure 3.3: IC 1531 moment 0 (3.3a), moment 1 (3.3b) and moment 2 (3.3c) maps created with the masked moment technique described in Section 3.3 using a data cube with a channel width of 20 km s^{-1}. The synthesised beam is shown in the bottom-left corner of each panel. The wedges to the right show the colour scale. In each panel, East is to the left and North to the top. The integrated spectral profile in panel 3.3d was extracted within a box of $1.6 \times 1.6\,\mathrm{arcsec}^2$, including all the CO emission. The spectral channels that are used to estimate the FWZI are highlighted in grey. The black dashed horizontal line indicates the zero flux level. In panels b – d, velocities are measured in the source frame and the zero-point corresponds to the intensity-weighted centroid of the CO emission, equivalent to v_{CO} in the LSRK frame (Table 3.5).

3.4 Results: individual sources

IC 1531

We detect a bright nuclear source in the continuum (Fig. 3.2a, top panel). Emission from the South-East jet is also detected. The archival VLA image of IC 1531 at 8.4 GHz (Fig. 3.2a, bottom panel) shows similar core-jet structure. No counter-jet to the North-West is detected at either frequency.

A disc of molecular gas is detected at 18σ significance (Fig. 3.3a). The disc is barely resolved in our observation, with a deconvolved major axis FWHM of 250 pc (Table 3.5). The estimated molecular gas mass is 1.1×10^8 $M_\odot$. The mean velocity map in Figure 3.3b shows a rotation pattern with an (s-shaped) distortion in the zero-velocity contour (i.e. the kinematic centre), possibly suggesting the presence of a warp in the molecular gas disc. This needs to be confirmed with higher resolution observations. The integrated spectral profile in Figure 3.3d exhibits the double-horned shape of a rotating disc. The moment 2 map (Fig. 3.3c) is likely to be dominated by beam smearing.

NGC 612

We detect a marginally-resolved nuclear source in the continuum map of NGC 612 (Fig. 3.2b, upper panel). Continuum emission from the central region of the extended radio source is also visible in an archival VLA 4.9 GHz map (Fig. 3.2b, bottom panel) but at much lower resolution. We detect a large-scale disc of molecular gas with an extent of 9.6 kpc along the major axis, by far the largest in our sample. The molecular gas distribution appears clumpy (Fig. 3.4a). The estimated molecular gas mass is 2.0×10^{10} $M_\odot$, larger by about two orders of magnitude than that of any other sample member (see Table 3.5). The mean velocity map (Fig. 3.4b) shows a regularly rotating disc with some asymmetries at its extreme edges, where the major axis of the velocity field changes orientation, suggesting the presence of a warp on large scales. A well-defined double-horned shape is visible in the integrated spectrum (Figure 3.4d), with some asymmetries reflecting those in the gas distribution, the higher peak in the integrated spectrum at positive velocities being associated with the larger extent of the disc to the South. The moment 2 map (Fig. 3.4c) shows the "x-shaped" morphology characteristic of a rotating disc (e.g. Davis et al. 2017). The velocity dispersion varies from $\sim$10 to $\sim$100 km s^{-1}, but the regions characterised by line widths $>$40 km s^{-1} are highly localised, while the bulk of the disc has a dispersion $<$30 km s^{-1}.

PKS 0718-34

A barely resolved nuclear source is detected in the 230 GHz continuum (Fig. 3.2c, upper panel). Faint, double-sided emission from the jets is also detected, extending

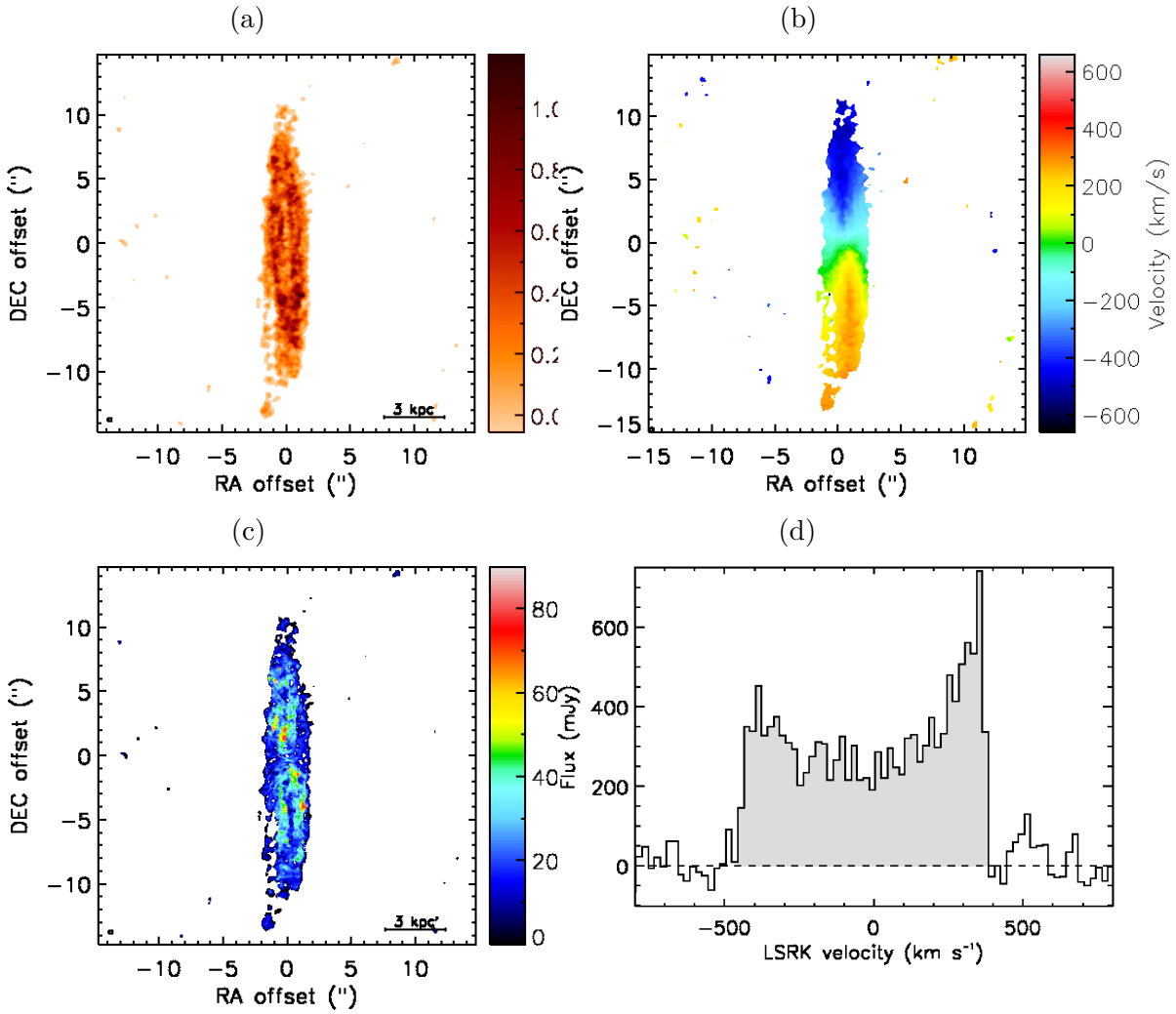

Figure 3.4: NGC 612 moment maps and spectral profile as in Fig. 3.3, created using a data cube with a channel width of 20 km s^{-1}. The integrated CO spectral profile was extracted within a box of 4×20 arcsec^2.

up to 3.2 kpc to the South-West and 1.8 kpc to the North-East of the nucleus. The 230 GHz continuum emission traces the radio structure observed at lower resolution in the archival 8.5 GHz VLA map (Fig. 3.2c, lower panel).

This object is undetected in CO, with estimated $M_{mol} < 6.7 \times 10^6$ $M_\odot$ on the assumption of a point source, or $\Sigma_{CO} < 2.7 \times 10^2$ $M_\odot$ pc^2 (Table 3.5).

NGC 3100

The 230 GHz continuum map of NGC 3100 (Fig. 3.2d, upper panel) shows a bright nuclear source. Extended emission from a two-sided jet is also detected. The northern and southern jets extend more than 400 pc and ≈300 pc from the nucleus,

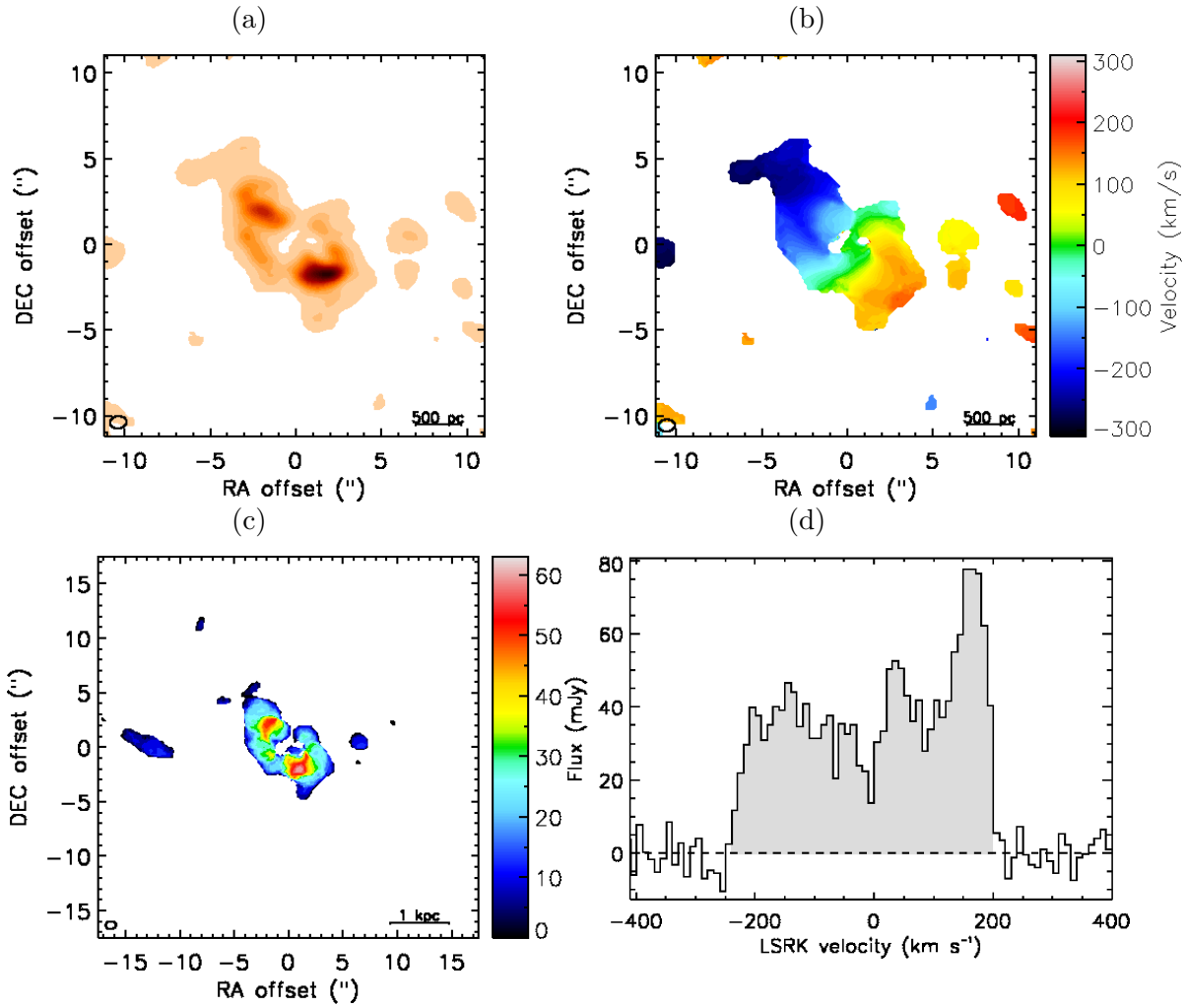

Figure 3.5: NGC 3100 moment maps and spectral profile as in Fig. 3.3, created using a data cube with a channel width of 10 km s^{-1}. The integrated CO spectral profile was extracted from the data cube within a 8.6 $\times$10 arcsec^2 box.

respectively. The continuum structures visible at 230 GHz and at 4.9 GHz match very well (Fig. 3.2d).

We detect well-resolved CO(2-1) emission with a FWHM of 1.6 kpc along the major axis. The moment 0 image (Fig. 3.5a) shows an incomplete ring with a gap to the North-West of the nucleus and flux density enhancements to the South-West and North-East. The mean velocity map (Fig. 3.5b) shows that the ring is rotating, but with some distortions in the rotation pattern. The iso-velocity contours are tilted and the major axis position angle clearly changes moving from the egde to the center of the ring, indicating the possible presence of a warp and/or non-circular motions. The velocity dispersion map (Fig. 3.5c) shows CO line broadening on

either side of the central hole, roughly consistent in position with the flux density enhancements. These features are suggestive of a physical interaction between the jets and the molecular gas disc. The integrated CO spectrum (Fig. 3.5d) exhibits the double-horned shape typical of a rotating disc, but with asymmetries reflecting those in the gas distribution.

Figure 3.5a also shows the presence of two structures at ≈1.3 kpc west and ≈2.3 kpc east from the outer edges of the central ring, detected at 7.5σ and 14σ, respectively. Including these two structures, we estimate a total molecular gas mass of $M_{mol} = 1.2 \times 10^8$ $M_\odot$. The velocity field in Figure 3.5b shows that the western and eastern regions have redshifted and blueshifted velocities, respectively, consistent with the nearest edges of the central ring but with different position angles. This leads us to speculate that they may trace the presence of a larger, warped molecular gas disc whose outer emission is below the detection threshold of our observations. Alternatively we may be seeing molecular clumps in a disc of atomic gas.

NGC 3557

The continuum map of NGC 3557 (Fig. 3.2e, upper panel) shows emission from the core and a two-sided jet. The eastern and western jets extend ≈900 pc and ≈1.2 kpc, respectively, from the nucleus. The continuum emission detected at 230 GHz traces the inner part of the radio structure visible on larger scales in the archival 4.9 GHz VLA map (Fig. 3.2e, lower panel).

We detect a CO disc (Fig. 3.6a) with $M_{mol} = 6.2 \times 10^7$ $M_\odot$. The disc is barely resolved in our observations, which have a beamwidth of 0.6 arcsec FWHM. The deconvolved major axis of the disc is ≈ 300 pc FWHM. The mean velocity map (Fig. 4.7a) shows that the gas is rotating regularly. This is also consistent with the symmetric double-horned shape of the integrated spectral profile (Fig. 3.6d). The velocity dispersion (Fig. 3.6c) decreases from ≈100 km s^{-1} in the centre to ≈20 km s^{-1} at the edges of the disc and shows a boxy profile; both features are likely to be due to beam smearing.

ESO 443-G 024

The source is detected in the continuum, showing a bright nuclear component and also faint extended emission from a two-sided jet (Fig. 3.2f, top panel). The South-East and North-West jets extend ≈900 pc and ≈1.6 kpc, respectively, from the nucleus. The extended emission detected at 230 GHz matches that observed at lower sensitivity in the archival 15 GHz VLA map (Fig. 3.2f, bottom panel).

ESO 443-G 024 is undetected in CO with estimated $M_{mol} < 3.5 \times 10^6$ $M_\odot$ assuming a point source, or $\Sigma_{CO} < 3.9 \times 10^2$ $M_\odot$ pc^2 (Table 3.5).

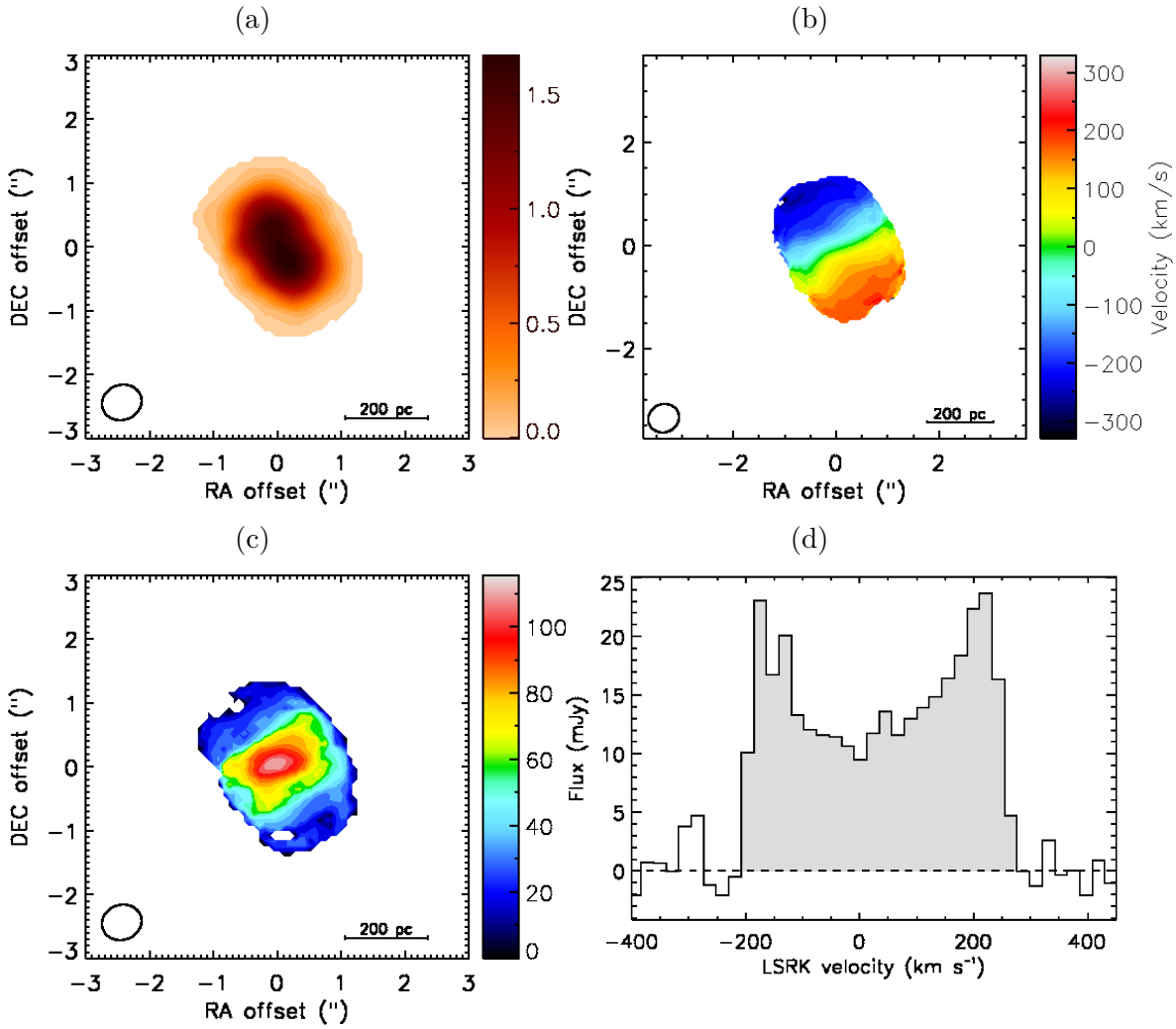

Figure 3.6: NGC 3557 moment maps and spectral profile as in Fig. 3.3, created using a data cube with a channel width of 22 km s^{-1}. The integrated CO spectral profile was extracted within a 3.0 × 3.0 arcsec^2 box.

IC 4296

A bright continuum nuclear source is detected at 230 GHz (Fig. 3.2g, upper panel), with a major axis FWHM of 30 pc. The inner jets are undetected at 230 GHz, but faint (7σ) emission is detected at a distance of about 950 pc North-West of the nucleus, coincident with the brighter knot of the North-West jet visible in the archival 4.9 GHz VLA map (Fig. 3.2g, bottom panel).

We detect CO(2-1) emission with an estimated molecular gas mass of 2.0×10^7 M$_\odot$. The CO integrated intensity map (Fig. 3.7a) shows a disc with a somewhat asymmetric morphology. The velocity field (Fig. 3.7b) shows an s-shaped zero-velocity contour, suggesting the presence of a warp in the disc, although better resolution ob-

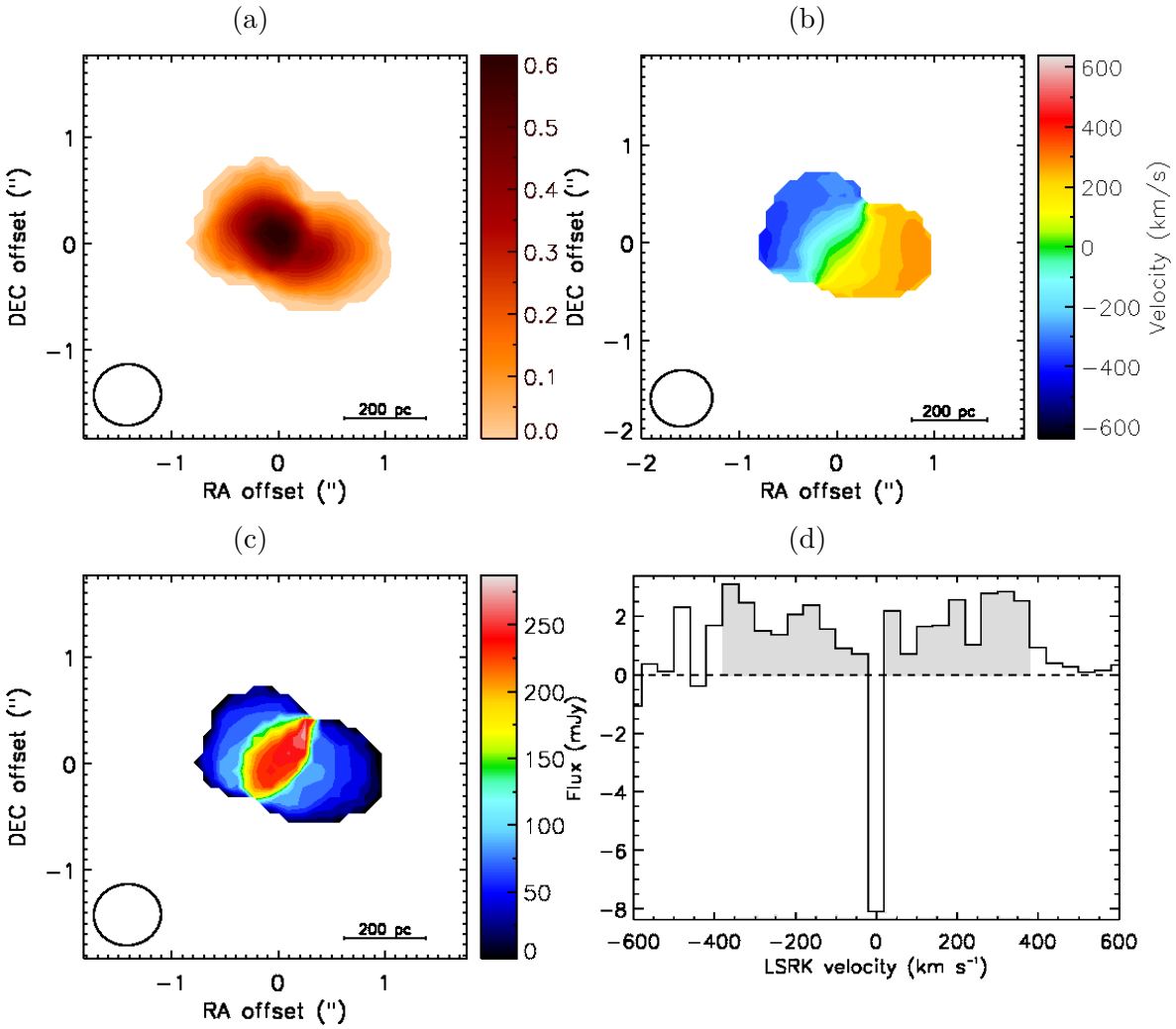

Figure 3.7: IC 4296 moment maps and spectral profile as in Fig. 3.3, created using a data cube with a channel width of 40 km s^{-1}. The integrated CO spectral profile was extracted within a 2×1.5 arcsec^2 box.

servations are necessary to confirm this hypothesis. The moment 2 map (Fig. 3.7c) is likely to be dominated by beam smearing. The integrated spectral profile (Fig. 3.7d) reveals the presence of a strong absorption feature that is discussed in more detail in Section 3.4.1.

Boizelle et al. (2017) presented Cycle 2 ALMA observations of IC 4296 in the same CO transition. They reported a 5σ CO(2-1) detection with an integrated flux of 0.76 Jy km s^{-1}, about a factor of two lower than that measured in this work. However, their CO(2-1) observation is a factor of two noisier than that presented in this paper (for the same channel width) and this may have caused them to miss some of the emission. We also note that they used different R_{21} and X_{CO} values. As a

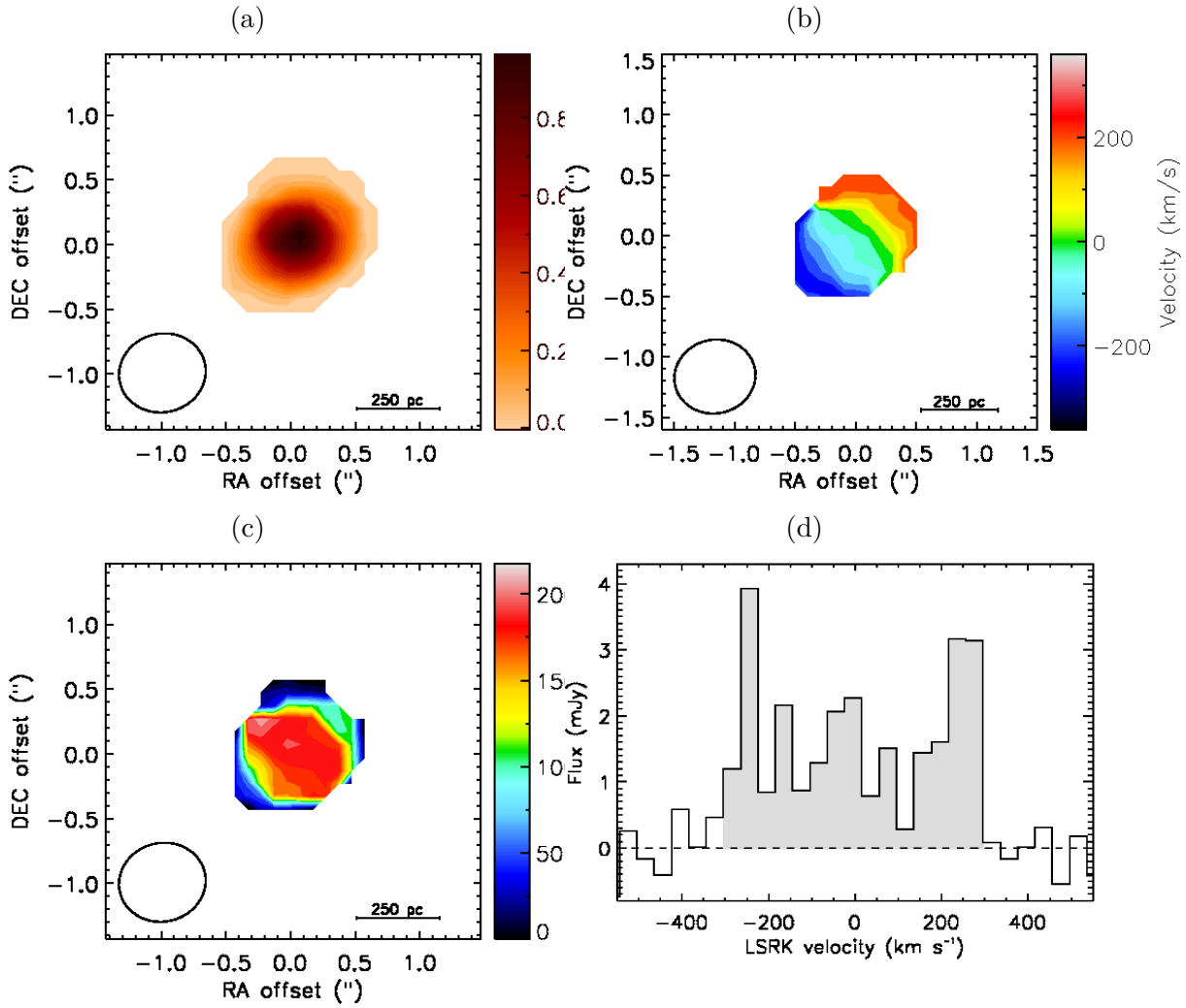

Figure 3.8: NGC 7075 moment maps and spectral profile as in Fig. 3.3, created using a data cube with a channel width of 40 km s^{-1}. The integrated CO spectral profile was extracted within a box of 1×1 arcsec^2.

consequence their mass estimate is a factor of three lower than ours. The integrated spectral profile of IC 4296 presented in Boizelle et al. (2017) is qualitatively similar to ours, with a line width of $\approx \pm 480$ km s^{-1}.

NGC 7075

A nuclear source is detected in our 230 GHz continuum map (Fig. 3.2h, upper panel), with a major axis FWHM of 40 pc. Faint emission from the eastern jet is also detected, extending to ≈1.9 kpc from the nucleus; the western (counter-) jet is undetected. The eastern jet is also visible in the archival 8.5 GHz VLA map (Fig. 3.2h, lower panel).

We detect a barely resolved CO(2-1) disc (Fig. 3.8a), with an estimated molecular gas mass of 2.9×10^7 $M_\odot$. The mean velocity map (Fig. 3.8b) shows regular gas rotation. The line-of-sight velocity dispersion (Fig. 3.8c) is likely to be dominated by beam-smeared rotation.

IC 1459

We detect continuum emission from a bright nuclear source (Fig. 3.2i, upper panel) with an estimated major axis FWHM of 10 pc. This marginally resolved continuum emission matches that visible in the archival 8.5 GHz VLA map (Fig. 3.2i, lower panel). The angular resolution (0.9″) of our observations does not allow us to resolve the pc-scale double-sided radio source detected with Very-Long Baseline Interferometry by Tingay & Edwards (2015).

Although HST optical imaging clearly shows the presence of cold ISM (in the form of dust) in this source (see Section 2.2.9), IC 1459 is undetected in CO with ALMA, with estimated $M_{mol} < 1.0 \times 10^6$ $M_\odot$ assuming a point source, or $\Sigma_{CO} < 7.6 \times 10^2$ $M_\odot$ pc^2 (Table 3.5).

3.4.1 Absorption in IC 4296

In order to investigate the absorption feature in IC 4296 in more detail, we re-imaged the visibility data into a cube at higher spectral resolution, with a channel width of 3 km s^{-1} (i.e. approximately twice the raw channel width). We then extracted the CO spectrum from a $0.4 \times 0.4\,\mathrm{arcsec}^2$ ($\approx 100 \times 100$ pc) box, centred on the 230 GHz core continuum emission. The resulting spectrum is shown in Figure 3.9. The absorption peak is at $3720 \pm 3\,\mathrm{km\,s^{-1}}$, consistent within the errors with the most accurate determination of the optical systemic velocity ($3737 \pm 10\,\mathrm{km\,s^{-1}}$; see Table 2.1). The maximum absorption depth measured from this spectrum is -20.2 mJy and the FWHM is $\approx$9 km s^{-1}, resulting in an integrated absorption flux of $\approx$0.14 Jy km s^{-1}. Morganti et al. (2001) presented a 3σ upper limit of $\tau < 0.041$ for the optical depth of the HI absorption in IC 4296. Following Morganti et al. (2001), we measured the peak optical depth, τ, using the core flux density derived from the continuum image (Table 3.3): the resulting optical depth is $\tau \approx 0.12$. If we assume an HI spin temperature of 100 K (e.g. Morganti et al. 2001), a CO excitation temperature of 10 K (e.g. Heyer et al. 2009), and an HI to H_2 column density ratio of $\sim 10^{-2}$, as estimated from HI and CO absorption in the radio emitting LINER PKS B1718−649 (Maccagni et al. 2014, 2018), we estimate an HI optical depth of $\tau \approx 1.2 \times 10^{-4}$, well below the upper limit calculated by Morganti et al. (2001).

The spectral profile in Figure 3.9 also exhibits fainter absorption features on either side of the peak (broader at blueshifted velocities). Similar structures are visible in the integrated spectrum of IC 4296 presented by Boizelle et al. (2017) with comparable channel width and extraction region. The observed asymmetric features

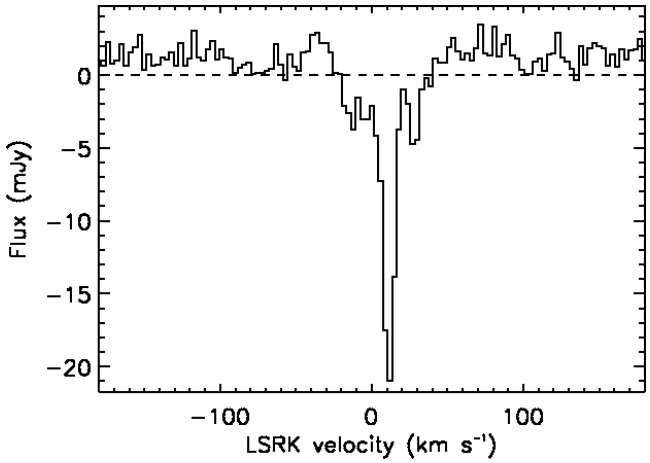

Figure 3.9: CO spectral profile of IC 4296 extracted within a $0.4 \times 0.4\,\mathrm{arcsec}^2$ box around the core. The spectrum has a channel width of $3\,\mathrm{km\,s^{-1}}$. The black dashed horizontal line indicates the zero flux level. Some unresolved CO emission is visible above the zero flux level. The line absorption feature has a FWHM of 9 km s^{-1}, with an absorption peak of ≈ -20.2 mJy.

may be a signature of the disc warping inferred on larger scales from the velocity field of CO in emission (see Section 3.4). Alternatively, they may be interpreted as an indication of the presence of non-circular motions in the central 100 pc of the CO disc. Higher-resolution observations are needed to differentiate between these two scenarios.

Chapter 4

Kinematics of the molecular gas

One of the main purpose of this work is to investigate the dynamical state of the molecular gas and derive its physical parameters. In particular, we are interested in searching for kinematical signatures that can be related to the AGN activity, such as deviations from circular motions (i.e. inflow/outflow), turbulence, instabilities. To this end, we carried out the 3D modelling of the six CO discs detected with ALMA by adopting a forward-modelling approach. The modelling is based on the data described in Chapter 3, with one notable exception, NGC 3557, for which higher-resolution CO(2-1) ALMA data taken during Cycle 4 have become recently publicly available in the ALMA archive (project 2015.1.00878.S, PI: Barth). Since the CO(2-1) disc of NGC 3557 is barely resolved at the resolution of our Cycle 3 ALMA observations ($0.6'' \simeq 130$ pc; Chapter 3), we combined our proprietary data with the archival dataset, to better constrain the kinematics of the molecular gas.

In this Chapter we present the method adopted to model the gas kinematics and the modelling results. This is followed by a more general discussion of the dynamical properties of the gas.

4.1 Archival ALMA Data

The Band 6 archival data of NGC 3557 were taken in July 2016. The total time-on-source was 19 minutes. The spectral window centred on the redshifted frequency of the CO(2-1) line is composed of 480 3.906 MHz-wide channels. 39 12-m antennas were arranged in a configuration with a maximum baseline length of 1.1 km. The achieved spatial resolution is $\approx$ 0.4 arcsec ($\approx$ 90 pc). We calibrated the data manually, using the same approach as for the other observations (see Chapter 3). The archival data were then combined with our observations, using the CASA task CONCAT. A continuum-subtracted CO data cube of the combined dataset was then produced using the CLEAN task with Briggs weighting (robust= 0.5), and a final channel width of 22 km s^{-1}. The 1σ rms noise level (determined in line-free channels) is 0.7 mJy beam^{-1}, and the achieved angular resolution is 0.44" (about 1.4

times better than that from our observations only; Table 3.2). The line parameters obtained from the combined data cube (i.e. integrated flux density, line FWHM and FWZI, etc.) are totally consistent (within the errors) with those reported in Table 3.5 using our Cycle 3 observations alone. The analysis reported in the following was carried out using this combined data cube.

4.2 Kinematic modelling: general description

We analysed the kinematics of the six CO detections using the publicly available KINematic Molecular Simulation tool (KinMS[1]; Davis et al. 2013). This routine is based on a forward-modelling approach: it allows to input guesses for the gas distribution and kinematics and, taking into account various observational effects (such as disc thickness, beam smearing, gas velocity dispersion, etc.), it produces mock ALMA cubes with the same beam, pixel size and channel width as the observed ones. The simulated data cube is generated by calculating the line-of-sight projection of the circular velocity for a given number ($10^5 - 10^6$) of point-like sources that represent the gas distribution. Additional velocity contributions can be added to take into account the velocity dispersion and non-circular motions.

The KinMS routines are coupled with the Markov Chain Monte Carlo (MCMC) code (KinMS_MCMC [2]), that fits the data and allows to obtain the full Bayesian posterior probability distribution (i.e. the best-fit model parameters).

4.2.1 Gas distribution

One of the inputs of the KinMS models is an arbitrary parametric function that describes the surface brightness of the gas disc as a function of the radius. In late-type disc galaxies the radial surface brightness profiles of the molecular gas have been studied in detail (e.g. Regan et al. 2001; Leroy et al. 2009). On small scales (< 100 pc), the clumpy nature of the ISM causes the molecular gas surface brightness to deviate from that of the stars, but at larger scales (such as those probed by our observations; see Table 3.2), they are found to tightly follow a common behaviour in most of the cases: the radial intensities have a central peak and then decline steadily as the radius increases. Indeed, as a result of the decrease in the density of stars, the surface brightnesses of galaxies fall at increasing radii. A good generalization to the structures observed in light profiles of (both early- and late-type) galaxies is provided by the empirically determined Sérsic function (Sérsic 1963):

$$\Sigma(r) = \Sigma_0 \; e^{\left[-\left(\frac{r}{R_{\rm e}}\right)^{1/n}\right]} \tag{4.1}$$

[1] https://github.com/TimothyADavis/KinMS

[2] https://github.com/TimothyADavis/KinMS_MCMC

where $\Sigma(r)$ is the surface brightness at radius r from the centre, Σ_0 is the central brightness, R_e is the scale length radius (i.e. the radius at which the light intensity drops by e^{-1}), and n is the Sérsic index (i.e. shape parameter). Late-type galaxies generally exhibit Sérsic profiles with $n = 1$ (i.e. exponential profile), whereas ETGs and the bulges of late-type galaxies commonly have Sérsic surface brightness profiles with $n = 4$ (i.e. de Vaucouleurs profile). In the framework of the ATLAS^{3D} survey (Cappellari et al. 2011), however, Davis et al. (2013) analysed the CO surface brightness profile of 41 nearby ETGs, showing that a simple exponential profile is also appropriate for describing the radial CO surface brightness curve of the majority of the ETGs in their sample (21/41; 51%; an example is shown in Figure 4.1). The remaining 49% of the sample shows varied CO light profiles (e.g. truncated, centrally deficient, etc.) that are mostly associated with disturbed gas distributions in galaxies undergoing interaction or merger events. At the resolution of our ALMA observations, however, the shapes of the observed gas surface brightness profiles turn out to be reasonably well described by a simple Gaussian function (with the only exception of NGC 3100; see Section 4.3.2)

$$\Sigma_{\rm CO} = \frac{1}{\sigma\sqrt{2\pi}} e^{-\frac{(x-\mu)^2}{2\sigma^2}} \tag{4.2}$$

where μ is the median of the Gaussian curve (i.e. the centre), and σ is the standard deviation (i.e. the width). Both parameters are left free to vary in the KinMS_MCMC fit. Additional free parameters describing the distribution of the gas disc are the integrated flux, kinematic position angle (PA), inclination ($\theta_{\rm inc}$), and kinematic centre (in RA, Dec and velocity). The inclination and position angles are initially fitted as single values throughout the disc. The CO disc is assumed to be thin and the model is intrinsically axi-symmetric (i.e. by construction, it does not reproduce asymmetries in the gas distribution).

4.2.2 Gas kinematics

A second fundamental input of the KinMS models is a function that describes the velocity profile of the molecular gas as a function of the radius (i.e. circular velocity curve). The kinematics of the molecular gas around the galaxy centre (where our CO detections are mostly distributed; see Table 3.5) contains a substantial contribution from the luminous matter (i.e. the stars), which dominate the mass budget (and hence the potential) in the central part of ETGs (e.g. Cappellari et al. 2006; Davis et al. 2013). For late-type spiral galaxies, it is currently well established that the velocity curve can be described by a solid body rotation in the very centre (with the circular velocity increasing almost linearly with radius, $v \propto R$), followed by a slowly rising or constant velocity in the outer parts, where the dark matter haloes dominates the mass budget (e.g. van Albada et al. 1985). In late-type objects, however, the motions of stars are dominated by ordered rotation and the large-scale

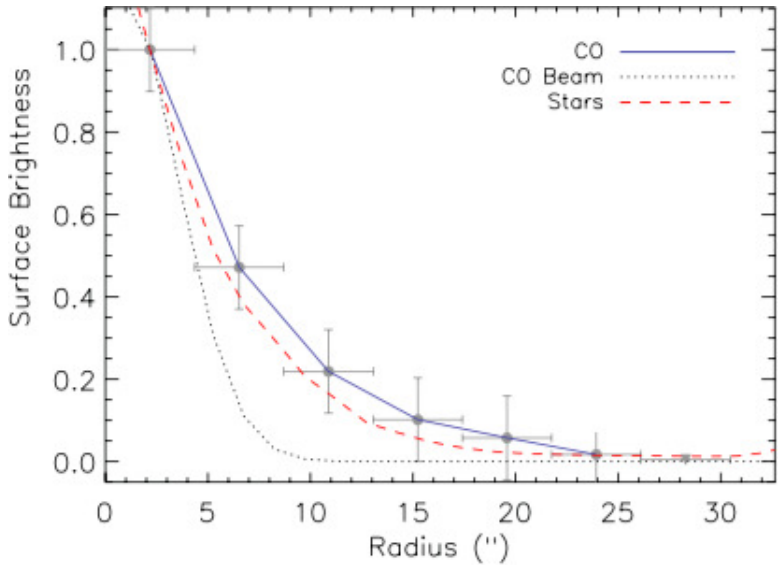

Figure 4.1: Surface brightness profile of the stars (red dashed line) and molecular gas (blue solid line) of a typical ETG analysed by Davis et al. (2013) in the framework of the ATLAS^{3D} project. The CO beam size is shown as a black dotted Gaussian.

HI discs from which they are typically surrounded also allow us to map their velocity profiles up to the outermost regions of the galaxy (e.g. Sofue & Rubin 2001). ETGs often lack these large cold gas discs and are more centrally concentrated than late-type galaxies of the same mass, suggesting that they may have circular velocities that are higher in the inner parts than in the outer parts (e.g. Rix et al. 1997; Graham 2004). Furthermore, the stellar dynamics in ETGs has been shown to be much more complex than that in disc galaxies, with random motions dominating the kinematics and kinematically decoupled components often observed in their centres, leading to substantial differences between individual objects (e.g. Cappellari et al. 2006; Weijmans et al. 2009; Emsellem et al. 2011). Accurate photometric studies (using high-resolution optical imaging) would be required to properly map the large variety of kinematics of the luminous component in ETGs. This would allow us to construct a stellar mass model and, in turn, the galaxy velocity curve via the stellar mass-to-light ratio (M/L, whereby $v_{\rm circ} \propto \sqrt{M/L}$; e.g. Davis et al. 2013), enabling the prediction of the circular velocity of the gas caused by the luminous matter. However, high resolution (e.g. HST) optical imaging is not available for the majority of our objects. Moreover, in almost all the cases the position-velocity diagrams (PVDs; i.e. velocity curves) show only a central (mostly featureless) rising component, since the gas do not extend beyond the turnover radius of the velocity curve (i.e. the radius that marks the transition between the central rising and the external flat part of the velocity curve) and/or the turnover is not resolved at the resolution of our observations. In cases like these, a detailed analysis of the galaxy optical photometry would not provide a significant improvement in the modelling

of the gas rotation curves, compared to arbitrary determined functional forms often proposed to empirically describe galaxy rotation curves (e.g. Courteau 1997). The simplest model that has been shown to provide a good fit to most rotation curves of ETGs on (sub-)kpc scales follows an arctangent function in the form (e.g. Swinbank et al. 2012; van de Voort et al. 2018):

$$v(R) = \frac{2v_{\rm flat}}{\pi} \arctan\left(\frac{R}{r_{\rm t}}\right) \tag{4.3}$$

where $v(R)$ is the circular CO velocity as a function of the radius R, $v_{\rm flat}$ is the asymptotic (or maximum) circular velocity in the flat part of the rotation curve, and $r_{\rm t}$ is the effective turnover radius (e.g. van de Voort et al. 2018). An example of the rotation curves obtained using this model is sketched in Figure 4.2. We adopted this function to describe the CO rotation curves of our sources (with the exception of NGC 3557; see Section 4.3.1). Both $v_{\rm flat}$ and $r_{\rm t}$ are left as free parameters in the fitting process, in order to find the best match to the observed gas velocity curves.

As a first step, we always assume that the gas is in purely circular motion (i.e. the rotation velocity varies only radially). This approach allows us to identify the possible presence of non-circular motions, if significant residuals (i.e. larger than the channel width) are found between the data and the model velocity fields. Another free parameter is the internal velocity dispersion of the gas ($\sigma_{\rm gas}$), assumed to be spatially constant.

4.2.3 Fitting process

To fit the model to the data we use the KinMS_MCMC code, which utilises Gibbs sampling and adaptive stepping[3] to explore the parameter space. To measure the goodness-of-fit of the model to the data a chi-squared statistics is used:

$$\chi^2 = \sum_i \left(\frac{{\rm data}_i - {\rm model}_i}{\sigma_i}\right)^2 = \frac{1}{\sigma^2}\sum_i ({\rm data}_i - {\rm model}_i)^2 \tag{4.4}$$

where the sum is performed over all the pixels within the region of the data cube that the model fits, and σ is the rms noise level measured in line-free channels of the data cube (see Table 3.4), assumed to be constant for all the pixels. The

[3]Gibbs sampling is an MCMC algorithm that produces samples from a posterior distribution conditioned on the observed data and thus allows to obtain final estimates of a model parameter. It is applicable when the joint distribution is not known explicitly or is difficult to sample from directly, but the conditional distribution of each variable is known and is easy to sample from. The Gibbs sampling algorithm generates an instance from the distribution of each variable in turn, conditional on the current values of the other variables. In the version used in this work it incorporates an adaptive stepping algorithm that allows us to explore the parameter space by progressively adapting the intervals within which the priors are left free to vary, in order to make the code converge faster.

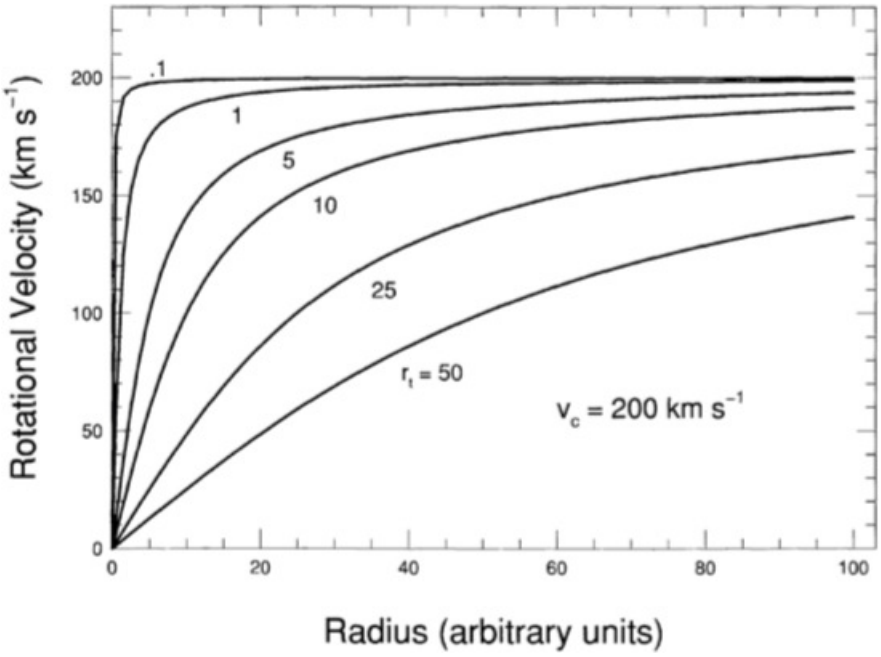

Figure 4.2: Example of the arctangent models used to fit the CO velocity curves (adapted from Courteau 1997). The different curves are for different values of the truncation radius, $r_{\rm t}$, and the same circular velocity in the flat part of the curve (here assumed to be $v_{\rm c} = 200$ km s^{-1}).

posterior distribution of each model is then described by the log-likelihood function $\ln \mathrm{P} = -\chi^2/2$. As in Smith et al. (2019), we re-scale the uncertainty of the fitted parameters by a factor of $(2N)^{0.25}$, where N is the number of pixels with detected emission in the mask, as defined in Section 3.3. This ensures that the uncertainty in the χ^2 statistics for high N does not lead to unrealistically small uncertainties in our final fit values.

To ensure our fitting process converges, we set reasonable priors for the physical parameters that are left free to vary in the fit. Specifically, the CO central velocity offset (i.e. the shift with respect to the kinematic centre) is allowed to vary within the channel widths of each data cube (listed in Table 3.2). The gas velocity dispersion ($\sigma_{\rm gas}$) is constrained to be less than the maximum line-of-sight velocity widths shown in Chapter 3. Within KinMS, the kinematic PA of the gas distribution on the sky is defined as the angle measured counterclockwise from the north to the receding side of the velocity field. We then made an initial estimate of the the kinematic PA by looking at the moment 1 maps of our CO detections, and then allowed it to vary by ± 40 degrees around the estimated values. By definition, the disc inclination ($\theta_{\rm inc}$) is the angle between the observer line-of-sight and the normal to the disc plane. In our modelling, we initially left it free to vary over the full physical range ($0^\circ - 90^\circ$, where 0° and 90° mean "face-on" and "edge-on",

Table 4.1: Best-fit model parameters.

Target	PA_{kin} (deg)	θ_{inc} (deg)	v_{flat} (km s^{-1})	r_{turn} (arcsec)	σ_{gas} (km s^{-1})	v_{offset} (v_{CO}) (km s^{-1})	R_{hole} (arcsec)	χ^2_{red}
(1)	(2)	(3)	(4)	(5)	(6)	(7)	(8)	(9)
IC 1531	356±1.0	32±2.5	272±29	0.07±0.02	3.4±2.3	−25±1.0 (7677)	–	1.2
NGC 612	183±0.05	81±0.01	453±0.04	1.2±0.05	20±0.02	−95±0.01 (8879)	0.3	1.2
IC 4296	240-220	68±1.5	404±1.5	0.01±0.002	64±1.5	−16 ± 2.0 (3691)	–	1.0
NGC 7075	322±4.0	46±1.5	446±56	0.03±0.02	5.1±2.6	7.8±3.0 (5491)	–	1.1

Notes. – Columns: (1) Target name. (2) Kinematic position angle of the CO disc (i.e. the PA measured counter-clockwise from North to the receding side of the velocity field). It is given as a range where a position angle warping is modelled. (3) Inclination angle of the disc. (4) Asymptotic (or maximum) circular velocity in the flat part of the rotation curve. (5) Effective radius at which the rotation curve turns over. (6) Gas velocity dispersion. (7) Velocity offset of the kinematic centre, i.e. offset between the expected and observed velocity zero-point of the line emission. Specifically, the expected zero-point corresponds to the redshifted frequency of the CO(2-1) transition listed in column (3) of Table 3.2; the observed zero-point consists in the best estimate of the line systemic velocity as inferred from the observed spectral profiles. The corresponding CO central velocity is reported in parentheses. (8) Radius of the central surface brightness cut-off. (9) Reduced χ^2 of the best-fit model.

respectively); in subsequent iterations, it is constrained to vary within ±20° of the value at which the first chain converges. The maximum circular velocity of CO (v_{flat}) and the turnover radius (r_{turn}) are constrained to lie within ±40 km s^{-1} and two beam widths, respectively, around best guess values determined by visually inspecting the velocity curves (PVD) of the six CO discs. In particular, in those cases in which the turn over of the velocity curve is resolved (e.g. NGC 612), we initially set v_{flat} as the velocity value associated with the flat part of the curve and r_{turn} as the radius where the curve starts to turn over; when the flattening of the velocity curve is not resolved (e.g. NGC 7075), we assume as best initial guesses for v_{flat} and r_{turn} the maximum sampled circular velocity and the corresponding radius, respectively.

Initially, the step size in each fit is manually scaled on a source-by-source basis to ensure a minimum acceptance fraction and the chain convergence. Once the MCMC chains converged, we re-ran the entire chain for an additional 10^5 steps to produce the full final posterior probability distribution. For each model parameter these probability surfaces are then marginalised over to produce a best-fit value (median of the marginalised posterior distribution) and associated 68 and 99% confidence levels (CL).

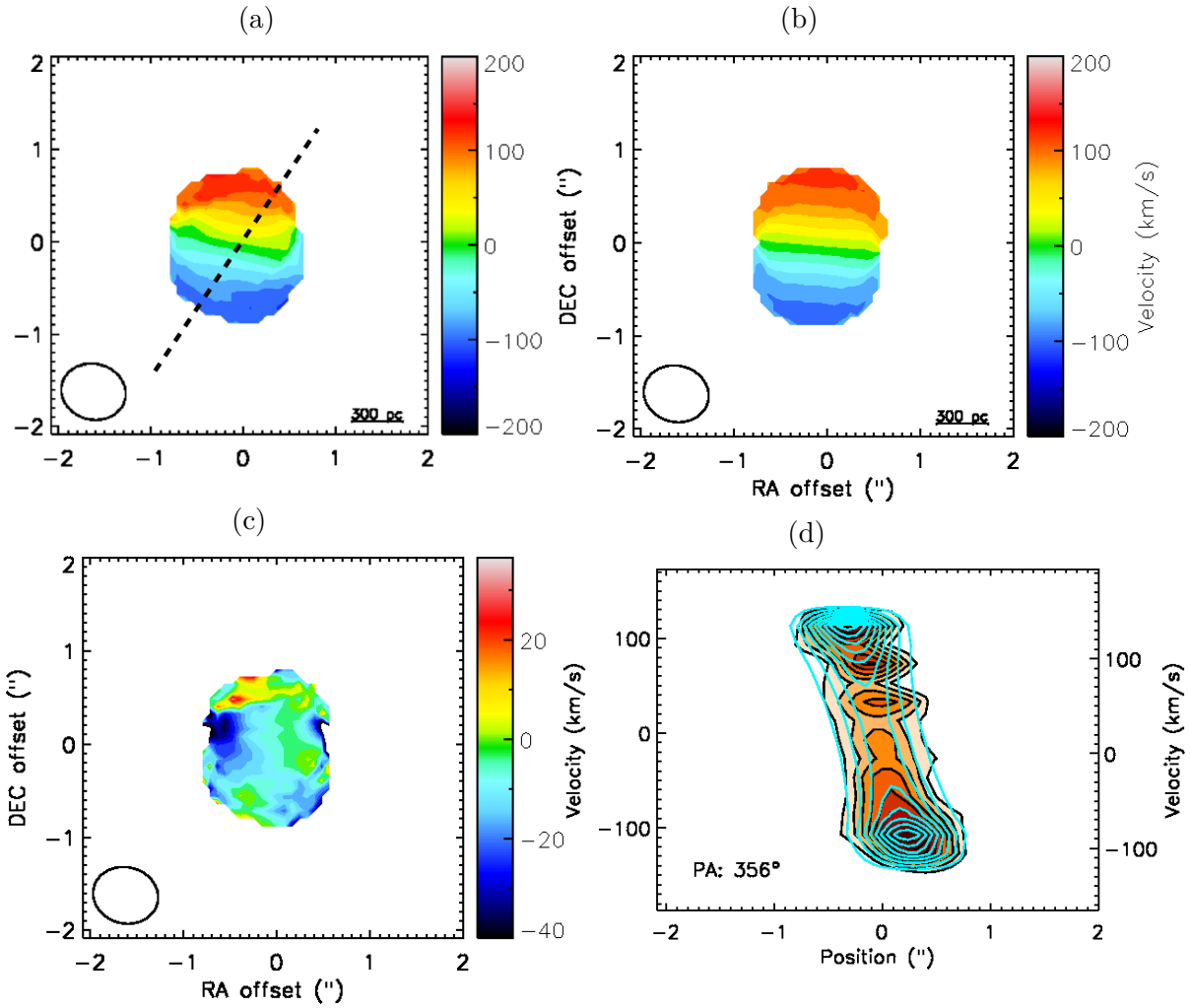

Figure 4.3: **IC 1531** observed, mock and residual (data-model) mean velocity maps (panels **a**, **b** and **c**, respectively). The black dashed line in panel **a** indicates the direction of the radio jet axis. The synthesised beam is shown in the bottom-left corner of each panel. The wedges to the right show the colour scale. East is to the left and North to the top. Velocities are measured in the source frame and the zero-point corresponds to the intensity-weighted centroid of the CO emission ($v_{\rm CO}$; see Table 4.1). The maps are created with the masked moment technique described in Section 3.3 of Chapter 3, using a data cube with a channel width of 20 km s^{-1}. CO PVD (panel **d**) extracted within a rectangular slit which includes all of the CO emission along the major axis. The starting point of the slit (i.e. the smallest offset value) is oriented with respect to the kinematic position angle, indicated in the bottom-left corner of the panel. The contours of the best-fit model are overlaid in cyan. The x-axis indicates the position offset along the extraction axis. The y-axes indicate the velocities centred on the expected (right axis) and observed (left axis) velocity zero-point of the line emission, reported in column (7) of Table 4.1 and in column (3) of Table 3.2, respectively. The contour levels are drawn at 1, 3, 9...times the 1σ rms noise level (see Table 3.4).

4.3 Kinematic modelling: individual sources

At the resolution of our ALMA observations (Table 3.2), the majority of the CO discs are only marginally resolved, so that the simple geometrical model described above reproduces reasonably well the bulk of the observed gas structures. Nevertheless, modifications to that basic model are required in some cases to fully reproduce the gas distribution and kinematics, by accounting for either the presence of warps or an inner surface brightness cut-off. Below we describe the modelling details for the four individual sources where no or minor modifications to the model are required to get a good fit to the data. The best-fit parameters, associated errors (including only random uncertainties at 99% confidence level), and the reduced chi-squared $(\chi^2_{\rm red})^4$ of the models adopted for these four objects are listed in Table 4.1. The upper panels of Figures 4.3 − 4.6 compare the observed and modelled mean velocity maps (moment 1; panels a and b). The middle panels of Figures 4.3 − 4.6 show the data-model residual moment 1 map (panel c) and the major axis PVD with the best-fit model over-plotted (cyan contours; panel d).

NGC 3557 and NGC 3100 are special cases: the asymmetries observed both in their morphology and kinematics require a more complex approach, discussed separately in Sections 4.3.1 and 4.3.2.

IC 1531

The barely resolved CO disc of IC 1531 mainly exhibits regular rotation pattern and morphology. Therefore, a simple axisymmetric model seems to reproduce reasonably well the observed gas features (Fig. 4.3). However, an s-shaped distortion is visible in the rotation pattern at $\approx 0.5''$, along the zero-velocity iso-contour (Fig. 3.3b). Asymmetric structures are also present at the same position in the velocity curve, between ≈ 0 and ≈ 100 km s^{-1} (Fig. 4.3d). Such distortions may trace the presence of warping and/or non-circular motions (e.g. inflow, outflow, streaming). We attempted to include both position and inclination angle warps in our model, but these were not favoured by the fitting routine. This may suggest that non-circular motions dominate, or that given the poor resolution of our data there was simply not enough information to constrain more complex models. The observed distortions not reproduced by the model likely give rise to the low-level residuals (≈ -30 km s^{-1}) visible in Figure 4.3c at one edge of the gas disc, at the position of the zero-velocity contour. The best-fit model in Figure 4.3, however, does not show significant departures from the data, suggesting that, if present, such radial motions or asymmetries are small in amplitude and do no critically affect our analysis. Higher resolution observations are needed to further investigate this object.

[4] $\chi^2_{\rm red} = \dfrac{\chi^2}{\rm d.o.f}$, where d.o.f. is the number of degrees of freedom for the adopted model.

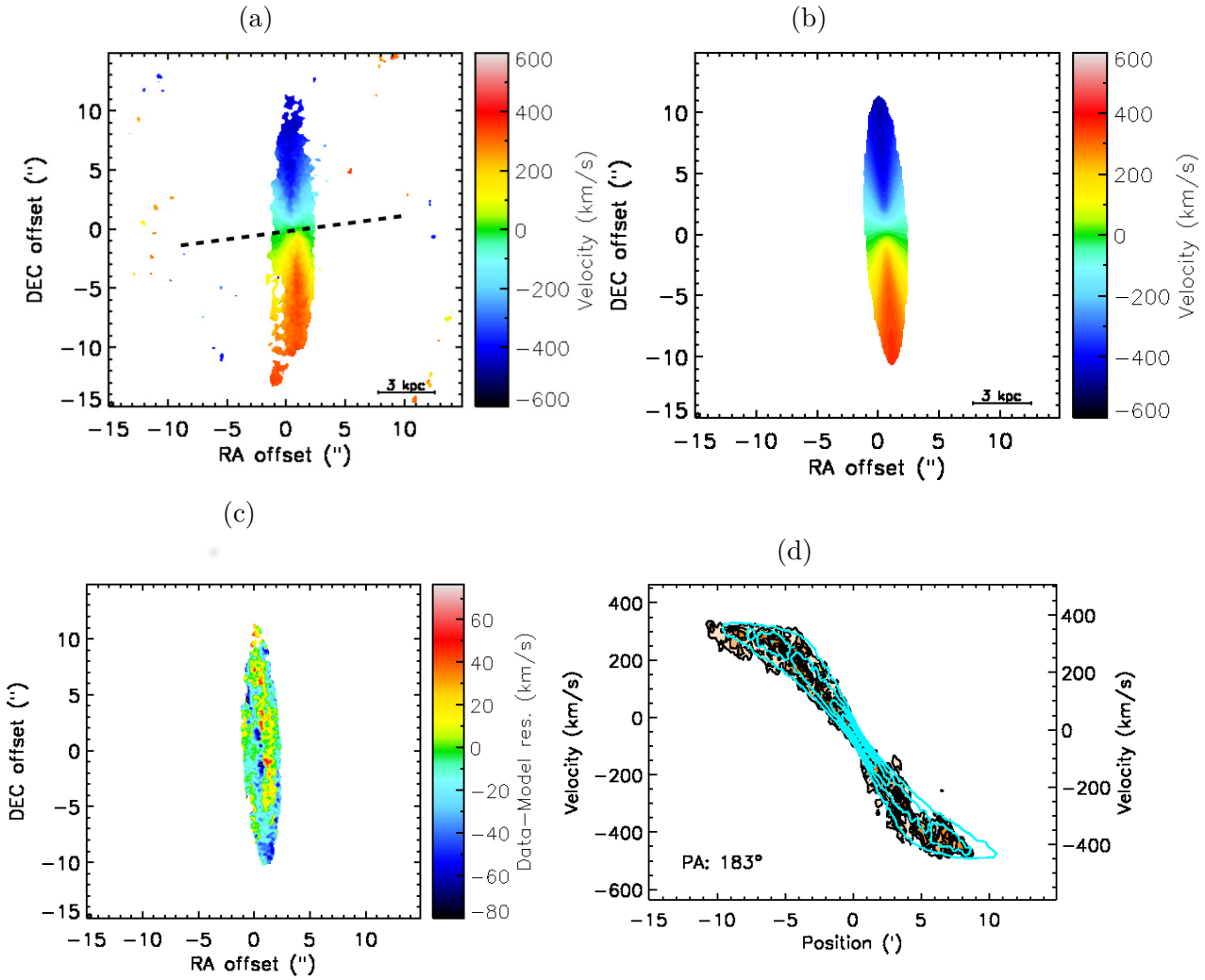

Figure 4.4: **NGC 612** observed, mock, residual mean velocity maps and PVD as in Figure 4.3, created using a data cube with a channel width of 20 km s^{-1}.

NGC 612

NGC 612 is exceptional among our sources: we detected a large CO(2-1) disc extending ≈10 kpc along the major axis, with an estimated molecular gas mass of 2.0×10^{10} M$_\odot$ (about two order of magnitude larger than the other CO detections; see Chapter 3).

In this case, our initial model left large residuals affecting the inner part of the disc (peak amplitudes≈ ±80 km s^{-1}). Furthermore, the sharp edges of the velocity curve (Fig. 4.4d) could not be well reproduced. The best-fit model shown in Figure 4.4 is obtained assuming a ring-like CO distribution with a Gaussian surface brightness profile. The size of the central hole was left free to vary and the best-fitting value was found to be ≈ 0.3″ (180 pc) (Table 4.1). It therefore seems

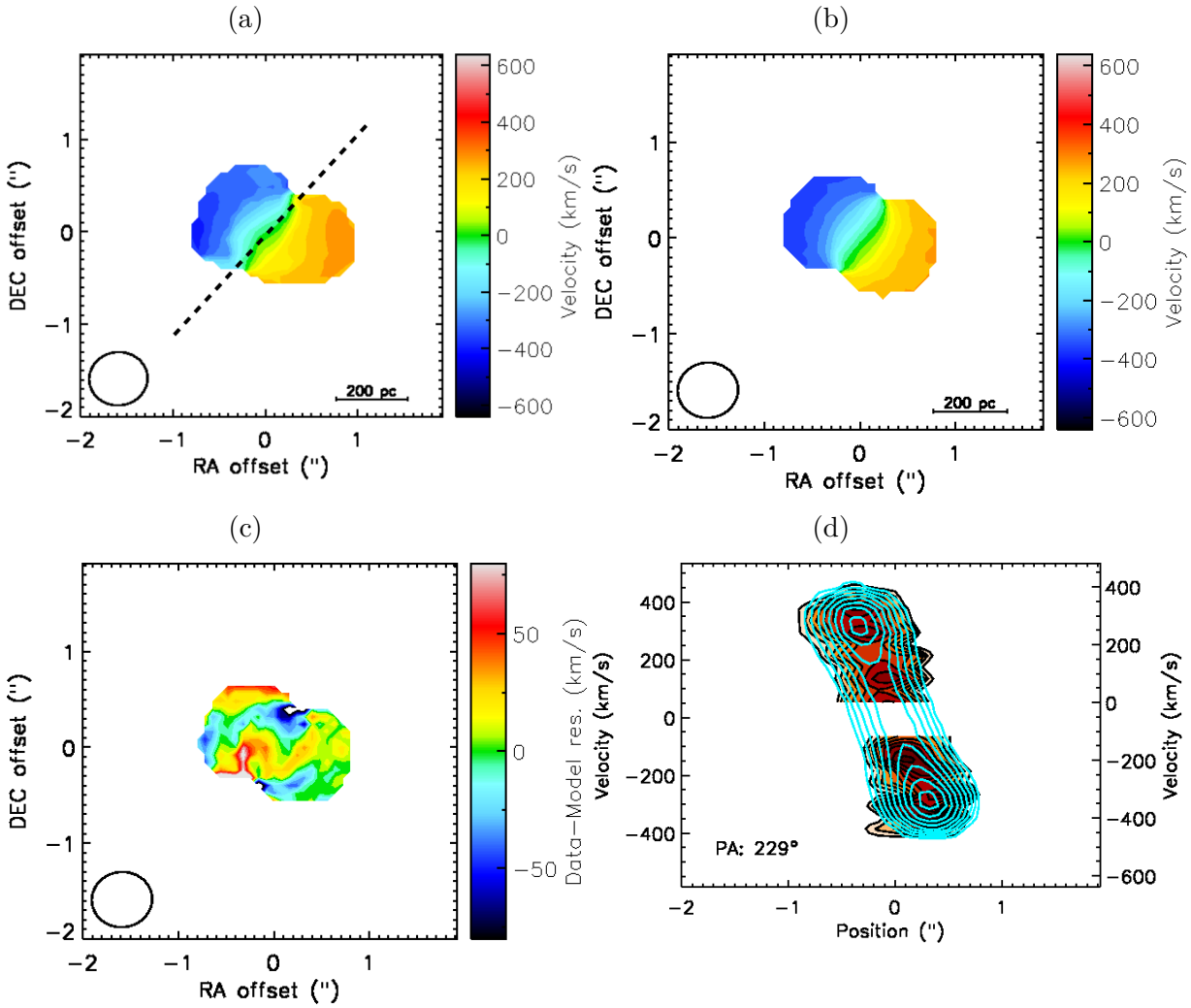

Figure 4.5: **IC 4296** observed, mock, residual mean velocity maps and PVD as in Figure 4.3, created using a data cube with a channel width of 40 km s^{-1}.

likely that the CO does not extend into the very centre of this disc. Some high-level residuals (peak amplitudes$\approx \pm$60 km s^{-1}) are still visible in the central part of the gas distribution, possibly suggesting the presence of non-circular motions. Significant residuals (peak amplitudes$\approx \pm$40 km s^{-1}) are also visible at the outer edges of the disc (Fig. 4.4c) and likely due to the corresponding observed asymmetries (Fig. 4.4a). These are likely associated with the presence of a warp that, if present, affects the disc only on the largest scales. For this reason, we did not attempt to model it.

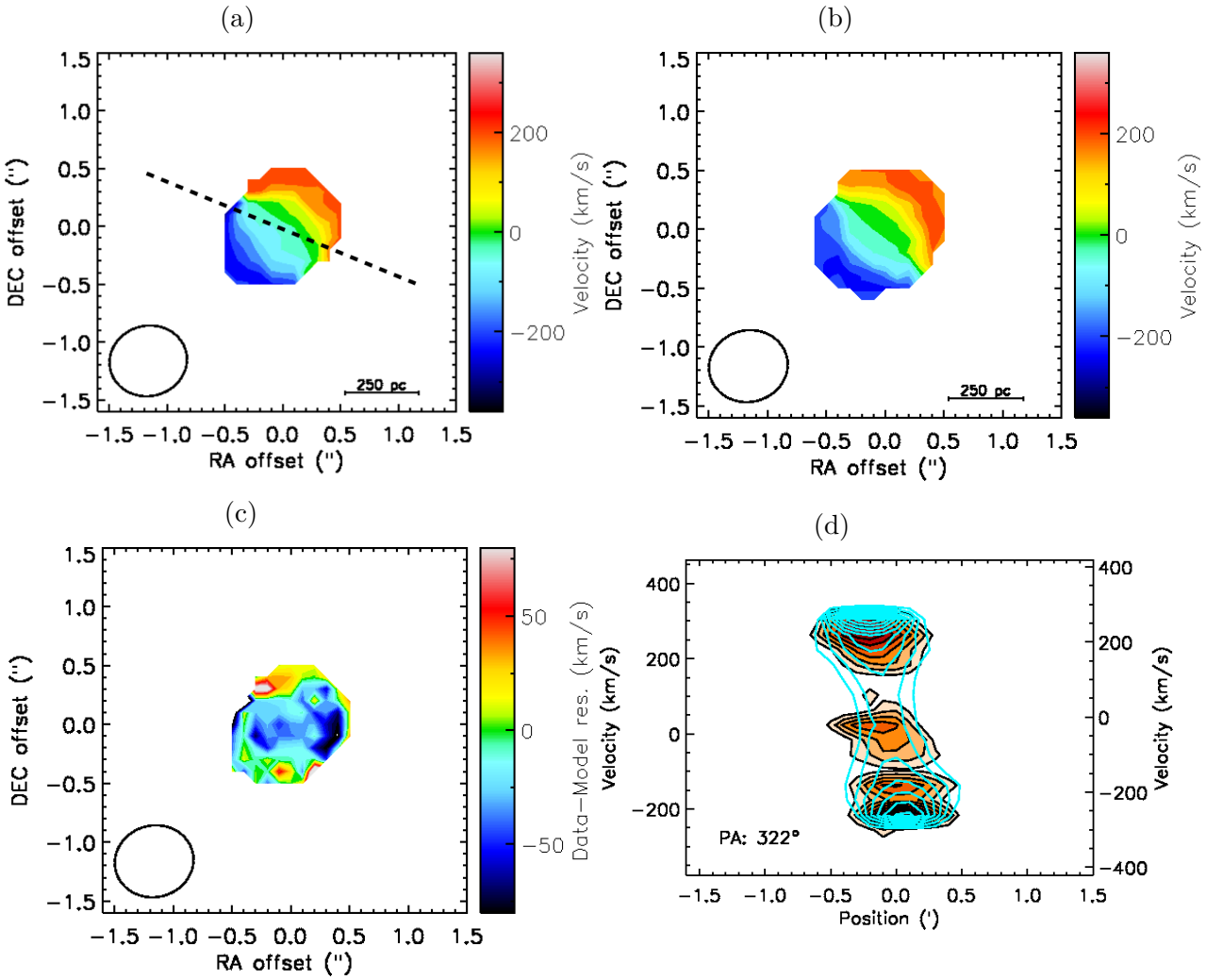

Figure 4.6: **NGC 7075** observed, mock, residual mean velocity maps and PVD as in Figure 4.3, created using a data cube with a channel width of 40 km s^{-1}.

IC 4296

Although the basic model described in Section 4.2.1 provides a good overall representation of the observed disc, the CO rotation pattern of IC 4296 is well reproduced only when accounting for the presence of a warp (Fig. 4.5a and 4.5b). Specifically, we let the kinematic position angle vary radially along the disc, finding that it the best-fitting value ranges between 240 and 220 degrees (Table 4.1). Nevertheless, low level residuals (slightly larger than the channel width= 40 km s^{-1}) are still visible along the disc minor axis (Fig. 4.5c), possibly suggesting the presence of non-circular motions. It is hard, however, to establish whether they are reliable or not, given the resolution of the current dataset (Table 3.2). In general, the gas distribution is well reproduced by the model, even tough the gas disc is lopsided at

its edges (Fig. 4.5a) and the intrinsic axisymmetry of the model does not allow us to reproduce the observed distortion. We note that an absorption feature against the radio core was detected in this source (see Chapter 3), giving rise to the hole in the gas distribution visible in the velocity curve (Fig. 4.5d). The channels in which the CO absorption dominates were excluded from the model.

NGC 7075

The CO disc in NGC 7075 is barely resolved by our ALMA observations (see Chapter 3). Our best-fitting basic model does not show significant departure from the observed disc. Some residuals are present (Fig. 4.6c), but given the poor resolution we are not able to further investigate their origin. Interestingly, there is an asymmetry in the PVD that is not reproduced by the model (Fig. 4.6d). Furthermore, a hole is visible in the gas distribution at positive velocities. These features indicate that some disturbance is occurring in the gas disc (both morphologically and kinematically). Higher resolution observations would be needed to further investigate the origin of the observed structures.

4.3.1 The case of NGC 3557

The CO(2-1) emission of NGC 3557 shows a disc-like structure, but asymmetric features are evident both in the rotation pattern (Fig. 4.7a) and the velocity curve (Fig. 4.7d). Distortions are clearly visible in the mean velocity map at $\approx -0.8''$ (positive velocities; Fig. 4.7a), likely corresponding to the asymmetry at the same position in the PVD (Fig. 4.7d). Furthermore, a region of high-velocity emission is visible in the PVD in the form of a slight upturn around the centre (positive velocities), in the locus of the turnover radius. This central velocity upturn is relatively faint and only seen within $+0.2''$ of the nucleus. Similar features may be the results of different potential phenomena (see Section 4.4). However, a velocity increase around the galaxy centre may also be associated with the Keplerian upturn arising from material orbiting around the central SMBH (e.g. Davis et al. 2017). Indeed, as described in Section 4.2.2, the mass budget (and hence the kinematics) in the central part of ETGs is dominated by their stars. Nevertheless, the kinematics of the molecular gas can contain contributions from both the luminous stellar mass and the central SMBH in regions in which the potential is dominated by the SMBH. Keplerian motions are expected from material within this region and are visible in observations where the sphere of influence (SOI)[5] of the SMBH is resolved and some

[5]The sphere of influence (SOI) is a region around a SMBH in which the gravitational potential of the black hole dominates the gravitational potential of the host galaxy. The radius of the sphere of influence is called the "(gravitational) influence radius". It is defined as $R_{\rm SOI} = \frac{GM_{\rm SMBH}}{\sigma_*^2}$, where G is the gravitational constant, $M_{\rm SMBH}$ is the SMBH mass and σ_* is the stellar velocity dispersion.

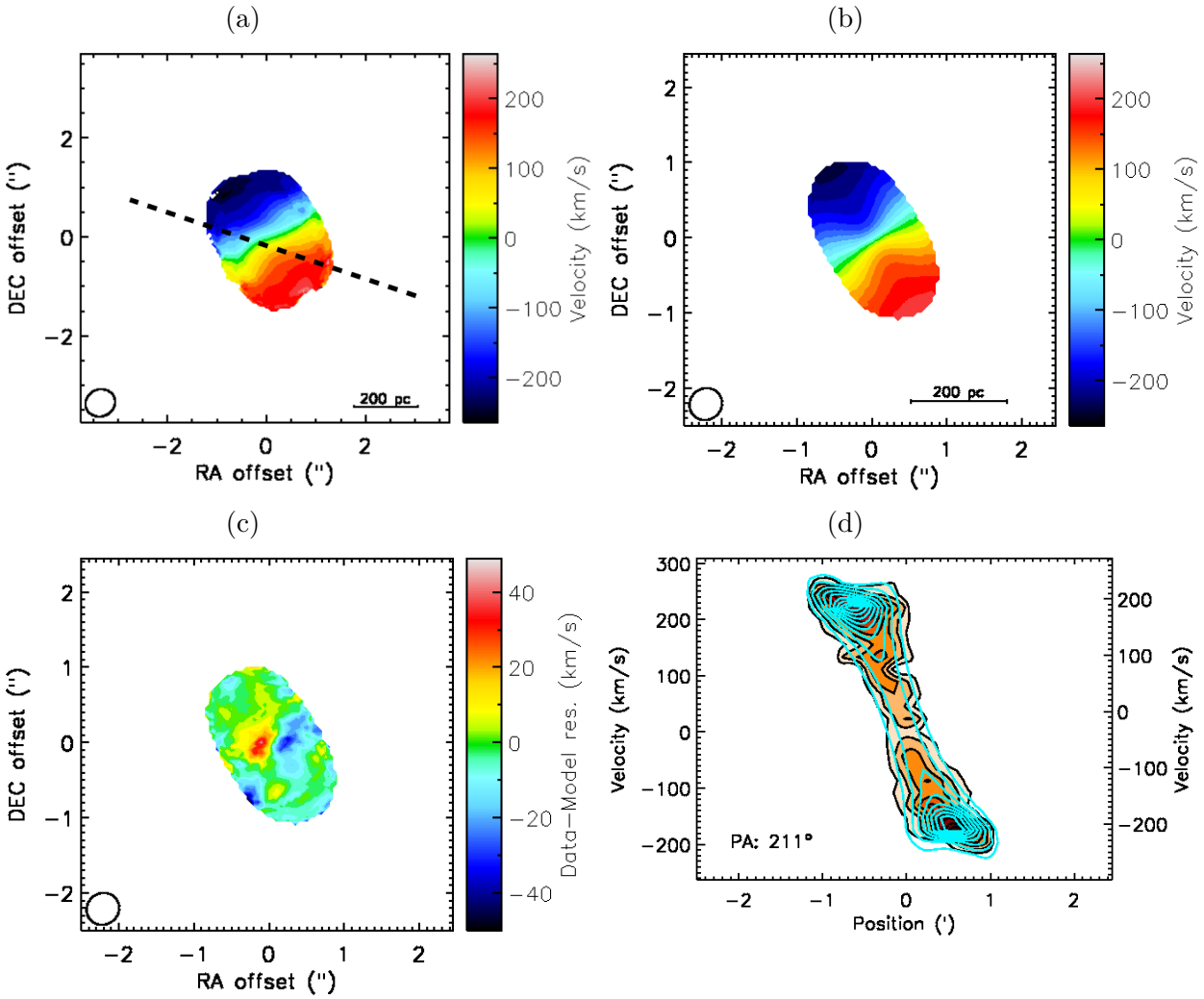

Figure 4.7: NGC 3557 observed, mock, residual mean velocity maps and PVD as in Figure 4.3, created using a data cube with a channel width of 22 km s^{-1}.

emission arises from within the SOI. Spatially resolving the Keplerian region allows to constrain the SMBH mass to high accuracy (see e.g. Onishi et al. 2017; Davis et al. 2017, 2018).

To explore this possibility, we first verified if the spatial resolution of the combined observations allows us to resolve the SOI of the SMBH. Assuming a central stellar velocity dispersion of ≈ 282 km s^{-1} (Brough et al. 2007), the SMBH mass would be $\log(M_{\rm SMBH}) \simeq 8.82$ $M_\odot$ (derived from the $M_{\rm SMBH} - \sigma_*$ relation of Tremaine et al. 2002). The resulting $R_{\rm SOI}$ is ≈ 60 pc, slightly smaller than the spatial resolution of the combined observations ($0.44'' \approx 90$ pc). It is then possible that the velocity increase around the disc centre traces Keplerian motions of gas close to a region where the potential is dominated by the SMBH.

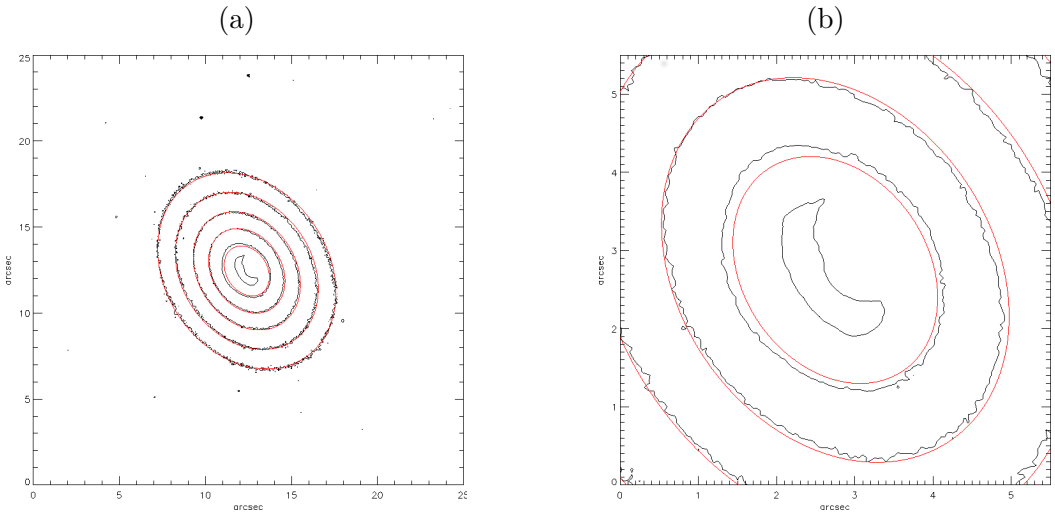

Figure 4.8: MGE model of NGC 3557 (red contours), overlaid on the HST optical (F555W) image (black contours) used for this analysis. Panel **a** shows the whole galaxy, while panel **b** shows a zoom in on the central region. The structure visible to the east of the nucleus in both panels corresponds to the region masked due to dust (see the text for details).

Table 4.2: MGE parameterisation of the NGC 3557 light profile.

$\log_{10} I_{\rm j}^{'}$ ($L_\odot\ pc^{-2}$)	$log_{10}\sigma_{\rm j}$ ($''$)	$q_j^{'}$
(1)	(2)	(3)
3.87	0.06	0.75
4.25	1.82	0.77
3.84	5.14	0.76

Notes. – Columns: Intensity (1), width (2), and axis ratio (3) of each Gaussian component.

In order to take into account this feature and also give an estimate of the SMBH mass at the centre of NGC 3557, we first need to remove the contribution of visible matter to the gas kinematics by carrying out the photometric analysis mentioned in Section 4.2.2 (see e.g. Onishi et al. 2017; Davis et al. 2017). The luminous matter distribution can be parametrised using the multi-Gaussian expansion (MGE; Emsellem et al. 1994) model adopted in the MGE_FIT_SECTORS package of Cappellari et al. (2002). In this technique, the three-dimensional stellar mass distribution of the galaxy is modelled by deprojecting a two-dimensional model of the observed stellar surface brightness and assuming a constant M/L. NGC 3557 satisfies one of the fundamental requirements to carry out this analysis, i.e. the availability of high-resolution optical imaging, thanks to an archival HST WFPC2

Table 4.3: NGC 3557 best-fit model parameters.

Parameter	Unit	ID	Value
PA_{kin}	(deg)	(1)	211±1.0
θ_{inc}	(deg)	(2)	56±1.0
σ_{gas}	(km s^{-1})	(3)	10±1.0
v_{offset} (v_{CO})	(km s^{-1})	(4)	15±1.0 (3014)
Stellar M/L	($M_\odot/L_\odot$)	(5)	5.4±0.1
$\log(M_{SMBH})$	($M_\odot$)	(6)	8.85±0.02

Notes. – Rows: (1) Kinematic position angle of the CO disc (i.e. the PA measured counterclockwise from North to the receding side of the velocity field). (2) Inclination of the disc. (3) Gas velocity dispersion. (4) Velocity offset of the kinematic centre, i.e. offset between the expected and observed velocity zero-point. The expected zero-point corresponds to the redshifted frequency of the CO(2-1) transition listed in column (3) of Table 3.2; the observed zero-point consists in the best estimate of the line systemic velocity as inferred from the observed spectral profiles. The corresponding CO central velocity is reported in parentheses. (5) Stellar mass-to-light ratio. (6) Logarithm of the super-massive black hole mass.

F555W image (Fig. 2.5a). The prominent dust ring seen in the HST image at the centre of the galaxy should be fully masked to reduce the effect of dust obscuration. The first fundamental step of the MGE fitting process, however, consists of the location of the precise position of the galaxy centre, a procedure that we experienced to be negatively affected by the masking of the entire region around the nucleus. Therefore, we decided to mask only the region to the east of the galaxy nucleus, where the dust absorption appears to be stronger (see Figure 2.5a). The obtained best-fit MGE model is shown in Figure 4.8 and is tabulated in Table 4.2. The resulting luminous matter distribution is then implemented in KinMS and used to calculate the circular velocity curve arising from this mass model using the MGE_CIRCULAR_VELOCITY function within the Jeans Axisymmetric Modelling (JAM) package (Cappellari 2008). By following the equations in Cappellari et al. (2002), this procedure allows to calculate the gravitational potential of the galaxy from the summation of the MGE model components multiplied by a constant M/L and the SMBH treated as a point-like mass. Both parameters are left free to vary in the fit. The circular velocity curve obtained in output is then

automatically used by the KinMS procedure to model the CO velocity curve. The inclination and position angles are fitted as single values throughout the disc. The molecular gas distribution is modelled as described in Section 4.2.1. The best-fit model parameters of NGC 3557 are listed in Table 4.3; a comparison between the observed and the modelled disc is shown in Figure 4.7.

Most of the observed disc structures seem to be well reproduced by our model, and accounting for the presence of a SMBH in the centre seems to match well the velocity increase visible at positive velocities around the centre of the galaxy. We find a best fit $M_{\rm SMBH} = (7.10\pm0.02)\times10^8$ M$_\odot$ (or $\log(M_{\rm SMBH}) = 8.85\pm0.02$ M$_\odot$), consistent with the expectation from the $M_{\rm SMBH} - \sigma_*$ relation (e.g. Tremaine et al. 2002; McConnell & Ma 2013). Nevertheless, some significant residuals (≈ 40 km s^{-1}) are visible in Figure 4.7c at the centre of the gas distribution, likely due to the fact that the model symmetrically reproduces the velocity increase at both positive and negative velocities, while only the former appears to be resolved in the data.

4.3.2 The case of NGC 3100

NGC 3100 is the best resolved source in our sample. The CO(2-1) detection shows a ring-like structure extending 1.6 kpc along the major axis, with a disruption to the North-West of the nucleus (see Chapter 3 and Figure 3.5a). The velocity field (Fig. 3.5b) indicates that the gas kinematics is clearly dominated by rotation, but with evident distortions in the rotation pattern. The iso-velocity contours are tilted and the major axis position angle changes moving from the edge to the centre of the ring, indicating the presence of a warp and/or non-circular motions.

In this case, an exponential profile with an inner truncation (i.e. a hole) seems to be more appropriate to reproduce the observed CO surface brightness profile. This simple profile alone, however, does not fit the overall gas distribution well, leaving large residuals in the moment one maps. This is true even when both a position angle and an inclination warp are added to model the distortions visible in the rotation pattern. We then found that the molecular gas distribution in NGC 3100 is consistent with a two armed spiral structure embedded in an exponential disc, with an inner truncation. The profile is then parametrised as

$$\Sigma_{\rm disc} \propto \begin{cases} e^{-\frac{r}{R_{\rm disc}}} & \text{r} > \text{R}_{\rm hole} \\ 0 & \text{r} \leq \text{R}_{\rm hole} \end{cases}$$

$$\Sigma_{\rm spiral} \propto \begin{cases} x = [a\ cos\theta\ e^{b\theta}, -a\ cos\theta\ e^{b\theta}] \\ y = [a\ sin\theta\ e^{b\theta}, -a\ sin\theta\ e^{b\theta}] \end{cases}$$

This distribution has 5 free parameters in our MCMC code: the exponential disc scale length ($R_{\rm disc}$), the inner truncation radius ($R_{\rm hole}$), the constants of the parametric form of the logarithmic spiral function (a and b), and the angle of the

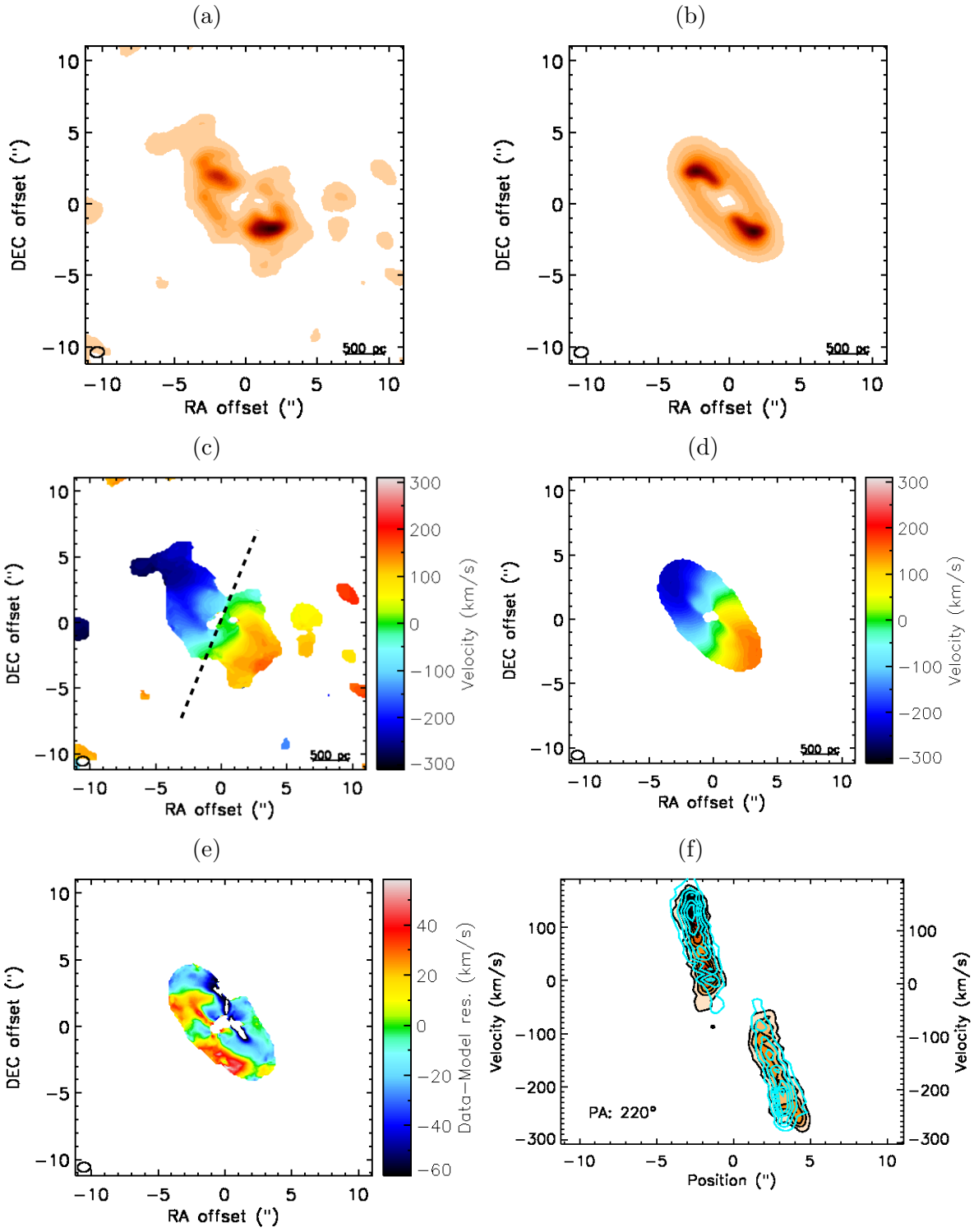

Figure 4.9: NGC 3100 observed and simulated integrated intensity maps (moment 0, panels **a** and **b**), observed, mock, and residual mean velocity maps (panels **c**, **d**, and **e**) and PVD (panel **f**) as in Figure 4.3, created using a data cube with a channel width of 10 km s^{-1}.

Table 4.4: NGC 3100 best-fit model parameters.

Parameter	Unit	ID	Value
PA_{kin}	(deg)	(1)	190−250
θ_{inc}	(deg)	(2)	20−80
v_{flat}	(km s^{-1})	(3)	354±0.01
r_{turn}	(arcsec)	(4)	2.68±0.01
R_{disc}	(arcsec)	(5)	3.36±0.01
R_{hole}	(arcsec)	(6)	0.9
σ_{gas}	(km s^{-1})	(7)	33.8±0.01
v_{offset} (v_{CO})	(km s^{-1})	(8)	91.5±0.01

Notes. − Rows: (1) Range of the CO disc kinematic position angle (i.e. the PA measured counterclockwise from North to the approaching side of the velocity field). (2) Range of the disc inclination. (3) Asymptotic (or maximum) circular velocity in the flat part of the rotation curve. (4) Effective radius at which the rotation curve turns over. (5) Scale length of the exponential surface brightness profile. (6) Radius of the central surface brightness cut-off. (7) Gas velocity dispersion. (8) Velocity offset of the kinematic centre, i.e. offset between the expected and observed velocity zero-point. The expected zero-point corresponds to the redshifted frequency of the CO(2-1) transition listed in column (3) of Table 3.2; the observed zero-point consists in the best estimate of the line systemic velocity as inferred from the observed spectral profiles. The corresponding central velocity is reported in parentheses.

spiral arms from the x-axis (θ). The adopted gas distribution model provides a significantly better fit to the data, reproducing well also the main features shown in the observed integrated intensity (moment 0) map (Fig. 3.5a). In particular, the regions of higher surface brightness at either side of the central hole are very well reproduced by the central spiral structure, as visible in Figure 4.9b.

We modelled the distortions in the rotation pattern by adding warps in both position angle and inclination. We also assumed that the disc is thin and the distribution axi-symmetric. The velocity curve was parametrised following Equation 4.3. The gas is assumed to be in purely circular motion. Table 4.4 summarises the best-fit ($\chi^2_{red} = 1.3$) model parameters. This model represents in general a good

fit to the data (Fig. 4.9), well reproducing most of the asymmetries in the rotation pattern. Nevertheless, the velocity field shows significant residuals, with peak amplitudes of $\approx \pm 40$ km s^{-1}. This suggests that the adopted model is not a complete representation of the gas kinematics and points towards the presence of non-circular motions.

Non-circular motions

In order to characterise the nature of the residuals in the velocity field of NGC 3100 (Fig. 4.9e) and check for the presence of non-circular motions (i.e. non-zero radial velocities) on the plane of the CO disc, we used the KINEMETRY package (Krajnović et al. 2006). This method performs surface photometry of line-of-sight velocity maps by determining the best-fit ellipses along which the profile of the moments can be extracted and analysed through harmonic expansion. Figure 4.10 shows the kinemetric parameters measured in the observed velocity field of NGC 3100. All the parameters are plotted versus the semi-major axis length of the fitted ellipses. According to the KINEMETRY formalism, Γ is the kinematic PA. The parameter q is the flattening of the fitted ellipses, and can be interpreted as a measure of the opening angle of the iso-velocity contours. In the case of a thin disc (the assumption for NGC 3100), the flattening is directly related to the inclination of the disc ($q = cos\ i$). k_1 is the first-order term of the harmonic expansion and describes the amplitude of the bulk motions (i.e. the rotation curve). k_5 is the fifth-order term of the harmonic expansion, indicating deviations from simple circular rotation: this term is sensitive to the presence of separate kinematic components. In Figure 4.10 the k_5 parameter is plotted in terms of a k_5/k_1 ratio, characterising the level of non-circular motions with respect to the circular rotation component. According to Krajnović et al. (2006), a single kinematic component is defined as having slowly varying Γ and q radial profiles, with a nearly featureless velocity curve (k_1 term) and a k_5/k_1 ratio consistent with zero. Instead, separate kinematic components can be identified when observing an abrupt change either with $q > 0.1$, or $\Gamma > 10°$, or with a double hump in k_1 with a local minimum in between. The transition between the different components is often emphasised also by a peak in k_5/k_1 (at the level of $\gtrsim 0.1$), which thus serves as an additional signature for such a change.

The curves in Figure 4.10 show that in the inner region ($r < 1.5''$), the flattening is low, the circular velocity is rising and the k_5/k_1 ratio is mostly consistent with zero (i.e. $k_5 \approx 0$). The kinematic PA slightly changes in this region, suggesting the presence of a mild warp. The region between $1.5''$ and $2''$ is characterised by a sharp change of the PA ($> 10°$), likely indicating a kinematic twist. The presence of a kinematically different component in this region can be inferred by the slight drop of the circular velocity, accompanied by a rise of the k_5/k_1 ratio (i.e. $k_5 > 0$). The rising of the flattening parameter likely suggest that the two components (the inner and that within $1.5''$-$2''$) are kinematically separate. Between $2''$ and $2.5''$

both the flattening and the k_5/k_1 ratio reach their maximum, whereas the PA has another abrupt change. Beyond $2.5''$, q and k_5/k_1 decrease, with the latter becoming consistent with zero at the edge of the disc, and the PA remains almost constant. The velocity curve is rising and featureless from $2''$ to the edge of the map.

In summary, these complex features seem to indicate the presence of at least two separate kinematic components: an inner ($r < 2.5''$) and an outer ($r > 2.5''$) component. The harmonic decomposition also suggests changes in the kinematic PA (Γ) and inclination (q), consistent with the position angle and inclination warp we take into account in the disc modelling. In particular, we find that the best-fitting inclination ranges from $\approx 80°$ in the inner region to $\approx 20°$ towards the edges of the disc (Table 4.4), reasonably in agreement with the variation observed in q. Similarly, the best-fitting position angle varies between $\approx$190° and $\approx$250°. The presence of two separate kinematic components may also be compatible with the best-fit parametrisation of the CO distribution, consistent with an inner (r$< 2.5''$) two-arms spiral structure embedded in an outer exponential disc. The non-zero k_5/k_1 ratio confirm that the radial motions are not negligible (10% of the circular velocity at the peak) and this likely explains the 40 km s^{-1} residuals in the velocity map (Fig. 4.9e).

NGC 3100: a case of fuelling?

The existence of two separate kinematical components within the gas disc is particularly interesting in the framework of our analysis.

Nuclear spirals are frequently observed in the cores of nearby ETGs (e.g. Simões Lopes et al. 2007), particularly in those hosting LINER-like AGN (e.g. Martini et al. 2003), and are usually associated with shocks in nuclear gas discs (e.g. Martini & Pogge 1999; Yuan & Yen 2004; Maciejewski 2004a,b; Combes 2006; van de Ven & Fathi 2010). The gas is compressed along the spiral arms and the density enhanced. As a consequence, the gas surface brightness increases in the region of the spiral shock. This may explain the regions of higher surface brightness visible in the integrated intensity map of NGC 3100 at either side of the central hole (Fig. 3.5a), perfectly matching the location of the spiral arms at the centre of the NGC 3100 gas distribution (Fig. 4.9b).

Nuclear spirals are often invoked as a promising mechanism capable of transporting gas from kpc scales to the nucleus and feeding the central SMBH. This hypothesis has found many confirmations, both on the theoretical and observational point of view (e.g. Wada et al. 2002; Maciejewski 2004a,b; Fathi et al. 2006; Simões Lopes et al. 2007; Casasola et al. 2008; van de Ven & Fathi 2010; Hopkins & Quataert 2010; Fathi et al. 2011, 2013; Combes et al. 2013). One of the main problems linked to the AGN fuelling is the removal of the gas angular momentum. Spiral shocks and associated turbulence can induce streaming motions that cause the gas to lose/gain angular momentum, then to move inward/outward. The resulting radial motions can be a significant fraction of the underlying circular velocity

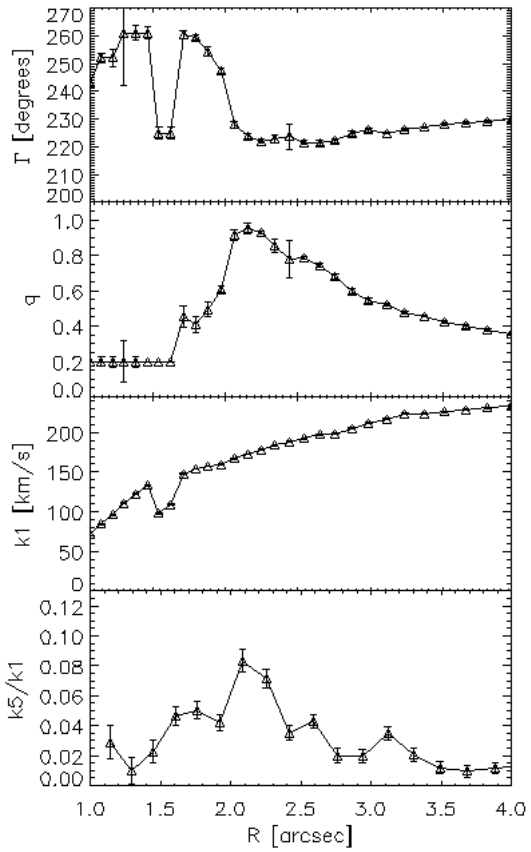

Figure 4.10: Coefficients derived from the harmonic decomposition of the line-of-sight velocity field of NGC 3100 (see Section 4.3.2 for details). From the top to the bottom: kinematic PA; axial ratio of the best-fitting ellipses (directly related to the inclination in the approximation of a thin disc); harmonic term k_1, describing the rotation curve; k_5/k_1 ratio, characterising the level of non-circular motions with respect to the circular rotation. k_5 is the fifth-order term of the harmonic expansion and is used to trace the presence of non-circular motions. The x-axis indicates the disc semi-major axis length.

(e.g. van de Ven & Fathi 2010). We then argue that the non-circular motions in the plane of the CO disc of NGC 3100 may be associated with the inflow/outflow streaming motions induced by the spiral perturbation. In particular, the residuals in Figure 4.9e exhibit mostly redshifted/blueshifted velocities to the eastern/western side of the CO ring, respectively. This implies gas inflow/outflow depending on the relative orientation of each side with respect to our line-of-sight. The B-I colour map of NGC 3100 (presented later in Chapter 5) shows that the dust absorption is stronger at the eastern side of the ring, indicating that this is the near side. This suggest that the molecular gas is likely (at least partially) inflowing.

Given the above considerations, it seems reasonable to assume that the molec-

ular gas at the centre of NGC 3100 can feed the SMBH, fuelling the AGN activity. However, theoretical studies (e.g. Maciejewski 2004a,b; Hopkins & Quataert 2010, 2011) indicate spiral instabilities as mechanisms capable of producing large accretion rates ($1 - 10$ $M_\odot$ yr^{-1}), comparable to those required to sustain the brightest radiatively efficient objects. The typical inflow rates estimated for LERGs like NGC 3100 indicate that, even when efficient mechanisms intervene to transport gas from kpc to ∼100 pc scales, other physical processes occur in the very inner regions of these objects, maintaining the accretion rate low. Higher-resolution observations probing the gas at scales relevant for the accretion process ($\ll$ 100 pc) would be needed to examine the kinematics around the central SMBH and draw more solid conclusions.

4.4 Further insights into the gas dynamical properties

The 3D modelling of the observed CO discs reveals that the gas kinematics is dominated by circular rotation, but with evident distortions (both in the morphology and kinematics) that are mostly not constrained by simple axisymmetric models. Such disturbances can trace interesting kinematic properties. In general, they indicate the presence of clumpy unrelaxed substructures in the gas disc, possibly caused by the presence of either warps or non-circular motions, or a combination of both. Indeed, both phenomena produce the same kinematic features (e.g. tilted or s-shaped velocity iso-contours). Differentiating between the two through disc modelling is not always straightforward, especially in discs where the gas distribution is only marginally (or even not) resolved (as in IC 1531, IC 4296, NGC 7075 and NGC 3557). In cases like these, however, a combination of observational and theoretical arguments can provide useful hints that can help us to constrain the physical processes giving rise to the observed features.

Asymmetries and deviations from purely circular motions in gas discs can be induced by various mechanisms. Among these there are bars in the stellar distribution. Non-axisymmetric gravitational instabilities induced by the presence of stellar bars can leave clear signs in the morphology and kinematics of circumnuclear molecular gas distributions (e.g. Combes et al. 2013). Although a detailed description of bar-induced perturbations is beyond the purposes of this Thesis, it is worth briefly recalling here the orbits and resonances in a barred potential to better understand this mechanism and its connection with some of the observed CO features (for a complete description see, e.g., Combes 2001b).

The motion of a star in a galaxy can be described by oscillations in three dimensions: radial oscillation, an oscillation perpendicular to the galactic plane, and an angular oscillation or rotation around the galactic centre. In general, these oscillations can be described by three instantaneous orbital frequencies: a radial or

epicyclic frequency k, a vertical frequency ν and angular frequency Ω. In barred galaxies, the radial oscillations are not small and orbits can be very elongated. A resonance happens if the dynamical frequencies of an orbit and the angular frequency of the rotation of the bar, $\Omega_{\rm B}$, satisfy the following relationship of commensurability:

$$\mathbf{l} \cdot \mathbf{\Omega} = m_{\rm B}\Omega_{\rm B} \tag{4.5}$$

where $\mathbf{l} = (l, m, n)$ is a vector of integers, $\mathbf{\Omega} = (k, \Omega, \nu)$ is a vector of frequencies and $m_{\rm B}$ is also an integer. If we assume $m_{\rm B} = m$ and $n = 0$ (i.e. motions close to the galactic plane; e.g. Ceverino & Klypin 2007), the resonant condition is reduced to

$$lk + m(\Omega - \Omega_{\rm B}) = 0 \tag{4.6}$$

Therefore, a planar resonance is described by a pair of integers, $(l : m)$. A resonant $(l : m)$ orbit is closed after l revolutions around the centre and m radial oscillations in the reference frame which rotates with the bar. Resonances can be of different types. One important example is the co-rotation resonance (CR; $\Omega = \Omega_{\rm B}$), whereby a star rotates around the galaxy centre with a speed equal to the rotation speed of the bar. Other important resonances are the inner and outer Lindblad resonances, wherein a star makes two radial oscillations during one angular revolution (and then its orbit has an ellipsoidal shape). In particular, the so-called inner Lindblad resonance (ILR) corresponds to the $(-1 : 2)$ resonance, whereby the star rotates faster than the bar ($\Omega > \Omega_{\rm B}$). The opposite case ($(1 : 2)$ resonance; $\Omega < \Omega_{\rm B}$) is called the outer Lindblad resonance (OLR). A sketch of the mentioned resonant orbits is shown in Figure 4.11.

Cold gas discs in barred galaxies usually have nuclear gaps relying on bar-induced gravitational torques that force the gas outwards to the ILR, or inwards on to the central SMBH (e.g. Combes 2001a). This is compatible with the presence of a central hole in the gas distribution of both NGC 612 (Figure 4.4 and Section 4.3) and NGC 3100 (Fig. 4.9). The same process can also give rise to significant deviations from circular motions (e.g Combes 2001a, 2006; Randriamampandry et al. 2015), consistent with the presence of high residuals (with peak amplitudes of ± 60 km s^{-1}) in the central part of the NGC 612 CO disc (Fig. 4.4c) and with the non-zero radial velocity component found in NGC 3100 (Fig. 4.10). Bars in edge-on galaxies leave also their kinematical signature in molecular gas PVDs, showing characteristic X-shapes (or simply sharp edges like those visible in NGC 612 PVD; Fig. 4.4d) that are indicative of the presence of two velocity components along the line of sight (e.g. Alatalo et al. 2013): an inner rapidly rising component associated with gas located within the ILR, and an outer slowly rising component associated with gas on nearly circular orbits beyond co-rotation. Non-axisymmetric perturbations induced by large-scale stellar bars have been also suggested as possible mechanism for the formation of nuclear spirals like that seen in NGC 3100 (e.g. Fathi et al. 2011). The gravitational potential associated with the bar gives rise to a shock front along

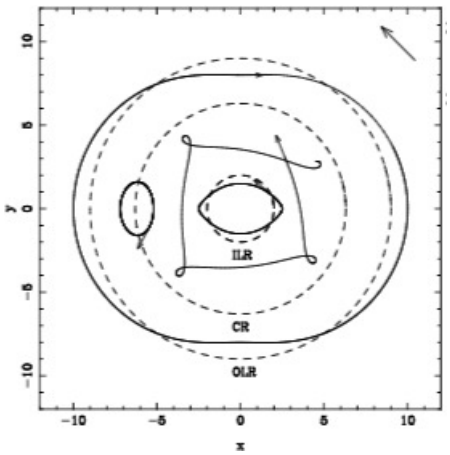

Figure 4.11: Sketch of various types of resonant orbits in a galaxy taken from Combes (2001b). The dashed curves illustrate the purely circular orbits expected in an unperturbed axisymmetric potential. The solid curves show the shape of the resonant orbits in a barred potential. The arrow in the top-right corner indicates the rotating frame. At the ILR, the orbit is closed and elongated, and is direct in the rotating frame. At co-rotation (CR), the orbit makes no turn, only an epicycle. At OLR, the orbit is closed, elongated and retrograde in the rotating frame.

the bar edges, leading to an inward/outward flow of material that can form nuclear spiral structures (e.g. Fathi et al. 2006; Casasola et al. 2011; Combes et al. 2013). The study of the stellar light distribution (using high-resolution optical imaging) is useful to infer the presence of stellar bars: indeed, they leave clear signatures in the optical morphology and the stellar kinematics (e.g. Emsellem et al. 2001). However, only low spatial resolution optical images are currently available for NGC 612 (see Chapter 5), preventing us from further investigating this hypothesis. Furthermore, the disc in NGC 612 is viewed almost edge-on (Table 4.1), hence projection effects (i.e. line-of-sight passing through material at many different radii) prevent us from carrying out a more detailed study of this complex kinematics. The optical morphology and B-I colour map of NGC 3100, on the other hand, do not highlight the presence of a bar in this galaxy. We then consider to be unlikely that a stellar bar is the dynamical mechanism originating the features seen in this source.

Lopsidedness, warps, distortions and/or non-circular motions like those observed in our sources are expected either when the gas has been accreted externally (i.e. from interactions or minor merger events) and is still in the process of settling into the potential of the host galaxy (e.g. Lauer et al. 2005) or in cases of interactions between the gas and the radio jets (e.g. Casasola et al. 2011; Alatalo et al. 2011; Combes et al. 2013; García-Burillo et al. 2014; Oosterloo et al. 2017). These hypotheses will be extensively discussed in Chapters 5 and 6, respectively.

In general, our analysis clearly shows that the observed molecular gas discs are not fully settled in a steady state into the stellar potential of the host galaxy:

low-level dynamical disturbances can be identified in all the objects. Disturbed CO discs are not commonly seen in local ETGs. In particular, significant differences are found between radio-loud (where the radio "loudness" is essentially associated with the presence of the radio jets) and radio-quiet objects. Interferometric observations of 40 nearby ETGs (mostly radio-quiet) imaged in CO(1-0) with the Combined Array for Research in Millimeter Astronomy (CARMA) in the framework of the ATLAS^{3D} survey show that 80% of the discs are settled, both dynamically and morphologically (i.e. they show regular rotation patterns and morphologies, without evident departures from symmetry or deviations from purely circular motions; Alatalo et al. 2013; Davis et al. 2013). Discs showing irregularities in their rotation pattern (such as s-shaped iso-velocity contours), warps, asymmetries and/or disruptions in their morphology (i.e. unsettled discs; 20%) are objects classified as low-luminosity (or "radio-weak") AGN (on the basis of their 5 GHz radio emission; Nyland et al. 2016), interacting systems or objects that have acquired their gas externally. However, the CO discs in the CARMA sample are imaged at much lower resolution ($> 4''$) than ours. Thus, although the proximity of these objects ($D_{\rm L} < 46$ Mpc) allows to sample spatial scales comparable to that of our observations (a few hundred parsecs) in most of the cases, caution is needed in drawing conclusions from this comparison. High-resolution ($\leq$100 pc) ALMA observations of CO(2-1) discs in nearby ETGs have been presented by Boizelle et al. (2017). By analysing the kinematics of the five brightest CO discs (hosted by radio-quiet ETGs), they find that deviations from models assuming gas in purely circular motions are very small ($\lesssim 10$ km s^{-1}) and warping of the gas discs are of low magnitude in all the cases ($\lesssim 10^{\circ}$), concluding that each CO distribution can be considered both dynamically and morphologically settled.

The emerging picture is that CO discs in LERGs (and, in general, in radio-loud objects) are significantly more disturbed than in radio-quiet objects. This provides additional clues on the potential connection between "jet-mode" AGN activity and the surrounding (sub-)kpc scale molecular gas discs and, more in general, on the interplay between the AGN and its host galaxy.

4.4.1 Gas disc stability

Molecular gas distributions are typically unstable against gravitational collapse, causing a fragmentation into clouds and successive burst of star formation. Cold gas discs in early-type hosts, however, are generally found to be gravitationally stable, with a consequent decrease of the nuclear star formation (e.g. Ho et al. 1997). The dynamical state of the observed gas discs can have important implications for the nuclear activity in LERGs. Indeed, the gravitational (in)stabilities of the gas discs could relate not only to the star formation activity, but also to the fuelling of the central SMBH: infall of molecular gas is expected if the gaseous disc is gravitationally unstable (Wada & Habe 1992).

The stability of a thin rotating gaseous disc against gravitational collapse can be assessed by calculating the Toomre parameter (Toomre 1964)

$$Q = \frac{\sigma_{\rm gas} k}{\pi G \Sigma_{\rm gas}} \tag{4.7}$$

where $\sigma_{\rm gas}$ and $\Sigma_{\rm gas}$ are the velocity dispersion and surface density, respectively, of the molecular gas, G is the gravitational constant, and k is the epicyclic frequency (i.e. the frequency at which a gas parcel oscillates radially along its circular orbit). The latter is calculated by

$$k = \sqrt{4\Omega^2 + R\frac{d\Omega^2}{dR}} \tag{4.8}$$

where R is the radius of the gas distribution and Ω is the angular frequency ($\Omega = v_{\rm circ}/R$, with $v_{\rm circ}$ being the circular velocity). We estimate average values of the Toomre parameter along the CO discs by adopting the best-fit velocity dispersions listed in Table 4.1 (assumed to be constant throughout the disc). The gas surface densities ($\Sigma_{\rm gas}$) are derived from those reported in Table 3.5 (and indicated as $\Sigma_{\rm CO}$). The adopted $v_{\rm circ}$ is the bulk circular velocity, that we assume to be the velocity at which the gas rotation curve reaches its maximum and then flattens (i.e. $v_{\rm flat}$; see Table 4.1). We note that to get $\Sigma_{\rm gas}$ and $v_{\rm circ}$ we need to correct the observed values for the inclination, to take into account projection effects. We summarise the parameters and the corresponding values of Q in Table 4.5.

Theoretically, the disc is expected to be unstable if Q$\lesssim$1, otherwise it is considered stable against gravitational collapse. In two cases (IC 1531 and NGC 612) we find a Q value below unity. This is expected in NGC 612, since it is known to form stars at a rate of ≈ 7 M$_\odot$ yr^{-1} (Duah Asabere et al. 2016). For IC 1531 the low stability parameter could be simply due to an unreliable very low best-fit value of the velocity dispersion (3.4 km s^{-1}; see Table 4.1), This $\sigma_{\rm gas}$ value is not well constrained at the channel width of the IC 1531 datacube (20 km s^{-1}). In fact, in interferometric line observations with moderate S/N, the smallest velocity dispersion that is possible to constrain is approximately $2\sqrt{2ln2}$ times smaller than the channel width, or $\approx$ 9 km s^{-1} in this case. Similar considerations can apply to NGC 7075. We derive Q=3.4 by adopting the best-fit velocity dispersion of 5.1 km $^{-1}$, whereas the smallest velocity dispersion that is possible to constrain in this case is $\approx$ 17 km s^{-1} (channel width= 40 km $^{-1}$). In both cases, we then consider the Q values listed Table 4.5 as lower limits. In IC 4296, on the other hand, Q is well above unity, but this is likely due to an unreliable very high best-fit velocity dispersion (64 km $^{-1}$; Table 4.1). Theoretically, such high velocity dispersion would indicate that the gas disc is not dynamically relaxed, then the gas pressure is high and stabilise the disc against collapse. In this case, however, the observed gas disc is only marginally resolved and viewed nearly edge-on, then the velocity dispersion

Table 4.5: Toomre stability parameter and related quantities.

Target	$\Sigma_{\rm gas}$ ($M_\odot$ pc^{-2})	$v_{\rm circ}$ (km s^{-1})	$< Q >$
(1)	(2)	(3)	(4)
IC 1531	3.2×10^3	189	>0.2
NGC 612	1.6×10^3	303	0.1
NGC 3100	5.8×10^2	169	2.5
NGC 3557	2.1×10^3	268	1.5
IC 4296	1.0×10^3	319	<29
NGC 7075	2.3×10^3	417	>3.4

Notes. – Columns: (1) Target name. (2) Gas surface density corrected for the inclination ($\Sigma_{\rm gas}$=$\Sigma_{\rm CO}$ $cos(\theta_{\rm inc})$, with $\Sigma_{\rm CO}$ being listed in Table 3.5). (3) Bulk circular velocity corrected for the inclination ($v_{\rm circ}$=$v_{\rm flat}/sin(\theta_{\rm inc})$). (4) Estimated average Toomre stability parameters.

can be overestimated by contributions due to beam smearing, disc thickness and projection effects. Therefore, we consider the estimated Q as an upper limit in this case.

Given the uncertainties in the best-fit gas velocity dispersions of IC 1531, NGC 7075 and IC 4296, we also derive Q assuming a canonical value of $\sigma_{\rm gas} = 8$ km s^{-1} (e.g. Davis et al. 2011; van de Voort et al. 2018), finding $Q \simeq 0.4$, 5.5 and 3.6, respectively. These values show the same trend as those obtained from the best-fit $\sigma_{\rm gas}$, then our conclusions would remain unchanged irrespective of which one we consider. We should note, however, that in all the cases the low-level perturbations that are not taken into account in our modelling can modify the best-fit velocity dispersion used in the estimation of the Q values (i.e. the velocity dispersion can be larger in perturbed gas distributions), adding further uncertainties.

Keeping all the caveats above in mind, in most of the cases the derived Q values indicate that the discs are stable against gravitational fragmentation, consistent with what found for 3C 31 (the prototypical LERG; Okuda et al. 2005). This supports a scenario in which the deep potentials of the massive host galaxies of LERGs (i.e. giant elliptical galaxies) stabilises the gas distributions against gravitational collapse. The mass transfer is likely to be slow in gravitationally stable discs and this may be consistent with the low accretion rates in LERGs. However, Q values above unity (up to 12) have also been found in nearby star-forming galaxies (Romeo & Mogotsi 2017). Conversely, numerical simulations show that gravitational instabilities cannot be completely excluded in regions where Q is slightly above unity (e.g. Li et al. 2005). In conclusion the Q values reported in Table 4.5 do not allow us

to put strong constraints on the dynamical state of the observed gas discs, although seem to suggest gravitational stability in most cases.

Chapter 5

Origin of the molecular gas

The detection of significant amount of molecular gas in the centre of LERGs, typically hosted by red massive ETGs (see Chapter 1), seems to point towards a recent regeneration of their gas reservoir (Young et al. 2014). The origin of this gas, however, is not fully established and still subject to debate: it may be either internally generated or externally accreted. Disentangling these two scenarios may have important implications for our understanding of the fuelling mechanism of kinetic-mode AGN.

In this Chapter we discuss the origin of the cold gas in our sample, through the analysis of various multi-wavelength indicators and their comparison with theoretical expectations.

5.1 Internal versus external accretion

ETGs can replenish their cold ISM reservoirs through either internal or external mechanisms. In the first case, in situ cold gas formation may be the result of either stellar evolution (i.e. stellar mass loss) or cooling from the hot halo.

Cold gas supply through stellar mass loss can always be present, at a rate depending on the number of stars present in each galaxy and its star formation history. In the most massive ETGs ($M_* > 10^{11}$ $M_\odot$; the typical hosts of LERGs, see Section 1.3) evolved (primarily asymptotic giant branch) stars can inject gas and dust into the ISM at significant rates (> 3 $M_\odot$ yr^{-1}, e.g. Jungwiert et al. 2001). This material can then collide with the mass lost from other stars or with the hot ambient medium within the galaxy, being mostly shocked to a temperature of the order of 10^6 K, thus joining the hot gas reservoir of the galaxy (see e.g. Mathews & Brighenti 2003, for a review). It may then be possible for this material to cool, recombine, fall towards the galaxy centre and eventually re-form molecules and dust grains, regenerating the cold ISM reservoirs (e.g. Parriott & Bregman 2008). In this case one would expect many ETGs to have detectable molecular gas. Recent results based on large volume-limited surveys of nearby (mostly radio-quiet;

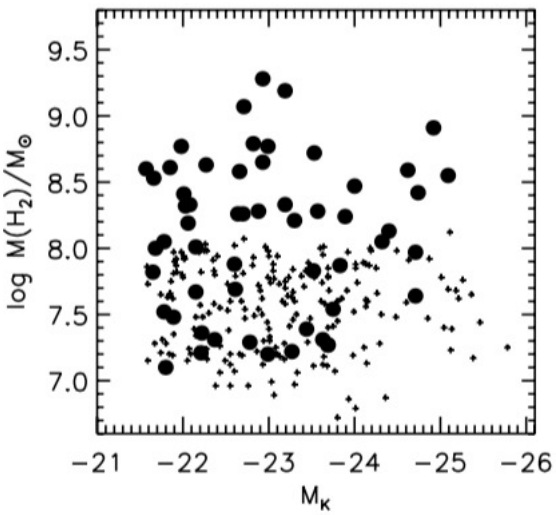

Figure 5.1: Distribution of molecular masses versus the host galaxy absolute K-band magnitude (M_K) in the volume-limited ATLAS^{3D} sample as presented in Young et al. (2011). The small crosses are ATLAS^{3D} sample galaxies that are not detected in the CO emission (3σ upper limits) and large filled circles are detections. See the text for details.

see Section 1.2) ETGs, such as the MASSIVE (Ma et al. 2014) and the ATLAS^{3D} (Cappellari et al. 2011) surveys, have found that only $\approx 22\%$ of local ETGs have detectable amounts of molecular gas, independently of their optical luminosity (and therefore of their mass), and large-scale environment (Davis et al. 2019). These findings are also consistent with previous work on representative samples of local ETGs (e.g. Combes et al. 2007; Welch et al. 2010), reporting cold gas detection rates ranging from 26% to 28%. These small detection rates suggest that the majority of the heated stellar ejecta do not cool to form molecules, but rather remain warm or hot. This is also consistent with the theoretical estimation of Parriott & Bregman (2008), who predicted that only a small fraction ($\lesssim 20\%$) of the stellar mass loss products remain (or become again) cold. If the observed cold gas is generated by mass loss from stars, then its total mass would be expected to correlate linearly with the galaxy optical luminosity (a proxy of the stellar mass; e.g. Wiklind et al. 1995). Instead the detected molecular gas masses are typically found to be independent of such host galaxy properties (Fig. 5.1). The absence of such a correlation supports a scenario where the observed molecular gas in unrelated to internal stellar mass loss (e.g. Young et al. 2011; Davis et al. 2011). Similar results have been found also for radio-loud ETGs. Ocaña Flaquer et al. (2010) studied the molecular gas properties of a sample of 52 nearby radio galaxies, finding that the molecular gas masses do not correlate with the host galaxy luminosities. Based on timescale arguments they also concluded that stellar mass loss is unlikely responsible for the build up of the observed molecular gas. All these findings seem to agree in excluding that the

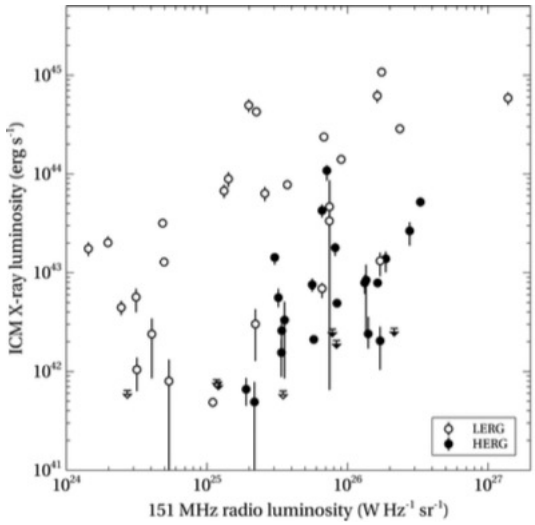

Figure 5.2: 150 MHz radio luminosity versus ICM X-ray luminosity (taken from Ineson et al. 2015) for a sample of 55 radio galaxies at $z < 0.1$ located in rich environments (i.e. groups and clusters). Filled and open symbols are for HERGs and LERGs, respectively.

mass lost from stars is the dominant mechanism for regenerating cold gas in either radio-quiet or radio-loud ETGs, although it can contribute for some fraction.

Large cold gas reservoirs can also be internally generated by cooling from the hot X-ray emitting gas phase, either smoothly (as predicted by e.g. Lagos et al. 2014; Negri et al. 2014; Lagos et al. 2015) or chaotically (as described in the framework of chaotic cold accretion models; see e.g. Gaspari et al. 2015, 2017). Indeed, as illustrated in Section 1.4, there is a general consensus that the hot halo provides the source of fuel for LERGs, either directly or after cooling (e.g. Allen et al. 2006; Hardcastle et al. 2007; Ching et al. 2017; Babyk et al. 2018; Hardcastle 2018; Gordon et al. 2019). This seems particularly plausible for LERGs in high density environments, where they are preferentially located (See Section 1.3; e.g. Best et al. 2006; Hardcastle et al. 2007; Best & Heckman 2012; Sabater et al. 2013; Ching et al. 2017; Hardcastle 2018). In fact, a strong correlation is found between the intra-cluster medium (ICM) X-ray luminosity (a proxy of the environmental richness) and the 150 MHz radio luminosity of LERGs at $z < 0.1$ (Fig. 5.2), providing evidence of a relationship between the properties of the ICM and the jet power of LERGs in groups and clusters, and supporting a scenario in which the hot medium surrounding the host galaxy likely plays a fundamental role in powering these systems (Ineson et al. 2015). Further support for this scenario is provided by high-resolution ALMA observations of the molecular gas component in massive nearby ETGs, most of which are kinetic-mode AGN associated with the BCG of groups or clusters (e.g. David et al. 2014; Werner et al. 2014; Russell et al. 2016; Temi et al. 2018; Tremblay et al. 2018; Nagai et al. 2019). These observations reveal that kpc-scale filamentary

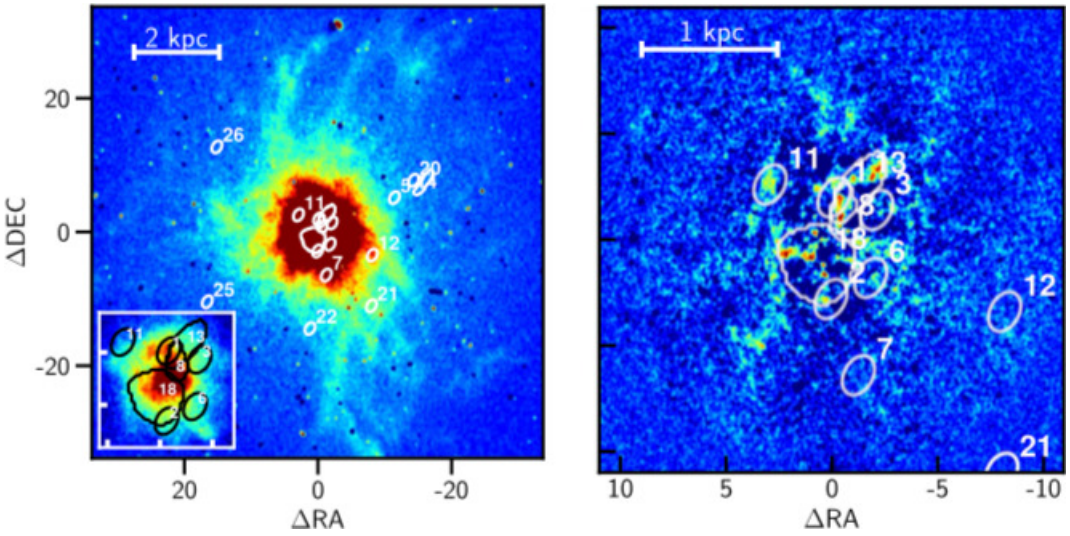

Figure 5.3: Maps of NGC 5044 from Temi et al. (2018) showing CO(2-1) clouds detected with ALMA overlaid on an optical Hα+[N II] emission image (left) and a dust absorption image (right). The colour sequence (blue green yellow red) indicates increasing Hα+[N II] and dust intensities. CO clouds, indicated with black (in the zoom-in inset on the left panel) and white contours, are defined as the area where the emission line S/N is greater than 4.

or blob-like cold gas structures are often present in these objects, likely tracing a hot gas cooling flow. A remarkable case is the one of NGC 5044, an ETG at the centre of an X-ray bright group observed during ALMA Cycle 0 in CO(2-1) (David et al. 2014; Temi et al. 2018). The data reveal the presence of 17 cold gas clouds within the central $\sim$ 6 kpc of the galaxy, each extending on scales of $<$ 300 pc (Fig. 5.3). Interestingly, these clouds appear to be mostly co-spatial with the warm gas phase (as visible in the Hα+[N II] map shown in the left panel of Figure 5.3) and with the X-ray emission (Werner et al. 2014), resulting in the multi-phase cooling gas distribution predicted in CCA simulations (Gaspari et al. 2017). A spatial correlation is mostly not found with the dust component (right panel of Figure 5.3), in agreement with the CCA scenario. Indeed, as described in Section 5.1, dust is continuously injected in the galactic environment through the stellar mass-loss process. However, shocks originating from the collisions with other stellar ejecta or with the hot (T$\approx 10^7$ K) gas phase lead the majority of the dust grains to be destroyed by thermal sputtering in very short time scales ($\leq 10^5 - 10^6$ yr; e.g. Mathews & Brighenti 2003). Therefore, hydrodynamical simulations show that freshly cooling cold gas structures at large distances from the galaxy centre (i.e. "young" cold gas association with short lifetime $t_{\rm dyn} \leq 10^7$ yr), are always expected to be essentially dustless, with typical gas-to-dust ratios of $\approx 10^5$ (e.g. Valentini & Brighenti 2015). On a longer-term, while the cooling gas is flowing towards the centre, dust can reform within the gas clouds by accretion

of condensable elements on to pre-existing grains (e.g. Hensley et al. 2014). This process, however, usually takes place on time-scales of the order of $10^8 - 10^9$ yr (or even longer), mainly depending on the gas density (i.e. dust reforms faster in denser gas clouds; e.g. Valentini & Brighenti 2015). Small discs or clouds of dust can also form in the galactic cores through stellar mass loss within the central ≈ 1 kpc (e.g. Temi et al. 2007), but in this case it would be obviously not correlated with the cold gas component that is cooling from the large halo scales. Therefore, a general prediction of the (chaotic) cooling scenarios is that the observed cold gas structures should be essentially dust-poor. This prediction seems to be confirmed by observations of chaotically cooling cold gas in massive ETGs at the centre of nearby cluster of galaxies, whereby many of the filamentary or blob-like gas structures (either on large or small galaxy scales) do not correlate with the dust component, like in the case of NGC 5044 (see also e.g. Lim et al. 2008; David et al. 2014; Russell et al. 2016; Temi et al. 2018).

IC 4296 is the only among the six CO detected sources in our sample that is located at the centre of a small cluster (Abell 3565). The soft X-ray spectrum (0.2−0.8 keV) of IC 4296 obtained using archival XMM-*Newton* data has been recently analysed by Grossova et al. (2019) and is shown in Figure 5.4. Lines typical of a cooling gas can be identified in the spectrum (such as FeXVII at 15Å and 17Å and O VIII at 19Å in the rest frame), implying a best-fit cooling rate of 5.4 $M_\odot$ yr^{-1}. Assuming that the majority of this material accretes onto the central SMBH and its potential energy is converted into the jet energy flux with a 10% efficiency (see Section 1.2), it would result in a jet power of $\approx 3 \times 10^{46}$ erg s^{-1}, which is more than two orders of magnitude higher than the actual estimated jet power ($\sim 10^{44}$ erg s^{-1}). Grossova et al. (2019) therefore concluded that the current rate of cooling is largely sufficient to produce the observed radio jets, supporting a CCA scenario in this object. Although we cannot exclude that at least a fraction of the molecular gas cooled from the halo, we find other observational constraints casting doubts on the exclusive role of this mechanism in originating the cold gas in IC 4296. This will be discussed in detail in Section 5.1.3.

While it is clear that brightest ETGs at the centre of groups or clusters have a preferential access to cool gas from their surrounding inter-group/cluster medium, the incidence of cooling from hot halos in isolated systems is not yet well established. As mentioned above, IC 4296 is an exception, as all of the other co-detected LERGs sit in low density environments (i.e. they are isolated, in pairs, or in poor groups; see Chapter 2). The fact that not all LERGs are in high density environments indeed suggests that other factors, in addition to cluster-scale cooling, can play a role in supplying ISM reservoirs to LERG, such as galaxy-galaxy interactions (e.g. Sabater et al. 2013; Storchi-Bergmann & Schnorr-Müller 2019). Minor mergers are also often proposed as an alternative to the hot halo cooling for refurbishing the cold gas content of these objects. However, recently Gordon et al. 2019 used deep optical imaging from the DECam Legacy Survey (DECaLS; Blum et al. 2016) to

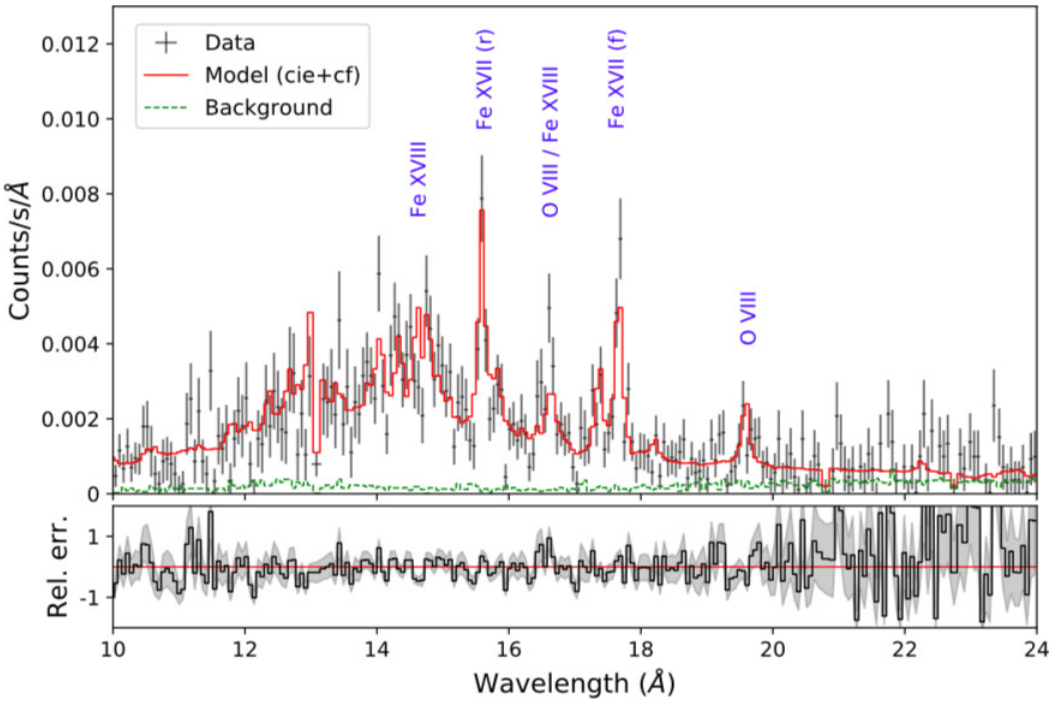

Figure 5.4: XMM-*Newton* soft X-ray (0.2−0.8 keV) spectrum of IC 4296 taken from Grossova et al. (2019). The black crosses are the spectral counts, the best-fit model is overlaid in red. The identified emission lines are labelled in blue. The lower panel shows the residuals between the data and the model.

test the role of mergers in fuelling LERGs by comparing the prevalence and intensity of large-scale tidal features (typical signatures in optical images of a recent merger event) in a sample of 282 LERGs and in a matched radio-quiet control sample of 1622 objects. Using this method, they found no excess of minor merger features in the LERG population relative to the control sample in any mass regime or large-scale environment. This led them to conclude that this mechanism likely does not play a significant role in fuelling LERGs. Nevertheless, various other observational studies point towards external accretion as the dominant mechanism for gas supply in ETG hosts located in field or poor environments (e.g. Kaviraj et al. 2012; Davis et al. 2015, 2019). Evidence for this comes from various indicators: morphological and kinematic disturbances in both the host galaxies and the central gas discs (e.g. Duc et al. 2015); a significant surplus of ISM compared to expectations from stellar mass loss (e.g. Kaviraj et al. 2012); observed wide ranges of gas-to-dust ratios and, in turn, metallicities with respect to those expected for internally generated ISM (e.g. Smith et al. 2012; Davis et al. 2015); kinematic misalignments between gas and stars (e.g. Sarzi et al. 2006; Davis et al. 2011), or lack of correlation between the gas/dust and the host galaxy properties (e.g. Annibali et al. 2010; Young et al. 2011; Alatalo et al. 2013). In the following we explore some of these indicators, in

the attempt to put some constraints on the origin of the observed molecular gas in our sample sources.

5.1.1 Stars and gas kinematic (mis-)alignment

Useful information on the origin of the cold gas may come from a comparison of the kinematic properties of the ISM and the underlying stellar population. Indeed, angular momentum conservation requires that cold gas reservoirs originating from internal processes (such as stellar mass loss) are expected to be closely aligned and co-rotate with stars (e.g. Sarzi et al. 2006). Cosmological simulations of isolated ETGs (e.g. van de Voort et al. 2015) show that externally accreted cold gas discs can instead exhibit significant misalignments with respect to the stellar rotation axis (up to 180°), so, in principle such misalignments can be ascribed to an external origin of the gas. This argument was used by Davis et al. (2011), to assess the origin of the cold gas in the CO-rich sub-sample of the ATLAS^{3D} ETGs (two third of the total sample). They proposed that misalignment angles $> 30°$ between the cold gas and the stellar projected direction of the angular momentum vector (i.e. the rotation axis) can be considered consistent with an external gas origin. Using this criterion, they concluded that a significant fraction of the gas found in local ETGs is likely to be supplied by external processes, finding kinematically misaligned gas and stars in 24±7% of the analysed ETGs (Fig. 5.5). Adopting the same approach of Davis et al. (2011), we find similar statistics in our sample with two out of six CO-detected sources (NGC 3100 and NGC 7075; 33±24%) showing large misalignments ($> 120°$) between the CO and stellar[1] angular momenta. This arguably excludes a secular origin of the gas (i.e. from stellar mass loss), but does not rule out the hot gas cooling scenario. In fact, gas that is cooling from a hot halo is not necessarily aligned with the stellar angular momentum, and large discrepancies between the stellar and gaseous rotation axes can be maintained ($> 30°$; e.g. Lagos et al. 2015). On the other hand, even when the gas and stars are observed to co-rotate (as in all the other sources in our sample), an external origin of the gas cannot be excluded. Indeed, as material from external sources enters a galaxy, it starts to settle down into the galaxy potential (see the following Section). Although kinematic misalignments between gas and stars can persist for several Gyr after the accretion event (van de Voort et al. 2015), externally accreted gas that has fully settled into the host galaxy eventually co-rotates with stars, becoming formally indistinguishable to gas that has been internally generated. In summary, the criterion of kinematic misalignment alone cannot be used to draw solid conclusions on the origin of the observed gas distributions.

[1]The information on the stellar kinematics is based on VIMOS/IFU and MUSE observations (Warren et al. in prep.).

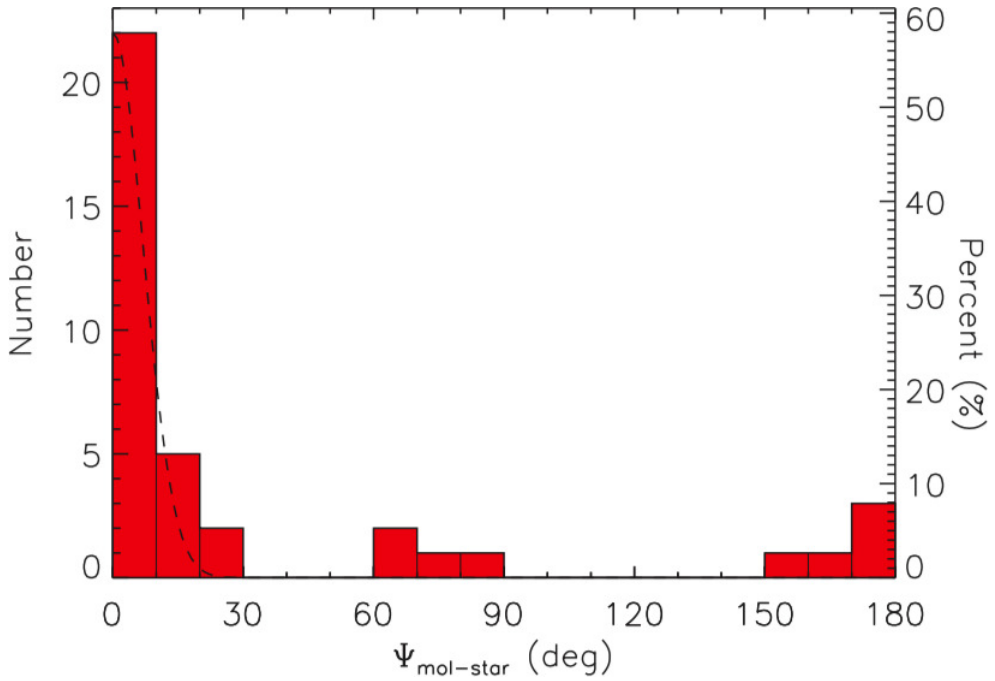

Figure 5.5: Histogram showing the kinematic misalignment angle between the molecular gas and the stars for the CO-rich ETGs of the ATLAS^{3D} survey (adapted from Davis et al. 2011). The dashed line overplotted is a normalized Gaussian distribution with its centre at zero and a standard deviation of 7°, showing the expected scatter in case of no misalignment.

5.1.2 Distortions, warps and lopsidedness

Gas that is dynamically relaxed and fully settled into the potential of the host galaxy is expected to show regular rotation patterns and compact disc- or ring-like morphologies, without evident departures from symmetry (e.g. Alatalo et al. 2013). Kinematical features such as warps, lopsidedness or distortions, as well as filamentary or patchy distributions, are indicative of perturbations to a steady configuration and can be indicative of external gas accretion (yet less extreme than kinematic misalignments). Indeed, as in the settling sequence proposed by Lauer et al. (2005) and predicted by hydrodynamic simulations of isolated ETGs (e.g. van de Voort et al. 2015), externally acquired gas takes time to settle down in the host galaxy environment, dynamically relax and co-rotate with stars. In this scenario, as the externally accreted gas starts to move through the surrounding "sea" of matter (i.e. stars and dark matter), the gravitational interaction leads it to experience either a drag (usually referred to as dynamical friction) or viscous torques (depending on the mass of the galaxy; dynamical friction is typically effective for very massive objects). In both cases, the gas consequently loses energy/momentum and slows down, thus spiralising towards the centre of the gravitational potential.

In the central kpc-scales, while it partially continues to spiral in, the residual gas angular momentum can also spread it into a disc. The stellar torques are stronger at the centre (where the density is higher), which therefore virialises faster than the outskirts: this results in warps and asymmetries, like the ones visible in the distribution and rotation pattern of NGC 3100 and at the edges of the disc of NGC 612 (Figs. 3.5b and 3.4b, respectively). Non-axisymmetric perturbations induced in gas that is undergoing dynamical friction can also give rise to spiral structures like those inferred in the inner region of the NGC 3100 disc (Fig. 3.5a and Section 4.3.2), and often observed in nearby ETGs known to have accreted their gas reservoirs externally (e.g. Malkan et al. 1998; Simões Lopes et al. 2007).

Warps, distortions and lopsidedness, however, are also often observed in molecular gas distributions known to experience chaotic cooling from the hot galaxy halo (e.g. Tremblay et al. 2018). Therefore, again, the observation of these features cannot be used alone to disentangle between internal and external gas origin, unless other information is available. In the case of NGC 612 an external origin of the cold gas was already suggested by Emonts et al. (2008), who reported the observation of a large-scale (140 kpc along its major axis) HI disc in this source. A prominent HI bridge connects NGC 612 with the HI-rich companion galaxy NGC 619. They thus conclude that a past galaxy interaction (or a major merger event) may be responsible for the formation of the HI disc in NGC 612 (see Section 2.2.2). Using interferometric HI observations, Oosterloo et al. (2010) and Serra et al. (2012) argued that ongoing accretion of cold atomic gas is common for field ETGs. In some cases, the atomic gas retains a large angular momentum and forms structures which are tens of kpc in extent (like the one observed in NGC 612; Fig. 2.2b), and are coincident with a molecular disc in the central few kpc of the galaxy. They thus propose that at least some of the molecular gas in ETGs may have been accreted in the form of atomic gas, settling into a regular disc and converting into molecular gas as its density increases. The CO disc of NGC 612 is located in the central region of the HI distribution, in agreement with this scenario. Most of the gas appears to be already settled into the host galaxy potential (consistently with being observed to co-rotate with stars), whereas it is still in the process of settling at its edges (where some asymmetries are observed). These observational evidence lead us to strongly support the scenario of external cold gas accretion first proposed by Emonts et al. (2008) for this object.

NGC 3100 also has a very nearby companion galaxy (Section 2.2.4). Deep large-scale observations providing direct evidence of a possible interaction with its companion are not available for NGC 3100. Nevertheless, the spiral features, prominent warping and kinematical asymmetries observed in the CO disc (Chapter 4), the gas/stars kinematic misalignment (Section 5.1.1), along with other constraints related to the dust component (see Section 5.1.3) are all together very strong indications of an external origin of the molecular gas also in NGC 3100.

The CO rotation pattern of IC 4296 shows the presence of a mild warp, well

reproduced by our modelling (Fig. 3.7b and Section 4.3). Based on the presence of a companion galaxy (Section 2.2.7), we may argue, as for NGC 612 and NGC 3100, that the molecular gas has an external origin. This, however, would be in apparent contrast with the gas cooling scenario proposed by Grossova et al. (2019, Section 5.1), especially considering that IC 4296 sits at the centre of a cluster.

We note that asymmetries are observed at lower levels in all the other CO-detected sources in our sample (Chapter 4). Specifically, the velocity curve of NGC 7075 shows a lopsidedness at its centre and a hole in the gas distribution (Fig. 4.6d and Section 4.3). In this case, however, the spatial resolution of our ALMA observations is too low to draw strong conclusions, despite the presence of a prominent kinematic misalignment between gas and stars (Section 5.1.1) and of a companion galaxy (Section 2.2.8). Low-level perturbations are also seen in both the gas distribution and velocity curve of IC 1531 and NGC 3557 (Figs. 4.3a, 4.3d, 4.7a and 4.7d, and Section 4.3). In these two cases, however, there are indications suggesting that the observed features may be induced by feedback mechanisms (such as a jet/disc interaction), rather than reflecting the gas origin. This will be discussed in more detail in Chapter 6.

Relaxation timescales

If the molecular gas reservoirs of NGC 612 and NGC 3100 have been acquired externally, it is interesting to determine at which stage of the settling sequence they are. This can give us clues on the time at which the accretion event occurred (e.g. Lauer et al. 2005; van de Voort et al. 2015, 2018). A rough estimate can be obtained by measuring the relaxation time, $t_{\rm relax}$, that is the time taken by the gas to dynamically relax and settle into a stable configuration. Different models predict a wide range of $t_{\rm relax}$, varying from 10^8 yr to the Hubble time, with typical values for ETGs of $\approx 10^9$ yr (e.g. van de Voort et al. 2015; Davis & Bureau 2016). Indeed, theoretical studies show that the relaxation process of unsettled gas discs in the potential of ETGs typically takes a few dynamical times ($t_{\rm dyn}$; Tohline et al. 1982; Lake & Norman 1983). Specifically, it was found that the relaxation time is approximately $t_{\rm dyn}/\epsilon$, where ϵ is the eccentricity of the potential. For lenticular galaxies (like NGC 612 and NGC 3100; see Table 2.1) $\epsilon \approx 0.2$ (Méndez-Abreu et al. 2008). We therefore assume

$$t_{\rm relax} \approx 5 \times t_{\rm dyn} = 5 \times \frac{2\pi R}{v_{\rm circ}} \tag{5.1}$$

where R is the radius at the transition between the unperturbed (relaxed) disc and the perturbed (not yet settled) gas structures, and $v_{\rm circ}$ is the corresponding deprojected (i.e. $v_{\rm circ}/sin(i)$, where i is the inclination of the disc) rotational velocity.

In NGC 612 we assume $R = 11'' \approx 7$ kpc and $V_{\rm rot} = 400$ km s^{-1}, estimating $t_{\rm relax} \simeq 5.2 \times 10^8$ yr. This value is shorter than the timescale since the last interaction/merger (>Gyr) discussed by Emonts et al. (2008) on the basis of the HI disc

(a) **IC 4296** (b) **NGC 3557**

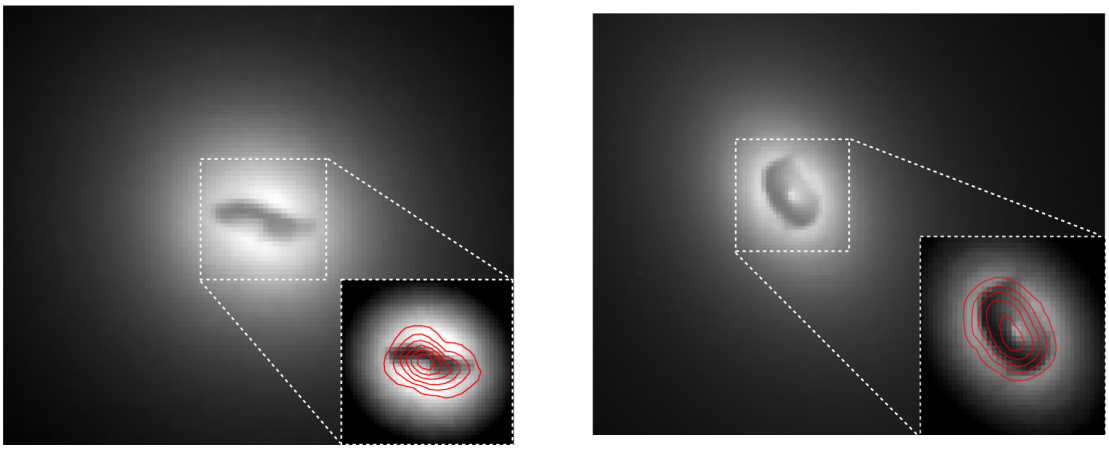

Figure 5.6: Archival HST images of **(a)** IC 4296 (7×7 arcsec^2) and **(b)** NGC 3557 (11×7 arcsec^2) taken in the F555W filter. In both images, the pixel scale and the image FWHM are 0.1 arcsec pixel^{-1} and 0.08 arcsec, respectively. The insets show superposed red contours of CO integrated intensity drawn at 1,3,9 times the 3σ rms noise level.

properties. This is unsurprising considering the much larger extent of the atomic gas disc. Our estimation, however, is in reasonable agreement with theoretical studies for ETGs in poor environments (Davis & Bureau 2016), and supports the idea that the molecular gas in NGC 612 is at an advanced stage of its settling sequence, with the bulk of the gas already relaxed within the host galaxy potential and co-rotating with stars.

The complex distribution and kinematics of the cold gas in NGC 3100 makes it hard to clearly identify a transition between relaxed and unsettled structures. However, knowing that nuclear rings are considered stable configurations in settling sequences (e.g. Lauer et al. 2005), we assume R and $V_{\rm rot}$ at the transition between the inner ring and the warped structures at its edges (Fig. 3.5b). Basing on this assumption, $R = 4'' \approx 1$ kpc, $V_{\rm rot} = 200$ km s^{-1}, and $t_{\rm relax} \simeq 9.5 \times 10^7$ yr. This shorter relaxation time suggests that NGC 3100 is in an earlier stage of its settling process, and indicate a more recent gas accretion event. The scenario of a more recent gas injection is in agreement with the observed stars/gas kinematic misalignment and distortions, as well as with the presence of large-scale gas and dust patches (discussed later in Section 5.1.3).

We note, however, that if the accretion of material is continuous, the relaxation process gets slower ($\approx 80 - 100\ t_{\rm dyn}$; e.g. van de Voort et al. 2015; Davis & Bureau 2016), making the aforementioned estimates lower limits to the true relaxation timescales for both sources.

(a) **NGC 3100** (b) **NGC 612**

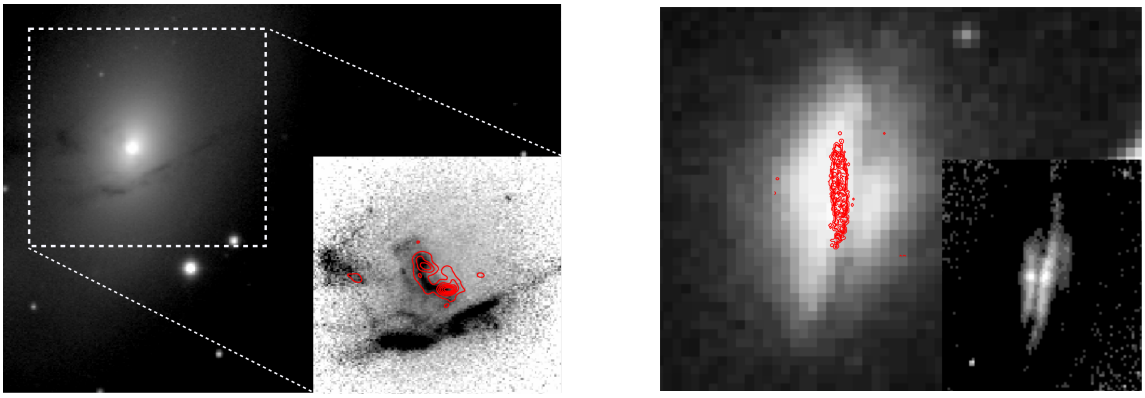

Figure 5.7: **(a):** Archival optical image of NGC 3100 taken with the Dupont 2.5 m Telescope using a blue filter (300-400 nm). The image scale and the resolution are 0.26 arcsec pixel^{-1} and 0.77 arcsec, respectively. The size of the panel is 112×80 arcsec^2. The inset in the bottom right corner shows the B−I colour (dust absorption) map in a box of 35×35 arcsec^2. The CO integrated intensity contours superimposed in red are drawn at 1,3,9....times the 3σ rms noise level. **(b):** Archival optical image of NGC 612 taken with the UK Schmidt telescope at 468 nm. The image scale is 1.7 arcsec pixel^{-1} and the image size is 80×65 arcsec^2. The contours of the CO integrated intensity map are superimposed in red and are drawn at 1,3,9....times the 3σ rms noise level. The figure in the bottom right corner shows the B−I colour (dust absorption) map adapted from Véron-Cetty & Véron (2001).

5.1.3 Dust and molecular gas co-spatiality

The association between the presence of nuclear dust discs and double-horned CO line profiles is well established both in radio-loud (Prandoni et al. 2007, 2010) and radio-quiet ETGs (Young et al. 2011), the latter also showing a clear morphological correspondence in nearly all imaging observations (e.g. Alatalo et al. 2013). This is generally interpreted as indicating that they trace the same component of the ISM. This co-spatiality seems to be confirmed also in the four of our CO-detected sources for which archival matched-resolution optical imaging is available.

Figure 5.6 shows the archival HST images of IC 4296 and NGC 3557, with the CO moment 0 contours overlaid. In both cases, the dust and molecular gas are clearly co-spatial. The lopsided CO morphology of IC 4296 accurately follows that of the dust (Fig. 5.6a), supporting the presence of a warp as suggested by the CO rotation pattern (Fig. 3.7b). The CO distribution in NGC 3557 appears to be settled in a regular disc, whereas the dust shows a well-defined ring-like structure (Fig. 5.6b). In this case, it is possible that the CO distribution would be resolved into a ring by observations with FWHM $\lesssim 0.3''$

Figure 5.7a shows the CO moment 0 contours of NGC 3100 overlaid on a B−I

dust absorption map[2]. The CO ring of NGC 3100 appears to be co-spatial with a nuclear dust ring, while the outer structure detected to the East seems to trace part of a diffuse dust patch on larger scales. Additional dust is visible beyond the detected CO emission, possibly suggesting the presence of a larger CO distribution which is beyond the FOV of our observations (26″, corresponding to a physical scale of ≈ 5 kpc in this case).

Figure 5.7b shows the CO moment 0 contours of NGC 612 overlaid on an archival photographic B band optical image;a B−I dust absorption map (adapted from Véron-Cetty & Véron 2001) is shown in the bottom right corner. The CO disc seems to be located slightly eastward of and skewed with respect to the dominant western dust lane visible in the B band image. The B−I colour map shows the presence of an inner dust lane, which may be co-spatial with the CO disc, although there appear to be still a slight apparent difference in position angle on the sky. Given the low spatial resolution of the B-band image and the absence of absolute astrometry for the colour map, the connection between CO and dust in this object cannot be fully established: higher-resolution optical observations are needed.

As anticipated in Section 5.1, the observational evidence of dust and molecular gas co-spatiality appears difficult to reconcile with the CCA scenario. Another piece of evidence that is hard to fit within this framework is that the kpc-scale blobs and filaments of cold gas predicted by CCA models (see Sections 1.4.1 and 5.1) are not detected within the field-of-view of our ALMA observations (26″, corresponding to spatial scales varying from ≈ 6 to ≈15 kpc at the redshift of our sources). The only exception is NGC 3100 in which we observe the presence of two cold gas structures at ≈1.3 kpc west and ≈2.3 kpc east from the outer edges of the central ring (Fig. 3.5b). However, as described in Section 3.4, the kpc-scale western and eastern structures in NGC 3100 have velocity patterns that are consistent with the respective nearest edges of the central ring, and thus may trace the presence of a larger rotating disc whose outer emission is below the detection threshold of our observations. In contrast, cold gas blobs and filaments associated with chaotic cooling are both predicted (e.g. Gaspari et al. 2017) and observed (e.g. David et al. 2014; Russell et al. 2016; Tremblay et al. 2018; Temi et al. 2018) to show very complex velocity patterns with little or no evidence of regular rotation, suggesting that the gas is not in a state of dynamical equilibrium. More in general, although we cannot exclude that gas deviating from regular rotation can occur on much smaller scales than that explored by our data (see, e.g. , the case of PKS 1718−64;

[2]The multi-wavelength set of optical images available for NGC 3100 (see Section 2.2.4) were used to produce a B-I colour map. Following De Koff et al. (2000) and De Ruiter et al. (2002), we used the Image Reduction and Analysis Facility (IRAF; Tody 1986) package to first scale the B image (where the dust absorption is most prominent) for the mean magnitude value measured in the I image (where the dust absorption is smallest), and then divide the B by the I image to obtain the colour map. Using this method, if dust absorption is absent, the value of each pixel in the resulting B-I map should be 1 everywhere. We assumed that dust absorption is present where the pixel values are ≤0.85 (i.e. where at least 15% of the stellar emission is absorbed).

Maccagni et al. 2018), all of the CO distributions detected in our sources appear to be mostly settled into stable configurations (i.e. rotating discs or rings), showing regular rotation with relatively minor asymmetries and/or dynamical disturbances. As outlined in Section 1.4.1, CCA models suggest that in clusters, groups, and massive ETGs the condensation of hot halo gas into extended cold gas filaments and clouds mainly occurs because of the presence of turbulence within the halo. If turbulence is not dominant, the halo can instead condense into a disc structure (because of angular momentum conservation). This regime, however, has been shown to be important only in low-mass late-type disc galaxies (e.g. Kim et al. 2013). It is expected that chaotically cooling cold gas can eventually settle down into stable configurations in the central regions of the galaxy, but this process again takes place over very long timescales ($> 10^8 - 10^9$ yr; Valentini & Brighenti 2015).

In short, all the considerations discussed above suggest two main possible scenarios for the origin of the cold gas distributions observed in our sources: one possibility is that the cold gas originates from the chaotic cooling of the hot halo, but that it is "old" enough to let the dust grains form again within the gas clouds and the cold gas dynamically relax at the centre of the host galaxy gravitational potential. The second possibility is that both the gas and the dust components have an external origin (from interactions or minor merger events). A third option, proposed by (e.g.) Martini et al. (2013), could be an hybrid origin of the cold ISM reservoirs. In this scenario, the cold gas originates from a combination of internal and external formation mechanisms, whereby part of the dust is produced by a continuous dust grain growth within the cold gas clouds and part is acquired from outside the galaxy system through accretion of dust-rich cold ISM.

Gas-to-dust ratio and metallicity in NGC 3100

A useful method to disentangle between the solutions described above is to measure the gas-phase metal abundances (i.e. metallicity) in the regions where the dust/CO co-spatiality is observed. Indeed, dusty cold gas which has been produced through internal processes (i.e. stellar mass loss or hot halo cooling) is expected to have a higher enrichment of heavy elements (i.e. super-solar metallicities) than ISM acquired from external mechanisms (e.g. Kaviraj et al. 2012; Martini et al. 2013; Davis et al. 2015). NGC 3100 is the only source in our sample for which data to extract spatially resolved information of both the molecular gas and the dust components are available, allowing a coherent estimate of the gas-phase metallicity in the areas where a tight dust/cold gas correlation is observed (i.e. essentially the central ring; Figure 5.7a).

Following the method adopted by Davis et al. (2015), the gas-phase metallicity in ETGs can be estimated as:

$$12 + log_{10}(O/H) = 12 + \log_{10}\left(\frac{4.57088 \times 10^{-2}}{M_{\rm gas}/M_{\rm dust}}\right) \tag{5.2}$$

Table 5.1: Summary of the multi-wavelength properties discussed in this Chapter.

Target	Kinematical warp	Stars/gas misalignment	Dust/gas co-spatiality	G/D (metallicity)	Environment	Gas origin
(1)	(2)	(3)	(4)	(5)	(6)	(7)
IC 1531	no	no	–	–	isolated	–
NGC 612	yes	no	yes	–	pair	external
NGC 3100	yes	yes	yes	860 (sub-solar)	pair	external
NGC 3557	no	no	yes	–	poor group	external/internal
IC 4296	yes	no	yes	–	cluster/companion	external/internal
NGC 7075	no	yes	–	–	pair	–

Notes. Columns: (1) Target name. (2) Kinematical warp. (3) Kinematical misalignment between the CO and the stellar rotation axes. (4) CO/dust co-spatiality. (5) Molecular gas-to-dust ratio and associated metallicity in parenthesis. (6) Large-scale environment in which the target is located. (7) Putative gas origin as inferred from the analysis carried out in this Chapter.

whereby the numerical factor is set so as to get the solar metallicity value at a gas-to-dust ratio of 100, i.e. $12 + \log_{10}(O/H) = 8.66$ (Asplund et al. 2004). $M_{\rm gas}/M_{\rm dust}$ is the gas-to-dust ratio in the region of interest, where $M_{\rm gas}$ refer to the total gas mass ($M_{\rm HI} + M_{\rm H2}$). Since interferometric observations of the atomic hydrogen are not available for NGC 3100, we can only estimate a molecular gas-to-dust ratio which, in turn, is likely to give just a lower limit of the true gas phase metallicity.

Based on the works of (e.g.)Tran et al. (2001); De Ruiter et al. (2002); Kaviraj et al. (2012), the mass of dust clumps and patches can be derived from the relation:

$$M_{\rm dust} = \Sigma < A_\lambda > \Gamma_\lambda^{-1} \tag{5.3}$$

where Σ is the area covered by the dust features, $< A_\lambda >$ is the wavelength-dependent mean extinction (i.e. dust absorption) of that area, and Γ_λ is the mass absorption coefficient at the observed wavelength. Assuming that the dust properties in ETGs are similar to that of our Galaxy (e.g. Finkelman et al. 2008), we adopt a Milky Way value for the B-band mass absorption coefficient ($\Gamma_{\rm B} = 8 \times 10^{-6}$ mag kpc^2 M$_\odot^{-1}$). Using this method, the estimated dust mass in the regions co-spatial with the molecular gas (Figure 5.7a) is 1.3×10^5 M$_\odot$. The molecular gas mass in the region co-spatial with the dust is estimated to be 1.1×10^8 M$_\odot$. These values imply a molecular gas-to-dust ratio of 860 and a gas-phase metallicity $<$7.73, which is more than eight times smaller than the solar metallicity. Similar low metal abundances have been measured in nearby ETGs and interpreted as indicating that the cold ISM have been accreted from external sources (e.g. Kaviraj et al. 2012; Davis et al. 2015). This result, along with all the other observational constraints discussed above, makes it plausible to conclude that the cold gas in NGC 3100 has an external origin, probably via interaction with the companion gas-rich star-forming spiral galaxy NGC 3095.

5.2 Summary and concluding remarks

In this Chapter we have investigated about the origin of the observed gas distributions by exploring various observational and theoretical constraints, such as the (mis-)alignment between the CO and the stellar rotation axes, the presence of warps, distortions and lopsidedness in the gas morphology and kinematics, and the comparison between the dust and the CO distributions. The latter, in particular, demonstrates CO/dust co-spatiality in all the four cases for which this analysis was possible. This evidence, along with the absence of dynamically disturbed kpc-scale blobs and filaments of cold gas, are rather difficult to reconcile with the *chaotic cold accretion* scenario (e.g. Gaspari et al. 2013, 2015), unless the chaotic cooling process is "old" enough to let the dust grains reform within the gas clouds and the cold gas to settle down at the centre of the galactic potential ($\approx 10^8 - 10^9$ yr; e.g. Valentini & Brighenti 2015). A summary of the possible inferred scenarios based on all the constraints discussed in this Chapter is reported in Table 5.1. Our analysis strongly suggests an external gas origin in NGC 612 and NGC 3100, probably via interaction with the respective companion galaxies. In both cases the CO is dusty and the gas distribution and/or rotation pattern reveal the presence of warps and asymmetries, expected in cases of perturbation to a steady configuration as it can occur when the gas has been acquired from outside the system and is still in the process of settling into the potential of the host galaxy (e.g. van de Voort et al. 2015). In NGC 612, the external cold gas accretion scenario was already suggested by Emonts et al. (2008), who presented HI observations of this galaxy showing the presence of a large-scale disc of atomic gas connected with a bridge to the companion galaxy NGC 619, supporting our hypothesis. In NGC 3100 the rotation axes of CO and stars are misaligned and the gas-phase metallicity of the central CO distribution is more than eight times smaller than the solar one and thus incompatible with an internal gas origin (e.g. Davis et al. 2015). The origin of the cold gas in NGC 3557 and especially in IC 4296 is unclear. In both cases the gas and dust components are co-spatial and the cold gas co-rotates with stars, the latter finding being consistent with either an internal origin or with external gas that has already settled into a stable configuration. Grossova et al. (2019), however, suggest a cold gas origin from chaotic cooling of the hot halo in IC 4296, which happens to be the only source among those detected in CO in our sample to be the BCG of a small cluster. Based on our considerations, in these two cases cooling of hot gas must have occurred over a long period, to allow the formation of the observed dust and regularly rotating cold gas reservoirs at the centre. Another option could be that the cold gas discs have formed by a combination of internal and external formation mechanisms (Martini et al. 2013). Both scenarios, however, would result in similar observed gas features, becoming formally indistinguishable using the information currently available for these two objects. In the remaining two cases, NGC 7075 and IC 1531, the available information is insufficient to allow us carrying

out proper considerations about the origin of their gas reservoirs, but we notice that also NGC 7075 is in a pair and shows a significant kinematic misalignment between the rotation axis of its CO disc and stars.

In general, it is clear from our analysis that in most of the cases the observed gas properties are not well fitted within the picture described in CCA models and observed in kinetic-mode AGN at the centre of groups and clusters. This corroborates the mounting idea that cold gas in LERGs located in different environments may have a different origin. In particular, it is interesting to note that all the objects that more plausibly have acquired (at least part of) their gas externally (i.e. NGC 612, NGC 3100 and IC 4296) have a companion galaxy, providing support to the idea that galaxy-galaxy interactions can have a major role in replenishing the cold ISM reservoirs of LERGs located in poor environments (e.g. Sabater et al. 2013; Storchi-Bergmann & Schnorr-Müller 2019).

Chapter 6

Jets and the molecular gas

One of the purposes of this Thesis is to investigate the relative orientation of the CO gas discs on (sub-)kpc scales and the radio jets. This information would allow us to explore the occurrence of jet/disc interactions in typical radio galaxies (as opposed to very gas-rich systems) and to analyse how the angular momentum vector of the cold gas relate to the jet axis (and therefore the spin axis of the black hole or inner accretion disc), with possible implications for the origin of the gas and the evolution of the black hole.

In this Chapter we first introduce the issue of the relative orientation between the jet and CO rotation axes, discussing earlier works and motivating our analysis. We then study the relative jet/disc inclinations of our sources in projection, using ALMA CO and continuum observations only. Afterwards, we present the newly-acquired JVLA observations at 10 GHz and describe the data analysis. We summarise the properties of the jets in FRI radio galaxies, before illustrating our modelling of the radio jets and their measured inclinations to the line of sight. We finally conclude by describing the 3D analysis of the jet/disc relative inclination and discussing the results obtained.

6.1 Relative jet/disc inclination in radio galaxies

Investigating the distribution of the relative orientations between the jet and the surrounding interstellar material (cold gas and dust) can constrain the physical processes that govern the inner regions of radio galaxies, possibly providing useful clues on the the origin of the observed ISM, as well as on the jet formation mechanism. Indeed, simulations of jet formation by black holes accreting at $\ll 0.01$ $\dot{M}_{\rm Edd}$, as inferred for LERGs, confirm that jets are launched along the spin axes of the holes and their inner accretion discs, primarily powered by electromagnetic energy extraction (Blandford & Znajek 1977; McKinney et al. 2012). For a simple axisymmetric system we might then expect a common rotation axis for the black hole, inner accretion disc and kpc-scale molecular gas and dust discs. In this case,

the jets and the plane of the discs on kpc-scales should be accurately orthogonal.

From the observational point of view, this issue has been widely investigated and discussed in the past, mostly based on the comparison between dust discs/lanes observed optically and the jet direction observed at radio wavelengths. Kotanyi & Ekers (1979) first found that seven nearby radio galaxies associated with ETGs (and including two LERGs in our sample, NGC 612 and NGC 1316) have disc-like dust distributions that appear to be orientated nearly perpendicular to the radio jets in projection. De Koff et al. (2000) later analysed a sample of 120 nearby ($z < 0.5$) radio galaxies selected from the 3CR catalogue and observed in the optical band with HST. Although a large range of values for the angle between the jets and dust lanes was found, they still suggested that the majority of the jets are aligned nearly perpendicular to the dust lanes (see also Van Dokkum & Franx 1995). De Ruiter et al. (2002) found that 79% of the radio galaxies in their sample (part of the B2 radio galaxy sample and mostly FRI LERGs) have large angles ($\geq 60°$) between the jet and the dust disc plane, whereas Schmitt et al. (2002) subsequently found less tendency to orthogonality by analysing a sample of 20 nearby radio galaxies. Therefore, in first instance, the observational analysis seemed to confirm the picture expected theoretically, but with some clear exceptions. All of these authors carried out their studies by looking at jet/disc position angle differences, i.e. they just compared the jet orientation to the dust disc/lane major axis orientation as they appear projected onto the plane of the sky. In Section 6.2 we perform a similar analysis for our sample sources detected both in continuum and in CO with ALMA. As emphasised by Schmitt et al. (2002), however, projection effects can significantly affect the observed distribution of alignment angles, so that analysing this issue in three dimensions is crucial in order to draw solid conclusions. Verdoes Kleijn & de Zeeuw (2005) first attempted to carry out a statistical analysis of the problem in 3D for a sample of 18 nearby radio galaxies observed in the optical band with HST. Specifically, they recovered the distribution functions of the (unknown) relative intrinsic orientation between jets and dust discs ($\theta_{\rm dj}$) starting from a sample of observational pairs (the jet/disc position angle difference, ΔPA, and the dust disc ellipticity, ϵ, that is a measure of its inclination to the line of sight) and assuming lower limits on $\theta_{\rm dj}$. This statistical analysis suggests that jet/dust disc orthogonality is restricted to galaxies with irregular dust lanes, whereas objects with more regular distributions do not have a preferred orientation. In conclusion, they could not rule out a model in which the relative inclinations of jets and the dust discs are completely random, although they found a marginal preference for a distribution of $\theta_{\rm dj}$ that is peaked around 45°. Although only statistical, the 3D study of Verdoes Kleijn & de Zeeuw (2005) seems then to outline a different picture with respect to that proposed by previous authors on the basis of projected information only. It clearly suggests that the alignment between the inner (black hole) and the outer (molecular gas and dust) systems is not always present and opens up interesting scenarios for both the black hole properties and the origin of the kpc-scale discs.

This will be discussed in detail in Section 6.5.

Our purpose here is to fully explore the relative disc/jet orientation in 3D (not only statistically) in our complete sample of LERGs. In order to do that, we need to know both the disc and jet inclinations to the line of sight accurately. This is possible for at least some of our sample sources. The spatial resolution of our ALMA observations (a few hundred parsecs; see Table 3.2) allows us to obtain reliable estimates of the inclination of the CO discs through 3D modelling (Table 4.1). An estimate of the jet inclination to the line of sight can be obtained by spatially resolving the jet structure at their bases and measuring the jet sidedness ratios. Deep high-resolution radio imaging was needed to this purpose. We then acquired new Karl G. Jansky Very Large Array (JVLA) observations at 10 GHz of a subset of our sample. This full set of information should be sufficient, in principle, to derive an accurate estimation of the intrinsic jet/disc orientations. As detailed in Section 6.5, however, the ambiguity on the near/far side of the CO disc (i.e. the side closer/farther to the observer) can introduce an uncertainty of 180° in the 3D geometry of the relative jet/disc system. Whenever possible (two out of four cases), we used the available archival optical imaging of the associated dust to resolve this uncertainty (see Section 6.5). Although a larger sample is obviously needed to derive a solid picture, this is the first time this method has been used and it can be extended to much larger samples in the future.

To avoid possible confusion, it is worth noting here that in the majority of the works cited above the relative inclination angles are measured between the (apparent) jet orientation and the major axis of the observed dust discs/lanes (i.e. the disc plane), whereby they are typically considered "orthogonal" for relative angles $\geq 60°$. A more physical definition takes the jet/disc (mis-)alignment angles to be that measured between the jet axis and the disc rotation axis (i.e. the axis orthogonal to the plane of the disc). In the following we always adopt this second definition, both in projection and in 3D.

6.2 Projected jet/disc orientations

In Chapter 3 we presented the 230 GHz continuum emission of the nine sample sources observed with ALMA (Fig. 3.2). The millimetre continuum is morphologically very similar to the radio continuum, and is therefore likely to be dominated by radio synchrotron emission from the core and jet structures (see Section 3.2.1).

We first use ALMA observations of those sources detected both in CO and continuum to obtain a measure of the jet/disc relative inclination in projection. Figure 6.1 shows the mean CO(2-1) velocity maps for the detected galaxies with the corresponding 230 GHz continuum contours superimposed. For those sources in which emission from the resolved jets was not detected at 230 GHz, we added dashed arrows to indicate the jet axes as determined from archival VLA data (see Chapter 2 and the lower panels of Figure 3.2). To carry out our analysis, we need

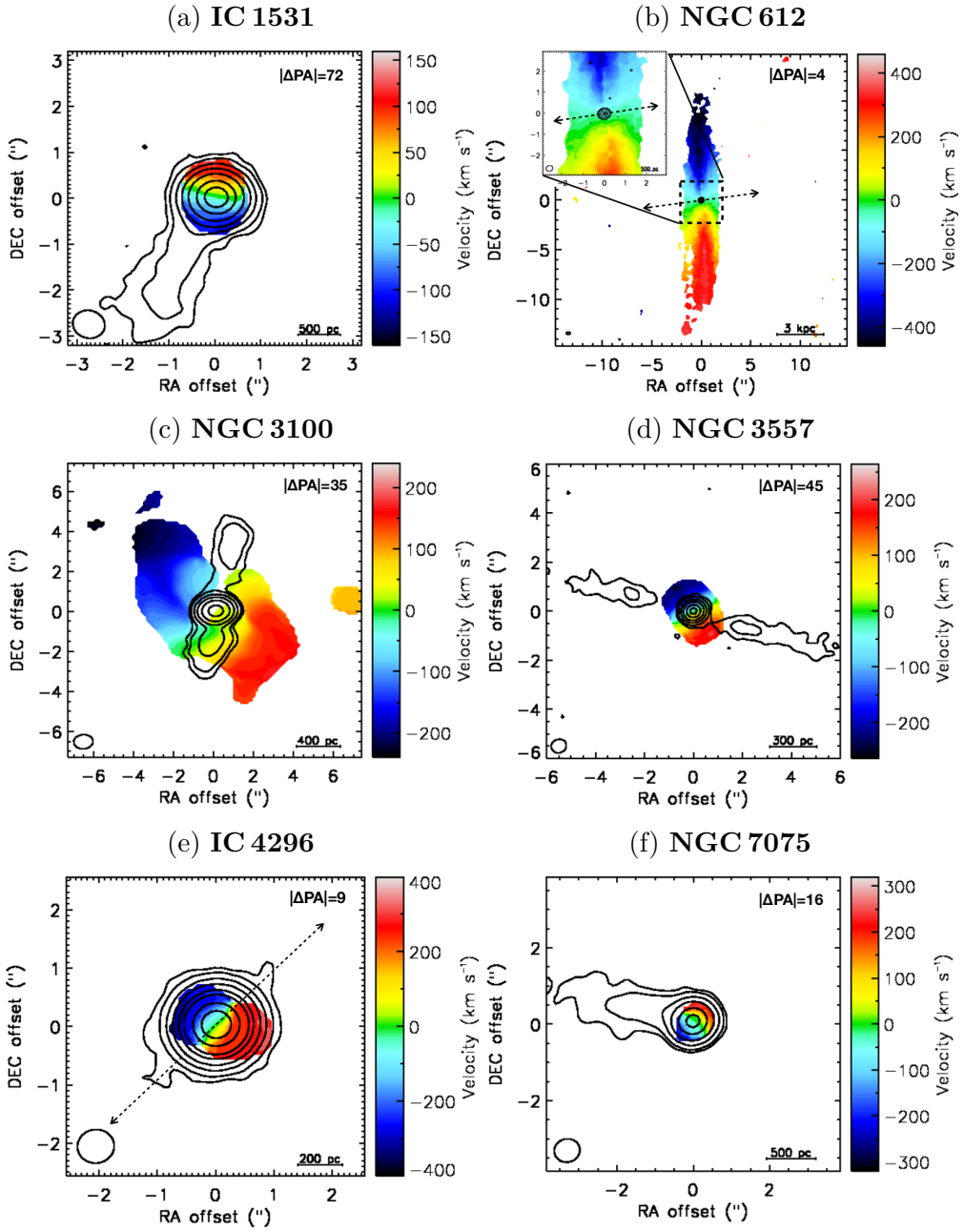

Figure 6.1: Mean velocity (moment 1) maps of the six ^{12}CO(2-1) detections, with 230 GHz continuum contours superimposed. Contours are drawn at 1,3,9..times the 3σ rms noise level. The wedge on the right shows the colour scale of the CO velocity maps. The beam and the physical scale bars are drawn in the bottom-left and bottom-right corner of each panel, respectively. Black dashed arrows indicating the jet axes are also included in panels b and e. The alignment angle between the jet axis and the CO disc rotation axis, $|\Delta PA|$, is given in the top-right corner of each panel (see the text for details).

Table 6.1: Alignment between jets and CO discs

Target	PA_{CO} (deg)	PA_{jet} (deg)	$\lvert\Delta PA\rvert$ (deg)
(1)	(2)	(3)	(4)
IC 1531	86	158	72
NGC 612	93	97	4
NGC 3100	130	165	35
NGC 3557	121	76	45
IC 4296	140	131	9
NGC 7075	52	68	16

Notes. − Columns: (1) Target name. (2) Position angle of the CO disc rotation axis (see the text for details). (3) Position angle of the jet axis (from North through East) derived from the 230 GHz continuum images (see also Table 3.3) or the archival radio images presented in this work. (4) Relative orientation angles between the jet axes and CO discs in projection, $|\Delta PA| = |PA_{CO} - PA_{jet}|$ ranged in $0 - 90°$.

to compare the position angle of the CO disc rotation axis and that of the jet axis (i.e. their orientation projected onto the plane of the sky). The position angles of the jet axis are measured from the ALMA continuum images (or the matched-resolution archival VLA maps in the lower panels of Figure 3.2) by performing 2D Gaussian fits within the regions covered by the resolved jet emission using the CASA task IMFIT. The obtained position angles are measured counterclockwise from North to East, and ranged within $0-180°$. The position angles of the rotation axis of the CO discs are obtained from the best-fit kinematic position angles presented in Chapter 4 (Tables 4.1, 4.3 and 4.4), knowing that the projection of the disc rotation axis onto the plane of the sky lies along the disc minor axis. We then estimated disc position angle as $PA_{CO} = PA_{kin} - 90°$ and ranged it within $0 - 180°$. Following De Koff et al. (2000) and De Ruiter et al. (2002), we finally measured the projected relative orientations as $|\Delta PA| = |PA_{CO} - PA_{jet}|$ ranged in $0 - 90°$. The obtained position angles and relative orientations between the CO disc and the jet axes are listed in Table 6.1.

From this analysis, the jet/disc relative orientations seem to span a wide range. Nevertheless, in four of the six detected galaxies (67±33%) the measured angles are relatively small ($|\Delta PA| \leq 35°$), meaning that the rotation axes of the gas and the jets are roughly parallel in projection (i.e. the jets are almost orthogonal to the disc plane); two sources (33±24%), however, have larger angles ($|\Delta PA| \geq 45°$), suggesting a larger misalignment between the projection of the jet and the disc

rotation axes. These results are statistically consistent with earlier findings based on the 2D analysis of jets and dust lanes, although the small number of objects in our sample does not allow us to draw significant conclusions about the form of the distribution.

NGC 3100 is a special case. While the jet and disc rotation axes appear almost aligned in projection, there are indications of a possible interaction between the gas and the jets. The ring-like CO distribution shows a clear discontinuity to the north of the nucleus, in the direction of the northern jet (Fig. 6.1c). Furthermore, the VIMOS IFU [OIII]λ5007 map of NGC 3100 shows clear equivalent width broadening (by a factor of 2) at the positions of the peaks of both radio jets (Warren et al. ,in preparation), reinforcing the case for a jet/gas interaction. This will be further discussed in Section 6.5.1.

6.3 JVLA data

6.3.1 The Very Large Array

The Very Large Array (VLA) is a centimetre-wavelength interferometric array located at an elevation of 2100 meters on the Plains of San Agustin in south-western New Mexico, and is managed from the Pete V. Domenici Science Operations Center (SOC) in Socorro, New Mexico. It was built between 1973 and 1980 (when it was formally inaugurated) and then completely upgraded in its technology in 2011, when it was renamed as the Karl G. Jansky Very Large Array (JVLA). The JVLA is composed of twenty-seven 25-meter antennas distributed along the three arms of a track arranged in an iconic "Y"-shape (Fig. 6.2), that can produce images of the radio sky at a wide range of frequencies and resolutions. Specifically, the VLA antennas are equipped with eight receivers providing a continuous frequency coverage from 1 to 50 GHz ($\approx$30 to 0.7 cm), and each receiver corresponds to frequency bands that are commonly referred to as L, S, C, X, Ku, K, Ka, and Q, from the lowest to the highest frequencies. In addition, all the VLA antennas have receivers for lower frequencies, enabling observations at P$-$band (230$-$470 MHz) and at 4$-$band (54 to 86 MHz). The spatial resolution of the VLA can vary over a range exceeding a factor of $\sim$50 (from $0.2''$ to $0.04''$) through different observing frequencies and antenna configurations. There are four basic configurations denoted as A, B, C and D, from the largest (maximum baseline length$\approx$ 36 km) to the tightest (maximum baseline length$\approx$ 600 m), respectively.

At radio (cm) wavelengths the problem of radio interferences from humans or nature becomes extremely important, since cosmic radio waves are billions of a billion times fainter than radio waves used to transmit information on Earth. The JVLA site is strategic in this sense because it is a desert area also ringed by mountains, which act like a natural shield against much of the artificial radio interference. Humidity is another big problem in radio astronomy, because water vapour distorts the

Figure 6.2: Aerial view of the Plains of San Agustin, the JVLA site, situated in the South-West of New Mexico at an elevation of about 2100 meters above the sea level.

wavefront of incoming radio waves passing through them and also produce their own emission that interferes with radio observations, particularly at higher frequencies. The desert climate of the San Agustin Plain is crucial in this respect, minimising the background signal from terrestrial water molecules.

From its inauguration in 1980, the JVLA had become an invaluable research tool, being the most versatile, widely-used radio telescope in the world. It is designed to allow investigations of many astronomical objects, including radio galaxies, quasars, pulsars, supernova remnants, gamma-ray bursts, radio-emitting stars, the sun and planets, astrophysical masers, black holes, and the neutral hydrogen (HI) hyperfine transition.

6.3.2 JVLA observations

As anticipated earlier in this Chapter, we proposed new JVLA observations for a subset of the sample sources observed with ALMA with the primary aim of deriving an estimation of the jet inclination using sensitive radio continuum data at comparable resolution to our ALMA images. Specifically, from the nine sources observed with ALMA (see Chapter 3), we selected the five that meet the following criteria:

- Resolved ^{12}CO(2-1) emission detected with ALMA.

Table 6.2: Main properties of the X-Band JVLA observations.

Target	Date	Time	$\theta_{\rm maj}$	$\theta_{\rm min}$	PA	Scale
		(min)	(arcsec)		(deg)	(pc)
(1)	(2)	(3)	(4)	(5)	(6)	(7)
IC 1531	2018-03-03	72	0.43	0.13	−19.6	220
NGC 3100	2018-03-24	66	0.37	0.14	6.41	70
NGC 3557	2018-03-24	66	0.47	0.12	0.70	100
IC 4296	2018-03-24	66	0.43	0.14	−15.2	110
NGC 7075	2018-03-03	72	0.46	0.13	0.62	180

Notes. − Columns: (1) Target name. (2) Observation dates. (3) Total integration time on-source. (4) Major axis FWHM of the synthesized beam. (5) Minor axis FWHM of the synthesized beam. (6) Position angle of the synthesized beam. (7) Spatial scale corresponding to the major axis FWHM of the synthesized beam.

- Images from archival VLA data show arcsec-scale jets.

The eligible targets were: IC 1531, NGC 3100, NGC 3557, IC 4296, and NGC 7075. It is worth noting here, however, that it was already clear from the archival VLA imaging (lower panel of Figure 3.2d) that NGC 3100 is an outlier with respect to the other sources, showing a sub-kpc jet structure that significantly deviates with respect to the standard FRI geometry (see Section 6.4). In cases like this, it is not possible to obtain a reliable estimate of the line-of-sight jet inclination. Nevertheless, we decided to propose NGC 3100 for new high-resolution JVLA observations with the primary aim of investigating the possible presence of an interaction between the jets and the gas disc on sub-kpc scales (see Section 6.2).

We used the JVLA X-Band ($\approx$ 10 GHz) in high-resolution A configuration to observe these five selected sources (project code: 18A-200; PI: I. Ruffa). Table 6.2 summarises the details of the observations. IC 1531 and NGC 7075 were observed in a single run on the 3rd of March 2018 for a total time-on-source of 72 minutes each. The other three sources were observed in a second run on the 24th of March 2018 for a total time-on-source of 66 minutes each. In both observing blocks the same spectral configuration was used: the frequency range of the X-band receiver (8-12 GHz) is divided into 32 spectral windows (SPWs) with 64 channels each and a channel width of 2 MHz. 3C48 and 3C286 were used as the standard primary flux calibrators; J2109-4110, J2359-3133, J1037-2934, J1147-3812 and J1316-3338 were used as phase calibrators.

The data were reduced using the CASA pipeline (version 5.4.1), which automatically processes each observing block by performing basic flagging and calibration. Specifically, the JVLA calibration pipeline does the following main steps (see also Section 3.2 for further details):

- Loads the data into from the archival JVLA data format (Science Data Model-Binary Data Format [SDM-BDF]) to the CASA MS, applies Hanning smooth-

ing (i.e. spectral averaging; this is applied when the data were not frequency averaged by the VLA correlator), and obtains information about the observing set-up from the MS;

- Applies "a priori" flags (e.g. shadowing, edge channels, auto-correlations, etc.);
- Sets amplitude and phase models for primary flux density calibrator;
- Corrects for the antenna position errors, the atmospheric opacity, and other pre-determined calibrations;
- Iteratively determines initial delay and bandpass calibrations, including flagging of Radio Frequency Interference (RFI) and some automated identification of system problems;
- Derives initial time-dependent (gain) calibration, and the spectral index of the bandpass calibrator; RFI flagging is done on data with the initial calibration applied;
- Derives final delay, bandpass, and gain calibrations, and applies them to the data;
- Runs the RFI flagging algorithm on the target data;
- Calculates data weights based on the inverse square RMS noise of the MS;
- Creates diagnostic images of the calibrators.

After the pipeline processing, we carefully checked the calibrated data for the presence of residual RFI signal, but no significant additional flags were needed.

6.3.3 Imaging

The deconvolution and imaging was performed using the CASA `clean` task in multifrequency synthesis (MFS) mode (Rau & Cornwell 2011). A second order Taylor series term was used (nterms= 2), to take into account the spectral behavior of the sources. All the continuum maps were made using Briggs weighting with robust= 0.0, in order to obtain a good trade-off between the spatial resolution and the signal-to-noise ratio (S/N). Since the cores are detected at high S/N (between 50 and 262) in all of the targets, multiple cycles of phase-only and one cycle of amplitude and phase self calibration were performed in all cases. Additional cycles of amplitude and phase self-calibration were performed for the brightest cores only. This allowed us to obtain root-mean square (rms) noise levels ranging from 4.8 to 14 μJy beam^{-1} for synthesized beams of $0.37''- 0.47''$ FWHM (see Table 6.2). The resulting maps are shown in Figure 6.3.

Table 6.3: Properties of the JVLA continuum images.

Target	rms	S_{10}	Size FWHM		PA
	(μJy beam^{-1})	(mJy)	(arcsec^2)	(pc^2)	(deg)
(1)	(2)	(3)	(4)	(5)	(6)
IC 1531	6.5	179±6.1			
core		150±6.0	(0.13 × 0.06)	(70 × 30)	149±4.2
SE jet[1]		28.8±1.1	–	–	–
NGC 3100	5.1	244±6.7			
core		156±6.2	(0.04×0.01)	(8.0×2.0)	17.3±6.4
N jet		31.0±1.2	(2.3×0.9)	(440×170)	172±6.1
S jet		57.0±2.3	(1.4×0.8)	(290×130)	153±2.4
NGC 3557	4.8	57.8±1.6			
core[1]		21.0±1.0	–	–	–
E jet		16.5±0.7	(1.8×0.5)	(380×110)	75±1.1
W jet		20.3±1.0	(4.3×0.6)	(915×130)	76±1.0
IC 4296	14	282±11.3			
core[1]		282±11.3	–	–	–
NGC 7075	4.8	35.0±1.0			
core[1]		19.0±0.80	–	–	–
E jet		15.8±0.60	(1.8×0.4)	(705×160)	77±1.8

Notes. – Columns: (1) Target name. (2) 1σ rms noise level measured in emission-free regions of the cleaned continuum map. (3) 230 GHz continuum flux density; the total, core and jet flux densities are quoted separately. The uncertainties are estimated as $\sqrt{\mathrm{rms}^2 + (0.04 \times S_{10})^2}$, and the second term dominates in all cases. Errors on total flux densities are obtained through error propagation. (4) Size (FWHM) deconvolved from the synthesized beam. The sizes were estimated by performing 2−D Gaussian fits to identifiable continuum components. (5) Spatial extent of each component corresponding to the angular sizes in column (4). (6) Position angle of the corresponding component, defined North through East.
[1]Unresolved component.

Two-dimensional Gaussian fits were performed within the regions covered by the continuum emission in order to estimate the spatial extent of each observed component. Table 6.3 summarises the main properties of the radio maps. The quoted flux density errors include the 4% for the flux calibration uncertainty of the VLA data (Perley & Butler 2013).

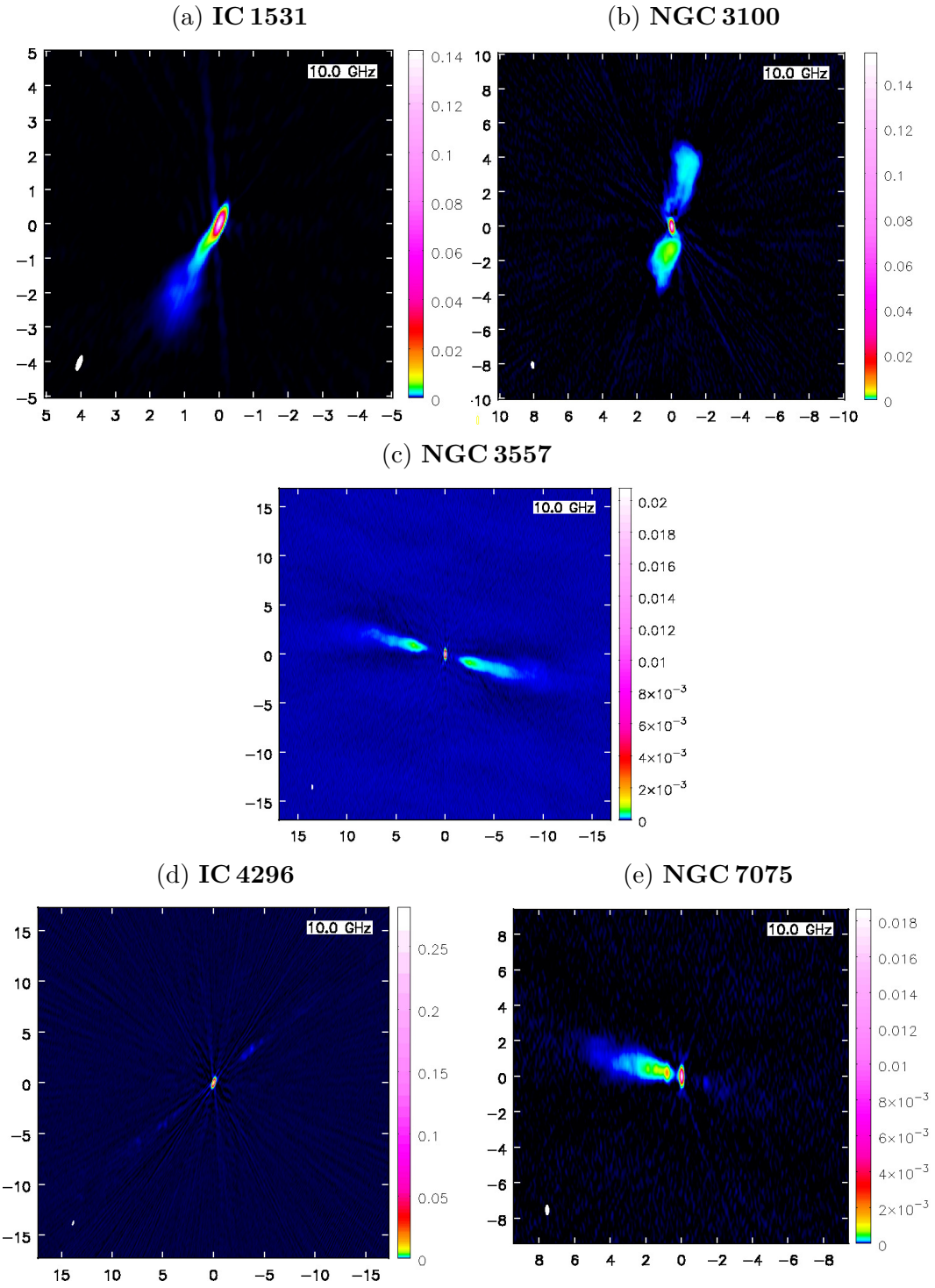

Figure 6.3: JVLA continuum maps at 10 GHz. The reference frequency of each observation is indicated in the top-right corner of the panel. The wedge on the right of each map shows the colour scale in Jy beam^{-1}. Coordinates are given as relative positions with respect to the image phase centre in arcseconds; East is to the left and North to the top. The synthesised beam is shown in white in the bottom-left corner of each panel.

6.4 Properties of the jets in FRI radio galaxies

Jets in (low-luminosity) FRI radio galaxies are typically bright close to the nucleus, whereas those in (high-luminosity) FRII sources are relatively faint until their terminal hotspots (see Section 1.3 and Figure 1.9). Over the years, evidence has been accumulated that jet flows in FRI radio galaxies are initially relativistic (e.g. Giovannini et al. 2001; Hardcastle et al. 2003) and then rapidly decelerate on kpc scales (e.g. Laing et al. 1999). Deceleration can be the result of either injection of mass lost by stars within the jet volume (e.g. Komissarov 1994; Bowman et al. 1996) or entrainment of the surrounding ISM (e.g. Baan 1980; Begelman 1982; Bicknell 1984, 1986; De Young 1996; Rosen et al. 1999; Rosen & Hardee 2000, see also Section 1.4.2). The idea that jets in FRI LERGs have initially relativistic speeds rests on various arguments:

- FRI sources are thought to be the side-on counterparts of BL Lac objects, in which relativistic motion on parsec scales is well-established (Urry & Padovani 1995).
- Superluminal motions have been seen on mas scales in several FRI jets (Giovannini et al. 2001) and on arcsec scales in M87 (Biretta et al. 1995).
- In FRI sources, the brighter jet (usually referred to as the main jet or simply the jet) is less depolarized than the fainter jet (called the counter-jet; Morganti et al. 1997).

The latter argument, in particular, can be explained if the main jet points toward the observer, suggesting that the asymmetry in brightness is caused by Doppler beaming (Laing 1988). The asymmetry decreases with distance from the nucleus, implying that the jets must decelerate (Laing et al. 1999).

In the last decades, the properties of straight, twin radio jets in typical FRI radio galaxies (i.e. physics, geometry, kinematics, etc.) have been extensively explored in a series of works, coupling observations with accurate modelling (see Laing & Bridle 2014, for an overview of the subject). This analysis shows that the jets and counter-jets in FRI radio galaxies can be accurately modelled as intrinsically identical, antiparallel, axisymmetric, decelerating relativistic flows, and the apparent differences between them are dominated by relativistic aberration. Furthermore, the inner parts of the jets in all of the modelled sources show several common features:

- an inner region, close to the core where the jets are launched, of well-collimated jet flow. In typical FRI radio galaxies (such as 3C31, the prototypical FRI LERG; Laing & Bridle 2002b) this region is typically observed as an initial gap, or extended region in which the radio emission is weak or undetectable.
- a brightness flaring point, that is an abrupt increase in their intrinsic brightness with increasing distance from the AGN.

- A flaring region, where the jets first expand more rapidly and then re-collimate. This can be usually identified as the region where there is a significant increases in the apparent jet opening angle with increasing distance from the AGN.

Within the flaring region, the jets decelerate from $\approx 0.8c$ to sub-relativistic speeds and develop transverse velocity gradients. Immediately downstream of the brightness flaring point, before deceleration commences, there is little variation of velocity across the jets, and they can be approximated as uniform, constant-velocity flows.

The systematic differences in brightness between the main and counter-jet in the inner region, before the jets decelerate, can provide essential clues on their orientation to the line of sight. Indeed, for intrinsically symmetrical, relativistic jets, the jet/counter-jet flux density ratio (R, also known as sidedness ratio) can be written as:

$$R = \frac{I_{\rm j}}{I_{\rm cj}} = \left(\frac{1+\beta\cos\theta}{1-\beta\cos\theta}\right)^{2-\alpha} \tag{6.1}$$

where θ ($0 \leq \theta \leq \pi/2$) is the angle to the line of sight of the approaching jet, $\beta = v/c$ (where v is the flow velocity) and α is the jet spectral index. For emission in total intensity which assumed to be is isotropic in the frame of the jet flow, Equation 6.1 does not allow β and θ to be determined independently. However, the detailed modelling of the relativistic jet flows in FRI radio galaxies carried out in Laing & Bridle (2014) has enabled accurate estimation of the jet inclination θ in a number of radio galaxies. This work also enabled a calibration of the relation between the jet/counter jet flux density ratio where the jets first brighten (within 1-2 kpc) and θ, which can be considered valid for FRI jets in general. The calibration relies on the inference that the dispersion in velocity just downstream of the flaring point is small both spatially across individual jets and between different sources means that we can determine the angle to the line of sight using a simple constant-velocity approximation. A version of that relation is presented in Figure 6.4, whereby the sidedness ratios were determined using the same method as used for our sources (see Section 6.4.1). The solid lines in Figure 6.4 are single-velocity models. The best-fit model (i.e. unweighted chi-squared minimisation; red solid line) is obtained for $\beta = 0.75$.

6.4.1 Jet sidedness ratios

Given the above considerations, a reasonable estimate of the jet inclination with respect to the line of sight can be obtained by the relation (following from Equa-

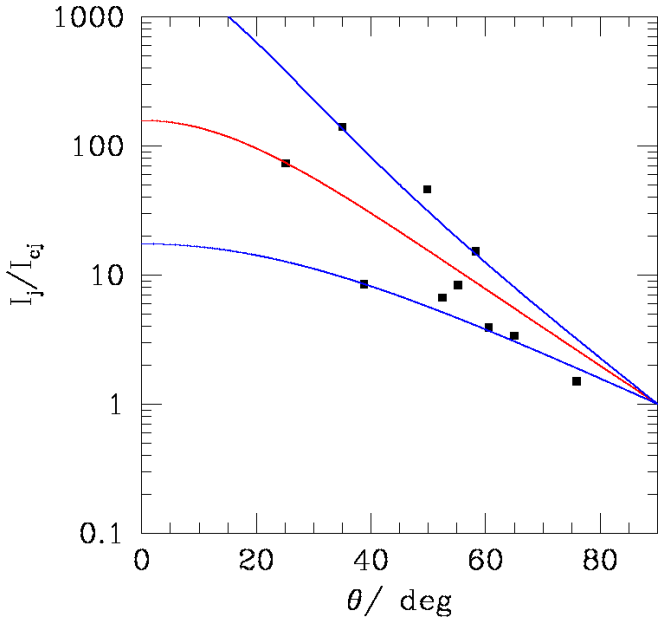

Figure 6.4: Jet/counter-jet flux density ratio versus inclination angle to the line of sight for the 10 sources in Laing & Bridle (2014). The solid lines are single-velocity models. Specifically, the red solid line is for $\beta = 0.75$ and is formally the best-fit. The blue solid lines below and above the best-fit are for $\beta = 0.5$ and 0.9, respectively, and roughly show the boundaries of the distribution.

tion 6.1):

$$\theta_{\rm jet} = \arccos\left(\frac{1}{\beta}\frac{R^{\frac{1}{2-\alpha}}-1}{R^{\frac{1}{2-\alpha}}+1}\right) \tag{6.2}$$

$$\tag{6.3}$$

where β is assumed to be equal to 0.75 (according to the best-fit single-velocity model of Figure 6.4). A good approximation for α is to use the mean spectral index typically seen between 1.4 and 4.9 GHz in FRI jets, $\alpha = -0.6$ (for our spectral-index definition; Laing & Bridle 2013).

Using the radio continuum maps in Figure 6.3, we aim at measuring the jet/counter-jet ratio (R) at the brightness flaring point, which usually has a well-defined onset in FRI jets (as explained above) and should be then identified with some precision in deep high-resolution radio images. The general approach adopted to carry out our analysis consists of the following steps:

- Set boxes covering 3 synthesised beams out from the flaring point, with widths covering the whole jet.
- Measure the total flux density in each box using the CASA task `imstat`.

Table 6.4: Jet sidedness ratios and corresponding inclination to the line of sight.

Target	R	$\theta_{\rm jet}$ (deg)
(1)	(2)	(3)
IC 1531	$\geq$22	$\leq$46
NGC 3557	1.0	90
IC 4296	1.2	86
NGC 7075	99	19

Notes. – Columns: (1) Target name. (2) Jet/counter-jet brightness ratio. (3) Jet inclination angle to the line of sight.

- Divide the flux density of the (brighter) jet by that of the counter (fainter) jet to obtain the sidedness ratio. Equation 6.4.1 is then used to estimate the jet inclination angle.

This standard method, however, works well only in two of the observed objects, NGC 3557 and NGC 7075. In these two cases, the resolution of our observations allows us to resolve the inner jet structure (perfectly matching the typical FRI jet geometry described in Section 6.4) and the achieved sensitivity allows us to detect emission from the (fainter) counter-jet. In the other two cases a different approach is needed.

In IC 1531 (Fig. 6.3a) the inner jet structure is unresolved at the resolution of our observations ($\approx$ 200 pc; see Table 6.2), then the brightness flaring point is not identifiable. Furthermore, emission from the counter-jet is not detected, although we cannot exclude the possibility that some emission from the inner counter-jet contributes to the unresolved core emission. In this case, given the observed structure, we placed the two boxes as close to the core as possible, at the same distance with respect to the phase centre. We then assumed the rms integrated over the north-west box as an upper limit to the integrated flux density of the counter-jet.

In IC 4296 (Fig. 6.3d) emission from the brightness flaring point of both the jet and counter-jet is only marginally detected in our observations ($\approx 3-5\sigma$), thus not allowing a reliable estimation of the jet/counter-jet ratio. We then used the deep high-resolution archival radio image at 4.9 GHz presented in Chapter 2 (Fig. 2.7c) to measure the sidedness ratio of IC 4296, following the method described above.

As already introduced in Section 6.3.2, NGC 3100 is a peculiar case, showing a non-standard FRI jet geometry that does not allow us to obtain a reliable estimation of the sidedness ratio and, in turn, of the line-of-sight jet inclination. This will be discussed in detail in Section 6.5.1.

The measured sidedness ratios and corresponding jet inclinations are listed in Table 6.4.

6.5 Intrinsic jet/disc orientation

We now attempt to constrain the intrinsic orientation of the jet axis relative to the rotation axis of the CO disc in those four objects for which a measure of the jet inclination has been obtained (see Table 6.4). Figure 6.5 illustrates the model parameters and coordinate systems used to describe the jet/disc geometry in 3D. We use a right-handed Cartesian coordinate system xyz, such that the origin in the core, the z axis is along the line-of-sight (positive sign towards the observer), the x axis is in the plane of the sky (by definition, the plane perpendicular to the line of sight) parallel to the projection of the jet axis (positive sign along the projection of the approaching jet). The angle between the approaching jet and the line of sight is $\theta_{\rm jet}$ (and it is allowed to vary in the range $0 \leq \theta_{\rm jet} \leq \pi/2$). In this system, a unit vector along the approaching jet is then

$$\begin{pmatrix} +\sin\theta_{\rm jet} \\ 0 \\ +\cos\theta_{\rm jet} \end{pmatrix}$$

Similarly, we define a second Cartesian coordinate system, $x'y'z'$, in which z' is again along the line-of-sight, but x' is along the projection of the disc rotation axis (i.e. the vector normal to the disc plane) on the plane of the sky. $\theta_{\rm disc}$ is the angle between the disc rotation axis and the line of sight ($0 \leq \theta_{\rm disc} \leq \pi/2$). The vector components of the disc axis in the primed coordinate system are

$$\begin{pmatrix} +\sin\theta_{\rm disc} \\ 0 \\ +\cos\theta_{\rm disc} \end{pmatrix}$$

The two coordinate systems are related by a rotation Δ about the common z (z') axis (the sign convention for Δ does not matter for this calculation), where in our specific case Δ coincides with the projected relative orientation angles between the jet and the disc axes listed in Column 4 of Table 6.1 (i.e. $\Delta = \Delta PA$). Note that CO observations alone cannot distinguish between the angles Δ and $\pi + \Delta$ (but with the opposite sense of gas motion), i.e. a rotation of 180° of the disc about the line-of-sight, which depends on the near/far side of the CO disc. If we observe dust associated with the CO disc, then we can differentiate between these possibilities based on the intensity of the dust absorption (i.e. the near side is that where the dust absorption is stronger). If $|\Delta| < \pi/2$, then the near side of the disc appears in projection on the receding jet side; if $|\Delta| > \pi/2$, then it is projected on the approaching jet.

The components of a vector in the xyz frame are related to the components in the $x'y'z'$ frame by

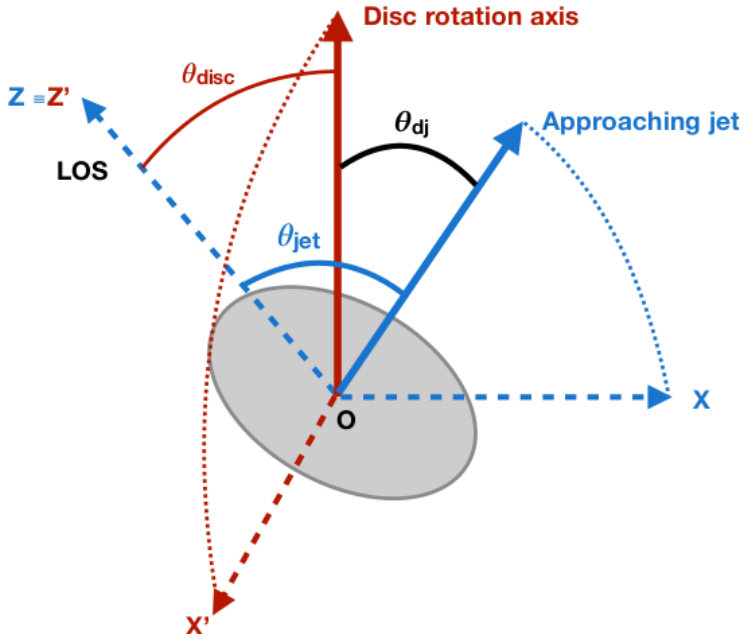

Figure 6.5: Model used to described the geometry of the jet/disc system in 3D. The Cartesian system $Oxyz$ is built so that the origin is in the core, the z axis is along the line of sight (positive sign towards the observed), and the x axis is in the plane of the sky parallel to the projection of the jet (positive sign along the projection of the approaching jet). The angle between the approaching jet and the line of sight is $\theta_{\rm jet}$. Similarly, in the $Ox'y'z'$ Cartesian system, the origin is in the core, the z' axis is again along the line of sight, and x' lies along the projection of the disc rotation axis (i.e. the vector normal to the disc plane, indicated as a solid red arrow). The inclination of the gas disc to the line of sight is given by the angle $\theta_{\rm disc}$. $\theta_{\rm dj}$ is the angle between the jet and the disc rotation axis and defines the intrinsic relative orientation between the CO disc and the radio jets.

$$\begin{pmatrix} x \\ y \\ z \end{pmatrix} = \begin{pmatrix} +\cos\Delta & +\sin\Delta & 0 \\ -\sin\Delta & +\cos\Delta & 0 \\ 0 & 0 & 1 \end{pmatrix} \begin{pmatrix} x' \\ y' \\ z' \end{pmatrix}$$

so the components of the disc axis vector in the xyz frame are

$$\begin{pmatrix} +\cos\Delta & +\sin\Delta & 0 \\ -\sin\Delta & +\cos\Delta & 0 \\ 0 & 0 & 1 \end{pmatrix} \begin{pmatrix} +\sin\theta_{\rm disc} \\ 0 \\ +\cos\theta_{\rm disc} \end{pmatrix} = \begin{pmatrix} +\cos\Delta\sin\theta_{\rm disc} \\ -\sin\Delta\sin\theta_{\rm disc} \\ +\cos\theta_{\rm disc} \end{pmatrix}$$

The angle between the jet and disc axis vectors, $\theta_{\rm dj}$, is given by taking the dot product of the two unit vectors:

$$\begin{pmatrix} +\cos\Delta\sin\theta_{\rm disc} \\ -\sin\sin\theta_{\rm disc} \\ +\cos\theta_{\rm disc} \end{pmatrix} . \begin{pmatrix} +\sin\theta_{\rm jet} \\ 0 \\ +\cos\theta_{\rm jet} \end{pmatrix} = \cos\Delta\sin\theta_{\rm disc}\sin\theta_{\rm jet} + \cos\theta_{\rm disc}\cos\theta_{\rm jet}$$

Table 6.5: Intrinsic alignment angle between the jet and the disc rotation axes.

Target	$\theta_{\rm disc}$ (deg)	$\theta_{\rm jet}$ (deg)	Δ (deg)	$\theta_{\rm dj}$ (deg)
(1)	(2)	(3)	(4)	(5)
IC 1531	32	$\leq$46	72	32-45 (32-62)
NGC 3557	56	90	45	53
IC 4296	68	86	9	27
NGC 7075	46	19	16	28 (64)

Notes. − Columns: (1) Target name. (2) Disc inclination angle (i.e. angle between the line of sight and the normal to the disc plane) obtained from the kinematical modelling presented in Chapter 4. (3) Jet inclination angle to the line of sight derived as described in Section 6.4.1. (4) Projected relative orientation between the jets and the rotation axis of the CO disc as listed in Table 6.1. (5) Intrinsic relative inclination between the jets and the CO disc rotation axes. In those sources in which the near/far side ambiguity is not solved (IC 1531 and NGC 7075), both possible values are reported (the value with a rotation $180+\Delta$ in parentheses). The ranges of IC 1531 are because the jet inclination is an upper limit in this case.

so

$$\cos\theta_{\rm dj} = |\cos\Delta\sin\theta_{\rm disc}\sin\theta_{\rm jet} + \cos\theta_{\rm disc}\cos\theta_{\rm jet}| \tag{6.4}$$

(modulus because we want to range in $[0, \pi/2]$). If we do not know which is the near side of the disc, then a second possible angle is given by replacing Δ by $\pi + \Delta$ (i.e. rotating the disc by 180° about the line of sight), in which case

$$\cos\theta_{\rm dj} = |-\cos\Delta\sin\theta_{\rm disc}\sin\theta_{\rm jet} + \cos\theta_{\rm disc}\cos\theta_{\rm jet}| \tag{6.5}$$

For NGC 3557, $\theta_{\rm jet} = 90°$, so the sign does not matter (i.e. we do not know which is the approaching jet) and $\theta_{\rm dj} = 53°$. For IC 4296, Figure 2.7a shows that the near side of the dust disc is North of the nucleus (and the approaching jet is also to the North-West). In that case, the correct value of $\Delta = 180° + 9° = 189°$ and $\theta_{\rm dj} = 27°$.

For NGC 7075, both solutions are possible, since we have no information on the dust component. The possibilities are $\Delta = 16°$ or 196°, giving $\theta_{\rm dj} = 28°$ or 64°. Finally, IC 1531 has $32° \leq \theta_{\rm dj} \leq 45°$ or $32° \leq \theta_{\rm dj} \leq 62°$. The ranges are because the jet inclination is an upper limit in this case (see Table 6.4). The obtained relative inclination angles are listed in Table 6.5, along with a summary of all the parameters used in Equation 6.4 (6.5).

For NGC 3557 and IC 4296 the results are mostly consistent with that obtained from the 2D analysis (Table 6.1): the jet and the disc rotation axes are roughly aligned in the latter case, whereas they show a larger misalignment in NGC 3557.

The ambiguity on the near far/side in NGC 7075 and the addition of the jet inclination uncertainty in IC 1531 do not allow us to obtain an accurate estimate of the 3D jet/disc orientation in these two cases. In IC 1531, however, there is an evident tendency for its upper limits to converge towards large relative orientation angles ($\geq 45°$), although the jet/disc rotation axes misalignment would be less prominent than that inferred from the 2D analysis (Table 6.1). In general, although the uncertainties and the small numbers clearly prevent us from robustly constraining the distribution, our results can be considered consistent with that of Verdoes Kleijn & de Zeeuw (2005, see Section 6.1): the orientation angles seem to vary widely within the sample ($27° - 64°$), but with a marginal preference for $\theta_{\rm dj}$ around 45° (i.e. mean values in the range $37° - 48°$). For comparison, we also used the information available in literature to measure the jet/disc relative inclination in 3C31 (the prototypical LERG), finding a result consistent with that conclusions. Indeed, from the gas/dust and jet analysis of 3C31 carried out by Okuda et al. (2005), Martel et al. (2000) and Laing & Bridle (2002b), we find: $\theta_{\rm jet} = 52.5°$, $\theta_{\rm disc} = 37°$, $\Delta = 70°$, and $\theta_{\rm dj} = 49°$.

As pointed out in Section 6.1, since jets in low accretion rate systems like LERGs are demonstrated to be launched along the spin axis of the central BH and the inner accretion disc, based on simple symmetry arguments we ideally expect a perfect alignment between the black hole, inner accretion disc and kpc-scale molecular disc rotation axes. As indicated by the results presented and discussed above, however, evidence has accumulated that such ideal axisymmetry rarely occurs, suggesting the opposite situation (jet/disc misalignment) to be more frequent. Models in which the jets can be misaligned with respect to the rotation axis of either the inner accretion disc (when present) or the larger-scale dust/molecular gas disc have therefore been discussed extensively in literature (e.g. Kinney et al. 2000; Schmitt et al. 2001, 2002; Verdoes Kleijn & de Zeeuw 2005; Gallimore et al. 2006; King & Nixon 2018; Liska et al. 2019). A detailed discussion of the origin of the jet/disc misalignment based on such theories is beyond the scope of this work. However, in the following we briefly explore some of the proposed scenarios, in an attempt to put at least some constraints on the origin of the observed relative orientations of discs and jets.

In the case of a gas distribution that is fully settled into the host galaxy potential and co-rotates with stars (as in the case of NGC 3557), one way to explain the jet/disc misalignment is that the jet is launched along the spin axis of the black hole, which in turn is determined by earlier merger events and is not aligned with an axis of the stellar gravitational potential (e.g. Wilson & Colbert 1995). Alternatively, if the jet direction is defined by the inner accretion disc, then warping of the disc may cause misalignment (Schmitt et al. 2002). The inner part of a tilted thin accretion disc is expected to become aligned with the black hole mid-plane via the Bardeen-Petterson effect (Bardeen & Petterson 1975), although the hole spin eventually becomes parallel to the angular momentum vector of the accreted matter (Rees 1978; Scheuer & Feiler 1996). Simulations by Liska et al. (2019) show that jets

are launched along the angular momentum vector of the outer tilted disc in this case. It is worth noting, however, that all these mechanisms are tested to work in thin accretion discs of radiatively efficient (Seyfert-like) systems, whereas it is still not clear whether they can work for the thick accretion discs thought to occur in LERGs (e.g. Zhuravlev et al. 2014, see Section 1.2).

Another way of explaining the jet/disc misalignment is that the molecular gas has an external origin (from a minor merger or interaction) and has not yet settled into a principal plane of the host galaxy potential (e.g. Lauer et al. 2005; Shabala et al. 2012; van de Voort et al. 2015, 2018). In this case, there is no reason for the angular momentum vector of the gas to be aligned with that of the central pre-existing black hole. Schmitt et al. (2002) and Verdoes Kleijn & de Zeeuw (2005) argue against this idea on the grounds that regular dust discs appear to rotate around the short axes of oblate-triaxial gravitational potentials and have therefore settled. This is consistent with the fact that the object in our sample with largest disc-jet misalignment (NGC 3557) shows mostly regular disc rotation (at least the resolution of our ALMA observations) and the gas and stars rotate together: in this case, if the gas has been accreted externally, it is likely to have settled or at least to be in an advanced state of the settling sequence (see Chapter 5). Gas in younger (and therefore smaller) radio galaxies might be more likely to be in the settling phase, but the majority of our sample (including NGC 3557) are mature radio galaxies with large-scale jets. Furthermore, the spectral ages and alignment angles for the B2 radio-galaxy sample (mostly FRI LERGs; Colla et al. 1975) were found not to correlate (Parma et al. 1999; De Ruiter et al. 2002). A recent misaligned inflow of molecular gas therefore seems not to explain all of the observations, although we cannot exclude that it may be relevant for some objects.

Independently of its origin, it is worth mentioning that the jet/disc misalignment can have important implication for the evolution of the central SMBH. Indeed, Hawking's theorem on rotating black holes states that any stationary state involving a black hole and external fields must be either static (i.e. non-rotating) or axisymmetric (Hawking 1972). Therefore, a spinning black hole in a non axi-symmetric situation must either try to lose all of its spin energy or evolve toward axisymmetry (e.g. King & Nixon 2018; Liska et al. 2019). In the second case, the hole and the surrounding matter must experience torques trying to remove the asymmetry and forcing the BH into alignment with the outer disc on very short timescales. This can in turn lead to rapid spin-up of the SMBH, which then removes part of this large angular momentum through powerful large-scale outflows (i.e. the jets; e.g. Liska et al. 2019).

6.5.1 Jet/disc interactions: the case of NGC 3100

As outlined in the introduction to this Chapter, one of the purposes of investigating the relative orientations of discs and jets was to explore the possible presence of

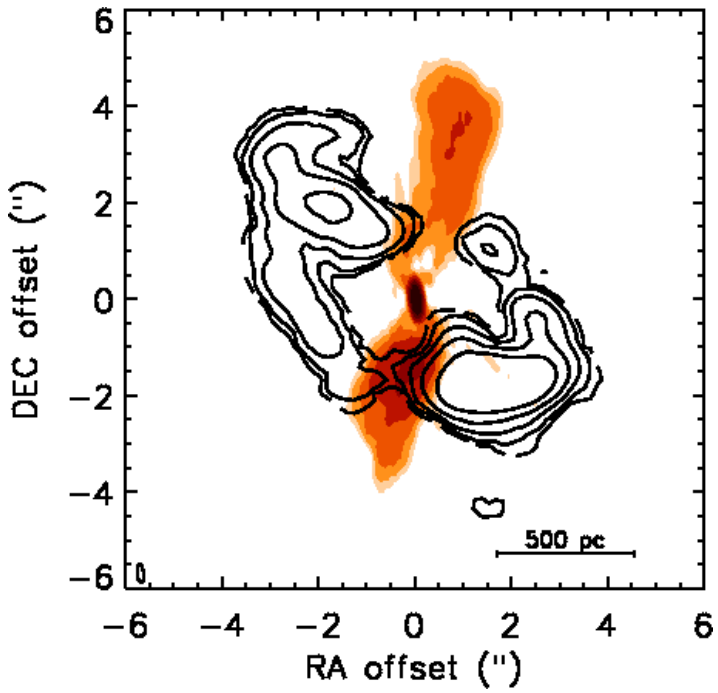

Figure 6.6: 10 GHz JVLA continuum map of NGC 3100 with CO integrated intensity contours superimposed. Contours are drawn at 1,3,9..times the 3σ rms noise level. The beam and the physical scale bars are drawn in the bottom-left and bottom-right corners, respectively.

interactions between the two components on sub-kpc scales. Indeed, although the jet/ISM interaction mechanisms can be varied (see Section 1.4.2), they all produce strong effects in both the gas and the jet distribution and kinematics on (sub-)kpc scales (e.g. outflow and/or fragmentation of the gas clouds; bending, spreading and deceleration of the jet flow): spatially resolved imaging of both the jet and cold gas components is then crucial to constrain the occurrence and the properties of these mechanisms.

NGC 3100 is a remarkably interesting object in this sense. The well-resolved inner jet structure is clearly geometrically different compared with that observed in the other four objects and in FRI LERGs in general (see Section 6.4). In particular, the two extended structures appear to be asymmetric with respect to each other, with the northern jet also showing an evident distortion. Figure 6.6 shows a masked version of the JVLA map of NGC 3100 with the CO contours overlaid in black. It is clear from this Figure that the distortion of the northern jet appears to be morphologically coincident with the region of the CO disc disruption (at Declination offsets between $2''$ and $4''$). Furthermore, the jet flow seems to rapidly decelerate and consequently increase its surface brightness, as it spreads just close to the core. All these features provide further support to the scenario of a jet/disc interaction

introduced in Section 6.2. Specifically, both the disc and the jet morphologies can be considered consistent with entrainment of the molecular gas into the jet flow, with the consequent disruption of the gas disc and the rapid deceleration of the jets from relativistic speeds (e.g. Laing & Bridle 2002a, see also Section 1.4.2).

Theoretical models suggest that the gas can be also compressed and shocked by the interaction with the expanding jet flow, possibly leading to the formation of spiral arms like those identified in the inner regions of the NGC 3100 CO disc (e.g Veilleux et al. 2005; see Section 4.3.2). However, in this scenario, the location of the radio jets should be coincident with that of the spiral arms (e.g. Fathi et al. 2011), while in NGC 3100 there is an evident misalignment between the two (see panel c of Figure 4.9). We then still favour external gas accretion as the mechanism giving rise to the spiral feature at the centre of this gas distribution (see Section 5.1.2). Jet/gas interactions are also expected to strongly affect the gas kinematics, possibly inducing outflows, line broadening and distortions in both the velocity pattern and curve (e.g. Alatalo et al. 2011; Morganti et al. 2015; Dasyra et al. 2016). However, the 3D modelling of the disc reveals no obvious kinematical signatures that can be attributed to such an interaction (Sections 4.3.2 and 4.3.2), likely indicating that, if present, this mechanism does not strongly affect the kinematics of the CO disc in NGC 3100 (at least at the current spatial resolution). A detailed analysis of the physics of the cold gas in NGC 3100 through ratios of multiple molecular line transitions (recently observed with ALMA during Cycle 6 and not included in this Thesis) will allow us to investigate this issue further.

Finally, we note that kinematical features likely to be associated with jet/disc interactions are similar to those seen in the rotation pattern and, correspondingly, the velocity curve of NGC 3557 (see Section 4.3.1). The observed asymmetries seem to be located in the direction of the jet axis (Panel a of Figure 4.7a), supporting the hypothesis of a jet/cold gas interaction proposed recently by Vila-Vilaro et al. (2019) based on multiple molecular line ratios. Interestingly, NGC 3557 shows a significant misalignment between the jet and the disc rotation axes (Table 6.5), making plausible a scenario in which the radio jets pierce the surrounding cold gas disc. Similar features are also observed along the direction of the jet axis in the rotation pattern and velocity curve of IC 1531 (Fig. 4.3a and Sect. 4.3). We speculate about a possible jet/gas interaction also in this source, although in both cases higher-resolution data and/or other molecular gas transitions are needed to explore our hypothesis further and to draw solid conclusions.

Conclusions and future perspectives

This Thesis was carried out as part of an international research project whose overall scope is a multi-phase (stars, warm/cold gas, dust and radio jets) study of a volume- and flux-limited ($z < 0.03$, $S_{2.7\ \mathrm{GHz}} \geq 0.25$ Jy) sample of eleven low-excitation radio galaxies (LERGs) in the southern sky. The main purpose of the project is to gain a better understanding of the AGN fuelling/feedback mechanisms in these sources. Although LERGs are the dominant radio galaxy population in the local Universe (e.g. Hardcastle et al. 2007), typically hosted by very massive ETGs ($M_* \geq 10^{11}\ M_\odot$; e.g. Best & Heckman 2012), there are few spatially resolved studies of these objects. The trigger mechanisms and associated AGN feeding/feedback processes in LERGs are thus still poorly understood (e.g. Hardcastle 2018). Investigating the nature of LERGs is crucial to shed light on the mechanisms which determine the observed properties of massive ETGs in the local Universe, isolating the role played by kinetic (jet-induced) feedback in shaping galaxies over cosmic times.

In this general context, the scientific purposes of this work were:

- Carrying out a detailed study of the morphological and kinematical properties of the molecular gas in the sub-set of the overall sample observed in ^{12}CO(2-1) with ALMA. This allowed us to investigate the role of cold gas in fuelling LERGs by determining its occurrence, quantity and dynamical state, searching for evidence of infall.

- Coupling our morphological and kinematical analysis with other observational and theoretical constraints to shed light on the origin of the observed molecular gas reservoirs (internal or external). This can have implications for the powering mechanism of LERGs (traditionally believed to be powered by accretion of the hot halo gas, either directly or after chaotic cooling), but may also provide clues on the putative role of the large-scale environment in determining the origin of the cold gas in these objects.

- Comparing ALMA CO(2-1) and 230 GHz continuum observations with newly-acquired radio JVLA data at 10 GHz of five sample sources to investigate the relative orientation of the angular momentum vectors of the cold gas discs

and the jet axis in three dimensions. This analysis allows us to explore the occurrence of interactions between the radio jets and molecular gas on (sub-) kpc scales, possibly providing clues on the interplay between the jet and molecular gas components in typical radio galaxies as opposed to very gas-rich late-type systems. The study of the jet-disc relative inclinations can also have implications for the origin of the gas and the evolution of the central black hole.

This is the first time that a systematic and detailed study like the one outlined above has been carried out for a complete, volume-limited sample of LERGs. The results of this Thesis can then provide a valuable contribution to answering the important question of how jets in LERGs are fuelled and interact with their surroundings on (sub-)kpc scales.

The main results of this work can be summarised as follows:

- **Molecular gas content.** We find that molecular gas is very common in LERGs. Indeed, six out of nine sources observed with ALMA have been detected in CO, with typical masses ranging from $\approx 10^7$ to $\approx 10^8$ M$\odot$. The detected CO emission appears distributed in rotating disc- or ring-like structures, on scales from a few hundred parsecs to a few kpc. NGC 612 is exceptional among our detections: it shows a massive (2×10^{10} M$_\odot$) molecular gas disc extending ≈10 kpc along its major axis. Double-horned integrated CO spectral profiles are observed in all of the sources, consistent with the resolved morphology and kinematics. One source (IC 4296) also shows a deep and narrow absorption feature against the bright continuum nuclear radio source. The CO absorption optical depth is $\tau \approx 0.12$. From this value we infer an HI absorption optical depth $\tau \approx 1.2 \times 10^{-4}$, consistent with the non-detection of HI absorption by Morganti et al. (2001).

- **Molecular gas kinematics.** The 3D modelling of the detected CO discs further demonstrates that the bulk of the gas is in ordered rotation (at least at the resolution of our ALMA observations), possibly explaining the relatively low accretion rate of these objects (as first suggested by Okuda et al. 2005 for 3C31). This is also consistent with our analysis on the gravitational stability of these discs (estimated through the Toomre parameter, Q; Toomre 1964). With some uncertainties, all but two of the discs can be considered stable against gravitational fragmentation ($Q > 1$), and this may have implications for the (low) inflow rate of LERGs. Nevertheless, low-level perturbations and/or hints of non-circular motions are ubiquitous, indicating that the gas is not fully relaxed into the host galaxy potential. This represents a significant difference with respect to the results found in existing spatially-resolved studies of the molecular gas component in radio-quiet ETGs (e.g. Alatalo et al. 2013; Boizelle et al. 2017), whereby the observed CO distribution are typically found to be both dynamically and morphologically fully settled. Our

best resolved case (NGC 3100) shows hints of inflow motions along its minor axis, making it the best candidate for cold gas feeding of the central SMBH.

- **Origin of the molecular gas.** We investigated the origin of the cold gas observed in our sources, coupling multi-wavelength observational properties with theoretical expectations to discriminate between internal or external accretion mechanisms. Our analysis strongly supports an external gas origin for at least two of our sample sources, NGC 612 and NGC 3100, probably via interaction with their companion galaxies. Based on the analysis carried out in this work and available in literature, the origin of the cold gas content in IC 4296 and NGC 3557 is unclear. In these two cases, the observed cold gas may then originate from either an aged hot gas cooling (i.e. cooling at a sufficiently late stage for dust to have re-formed within the gas clouds) or a combination of internal and external accretion mechanisms. Both scenarios, however, would result on the same observed features, becoming formally indistinguishable using the information currently available to us. In NGC 7075 and IC 1531, the available information is simply insufficient to allow us a detailed investigation about the origin of their gas reservoirs.
  Given that all of the CO detected sources in our sample, except IC 4296, inhabit poor environments (whereas LERGs are preferentially found at the centres of groups and clusters), we speculate that external accretion mechanisms (in particular galaxy-galaxy interactions) may be important in powering LERGs located in low density environments.

- **Jets and molecular gas.** The analysis of the relative orientation between the jet and the CO disc rotation axes was carried out first in projection (using ALMA observations only), and then in three dimensions by comparing the line-of-sight inclination of the CO disc (obtained from the 3D modelling) and that of the jets (obtained from the analysis of the newly-acquired high-resolution JVLA data at 10 GHz). The latter, in particular, shows that the relative inclination angle distribution can span a wide range ($27^\circ - 64^\circ$), with mean values in the range $37^\circ - 48^\circ$, depending on the assumptions on the near/far sides of the CO discs. This is consistent with previous statistical 3D studies of the relative inclination between the jets and the dust discs in radio galaxies (Verdoes Kleijn & de Zeeuw 2005), and argues against a simple axisymmetric scenario according to which one would expect a common rotation axis for the central black hole, the inner accretion disc and the kpc-scale disc. In NGC 3100 the geometry of the sub-kpc jets significantly deviates from that of typical FRI radio galaxies, showing a clear distortion of the northern jet that coincides in projection with a disruption observed in the CO disc. The jets seem to rapidly decelerate and expand in the region close to the core (≈ 160 pc). The observed structures, along with a broadening of the [O III] equivalent width along the jet axis (Warren et al. , in preparation),

corroborates the hypothesis of a jet/disc interaction in this source, whereby the jet entrain the surrounding molecular gas, causing fragmentation of the gas clouds and jets deceleration from relativistic speeds close to the region where they are launched. Hints of the presence of a jet/disc interaction are also tentatively found in the kinematics of NGC 3557 and IC 1531, the former also being the object in which we measure the largest jet/disc misalignment (53°).

The results summarised above have been published in two papers, Ruffa et al. (2019a, 2019b). A third paper, focused on the analysis of the 3D relative jet/CO disc orientation is in preparation. We finally note that a recent review on SMBH feeding mechanisms has been presented by Storchi-Bergmann & Schnorr-Müller (2019). Interestingly, although mainly based on optically-selected samples of Seyfert-like (radio-quiet) AGN, the observational constraints discussed in this review corroborate our findings on some fundamental points:

- Various works have found a higher occurrence of low-luminosity AGN (typically associated to kinetic-mode AGN) hosted by galaxies in close pairs, suggesting that galaxy-galaxy interactions are conducive environments for powering this class of objects.
- Chaotic cold accretion (CCA) from the hot halo is acknowledged as the most likely fuelling mode of kinetic-mode AGN hosted by galaxies located in high-density environments (e.g. bright ETGs at the centre of groups and clusters). Its incidence in similar objects situated in poor environments is currently poorly constrained, and thus remains controversial.
- Dusty spiral perturbations on (sub-)kpc scales are believed to play a major role in channelling matter to the central SMBH of early-type AGN hosts, generating inflow rates that are of the order of those typically required to power low-luminosity (kinetic-mode) AGN.

Future perspectives

The study presented here has stimulated a number of follow-up projects.

First of all, we plan in the next future to further investigate the apparent disagreement with the *chaotic cold accretion* scenario along two main lines. First, we aim at analysing the hot gas component through X-ray observations (already available for some sources of the current sample). This will allow us to investigate the relation between the hot and the cold gas phases in LERGs, providing us with further clues on the origin of the cold gas. Secondly, we will expand the study to a larger sample, probing a wider range of environments. Almost all the objects studied in this Thesis are isolated or in poor groups; considering sources in richer environments would be crucial to probe the possible role of the large-scale environment in determining the origin of the cold gas reservoirs observed in LERGs.

NGC 3100 is certainly the most interesting source in our sample, being also our best candidate for a jet/gas disc interaction. We have therefore proposed and obtained follow-up ALMA observations of multiple molecular transitions in this object in Bands 3, 4 and 7 (Cycle 6; PI: I. Ruffa). These data will allow us to infer the physical conditions of the molecular gas in NGC 3100, and fully assess the impact of the radio jets on the physics of the surrounding environment. On a longer timescale we plan to propose higher resolution multi-species observations for (at least some of) the other LERGs in the current sample.

Bibliography

Alatalo, K., Blitz, L., Young, L. M., et al. 2011, Astrophysical Journal, 735, 88

Alatalo, K., Davis, T. A., Bureau, M., et al. 2013, Monthly Notices of the RAS, 432, 1796

Allen, S. W., Dunn, R. J. H., Fabian, A. C., Taylor, G. B., & Reynolds, C. S. 2006, Monthly Notices of the RAS, 372, 21

Annibali, F., Bressan, A., Rampazzo, R., et al. 2010, Astronomy and Astrophysics, 519, A40

Antonucci, R. 1993, Annual Review of Astronomy and Astrophysics, 31, 473

Antonucci, R. 2012, Astronomical and Astrophysical Transactions, 27, 557

Asplund, M., Grevesse, N., Sauval, A. J., Allende Prieto, C., & Kiselman, D. 2004, Astronomy and Astrophysics, 417, 751

Baan, W. A. 1980, Astrophysical Journal, 239, 433

Babyk, I. V., McNamara, B. R., Tamhane, P. D., et al. 2018, arXiv e-prints, arXiv:1810.11465

Baldi, R. D., Capetti, A., & Giovannini, G. 2019, Monthly Notices of the RAS, 482, 2294

Baldi, R. D., Capetti, A., & Massaro, F. 2018, Astronomy and Astrophysics, 609, A1

Baldi, R. D., Giroletti, M., Capetti, A., et al. 2015, Astronomy and Astrophysics, 574, A65

Baldry, I. K., Balogh, M. L., Bower, R. G., et al. 2006, Monthly Notices of the Royal Astronomical Society, 373, 469

Baldry, I. K., Glazebrook, K., Brinkmann, J., et al. 2004, Astrophysical Journal, 600, 681

Baldwin, J. A., Phillips, M. M., & Terlevich, R. 1981, Publications of the Astronomical Society of the Pacific, 93, 5

Balmaverde, B., Baldi, R. D., & Capetti, A. 2008, Astronomy and Astrophysics, 486, 119

Balmaverde, B. & Capetti, A. 2006, Astronomy and Astrophysics, 447, 97

Bardeen, J. M. & Petterson, J. A. 1975, Astrophysical Journal, Letters, 195, L65

Becker, R. H., White, R. L., & Helfand, D. J. 1995, Astrophysical Journal, 450, 559

Begelman, M. C. 1982, in IAU Symposium, Vol. 97, Extragalactic Radio Sources, ed. D. S. Heeschen & C. M. Wade, 223–225

Best, P. N. & Heckman, T. M. 2012, Monthly Notices of the RAS, 421, 1569

Best, P. N., Kaiser, C. R., Heckman, T. M., & Kauffmann, G. 2006, Monthly Notices of the RAS, 368, L67

Best, P. N., Kauffmann, G., Heckman, T. M., et al. 2005a, Monthly Notices of the Royal Astronomical Society, 362, 25

Best, P. N., Kauffmann, G., Heckman, T. M., & Ivezić, Ž. 2005b, Monthly Notices of the Royal Astronomical Society, 362, 9

Bianchi, S., Maiolino, R., & Risaliti, G. 2012, Advances in Astronomy, 2012, 782030

Bicknell, G. V. 1984, Astrophysical Journal, 286, 68

Bicknell, G. V. 1986, Astrophysical Journal, 300, 591

Bicknell, G. V. 1994, Astrophysical Journal, 422, 542

Biretta, J. A., Zhou, F., & Owen, F. N. 1995, Astrophysical Journal, 447, 582

Birkinshaw, M. & Davies, R. L. 1985, Astrophysical Journal, 291, 32

Blandford, R. D. & Znajek, R. L. 1977, Monthly Notices of the RAS, 179, 433

Blum, R. D., Burleigh, K., Dey, A., et al. 2016, in American Astronomical Society Meeting Abstracts, Vol. 228, American Astronomical Society Meeting Abstracts #228, 317.01

Blundell, K. M. & Rawlings, S. 2000, Astronomical Journal, 119, 1111

Boizelle, B. D., Barth, A. J., Darling, J., et al. 2017, Astrophysical Journal, 845, 170

Bolatto, A. D., Wolfire, M., & Leroy, A. K. 2013, Annual Review of Astronomy and Astrophysics, 51, 207

Bondi, H. 1952, Monthly Notices of the RAS, 112, 195

Bosma, A. 1981a, Astronomical Journal, 86, 1791

Bosma, A. 1981b, Astronomical Journal, 86, 1825

Bowman, M., Leahy, J. P., & Komissarov, S. S. 1996, Monthly Notices of the RAS, 279, 899

Braine, J. & Combes, F. 1992, Astronomy and Astrophysics, 264, 433

Brough, S., Proctor, R., Forbes, D. A., et al. 2007, Monthly Notices of the RAS, 378, 1507

Burke-Spolaor, S., Ekers, R. D., Massardi, M., et al. 2009, Monthly Notices of the RAS, 395, 504

Buttiglione, S., Capetti, A., & Celotti, A. 2008, , 79, 1018

Buttiglione, S., Capetti, A., Celotti, A., et al. 2010, Astronomy and Astrophysics, 509, A6

Capetti, A. & Balmaverde, B. 2005, Astronomy and Astrophysics, 440, 73

Cappellari, M. 2008, Monthly Notices of the RAS, 390, 71

Cappellari, M., Bacon, R., Bureau, M., et al. 2006, Monthly Notices of the RAS, 366, 1126

Cappellari, M., Emsellem, E., Krajnović, D., et al. 2011, Monthly Notices of the RAS, 413, 813

Cappellari, M., Verolme, E. K., van der Marel, R. P., et al. 2002, Astrophysical Journal, 578, 787

Carilli, C. L. & Walter, F. 2013, Annual Review of Astronomy and Astrophysics, 51, 105

Casasola, V., Combes, F., García-Burillo, S., et al. 2008, Astronomy and Astrophysics, 490, 61

Casasola, V., Hunt, L. K., Combes, F., García-Burillo, S., & Neri, R. 2011, Astronomy and Astrophysics, 527, A92

Cattaneo, A. & Best, P. N. 2009, Monthly Notices of the RAS, 395, 518

Ceverino, D. & Klypin, A. 2007, Monthly Notices of the RAS, 379, 1155

Chiaberge, M. & Marconi, A. 2011, Monthly Notices of the Royal Astronomical Society, 416, 917

Ching, J. H. Y., Croom, S. M., Sadler, E. M., et al. 2017, Monthly Notices of the RAS, 469, 4584

Choi, E., Ostriker, J. P., Naab, T., Oser, L., & Moster, B. P. 2015, Monthly Notices of the Royal Astronomical Society, 449, 4105

Ciotti, L., Ostriker, J. P., & Proga, D. 2010, Astrophysical Journal, 717, 708

Colbert, J. W., Mulchaey, J. S., & Zabludoff, A. I. 2001, Astronomical Journal, 121, 808

Colla, G., Fanti, C., Fanti, R., et al. 1975, Astronomy and Astrophysics, Supplement, 20, 1

Colless, M., Peterson, B. A., Jackson, C., et al. 2003, arXiv e-prints, astro

Collobert, M., Sarzi, M., Davies, R. L., Kuntschner, H., & Colless, M. 2006, Monthly Notices of the RAS, 370, 1213

Combes, F. 2001a, in Astronomical Society of the Pacific Conference Series, Vol. 230, Galaxy Disks and Disk Galaxies, ed. J. G. Funes & E. M. Corsini, 213–220

Combes, F. 2001b, in Advanced Lectures on the Starburst-AGN, ed. I. Aretxaga, D. Kunth, & R. Mújica, 223

Combes, F. 2006, arXiv Astrophysics e-prints [astro-ph/0608616]

Combes, F. 2017, Frontiers in Astronomy and Space Sciences, 4, 10

Combes, F., García-Burillo, S., Casasola, V., et al. 2013, Astronomy and Astrophysics, 558, A124

Combes, F., Young, L. M., & Bureau, M. 2007, Monthly Notices of the RAS, 377, 1795

Condon, J. J., Cotton, W. D., Greisen, E. W., et al. 1998, Astronomical Journal, 115, 1693

Courteau, S. 1997, Astronomical Journal, 114, 2402

Dame, T. M. 2011, ArXiv e-prints [[arXiv]1101.1499]

Dasyra, K. M., Bostrom, A. C., Combes, F., & Vlahakis, N. 2015, Astrophysical Journal, 815, 34

Dasyra, K. M., Combes, F., Oosterloo, T., et al. 2016, Astronomy and Astrophysics, 595, L7

David, L. P., Lim, J., Forman, W., et al. 2014, Astrophysical Journal, 792, 94

David, L. P., Nulsen, P. E. J., McNamara, B. R., et al. 2001, Astrophysical Journal, 557, 546

Davies, R., Förster Schreiber, N. M., Cresci, G., et al. 2011, Astrophysical Journal, 741, 69

Davis, T. A., Alatalo, K., Bureau, M., et al. 2013, Monthly Notices of the RAS, 429, 534

Davis, T. A., Alatalo, K., Sarzi, M., et al. 2011, Monthly Notices of the RAS, 417, 882

Davis, T. A. & Bureau, M. 2016, Monthly Notices of the RAS, 457, 272

Davis, T. A., Bureau, M., Onishi, K., et al. 2017, Monthly Notices of the RAS, 468, 4675

Davis, T. A., Bureau, M., Onishi, K., et al. 2018, Monthly Notices of the RAS, 473, 3818

Davis, T. A., Greene, J. E., Ma, C.-P., et al. 2019, Monthly Notices of the RAS, 486, 1404

Davis, T. A., Rowlands, K., Allison, J. R., et al. 2015, Monthly Notices of the RAS, 454, 657

De Koff, S., Best, P., Baum, S. A., et al. 2000, Astrophysical Journal, Supplement, 129, 33

De Ruiter, H. R., Parma, P., Capetti, A., Fanti, R., & Morganti, R. 2002, Astronomy and Astrophysics, 396, 857

De Vaucouleurs, G. 1976, in Royal Greenwich Observatory Bulletins, Vol. 182, The Galaxy and the Local Group, ed. R. J. Dickens, J. E. Perry, F. G. Smith, & I. R. King, 177

De Young, D. S. 1996, in Astronomical Society of the Pacific Conference Series, Vol. 100, Energy Transport in Radio Galaxies and Quasars, ed. P. E. Hardee, A. H. Bridle, & J. A. Zensus, 261

Dekel, A., Birnboim, Y., Engel, G., et al. 2009, Nature, 457, 451

Dopita, M. A., Shastri, P., Davies, R., et al. 2015, Astrophysical Journal, Supplement, 217, 12

Drory, N., Bundy, K., Leauthaud, A., et al. 2009, The Astrophysical Journal, 707, 1595

Duah Asabere, B., Horellou, C., Jarrett, T. H., & Winkler, H. 2016, Astronomy and Astrophysics, 592, A20

Duc, P.-A., Cuillandre, J.-C., Karabal, E., et al. 2015, Monthly Notices of the RAS, 446, 120

Ekers, R. D., Goss, W. M., Kotanyi, C. G., & Skellern, D. J. 1978, Astronomy and Astrophysics, 69, L21

Ekers, R. D., Wall, J. V., Shaver, P. A., et al. 1989, Monthly Notices of the RAS, 236, 737

Elvis, M. 2012, in Journal of Physics Conference Series, Vol. 372, Journal of Physics Conference Series, 012032

Emonts, B. H. C., Morganti, R., Oosterloo, T. A., et al. 2008, Monthly Notices of the RAS, 387, 197

Emsellem, E., Cappellari, M., Krajnović, D., et al. 2011, Monthly Notices of the RAS, 414, 888

Emsellem, E., Greusard, D., Combes, F., et al. 2001, Astronomy and Astrophysics, 368, 52

Emsellem, E., Monnet, G., & Bacon, R. 1994, Astronomy and Astrophysics, 285, 723

Faber, S. M., Willmer, C. N. A., Wolf, C., et al. 2007, Astrophysical Journal, 665, 265

Fabian, A. C. 1994, Annual Review of Astronomy and Astrophysics, 32, 277

Fabian, A. C. 2012, Annual Review of Astronomy and Astrophysics, 50, 455

Fanaroff, B. L. & Riley, J. M. 1974, Monthly Notices of the RAS, 167, 31P

Fasano, G., Falomo, R., & Scarpa, R. 1996, Monthly Notices of the RAS, 282, 40

Fathi, K., Axon, D. J., Storchi-Bergmann, T., et al. 2011, Astrophysical Journal, 736, 77

Fathi, K., Lundgren, A. A., Kohno, K., et al. 2013, Astrophysical Journal, Letters, 770, L27

Fathi, K., Storchi-Bergmann, T., Riffel, R. A., et al. 2006, Astrophysical Journal, Letters, 641, L25

Finkelman, I., Brosch, N., Kniazev, A. Y., et al. 2008, Monthly Notices of the RAS, 390, 969

Gallimore, J. F., Axon, D. J., O'Dea, C. P., Baum, S. A., & Pedlar, A. 2006, Astronomical Journal, 132, 546

García-Burillo, S., Combes, F., Usero, A., et al. 2014, Astronomy and Astrophysics, 567, A125

Gaspari, M., Brighenti, F., & Temi, P. 2015, Astronomy and Astrophysics, 579, A62

Gaspari, M., Ruszkowski, M., & Oh, S. P. 2013, Monthly Notices of the RAS, 432, 3401

Gaspari, M., Temi, P., & Brighenti, F. 2017, Monthly Notices of the RAS, 466, 677

Gendre, M. A., Best, P. N., Wall, J. V., & Ker, L. M. 2013, Monthly Notices of the Royal Astronomical Society, 430, 3086

Gendre, M. A., Wall, J. V., & Best, P. 2010, in IAU Symposium, Vol. 267, Co-Evolution of Central Black Holes and Galaxies, ed. B. M. Peterson, R. S. Somerville, & T. Storchi-Bergmann, 109–109

Giovannini, G., Cotton, W. D., Feretti, L., Lara, L., & Venturi, T. 2001, Astrophysical Journal, 552, 508

Giovannini, G., Taylor, G. B., Arbizzani, E., et al. 1999, Astrophysical Journal, 522, 101

Gopal-Krishna & Wiita, P. J. 2000, Astronomy and Astrophysics, 363, 507

Gordon, Y. A., Pimbblet, K. A., Kaviraj, S., et al. 2019, arXiv e-prints, arXiv:1905.00018

Goss, W. M., Danziger, I. J., Fosbury, R. A. E., & Boksenberg, A. 1980, Monthly Notices of the RAS, 190, 23P

Govoni, F., Falomo, R., Fasano, G., & Scarpa, R. 2000a, Astronomy and Astrophysics, Supplement, 143, 369

Govoni, F., Falomo, R., Fasano, G., & Scarpa, R. 2000b, Astronomy and Astrophysics, 353, 507

Graham, A. W. 2004, in American Astronomical Society Meeting Abstracts, Vol. 204, American Astronomical Society Meeting Abstracts #204, 65.07

Greene, J. E., Janish, R., Ma, C.-P., et al. 2015, Astrophysical Journal, 807, 11

Grossova, R., Werner, N., Rajpurohit, K., et al. 2019, arXiv e-prints [[arXiv]1903.03198]

Hardcastle, M. 2018, Nature Astronomy, 2, 273

Hardcastle, M. J., Evans, D. A., & Croston, J. H. 2007, Monthly Notices of the RAS, 376, 1849

Hardcastle, M. J., Worrall, D. M., Kraft, R. P., et al. 2003, Astrophysical Journal, 593, 169

Harrison, C. M. 2017, Nature Astronomy, 1, 0165

Hawking, S. W. 1972, Communications in Mathematical Physics, 25, 152

Heckman, T. M. 1980, Astronomy and Astrophysics, 500, 187

Heckman, T. M. & Best, P. N. 2014, Annual Review of Astronomy and Astrophysics, 52, 589

Heesen, V., Croston, J. H., Morganti, R., et al. 2018, Monthly Notices of the RAS, 474, 5049

Hensley, B. S., Ostriker, J. P., & Ciotti, L. 2014, Astrophysical Journal, 789, 78

Hernquist, L. & Barnes, J. E. 1991, Nature, 354, 210

Heyer, M., Krawczyk, C., Duval, J., & Jackson, J. M. 2009, Astrophysical Journal, 699, 1092

Heywood, I., Blundell, K. M., & Rawlings, S. 2007, Monthly Notices of the Royal Astronomical Society, 381, 1093

Ho, L. C. 2008, Annual Review of Astronomy and Astrophysics, 46, 475

Ho, L. C., Filippenko, A. V., & Sargent, W. L. W. 1997, Astrophysical Journal, 487, 579

Ho, L. C., Li, Z.-Y., Barth, A. J., Seigar, M. S., & Peng, C. Y. 2011, Astrophysical Journal, Supplement, 197, 21

Holt, J., Tadhunter, C. N., González Delgado, R. M., et al. 2007, Monthly Notices of the RAS, 381, 611

Hopkins, P. F., Hernquist, L., Cox, T. J., Robertson, B., & Springel, V. 2006, Astrophysical Journal, Supplement, 163, 50

Hopkins, P. F. & Quataert, E. 2010, Monthly Notices of the RAS, 407, 1529

Hopkins, P. F. & Quataert, E. 2011, Monthly Notices of the RAS, 415, 1027

Horellou, C., Black, J. H., van Gorkom, J. H., et al. 2001, Astronomy and Astrophysics, 376, 837

Ineson, J., Croston, J. H., Hardcastle, M. J., et al. 2015, Monthly Notices of the RAS, 453, 2682

Janssen, R. M. J., Röttgering, H. J. A., Best, P. N., & Brinchmann, J. 2012, Astronomy and Astrophysics, 541, A62

Jones, D. H., Read, M. A., Saunders, W., et al. 2009, Monthly Notices of the RAS, 399, 683

Jungwiert, B., Combes, F., & Palouš, J. 2001, Astronomy and Astrophysics, 376, 85

Kauffmann, G. & Heckman, T. M. 2009, Monthly Notices of the Royal Astronomical Society, 397, 135

Kauffmann, G., Heckman, T. M., Tremonti, C., et al. 2003, Monthly Notices of the Royal Astronomical Society, 346, 1055

Kaviraj, S., Ting, Y.-S., Bureau, M., et al. 2012, Monthly Notices of the RAS, 423, 49

Kellermann, K. I., Sramek, R., Schmidt, M., Shaffer, D. B., & Green, R. 1989, Astronomical Journal, 98, 1195

Kewley, L. J., Groves, B., Kauffmann, G., & Heckman, T. 2006, Monthly Notices of the Royal Astronomical Society, 372, 961

Killeen, N. E. B., Bicknell, G. V., & Ekers, R. D. 1986, Astrophysical Journal, 302, 306

Kim, C.-G., Ostriker, E. C., & Kim, W.-T. 2013, Astrophysical Journal, 776, 1

King, A. & Nixon, C. 2015, Monthly Notices of the RAS, 453, L46

King, A. & Nixon, C. 2018, Astrophysical Journal, Letters, 857, L7

King, A. R. & Pringle, J. E. 2007, Monthly Notices of the RAS, 377, L25

Kinney, A. L., Schmitt, H. R., Clarke, C. J., et al. 2000, Astrophysical Journal, 537, 152

Koay, J. Y., Vestergaard, M., Casasola, V., Lawther, D., & Peterson, B. M. 2016, Monthly Notices of the RAS, 455, 2745

Komissarov, S. S. 1994, Monthly Notices of the RAS, 266, 649

Kormendy, J. & Ho, L. C. 2013, Annual Review of Astronomy and Astrophysics, 51, 511

Kotanyi, C. G. & Ekers, R. D. 1979, Astronomy and Astrophysics, 73, L1

Krajnović, D., Cappellari, M., de Zeeuw, P. T., & Copin, Y. 2006, Monthly Notices of the RAS, 366, 787

Lagos, C. d. P., Davis, T. A., Lacey, C. G., et al. 2014, Monthly Notices of the RAS, 443, 1002

Lagos, C. d. P., Padilla, N. D., Davis, T. A., et al. 2015, Monthly Notices of the RAS, 448, 1271

Laing, R. A. 1988, Nature, 331, 149

Laing, R. A. 1996, in Astronomical Society of the Pacific Conference Series, Vol. 100, Energy Transport in Radio Galaxies and Quasars, ed. P. E. Hardee, A. H. Bridle, & J. A. Zensus, 241

Laing, R. A. & Bridle, A. H. 2002a, Monthly Notices of the RAS, 336, 1161

Laing, R. A. & Bridle, A. H. 2002b, Monthly Notices of the RAS, 336, 1161

Laing, R. A. & Bridle, A. H. 2013, Monthly Notices of the RAS, 432, 1114

Laing, R. A. & Bridle, A. H. 2014, Monthly Notices of the RAS, 437, 3405

Laing, R. A., Jenkins, C. R., Wall, J. V., & Unger, S. W. 1994, in Astronomical Society of the Pacific Conference Series, Vol. 54, The Physics of Active Galaxies, ed. G. V. Bicknell, M. A. Dopita, & P. J. Quinn, 201

Laing, R. A., Parma, P., de Ruiter, H. R., & Fanti, R. 1999, Monthly Notices of the RAS, 306, 513

Lake, G. & Norman, C. 1983, Astrophysical Journal, 270, 51

Lauer, T. R., Faber, S. M., Gebhardt, K., et al. 2005, Astronomical Journal, 129, 2138

Laurikainen, E., Salo, H., Buta, R., et al. 2006, Astronomical Journal, 132, 2634

Ledlow, M. J. & Owen, F. N. 1996, Astronomical Journal, 112, 9

Leroy, A. K., Walter, F., Bigiel, F., et al. 2009, Astronomical Journal, 137, 4670

Li, Y., Mac Low, M.-M., & Klessen, R. S. 2005, Astrophysical Journal, 626, 823

Lilly, S. J., Carollo, C. M., Pipino, A., Renzini, A., & Peng, Y. 2013, Astrophysical Journal, 772, 119

Lim, J., Ao, Y., & Dinh-V-Trung. 2008, Astrophysical Journal, 672, 252

Lin, Y.-T., Shen, Y., Strauss, M. A., Richards, G. T., & Lunnan, R. 2010, The Astrophysical Journal, 723, 1119

Liska, M., Tchekhovskoy, A., Ingram, A., & van der Klis, M. 2019, Monthly Notices of the RAS, 487, 550

Ma, C.-P., Greene, J. E., McConnell, N., et al. 2014, Astrophysical Journal, 795, 158

Maccagni, F. M., Morganti, R., Oosterloo, T. A., & Mahony, E. K. 2014, Astronomy and Astrophysics, 571, A67

Maccagni, F. M., Morganti, R., Oosterloo, T. A., Oonk, J. B. R., & Emonts, B. H. C. 2018, Astronomy and Astrophysics, 614, A42

Maciejewski, W. 2004a, Monthly Notices of the RAS, 354, 883

Maciejewski, W. 2004b, Monthly Notices of the RAS, 354, 892

Malkan, M. A., Gorjian, V., & Tam, R. 1998, Astrophysical Journal, Supplement, 117, 25

Mancuso, C., Lapi, A., Shi, J., et al. 2016, The Astrophysical Journal, 833, 152

Mao, M. Y., Owen, F., Duffin, R., et al. 2015, Monthly Notices of the RAS, 446, 4176

Marconi, A. & Hunt, L. K. 2003, Astrophysical Journal, Letters, 589, L21

Martel, A. R., Turner, N. J., Sparks, W. B., & Baum, S. A. 2000, Astrophysical Journal, Supplement, 130, 267

Martini, P., Dicken, D., & Storchi-Bergmann, T. 2013, Astrophysical Journal, 766, 121

Martini, P. & Pogge, R. W. 1999, Astronomical Journal, 118, 2646

Martini, P., Regan, M. W., Mulchaey, J. S., & Pogge, R. W. 2003, Astrophysical Journal, 589, 774

Mateos, S., Carrera, F. J., Alonso-Herrero, A., et al. 2016, Astrophysical Journal, 819, 166

Mathews, W. G. & Brighenti, F. 2003, Annual Review of Astronomy and Astrophysics, 41, 191

McConnell, N. J. & Ma, C.-P. 2013, Astrophysical Journal, 764, 184

McKinney, J. C., Tchekhovskoy, A., & Blandford, R. D. 2012, Monthly Notices of the RAS, 423, 3083

McMullin, J. P., Waters, B., Schiebel, D., Young, W., & Golap, K. 2007, in Astronomical Society of the Pacific Conference Series, Vol. 376, Astronomical Data Analysis Software and Systems XVI, ed. R. A. Shaw, F. Hill, & D. J. Bell, 127

McNamara, B. R. & Nulsen, P. E. J. 2007, Annual Review of Astronomy and Astrophysics, 45, 117

McNamara, B. R., Rohanizadegan, M., & Nulsen, P. E. J. 2011, Astrophysical Journal, 727, 39

Méndez-Abreu, J., Aguerri, J. A. L., Corsini, E. M., & Simonneau, E. 2008, Astronomy and Astrophysics, 487, 555

Merloni, A. & Heinz, S. 2007, Monthly Notices of the RAS, 381, 589

Mingo, B., Croston, J. H., Hardcastle, M. J., et al. 2019, Monthly Notices of the RAS, 488, 2701

Morganti, R., Holt, J., Tadhunter, C., et al. 2011, Astronomy and Astrophysics, 535, A97

Morganti, R., Killeen, N. E. B., & Tadhunter, C. N. 1993, Monthly Notices of the RAS, 263, 1023

Morganti, R., Oosterloo, T., Oonk, J. B. R., Frieswijk, W., & Tadhunter, C. 2015, Astronomy and Astrophysics, 580, A1

Morganti, R., Oosterloo, T., & Tsvetanov, Z. 1998, Astronomical Journal, 115, 915

Morganti, R., Oosterloo, T. A., Tadhunter, C. N., et al. 2001, Monthly Notices of the RAS, 323, 331

Morganti, R., Parma, P., Capetti, A., Fanti, R., & de Ruiter, H. R. 1997, Astronomy and Astrophysics, 326, 919

Morokuma-Matsui, K., Serra, P., Maccagni, F. M., et al. 2019, , 71, 85

Nagai, H., Onishi, K., Kawakatu, N., et al. 2019, arXiv e-prints, arXiv:1905.06017

Narayan, R. & Yi, I. 1995, Astrophysical Journal, 452, 710

Nayakshin, S., Power, C., & King, A. R. 2012, Astrophysical Journal, 753, 15

Negri, A., Posacki, S., Pellegrini, S., & Ciotti, L. 2014, Monthly Notices of the RAS, 445, 1351

Netzer, H. 2015, Annual Review of Astronomy and Astrophysics, 53, 365

North, E. V., Davis, T. A., Bureau, M., et al. 2019, arXiv e-prints, arXiv:1909.05884

Nyland, K., Young, L. M., Wrobel, J. M., et al. 2016, Monthly Notices of the RAS, 458, 2221

Ocaña Flaquer, B., Leon, S., Combes, F., & Lim, J. 2010, Astronomy and Astrophysics, 518, A9

Okuda, T., Kohno, K., Iguchi, S., & Nakanishi, K. 2005, Astrophysical Journal, 620, 673

Onishi, K., Iguchi, S., Davis, T. A., et al. 2017, Monthly Notices of the RAS, 468, 4663

Oosterloo, T., Morganti, R., Crocker, A., et al. 2010, Monthly Notices of the RAS, 409, 500

Oosterloo, T., Raymond Oonk, J. B., Morganti, R., et al. 2017, Astronomy and Astrophysics, 608, A38

Oser, L., Ostriker, J. P., Naab, T., Johansson, P. H., & Burkert, A. 2010, Astrophysical Journal, 725, 2312

O'Sullivan, E., Sanderson, A. J. R., & Ponman, T. J. 2007, Monthly Notices of the RAS, 380, 1409

Owen, F. N. 1993, Steps Toward a Radio H-R Diagram, ed. H.-J. Röser & K. Meisenheimer, Vol. 421, 273

Owen, F. N. & Ledlow, M. J. 1994, in Astronomical Society of the Pacific Conference Series, Vol. 54, The Physics of Active Galaxies, ed. G. V. Bicknell, M. A. Dopita, & P. J. Quinn, 319

Owen, F. N. & White, R. A. 1991, Monthly Notices of the RAS, 249, 164

Padovani, P. 2016, Astronomy and Astrophysics Reviews, 24, 13

Padovani, P. 2017, Nature Astronomy, 1, 0194

Padovani, P., Alexander, D. M., Assef, R. J., et al. 2017, Astronomy and Astrophysics Reviews, 25, 2

Padovani, P., Miller, N., Kellermann, K. I., et al. 2011, Astrophysical Journal, 740, 20

Parma, P., Murgia, M., Morganti, R., et al. 1999, Astronomy and Astrophysics, 344, 7

Parriott, J. R. & Bregman, J. N. 2008, Astrophysical Journal, 681, 1215

Perley, R. A. & Butler, B. J. 2013, Astrophysical Journal, Supplement, 204, 19

Prandoni, I., Laing, R. A., de Ruiter, H. R., & Parma, P. 2010, Astronomy and Astrophysics, 523, A38

Prandoni, I., Laing, R. A., Parma, P., et al. 2007, in Astronomical Society of the Pacific Conference Series, Vol. 375, From Z-Machines to ALMA: (Sub)Millimeter Spectroscopy of Galaxies, ed. A. J. Baker, J. Glenn, A. I. Harris, J. G. Mangum, & M. S. Yun, 271

Ramos Almeida, C. & Ricci, C. 2017, Nature Astronomy, 1, 679

Randriamampandry, T. H., Combes, F., Carignan, C., & Deg, N. 2015, Monthly Notices of the RAS, 454, 3743

Rau, U. & Cornwell, T. J. 2011, Astronomy and Astrophysics, 532, A71

Rees, M. J. 1978, Nature, 275, 516

Regan, M. W., Thornley, M. D., Helfer, T. T., et al. 2001, Astrophysical Journal, 561, 218

Ricci, T. V., Steiner, J. E., & Menezes, R. B. 2015, Monthly Notices of the RAS, 451, 3728

Rix, H.-W., de Zeeuw, P. T., Cretton, N., van der Marel, R. P., & Carollo, C. M. 1997, Astrophysical Journal, 488, 702

Romeo, A. B. & Mogotsi, K. M. 2017, Monthly Notices of the RAS, 469, 286

Rosen, A. & Hardee, P. E. 2000, Astrophysical Journal, 542, 750

Rosen, A., Hardee, P. E., Clarke, D. A., & Johnson, A. 1999, Astrophysical Journal, 510, 136

Ruffa, I., Prandoni, I., Laing, R. A., et al. 2019a, Monthly Notices of the RAS, 484, 4239

Rupen, M. P. 1999, in Astronomical Society of the Pacific Conference Series, Vol. 180, Synthesis Imaging in Radio Astronomy II, ed. G. B. Taylor, C. L. Carilli, & R. A. Perley, 229

Russell, H. R., McNamara, B. R., Edge, A. C., et al. 2013, Monthly Notices of the RAS, 432, 530

Russell, H. R., McNamara, B. R., Fabian, A. C., et al. 2016, Monthly Notices of the RAS, 458, 3134

Sabater, J., Best, P. N., & Argudo-Fernández, M. 2013, Monthly Notices of the RAS, 430, 638

Sabater, J., Best, P. N., & Heckman, T. M. 2015, Monthly Notices of the Royal Astronomical Society, 447, 110

Salim, S., Rich, R. M., Charlot, S., et al. 2007, Astrophysical Journal, Supplement, 173, 267

Sandage, A. & Brucato, R. 1979, Astronomical Journal, 84, 472

Sanders, R. H. 1981, Nature, 294, 427

Sandstrom, K. M., Leroy, A. K., Walter, F., et al. 2013, Astrophysical Journal, 777, 5

Sarzi, M., Falcón-Barroso, J., Davies, R. L., et al. 2006, Monthly Notices of the RAS, 366, 1151

Schawinski, K., Urry, C. M., Simmons, B. D., et al. 2014, Monthly Notices of the Royal Astronomical Society, 440, 889

Scheuer, P. A. G. & Feiler, R. 1996, Monthly Notices of the RAS, 282, 291

Schiminovich, D., Wyder, T. K., Martin, D. C., et al. 2007, The Astrophysical Journal Supplement Series, 173, 315

Schmitt, H. R., Pringle, J. E., Clarke, C. J., & Kinney, A. L. 2002, Astrophysical Journal, 575, 150

Schmitt, H. R., Ulvestad, J. S., Kinney, A. L., et al. 2001, in Astronomical Society of the Pacific Conference Series, Vol. 249, The Central Kiloparsec of Starbursts and AGN: The La Palma Connection, ed. J. H. Knapen, J. E. Beckman, I. Shlosman, & T. J. Mahoney, 230

Serra, P., Oosterloo, T., Morganti, R., et al. 2012, Monthly Notices of the RAS, 422, 1835

Sérsic, J. L. 1963, Boletin de la Asociacion Argentina de Astronomia La Plata Argentina, 6, 41

Shabala, S. S., Ting, Y.-S., Kaviraj, S., et al. 2012, Monthly Notices of the RAS, 423, 59

Shakura, N. I. & Sunyaev, R. A. 1973, Astronomy and Astrophysics, 24, 337

Simões Lopes, R. D., Storchi-Bergmann, T., de Fátima Saraiva, M., & Martini, P. 2007, Astrophysical Journal, 655, 718

Smith, M. D., Bureau, M., Davis, T. A., et al. 2019, Monthly Notices of the RAS[[arXiv]1903.03124]

Smith, M. W. L., Gomez, H. L., Eales, S. A., et al. 2012, Astrophysical Journal, 748, 123

Smith, R. J., Lucey, J. R., Hudson, M. J., Schlegel, D. J., & Davies, R. L. 2000, Monthly Notices of the RAS, 313, 469

Soares, D. S. L., de Souza, R. E., de Carvalho, R. R., & Couto da Silva, T. C. 1995, Astronomy and Astrophysics, Supplement, 110, 371

Sofue, Y. & Rubin, V. 2001, Annual Review of Astronomy and Astrophysics, 39, 137

Sparks, W. B., Wall, J. V., Thorne, D. J., et al. 1985, Monthly Notices of the RAS, 217, 87

Spinrad, H., Djorgovski, S., Marr, J., & Aguilar, L. 1985, Publications of the Astronomical Society of the Pacific, 97, 932

Storchi-Bergmann, T. & Schnorr-Müller, A. 2019, Nature Astronomy, 3, 48

Strauss, M. A., Weinberg, D. H., Lupton, R. H., et al. 2002, The Astronomical Journal, 124, 1810

Swinbank, A. M., Sobral, D., Smail, I., et al. 2012, Monthly Notices of the RAS, 426, 935

Tadhunter, C., Morganti, R., Rose, M., Oonk, J. B. R., & Oosterloo, T. 2014, Nature, 511, 440

Tadhunter, C. N., Morganti, R., di Serego-Alighieri, S., Fosbury, R. A. E., & Danziger, I. J. 1993, Monthly Notices of the RAS, 263, 999

Tamura, T., Kaastra, J. S., Peterson, J. R., et al. 2001, Astronomy and Astrophysics, 365, L87

Temi, P., Amblard, A., Gitti, M., et al. 2018, Astrophysical Journal, 858, 17

Temi, P., Brighenti, F., & Mathews, W. G. 2007, Astrophysical Journal, 666, 222

Thomas, D., Maraston, C., Bender, R., & Mendes de Oliveira, C. 2005, Astrophysical Journal, 621, 673

Tingay, S. J. & Edwards, P. G. 2015, Monthly Notices of the RAS, 448, 252

Tingay, S. J., Edwards, P. G., & Tzioumis, A. K. 2003, Monthly Notices of the RAS, 346, 327

Tody, D. 1986, in Society of Photo-Optical Instrumentation Engineers (SPIE) Conference Series, Vol. 627, , ed. D. L. Crawford, 733

Tohline, J. E., Simonson, G. F., & Caldwell, N. 1982, Astrophysical Journal, 252, 92

Toomre, A. 1964, Astrophysical Journal, 139, 1217

Tran, H. D., Tsvetanov, Z., Ford, H. C., et al. 2001, Astronomical Journal, 121, 2928

Tremaine, S., Gebhardt, K., Bender, R., et al. 2002, Astrophysical Journal, 574, 740

Tremblay, G. R., Combes, F., Oonk, J. B. R., et al. 2018, Astrophysical Journal, 865, 13

Tremblay, G. R., Oonk, J. B. R., Combes, F., et al. 2016, Nature, 534, 218

Urry, C. M. & Padovani, P. 1995, Publications of the Astronomical Society of the Pacific, 107, 803

Valentini, M. & Brighenti, F. 2015, Monthly Notices of the RAS, 448, 1979

van Albada, T. S., Bahcall, J. N., Begeman, K., & Sancisi, R. 1985, Astrophysical Journal, 295, 305

van de Ven, G. & Fathi, K. 2010, Astrophysical Journal, 723, 767

van de Voort, F., Davis, T. A., Kereš, D., et al. 2015, Monthly Notices of the RAS, 451, 3269

van de Voort, F., Davis, T. A., Matsushita, S., et al. 2018, Monthly Notices of the RAS, 476, 122

van der Kruit, P. C. & Shostak, G. S. 1982, Astronomy and Astrophysics, 105, 351

Van Dokkum, P. G. & Franx, M. 1995, Astronomical Journal, 110, 2027

Veilleux, S., Cecil, G., & Bland-Hawthorn, J. 2005, Annual Review of Astronomy and Astrophysics, 43, 769

Venturi, T., Giovannini, G., Feretti, L., Comoretto, G., & Wehrle, A. E. 1993, Astrophysical Journal, 408, 81

Venturi, T., Morganti, R., Tzioumis, T., & Reynolds, J. 2000, Astronomy and Astrophysics, 363, 84

Verdoes Kleijn, G. A. & de Zeeuw, P. T. 2005, Astronomy and Astrophysics, 435, 43

Verdoes Kleijn, G. A., van der Marel, R. P., Carollo, C. M., & de Zeeuw, P. T. 2000, Astronomical Journal, 120, 1221

Véron-Cetty, M. P. & Véron, P. 2001, Astronomy and Astrophysics, 375, 791

Vila-Vilaro, B., Espada, D., Cortes, P., et al. 2019, Astrophysical Journal, 870, 39

Wada, K. & Habe, A. 1992, Monthly Notices of the RAS, 258, 82

Wada, K., Meurer, G., & Norman, C. A. 2002, Astrophysical Journal, 577, 197

Wada, K., Papadopoulos, P. P., & Spaans, M. 2009, Astrophysical Journal, 702, 63

Wagner, A. Y., Bicknell, G. V., & Umemura, M. 2012, Astrophysical Journal, 757, 136

Weijmans, A.-M., Cappellari, M., Bacon, R., et al. 2009, Monthly Notices of the RAS, 398, 561

Welch, G. A., Sage, L. J., & Young, L. M. 2010, Astrophysical Journal, 725, 100

Werner, N., Oonk, J. B. R., Sun, M., et al. 2014, Monthly Notices of the RAS, 439, 2291

Westerlund, B. E. & Stokes, N. R. 1966, Astrophysical Journal, 145, 354

Wiklind, T., Combes, F., & Henkel, C. 1995, Astronomy and Astrophysics, 297, 643

Willott, C. J., Rawlings, S., Blundell, K. M., & Lacy, M. 1999, Monthly Notices of the RAS, 309, 1017

Wilson, A. S. & Colbert, E. J. M. 1995, Astrophysical Journal, 438, 62

Wright, E. L., Eisenhardt, P. R. M., Mainzer, A. K., et al. 2010, Astronomical Journal, 140, 1868

Wrobel, J. M. & Walker, R. C. 1999, in Astronomical Society of the Pacific Conference Series, Vol. 180, Synthesis Imaging in Radio Astronomy II, ed. G. B. Taylor, C. L. Carilli, & R. A. Perley, 171

Yan, R. & Blanton, M. R. 2012, Astrophysical Journal, 747, 61

York, D. G., Adelman, J., Anderson, John E., J., et al. 2000, Astronomical Journal, 120, 1579

Young, L. M., Bureau, M., Davis, T. A., et al. 2011, Monthly Notices of the RAS, 414, 940

Young, L. M., Scott, N., Serra, P., et al. 2014, Monthly Notices of the RAS, 444, 3408

Yuan, C. & Yen, D. C. C. 2004, in Astronomical Society of the Pacific Conference Series, Vol. 323, Star Formation in the Interstellar Medium: In Honor of David Hollenbach, ed. D. Johnstone, F. C. Adams, D. N. C. Lin, D. A. Neufeeld, & E. C. Ostriker, 67

Zhuravlev, V. V., Ivanov, P. B., Fragile, P. C., & Morales Teixeira, D. 2014, Astrophysical Journal, 796, 104